Continuous-flow, Well-mixed, Microfluidic Devices for Screening of Crystalline Materials

By

PARIA COLIAIE

B.Sc., Sharif University of Technology, 2016

THESIS

Submitted as partial fulfillment of the requirements
for the degree of Doctor of Philosophy in Chemical
Engineeringin the Graduate College of the
University of Illinois at Chicago, 2021

Chicago, Illinois

Defense Committee:

Dr. Meenesh Singh, Chair and Advisor, Department of Chemical Engineering
Dr. David Eddington, Department of Bioengineering
Dr. Ying Liu, Department of Chemical Engineering
Dr. Nandkishor Nere, Department of Chemical Engineering
Dr. Ian Papautski, Department of Bioengineering
Dr. Jie Xu, Department of Mechanical Engineering

ACKNOWLEDGMENTS

My heartfelt thanks go to all who motivated me, influenced me, and helped me on my way toward my Ph.D. First and foremost, I am extremely grateful to my supervisor, Prof. Meenesh R. Singh, who provided me with invaluable advice, continuous support, and critical guidance and ensured my project was headed in the right direction. He always encouraged me to think and work independently and made my Ph.D. journey enriching. Under his supervision, I have acquired many skills that have helped me become more confident and advance toward my career goal, and I am grateful for what he has offered me.

My sincere gratitude goes to Dr. Nandkishor K. Nere, Dr. Manish S. Kelkar, and Dr. Moussa Boukerche, who provided me with an enormous amount of support since the beginning of my Ph.D. Their insightful feedback and constructive suggestions pushed me to sharpen my thinking and elevated my work significantly. I am deeply grateful for their mentorship and the wonderful summer internship opportunities at AbbVie Inc.These invaluable practical industrial exposures helped me gain an in-depth understanding of crystallization processes and learn about different analysis techniques that further enriched my fundamentals in chemical engineering.

I am extremely grateful to my thesis committee members Dr. David Eddington, Dr. Ying Liu, Dr. Ian Papautski, Dr. Nandkishor Nere, and Dr. Jie Xu from different engineering departments at UIC, who provided valuable advice on my research and career development.

My research has been a highly collaborative effort, and I am grateful to the Process R&D division of AbbVie Inc., North Chicago, for providing me with several internship opportunities to investigate broader applications of my research ideas. I am grateful for the leadership support from Dr. Samrat Mukherjee, Dr. Ahmad Sheikh, and Dr. Shailendra Bordawekar of AbbVie Inc. My

special thanks also go to Dr. John Gaertner, Dr. Daniel Pohlman, Dr. Jie Chen, Dr. Bradley Greiner, Dr. Kushal Sinha, and Dr. Pankaj Shah for their insightful insights and suggestions.

I would also like to acknowledge the financial support from Enabling Technology Consortium (specifically Abbvie, Biogen, Bristol Myers Squibb, and Takeda Pharmaceuticals). Many thanks to all ETC group members for their constructive comments and suggestion: Dr. Akshay Korde, Dr.Marianne Langston, Dr.Chengxiang Liu, Dr.Neda Nazemifard, Dr. Daniel Patience, and Dr. Dimitri Skliar.

I would also like to thank other members of the Materials and Systems Engineering Laboratory at the University of Illinois at Chicago, particularly Aditya Prajapati and Anish V. Dighe, for their support and fruitful discussions about life and research. They truly made my Ph.D. journey enjoyable.

Lastly, I would like to thank all of my friends for their unconditional support and care, my husband, Alireza, who has been a constant source of support and was always there with a helping hand and loving words, and my parents and my sisters have supported and continue to motivate me throughout my career.

DEDICATION

This thesis is dedicated to my beloved husband Alireza, who has always supported me in each and every challenge in my Ph.D. journey. I would also like to dedicate my thesis to my parents back in Iran.

CONTRIBUTION OF AUTHORS

Chapter 1 provides a general overview of the dissertation. First, the state of knowledge is outlined, followed by the research objectives and the significance of the study. Toward the end of this chapter, I outline the topics discussed in the following chapters of my dissertation.

Chapters 2 and **3** discuss two published works in the Lab on Chip journal (LoC) which I was the first author, primary, and one of the major contributors to the research. My research advisor, **Dr. Meenesh R. Singh**, conceived and supervised the project and contributed to the manuscript revision and scientific discussion. Our collaborators **Dr. Manish S. Kelkar** and **Dr. Nandkishor K. Nere** from the Process R&D division of AbbVie Inc, provided critical feedback and helped shape the research, analysis, and manuscript, and provided insights.

Chapter 4 presents the work to the submitted manuscript to the Lab on chip journal (LoC), of which I was the first author, primary, and the major contributor to the research. My research advisor, **Dr. Meenesh R. Singh**, conceived and supervised the project, provided insights, and contributed to the manuscript revision and scientific discussion. Other authors who are our collaborators from Enabling Technology Consortium (ETC: https://www.etconsortium.org/, specifically AbbVie, Biogen, Bristol Myers Squibb, and Takeda Pharmaceuticals) provided insights and critical feedback and helped me to shape the research, analysis, and manuscript.

Chapter 5 discusses an unpublished manuscript in which I was the first author, primary, and major contributor to the research. My research advisor, **Dr. Meenesh R. Singh**, conceived and supervised the project, provided insights, and contributed to the manuscript revision and scientific discussion**. Rabia Ali** helped me with the post-fabrication processes of the 3D-printed devices and performed a few experiments. Other authors who are our collaborators from Enabling Technology

Consortium (ETC: https://www.etconsortium.org/, specifically AbbVie, Biogen, Bristol Myers Squibb, and Takeda Pharmaceuticals) provided insights and critical feedback and helped shape the research, analysis, and manuscript.

Chapters 6 presents an unpublished work in which I was the first author and the primary contributor to the research. My research advisor, **Dr. Meenesh R. Singh**, conceived and supervised the project, provided insights, and contributed to the manuscript revision and scientific discussion. **Aditya Prajapati** helped me with the design and development of the electrochemical sensor and verified the analytical methods. He also permed the machine learning analysis and developed the prediction model for the supersaturation. **Rabia Ali** helped me with electrochemical impedance spectroscopy (EIS) experiments for the batch sensitivity measurements of different metals. Our collaborators **Dr. Manish S. Kelkar** and **Dr. Nandkishor K. Nere** from the Process R&D division of AbbVie Inc, provided critical feedback and helped shape the research, analysis, and manuscript, and provided insights.

Chapters 7 presents an unpublished work in which I was the first author and the primary contributor to the research. My research advisor, **Dr. Meenesh R. Singh**, conceived and supervised the project, provided insights, and contributed to the manuscript revision and scientific discussion. **Aditya Prajapati** helped me with the design and development of the photosensitive turbidity sensor and verified the analytical methods. **Rabia Ali** helped me with the post-fabrication processes of the 3D-printed device and performed multiple experiments regarding the detection of the liquid-liquid phase separation boundaries. Our collaborators **Dr. Manish S. Kelkar** and **Dr. Nandkishor K. Nere** from the Process R&D division of AbbVie Inc, provided critical feedback and helped shape the research, analysis, and manuscript, and provided insights.

Chapter 8 discusses the work to the manuscript, submitted to ACS applied materials and interfaces which I was the first author, primary, and the major contributor to the research. My research advisor, **Dr. Meenesh R. Singh**, conceived and supervised the project, provided insights, and contributed to the manuscript revision and scientific discussion. **Rajan Bhawnani** performed the feed-forward, time-resolved FT-IR for kinetics measurements of HKUST-1. **Aditya Prajapati** performed scanning electron microscopy and obtained the reported SEM images. **Rabia Ali** helped me with the post-fabrication processes of the 3D-printed devices and performed multiple experiments regarding the growth rate measurement using the continuous-flow microfluidic device. Other authors who are our collaborators from Enabling Technology Consortium (ETC: https://www.etconsortium.org/, specifically AbbVie, Biogen, Bristol Myers Squibb, and Takeda Pharmaceuticals) provided insights and critical feedback and helped shape the research, analysis, and manuscript.

Chapter 9 presents an unpublished work initiated by **Ragavendra Hari**, who developed the theoretical formalism, performed the initial version of the analytic and numerical simulations. My research advisor, **Dr. Meenesh R. Singh**, conceived and supervised the project, provided insights, and contributed to the manuscript revision and scientific discussion. **Anish V. Dighe** and I collaborated, planned, and carried out the simulations and worked on the technical details. In addition, I performed the suggested experiment for the validation of the mathematical model. Our collaborators from **Dr. Manish S. Kelkar** and **Dr. Nandkishor K. Nere** from the Process R&D division of AbbVie Inc provided critical feedback and helped shape the research, analysis, and manuscript, and provided insights.

TABLE OF CONTENT

LIST OF FIGURES

LIST OF TABLES

LIST OF ABBREVIATIONS

2D	2 Dimensional
3D	3 Dimensional
AE	Area Enhancement
API	Active Pharmaceutical Ingredient
BMF	Boston Microfluidic Fabrication
CGG	Concentration Gradient Generator
CQA	Critical Quality Attributes
CV	Cyclic Voltammetry
EIS	Electrochemical Impedance Spectroscopy
FBRM	Focused Beam Reflectance Measurement
FDA	Food and Drug Administration
FPCR	Continuous Flow Polymerase Chain Reaction
FT-IR	Fourier Transformation In frared Spectroscopy
GB	Gradient Boosting
GR	Growth Rate
HKUST-1	Hong Kong University of Science and Technology
HT	High Throughput
IPA	Isopropyl Alcohol
LLPS	Liquid-Liquid Phase Separation
MIL-53	Matériaux de l′Institut Lavoisier
ML	Machine Learning

MOF	Metal Organic Framework
NN	Neural Network
o-ABA	o Amino Benzoic Acid
PAT	Process Analytical Technology
PC	Parent Compound
PCR	Polymerase Chain Reaction
PSD	Particle Size Distribution
PVM	Particle Vision and Measurement
RF	Random Forest
SAXS	Small-Angle X-ray Scattering
SD	Standard Deviation
SEM	Scanning Electron Microscopy
SF	Salt Former
SLA	Stereolithography
SVM	Support Vector Machine
TA	Trimesic Acid
TEM	Transmission Electron Microscopy
UIO-66	Universitetet i Oslo
WAXS	Wide-Angle X-ray Scattering
XRD	X-ray Diffraction
ZIF-8	Zeolite Imidazole Framework-8

SUMMARY

Screening crystal polymorphs and morphology and measuring crystallization kinetics in a controlled supersaturated environment is crucial for developing crystallization processes for pharmaceuticals, agrochemicals, semiconductors, catalysts, and other specialty chemicals. The current tools, such as microtiter plates and droplet-based microfluidic devices, are susceptible to supersaturation depletion in small compartments due to crystallization and nucleation. Such variation in supersaturation affects the outcome and leads to impediments during the scale-up of the crystallizer. Here we develop an innovative technique using cyclone mixer designs to study antisolvent crystallization at constant supersaturation maintained by a continuous solution flow. The developed continuous-flow microfluidic mixer device is used to analyze the polymorphs and morphology of o-aminobenzoic acid (o-ABA) at different supersaturations. A comparative study is done with a microtiter plate assay to demonstrate the effect of the supersaturation depletion on the polymorphs and morphology in the batch screening systems.

To further extend the throughput scale of the continuous-flow screening, a multi-well microfluidic device is proposed for parallel continuous-flow screening. A flow-controlled microfluidic device for parallel and combinatorial screening of crystalline materials can profoundly impact the discovery and development of active pharmaceutical ingredients and other crystalline materials. While the existing continuous-flow microfluidic devices allow crystals to nucleate under controlled conditions in the channels, their growth consumes solute from the solution leading to variation in the downstream composition. The materials screened under such varying conditions are not quite reproducible in large-scale synthesis. There exists no continuous-flow microfluidic device that traps and grows crystals under controlled conditions for parallel screening. Here, we illustrate the blueprint of such a microfluidic device that has parallel-connected micromixers to

trap and grow crystals under multiple conditions simultaneously. The efficacy of a multi-well microfluidic device is demonstrated to screen polymorphs, morphology, and growth rates of L-histidine via antisolvent crystallization at eight different solution conditions, including variation in molar concentration, vol% of ethanol, and supersaturation.

The developed continuous-flow microfluidic device is then modified to be implemented for cooling crystallization. Cooling crystallization is a well-established technique for developing active pharmaceutical ingredients, driven by the significant solubility difference of active pharmaceutical ingredients (APIs) at higher and lower temperatures. The biggest challenge of continuous cooling crystallization is growing and trapping crystals under controlled temperatures. In the existing continuous-flow microfluidic devices, either the temperature control is not precise, and a temperature gradient exists during the crystal growth, or the crystal growth consumes solute from the solution and leads to variation in the downstream composition. The obtained kinetic data from such varying conditions are not reliable for large-scale synthesis. To overcome this issue, two temperature control strategies are incorporated within the developed continuous-flow microfluidic device to enable continuous-flow cooling crystallization under controlled conditions. The first strategy is implementing a cooling jacket around the micromixer to manipulate the temperature of the entering streams and generate the necessary temperature gradient and driving force for nucleation. In the second strategy, saturated hot and cold streams of API are pumped into the micromixer, and the temperature of the mixture will be lower than the hot saturated stream. The efficacy of these strategies is compared by measuring the equilibrium temperature profile from computational modeling analysis. Additionally, the feasibility of the two temperature control strategies is demonstrated with screening polymorphs, morphology, and growth rates of cooling crystallization of L-glutamic acid.

Moving toward a higher-throughput screening system, we develop a snap-on adaptor that converts every well in a conventional batch screening assay (microtiter plates) into a continuous-flow microfluidic device. Microtiter plate assay is a conventional and standard tool for high-throughput (HT) screening that allows growing, harvesting, and screening crystals. The microtiter plate screening assays require a small amount of APIs in each experiment which is adequate for a solid-state crystal analysis such as X-ray diffraction (XRD) or Raman spectroscopy. Despite the advantages of these high throughput assays, the batch operational nature results in a continuous decrease in the supersaturation during the screening procedure due to crystal nucleation and growth. To benefit from the advantages of these HT screening tools while avoiding the batch type of operations, we developed a snap-on adapter that converts a microtiter plate assay into a continuous-flow microfluidic device. The developed snap-on adaptor is plugged in a 24-well plate assay and implemented for salt screening of naproxen.

Microfluidic sensors are integrated into the developed continuous-flow microfluidic device for extending its application. Sensors are significant assets for quick and sensitive detection inside miniaturized devices where the sample is small. The incorporation of sensors into continuous-flow microfluidic systems allows for precise control of experimental conditions. One of the potential applications of a sensor-integrated microfluidic system is to measure the concentration of the solution. In this study, we have paired the previously developed continuous-flow microfluidic mixer with an electrochemical sensor to enable in-situ measurement of the supersaturation during an antisolvent crystallization of L-histidine in a water-ethanol mixture. The sensitivity of different metals towards L-histidine is measured in a batch system to choose the best material for the sensor. The chosen metal is subsequently used as the working electrode of a three-electrode surface printed sensor attached below the continuous-flow microfluidic device. The sensor is externally connected

to a potentiostat device, and anodic cyclic voltammetry slopes are measured. The sensor is calibrated for different ratios of antisolvent and concentrations of L-histidine. Additionally, machine learning algorithms were implemented to develop a supersaturation prediction model from the experimental data.

One of the other sensors integrated within the microfluidic platform is a photosensitive turbidity sensor that can identify the liquid-liquid phase separation (LLPS) boundaries. This phenomenon is also known as oiling-out, which is the appearance of a droplet in a supersaturated solution. Oiling-out is a common phenomenon among hydrophobic pharmaceutical compounds. However, the spontaneous nature of the transformation of oil droplets into solids makes LLPS very hard to control. As a result, it is considered an undesired phenomenon and is typically avoided during crystallization.

Consequently, the most critical step is to obtain the phase diagram to ensure the crystallization does not occur within the LLPS zone. The developed microfluidic mixer is coupled with an Arduino chip, a photoresist, and an LED light to detect the formation of the oil droplets within the mixture. This sensor is implemented to detect the LLPS boundaries of the beta-alanine in water and IPA.

The continuous-flow microfluidic device is proposed to be integrated with different sonication tools to be integrated with a prediction model for breakage. An innovative solution to the breakage population balance problem is developed in the final section of this study. Milling or attrition of particles is an important part of many applications, and there is not much of a comprehensive understanding of the mechanisms of this process, and there is no refined analytical approach for

the simple or complex kernels. Through predictive modeling, we demonstrate an innovative approach to understanding milling mechanics.

I. INTRODUCTION

1.1 Background

Crystallization is a key unit operation in chemical and pharmaceutical industries for synthesis, separation, purification, or solid screening[1]. The principle behind crystallization is the finite solubility of a compound in a solvent at a given thermodynamic condition. Consequently, any change toward a state with lower solubility of the compound leads to crystallization. The properties of crystalline products are influenced by operating factors such as the solvent, co-solvent, additives, pH, temperature, pressure, and the choice of solvent[2]. Many potential drug candidates do not meet the criteria for approval in pharmaceutical industries due to poor physicochemical properties that affect their bio pharmacological properties, such as bioavailability, toxicity, and stability[3]. The physicochemical properties of these compounds are generally assessed by screening, crystallization, and subsequently analyzing the solid forms, which is a major factor contributing to the high costs and lengthy turnaround times associated with drug development[4]. The increasing costs and the long turnaround times of drug development have given pharmaceutical companies the incentive to develop more efficient screening strategies before launching a new drug. The development of robust screening systems to adjust the crystal properties such as size distribution, crystal shape, polymorphism, and purity is highly demanding. Based on the insights gained in the discovery phase and screening, drugs formulations, storage, and delivery strategies can be efficiently carried out. The commonly employed screening techniques to identify crystal polymorphs and morphology are classified into four categories depending on their size scales[5]. The first category includes batch crystallizers which can hold between 100 mL to 1 L of solution.

For instance, the 100 mL to 1 L batch crystallizers such as Mettler Toledo EasyMax 402, HEL CrystalSCAN, and Syrris Atlas HD Crystallization may use a few g to 100 g of solute to study growth and nucleation kinetics under well-mixed and well-controlled conditions. While it is expensive and time-consuming to screen crystallization conditions in such a setup, the kinetic data obtained are reliable and can provide consistent results from the lab-scale to large-scale synthesis. The second category includes the mini-batch crystallizers with a total volume of up to 1 mL, such as Crystal16 (Technobis Crystal16®, Crystalline®). However, the smaller size of the crystallizer allows multiple mini crystallizers to run simultaneously in parallel to obtain solubility curves, screen polymorphs, and screen morphology and polymorphs simultaneously. Magnetic stirring in such crystallizers leads to crystal breakage, which is problematic for the screening of morphology.

The third category includes microtiter plates. Microtiter plates of 96, 384, or 1584 wells holding volumes from 1 mL to as low as 1 μL (e.g., Chemspeed Swing Crystal) can evaluate up to 192 conditions per run and ∼10 000 conditions per day to screen salts, co-crystals, polymorphs, and solubility. The microtiter plate assays have been fully automated for high-throughput screening, which requires a small amount of API in each experiment and is amenable to a solid-state analysis of crystals using X-ray diffraction or Raman spectroscopy[5]. Microtiter plates assays were used for studying the effect of compartment volume[6], shape[7], and interface[8] on directing polymorphism[9] [10]and trapping metastable polymorphs[11]. The last category includes microfluidic devices used in batch or continuous-flow screenings. Hanging-drop crystallization[9] is a technique similar to microtiter plate methods, in which several drops of premixed solution are placed onto a substrate and are inspected under a microscope to see their polymorphs and shapes. Microfluidic crystallization is a relatively nascent technology that needs a much smaller volume (<1 μL) and API material per compartment to screen up to 2500 conditions per run. With the development of miniaturized compartments, screening techniques are evolving to accommodate more experiments

on a single device. The current screening techniques are similar to a well-mixed batch crystallizer and allow for controlling external conditions such as temperature and solvent composition but the internal conditions such as supersaturation decrease continuously. Depletion of supersaturation (driver for crystallization) is the major reason for setbacks during the scale-up and technology transfer to manufacturing API and is mainly due to the nucleation and growth of API crystals in a closed, batch environment. Such variation in supersaturation affects the outcome and leads to impediments during the scale-up of the crystallizer. Therefore, a controlled screening technique where crystals can be nucleated and grown in a controlled supersaturation is needed to facilitate the crystallization development process. This type of continuous-flow crystallization screening tool has not yet been developed as it is difficult to achieve a well-mixed condition in a continuous-flow microfluidic device in the absence of convective or mechanical mixing[12,13].

Furthermore, it is difficult to track and monitor crystals when crystallization occurs in a flowing solution leaving the device. Such in-flow crystallization is comparable to batch crystallization since the supersaturation within a small volume of solution containing crystals depletes as crystals are nucleating. An example of the latter issue is a continuous-flow microfluidic device that uses hydrodynamic focusing to mix a solvent and antisolvent followed by inflow crystallization.

High-throughput screening in continuous-flow microfluidic devices requires the simultaneous operation of multiple microchannels. Valve-controlled (active) and hydraulic-network-controlled (passive) approaches are the two ways of automating parallel operations. In valve-controlled approaches, pressure-actuated valves allow automated sampling, dilution, and mixing of up to 648 conditions simultaneously along eight microchannels[14]. The second approach uses a split-flow pyramidal hydraulic network to distribute and mix the primary solutions. Despite distributing

chemicals in microchannels for the parallel screening, the systems are either batch processes or incapable of trapping crystals for solid-state analysis.

The cooling crystallization technique is preferred whenever selective separation of dissolved species is required from a solution without adding any external agents. In order for cooling crystallization to occur, the temperature of the solution must be lowered so that its solubility decreases[15]. In this case, it is critically important to keep the solution at a homogenous temperature and to minimize temperature gradients between the mixture and crystallizers. In conventional flow and batch crystallizers, rapid cooling is typically achieved by incorporating a convection cooling jacket with an external control system. On the other hand, microfluidic devices have quite different temperature control strategies than conventional crystallizes because of their size limitations. There are several types of cooling techniques implemented with the microtiter and microfluidic systems[16,17]. Peltier cooling is a popular thermoelectric cooling method that requires microfluidic devices to be fabricated from materials with higher thermal conductivity. However, most microfluidic devices are made from polymers with a low thermal conductivity resulting in inefficient contact and entrance effects. Another method of cooling microchannels is through endothermic mixing or reaction, which causes temperature gradients along the microchannels because of reduced reaction rates due to the depletion of the reactants.

Alternately, coolants with a higher specific heat capacity can be used to maintain a uniform temperature for the separated droplets. By diffusive heat transfer, droplets flowing cool down continuously. The temperature gradient within a capillary explains why this method is mainly used to study slowly nucleating crystals like proteins with longer onset times. Another method to cool hot solutions is convective mixing of hot and cold solutions. Slugs are formed by mixing hot and cold solutions at T-junctions and pumping them along with air into the channels. However, there

are limitations to this method in terms of accessibility of the temperature and concentration ranges. Regardless of the possibility of imposing supersaturation by cooling, these methods suffer from supersaturation depleting. Furthermore, the nucleated crystals can clog the microchannels.

Pharmaceutical development relies on the advent of high-throughput screening tools that allow studying salt forms, co-crystals, hydrates, and solvates. The most preferred solid form of a compound is normally the most thermodynamically stable. However, the stable form of the compound can have poor solubility. Therefore, salt forms of pharmaceutically acceptable acids and bases are commonly prepared to enhance the bioavailability of APIs. A well or vial-based HT screening device is usually used to analyze crystals. Miniaturized systems have been adapted for multiple experiments to be carried out simultaneously on a single device. Screening techniques that are currently employed resemble well-mixed batch crystallizers. Due to the supersaturation depletion in these batch screening systems, efforts have been made to design a complementary system for the existing batch HT systems to enable continuous screening. Murphy and coworkers developed a continuous-flow HT screening tool by designing a passive micro-assembly for fluidic control for a continuous flow-polymerase-chain reaction chip (FPCR). This development allowed them to take advantage of the existing MicroCFPCR devices, including rapid reactions and reduced reagent consumption, in a continuous-flow mode. Eddington et al. developed a 3D-printed device coupled with gas-permeable membranes applied to a 24-well oxygen control device for standard multi-well plates. Nevertheless, there has not been any complementary part developed to convert a batch HT screening tool to a continuous-flow device for solid-state screening.

Process analytical technology (PATs) instrumentation and sensors are used in batch and continuous screening systems to design, analyze, and control manufacturing processes to ensure the quality of final goods. Measurement techniques such as attenuated total reflectance Fourier-

transform infrared (ATR-FTIR), focused beam reflectance measurement (FBRM), Raman spectroscopy, particle vision and measurement (PVM), electrical capacitance tomography, electrical resistance tomography, and ultrasound tomography are among the most widely used PAT technologies. Microfluidic systems have benefited greatly from sensor technology during the past few decades. A sensor provides fast response times at low cost at low concentrations in complex matrix situations and allows continuous monitoring of multiparametric analysis. The ease of integration and the simplicity of fabrication of sensors make them an excellent addition to microfluidic platforms. Optical sensors measure the refractive index of liquids and solids, which depends on the type and concentration of the dissolved substance. Several drawbacks are associated with using optical sensors in feedback control systems. Light emitted by the ambient environment can interfere with the operation of optical sensors, their dynamic range of detection is limited, and their shelf life is finite due to photobleaching. The fiber optic sensor consists of optical glasses allowing them to measure the API concentrations. Fiber optic sensors have their benefits but are expensive to install and require precise procedures. Infrared spectroscopy can control the desired size and shape during crystallization by monitoring the supersaturation level online. Laser backscattering data are used together to tell if primary and secondary crystal nucleation occurs in the process. However, IR sensors are limited in their detection range, require line of sight, and get obstructed by solid objects, slowing down data transfer.

Meanwhile, electrochemical (EC) sensors offer high resolutions with low energy requirements, making them practical detection tools. However, despite the accurate, repeatable data collection in real-time, EC sensors have not been previously integrated with continuous-flow screening tools for screening the concentration of APIs. Another important phenomenon in crystallization industries is liquid-liquid phase separation (LLPS), known as oiling out. LLPS has detrimental

effects on crystallization since it decreases crystallization rate, triggers agglomeration events, and forms impurities.

Increasing interest in reactive crystallization of metal-organic frameworks (MOFs) is being pursued in materials science and engineering due to the outstanding properties of MOFs.The majority of synthesis routes used for early-stage exploration are batch processes, which suffer from significant drawbacks such as low efficiency, inflexibility for in-situ monitoring, and difficulty tuning the final product. Due to the prolonged synthesis times and the harsh experimental conditions, these synthesis routes do not provide quantitative information about the product formation process. Contrary to batch synthesis, continuous-flow synthesis offers enhanced mass and heat transfers, as well as real-time monitoring. In light of that, microreactors are an excellent tool for performing early stages of testing and optimizing the reaction conditions. Previous studies have focused on developing continuous-flow microreactors to synthesize MOFs. De Vos and coworkers implemented droplet-based microfluidic devices to synthesize MOFs using a self-completing growth mechanism. Kim et al. explored the continuous and ultrafast synthesis of MOF crystals and composites in droplet-based microfluidic devices. T-junction microfluidic designs were also studied for high-temperature synthesis of MOFs by premixing the precursors with high-temperature water flow right before the inlet. These screening techniques have the disadvantage of batch screening (in the case of droplet-based microfluidic devices) or microchannels being clogged caused by nucleation and growth (in the case of T-junction microfluidic devices). So far, no continuous-flow screening system has been developed for the reactive crystallization of MOFs, which does not require harsh experimental conditions while providing reliable kinetic information of MOFs synthesis under controlled conditions.

Solid-state properties such as particle size distribution and morphology significantly affect downstream filtration steps and the quality of the drug substances. That being the case, several post-processing techniques have been widely studied and implemented to break down crystals into the optimum size and ultimately improve the critical quality attributes (CQAs). Particle milling or attrition plays an important role in crystallization industries, but its mechanism is not fully understood, and no analytical method has been developed for obtaining the particle size distribution for the simple or complex kernels. Analytical and numerical solutions have been obtained by a variety of methods such as moments, analytical solutions, and the discretization technique using fixed pivot and moving pivot. However, for a simple prediction of the population balance equation, they resulted in inaccurate results for some kernels, loss of efficiency for multivariate distributions, and lack realism in predicting the entire particle size distribution.

1.2 Research Objectives

The overall motivation of this work is to invent a continuous-flow, microfluidic device that ensures well-mixed and constant supersaturation conditions during crystallization. Upon modification of this microfluidic device, the device can accommodate different types of crystallization, such as antisolvent, cooling, and reactive crystallization. It has also been adapted to accommodate a higher throughput screening process and integrated with a different type of sensor to provide real-time monitoring. The specific research objectives are as follows:

(1) Development of a continuous-flow, well-mixed, microfluidic crystallization device to screen polymorphs, morphology, and crystallization kinetics at controlled supersaturation: We present the first-ever continuous-flow, well-mixed, microfluidic device to screen polymorphs and morphology in a controlled supersaturated environment. The device allows for continuous crystallization of solute by either mixing an antisolvent or cooling a saturated solution. This

innovative continuous-flow microfluidic device creates a vortex that allows crystals to settle down in the costs for further analysis. Additionally, our microfluidic device will also help pharmaceutical companies comply with an FDA initiative to move from batch-based production to continuous manufacturing, spurring the advancements in drug production and lowering costs.

(2) Advancing the design of the continuous-flow microfluidic device for parallel screening of crystal polymorphs, morphology, and kinetics at controlled supersaturation: In this work, we modified a previously reported design of a multi-inlet, single-well microfluidic device via the consolidation of the tangential inlets to eliminate geometric restriction for adjacent wells and the time lag between inlet flow rates. The 3D-printed multi-well microfluidic device is first computationally evaluated and experimentally benchmarked against previously reported screening results of ortho-aminobenzoic acid (o-ABA) and then implemented to screen L-histidine polymorphs and morphology by anti-solvent crystallization. In addition, the multi-well microfluidic device was used to determine the solubility of L-histidine.

(3) Development of on-the-spot quenching techniques for effective implementation of cooling crystallization in the continuous-flow microfluidic device: Here, we developed effective quenching strategies to cool down the inlet solution with minimum possible spatial gradient. The first strategy borrows the principle of jacketed mixed-suspension mixed-product removal reactors designed for batch and semi-batch cooling crystallization on a larger scale. The cooling jacket is implemented around the microwell at the inlet location, where the solution is quenched as it enters. Coolant is recirculated through separate inlets and outlets on the jacket. The second on-the-spot quenching technique involves the mixing of two different saturated solutions at different temperatures. The mixed solution reaches a lower temperature than the entering hot solution and attains a steady supersaturation. The temperature profile is initially evaluated for both strategies at

different flow rates and temperatures of entering solution and coolant and then assessed for the accessible range of supersaturations. The experimental and computational evidence confirm the attainable temperature and supersaturation ranges. These microfluidic devices are 3D-printed and tested to evaluate the growth rate, morphology, and polymorph of L-glutamic acid crystals by cooling crystallization.

(4) Development of a snap-on adaptor that transforms microtiter plates into continuous-flow microfluidic devices for screening crystalline materials: In this study, we developed a snap-on adaptor that can transform any microtiter plate assay into a continuous-flow microfluidic device without demanding many fluid handling systems. Snap-on adapter consists of two separate compartments: The first entails the cyclone mixer design with the merged inlets. Each inlet enters the mixer from two different channels, resulting in homogeneous concentration in each well.nThe second compartment was the flow distributor or concentration gradient generator (CGG). The combination of different combinations of flow distributors and CGGs gives more degrees of freedom for experimental design. In addition, 3D printing has greatly simplified the process. This 24-well plate snap-on microfluidic device was to screen naproxen salt more rapidly and comprehensively.

(5) Integration of an electrochemical sensor with a continuous flow, a microfluidic device for monitoring and predicting supersaturation using the machine learning algorithms: In this study, we integrated the previously developed continuous-flow microfluidic device with an electrochemical sensor to detect and measure the concentration of API. By integrating the sensor into the continuous flow microfluidic device, API crystal screening is given an unprecedented level of control. This system was evaluated to predict the supersaturation for the antisolvent crystallization of L-histidine, and sensor calibration is performed with different antisolvent ratios

and concentrations of L-histidine. The data are then analyzed using machine learning algorithms, leading to developing a supersaturation prediction model.

(6) Integration of a photosensitive sensor with a continuous flow, a microfluidic device for in-line detection of oiling out boundaries: Our turbidity sensor uses an infrared LED and a photodiode to provide indirect turbidity measurements. The turbidity of the mixture is determined by measuring the Infrared scattered light by droplets formed in the mixture and the amount of light absorbed by the emitter. With its low cost, this continuous-flow turbidity sensor is well suited for incorporation into miniaturized continuous-flow reactors.

(7) Developed patterned-surfaces microfluidic devices for rapid screening of metal-organic frameworks to gain insights into polymorphism and non-monotonic growth: In this study, we developed a continuous-flow approach for reactive crystallization of MOFs that eliminates the need for harsh experimental conditions. This study utilizes a 3D-printed microfluidic device coupled with in-situ imaging and Fourier Transformed Infrared (FT-IR) to investigate the growth kinetics. The previously developed continuous-flow microfluidic device was enhanced with a patterned surface to compensate for the slow settling speed of nano-sized crystals.

(8) Fundamental insights into crystal breakage pathways using the transition matrix: In this study, we have proposed the integration of the microfluidic mixer with sonication tools for developing a novel solution to the breakage problem, which involves minimum calculation as opposed to the existing solutions and can be automated for studying breakage problems or used for solving similar problems.

1.3 Outline of Thesis

In total, this thesis consists of ten chapters. In **chapter 1**, the reader will learn about the current state of continuous-flow microfluidics and their implementation in different types of crystallization, including antisolvent, cooling, reactive, and oiling out. It also describes state of the art for continuous-flow high-throughput systems and integrating sensors and feedback control within existing technologies.

Chapter 2 presents my published research on designing and developing the continuous-flow microfluidic device for antisolvent crystallization under controlled supersaturation. The article published on the results of this work is entitled "Continuous-flow, well-mixed, microfluidic crystallization device for the screening of polymorphs, morphology, and crystallization kinetics at controlled supersaturation." Further, it outlines the objectives, research plans for possible modifications to this continuous-flow micromixer, and future applications of this system in the following chapters.

Chapter 3 presents the first-ever comparative device for a continuous-flow microfluidic device that traps and grows crystals under controlled conditions for parallel screening. The results of this study have been published under the title "Advanced continuous-flow microfluidic device for parallel screening of crystal polymorphs, morphology, and kinetics at controlled supersaturation.

Chapter 4 introduces temperature control approaches for the developed continuous-flow microfluidic device that enables continuous-flow cooling crystallization under controlled conditions. This study demonstrates the feasibility of the two temperature control strategies for screening polymorphs, morphology, and growth rates of cooling crystallization of APIs.

Chapter 5 outlines the development of a snap-on adapter that converts a microtiter plate assay into a continuous-flow microfluidic mixer device and enables high-throughput screening of crystalline materials. Throughout the next two chapters, we demonstrate the potential of

integrating sensors with the developed continuous-flow microfluidic device. Sensors provide quick and sensitive detection and allow for precise control of the crystallization process.

Chapter 6 describes how a continuous-flow microfluidic mixer is coupled with an electrochemical sensor to measure supersaturation in-situ. By using machine learning algorithms, the supersaturation is predicted precisely with the electrochemical sensor.

Chapter 7 introduces a continuous-flow microfluidic device with an integrated photosensitive turbidity sensor to detect the boundary of the liquid-liquid phase separation to prevent oiling out crystallizations.

Chapter 8 discusses how patterned surfaces can be integrated into the continuous-flow microfluidic device to increase surface area and promote the crystallization of metal-organic frameworks (MOFs).

Finally, **chapter 9** discusses the future integration of the continuous-flow microfluidic mixer with sonication tools and the development of a novel solution to the population balance equation to develop a model for the breakage problem. By integrating sonication tools with continuous-flow microfluidic devices, particle size distributions can be predicted through this model.

II. CONTINUOUS-FLOW, WELL-MIXED MICROFLUIDIC CRYSTALLIZATION DEVICE FOR SCREENING OF POLYMORPHS, MORPHOLOGY, AND CRYSTALLIZATION KINETICS AT CONTROLLED SUPERSATURATION

Reproduced from Ref.41 with permission from Royal Society of Chemistry

2.1 Introduction

Crystallization is an industrially important unit operation for the isolation, purification, and manufacturing of a wide range of inorganic and organic materials, including pharmaceuticals, agrochemicals, semiconductors, catalysts, metal-organic frameworks, and other specialty chemicals[1]. Developing and subsequently controlling a crystallization process is challenging due to various factors such as solute, solvent, co-solvent, additives, pH, temperature, pressure, and hydrodynamic conditions affecting the physical properties of crystals[2]. It is often required to isolate a desired polymorphic or solvate form of crystalline material while maintaining the high crystal quality with respect to morphology (or shape) and size distributions[7]. Organic molecules such as active pharmaceutical ingredients (API) can take multiple polymorphic forms with distinctive physicochemical properties[18,19] affecting bioavailability in the human body when administrated orally. Therefore, the theoretical or experimental understanding of polymorphism is important in the early stages of drug development and during phase trials in pharmaceutical industries[20]. Since most theoretical models[8,21-24] rely on parameters estimated from representative crystallization experiments, their scope of predicting polymorph, morphology, and crystal size is limited to the range of those crystallization conditions. It usually fails to predict crystallization beyond the conditions used to estimate model parameters.

Therefore, the experimental screening techniques are frequently employed in the early stage of crystallization process development to identify solution composition and crystallization conditions

favoring specific polymorph and morphology of crystals. The screening techniques to identify crystal polymorphs and morphologies can be categorized into four types based on their size scales[25,26] – (i) 100 mL to 1 L batch crystallizers, (ii) mini-batch crystallizers, (iii) microtiter plates, and (iv) microfluidic devices. For example, the 100 mL – 1L batch crystallizers such as Mettler Toledo EasyMax 402, HEL CrystalSCAN, Syrris Atlas HD Crystallization may use a few grams to 100 grams of solute to study growth and nucleation kinetics in well-mixed and well-controlled conditions. While it is expensive and time-consuming to vary solution compositions and crystallization conditions in such a setup, the kinetic data obtained are reliable and can provide consistent results from the lab- to large-scale synthesis. The mini-batch crystallizers (e.g., Technobis Crystal16®, Crystalline®) of 1 mL volume have a similar design to 100 mL to 1L batch crystallizers. However, the smaller size of the crystallizer allows parallel operation of multiple mini crystallizers to screen up to 16 conditions per run to obtain solubility curve, screen polymorphs, and morphology. The breakage of crystals due to magnetic stirring in such crystallizers is an issue for morphology screening. The microtiter plates of 96-, 384- or 1584-wells holding volumes from 1 mL to as low as one μL (e.g., Chemspeed Swing Crystal) can evaluate up to 192 conditions per run ~10,000 conditions per day to screen salts, co-crystals, polymorphs, and solubility. Microtiter plate technique[27,28] has also been fully automated for high-throughput (HT) screening, requiring a small amount of API in each experiment and is amenable to a solid-state analysis of crystals using either X-ray diffraction (XRD) or Raman spectroscopy[29]. Microtiter plates have also been used to study the effect of compartment volume[30], shapes[31], and interface[32] on directing polymorphism[28,33] and trapping metastable polymorphs[34]. A technique similar to a microtiter plate is the hanging-drop crystallization[28], where several drops of premixed solution are placed on a substrate in a humidified environment, and the polymorphs and shape of crystals are monitored directly under the microscope. Microfluidic crystallization is a relatively nascent

technology that needs much smaller volume < 1 μL and API material per compartment to screen up to 2,500 conditions per run. The drop-generating microfluidic device producing up to 1,000 drops per second has been used to obtain the nucleation and growth kinetics under stationary conditions. Another microfluidic device primarily used for the HT application is the array-based micropatterning system, where several compartments are connected with channels, and sometimes channels are controlled with the elastomeric valves[35-37] for mixing of solvent and antisolvents.

The screening techniques are evolving to accommodate several experiments in a single device by miniaturizing compartments. However, the compartments in the screening techniques (i–iv) mentioned above are similar to a well-mixed batch crystallizer, where the external conditions such as temperature and solvent composition can be maintained constant, but the internal conditions such as supersaturation decrease continuously due to nucleation and growth of crystals and thereby influencing the polymorph formation. Since supersaturation affects polymorphs, morphology, size of the crystals, and crystallization kinetics, the screening techniques may produce relevant polymorphs initially, but then those polymorphs and the associated morphology may gravitate towards a different form because of supersaturation decreasing. Setbacks are often encountered when conditions favoring specific polymorphs obtained from the screening techniques are used in the large-scale crystallizer where supersaturation is more precisely controlled. Therefore, a controlled screening technique where crystals can be nucleated and grown in a controlled supersaturation is needed to facilitate the crystallization development process.

Here we show for the first time a continuous-flow, well-mixed, microfluidic device for the screening of polymorphs and morphology in a controlled supersaturated environment. The device allows for continuous crystallization of solute by either mixing an anti-solvent or cooling a saturated solution. There are two reasons why such a continuous crystallization screening device has not been implemented yet – (i) it is difficult to achieve a well-mixed condition in a continuous-

flow microfluidic device in the absence of convective or mechanical mixing, and (ii) it is hard to track and monitor single crystals when crystallization is occurring in a flowing solution. Moreover, such in-flow crystallization is similar to a batch crystallizer where the supersaturation in a small volume of solution carrying crystals is constantly depleting as crystals are nucleating and growing in it. The later issue is exemplified in the more recent case of a continuous-flow microfluidic device utilizing hydrodynamic focusing to mix solvent and antisolvent followed by in-flow crystallization[38]. A mechanism to trap crystals in a continuous-flow device is necessary to avoid such an issue while continuously feeding supersaturated solutions to the trapped crystals. The study aims to design, implement and evaluate the continuous-flow microfluidic device for screening crystal polymorph and morphology at controlled supersaturation. Various conventional devices such as T-junction, cross-flow, cell-sorter, and novel devices such as H-shaped and cyclone mixer were analyzed theoretically and experimentally. The dimension of the device was optimized by simulating heat, mass, and momentum transfer to attain constant temperature, supersaturation, and mixing, respectively, in the crystallization compartment of the microfluidic device. The optimal geometry of the device was fabricated using a stereolithography 3D printer for affordable production of the microfluidic device. The continuous-flow microfluidic device was evaluated to screen polymorph and morphology of o-aminobenzoic acid (o-ABA) crystals at different supersaturation, and the screening results were compared with the polymorphs and morphology obtained from a conventional 96-well plate assay. The comparative study illustrated that the proposed continuous-flow microfluidic device could resolve metastable and stable polymorphs of o-ABA while the 96-well plate showed the conversion of the metastable polymorph to the stable polymorph and different morphologies at similar supersaturations.

The theoretical and computational methods used to simulate heat, mass, momentum, and particle transport in various geometries are discussed in section 2.2. In section 2.3, details regarding

materials, fabrication method, and the experimental setup to are provided. Section 2.4 shows optimal dimensions of the microfluidic device to operate at a constant temperature, supersaturation, and homogeneous mixing. Various geometries are also evaluated for crystal trapping capabilities. The polymorphs and morphologies of o-ABA at different supersaturations in a continuous-flow microfluidic device are compared with the 96-well plate device. Section 2.5 concludes the study and provides an outlook for enabling HT screening using the continuous-flow microfluidic device.

2.2 Theoretical Methods

Figure 1 shows geometries of various types of continuous-flow microfluidic devices evaluated in this work, including conventional designs such as (A) T-junction, (B) cross-flow, and (C) cell-sorter; and novel designs such as (D) H-shaped, and (E) cyclone mixer. There are three different sections in each design such as (i) thermalizer, (ii) mixer, and (iii) diffuser. The thermalizer allows the entering streams to cool down to attain a homogeneous temperature and desired supersaturation for cooling crystallization. The purpose of the mixer is to facilitate the antisolvent crystallization by passively mixing inlet streams of different solvents to attain homogeneous supersaturation. For cooling crystallization, the mixer is replaced by the thermalizer to attain target supersaturation near the entrance of the diffuser section. Such configurations with a mixer (for antisolvent crystallization) and without a mixer (for cooling crystallization) ensure achieving target supersaturation followed by the onset of crystallization before the solution enters the diffuser section. The diffuser is designed to trap crystals while allowing the mother liquor to flow out smoothly. Each design in Figure 1 has a different mechanism for trapping crystals- T-junction (A) and cross-flow (B) relied on stagnation point to trap crystals, cell-sorter (C) traped crystals in the eddies created by the jetting of inlet stream through the circular portion, H-shaped design (D)

traped crystals in the passive mixer sandwiched between two parallel streams, and cyclone mixer design (E) used gravitational settling to trap crystals in the mixer.

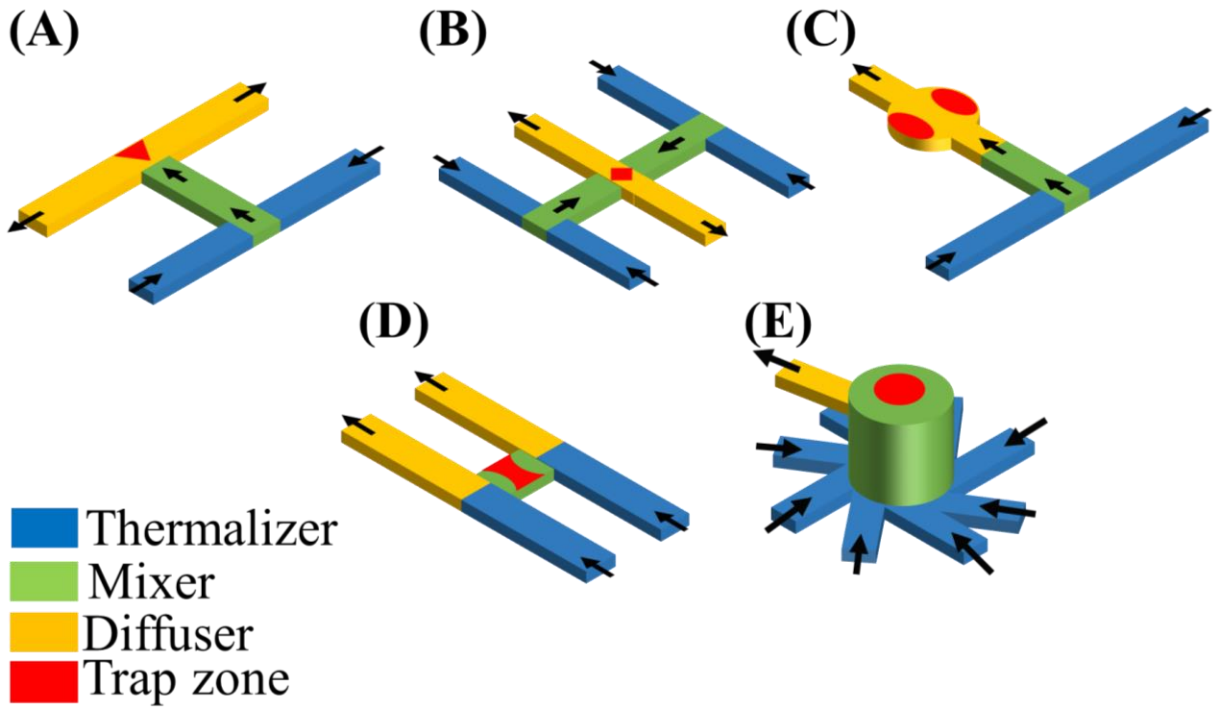

Figure 1: Various geometries of continuous-flow microfluidic devices are considered here to evaluate their ability to trap and grow crystals at constant supersaturation – (A) T-junction, (B) cross-flow, (C) cell-sorter, (D) H-shaped, and (E) cyclone mixer. There are three sections in each geometry – i) thermalizer (blue) to cool down the inlet solution for cooling crystallization, ii) mixer (green) to mix solvents for anti-solvent crystallization, and iii) diffuser (yellow) with trap zone (red) to trap crystals while allowing mother liquor to flow-out.

2.2.1 Heat Transport in Thermalizer

The thermalizer in the microfluidic device can maintain a constant temperature using an external thermoelectric system. In cooling crystallization, the solution entering the microfluidic device cools down as it flows through the thermalizer. Therefore, it is essential to determine the critical length of thermalizer required for the entering solution to achieve, e.g., 99% of the external temperature so that the desired supersaturation can be realized near the diffuser section. The steady-state, extended Graetz problem with Dirichlet wall boundary conditions for square conduit was solved to obtain the dependence of critical length on the velocity of fluid and width of the channel.

2.2.1.1 CFD Simulation of the Temperature Profile in the Thermalizer

The critical length of the thermalizer was calculated from the temperature profile. The Navier-Stokes equation was coupled with the energy balance equation to obtain the temperature profile. First, from the momentum balance or Navier-Stokes equation (eq 1), the velocity profile was calculated and substituted in the energy balance equation. The Navier-Stokes equation is shown as follows:

$$\rho\left(\frac{\partial u}{\partial t} + u.\nabla u\right) = -\nabla p + \nabla.\left(\mu(\nabla u + (\nabla \mathrm{u})^{\mathrm{T}}) - \frac{2}{3}\mu(\nabla.u)I\right) + F \qquad (1)$$

In this equation, u is the fluid velocity vector, p is the fluid pressure, ρ is the fluid density, μ is the dynamic viscosity of the fluid, and F is the vector of external forces. The different terms marked in the equation above are respectively defined as inertial forces (1), pressure forces (2), viscous forces (3), and the external forces which are applied to the fluid (4). The following assumptions were applied to obtain the velocity profile:

- The fluid is incompressible;
- The velocity profile is obtained for 2D flow neglecting the effect of the finite height of the channels to reduce meshing and computation time;
- Flow in the channel is set to be laminar since the calculated Reynolds number for the system is less than 2100;
- No external force other than the gravitational force is applied to the system;

By applying the assumptions mentioned above, the simplified Navier-Stokes equation was simplified to:

$$\rho\left(\frac{\partial v_x}{\partial t} + v_x\frac{\partial v_x}{\partial x}\right) = -\frac{\partial P}{dx} + \left[\frac{\partial \tau_{xx}}{\partial x} + \frac{\partial \partial \tau_{yz}}{\partial y} + \frac{\partial \partial \tau_{zx}}{\partial z}\right] + \rho_x \qquad (2)$$

where τ was shear stress, and v was the component of velocity vector u. The boundary conditions for this system were defined in Table 1:

Table 1: Boundary conditions of the Navier-Stokes equation.

Boundary	**Boundary Condition**
Inlet	The average velocity of laminar flow is set as $u = u_0$ (u_0 is varied from 0.2 to 1 $cm.s^{-1}$)
Outlet	The pressure is set to be equal to atmospheric pressure, $P_0 = 1(atm)$
Walls	No-slip boundary condition, $u = 0$.

From here, the calculated velocity profile was substituted in the energy balance equation shown in equation 3:

$$d_z \rho c_p u.\nabla T + \nabla.q = d_z Q + q_0 + d_z Q_p + d_z Q_{vd} \quad (3)$$

where q is defined as:

$$q = -d_z k \nabla T \quad (4)$$

In equation 4, d_z is the width of the channel, T is the temperature, ρ is the fluid density, c_p is the fluid heat capacity at constant pressure, k is the fluid thermal conductivity, u is the fluid velocity field (substituted from the Navier-Stokes equation), and Q is the heat source (or sink). Several assumptions were considered to simplify the energy balance equation above:

- No external heat source exists in the system;
- The fluid has constant physical properties;

The simplified equation was:

$$\rho c_p \left(v_x \frac{\partial T}{\partial x}\right) = -\left(\frac{\partial q_x}{\partial x} + \frac{\partial q_y}{\partial y}\right) \quad (5)$$

The implemented boundary conditions for the energy balance equation are shown in Table 2.

Table 2: Boundary conditions of the energy balance equation.

Boundary	Boundary Condition
Inlet	$T(y,0) = T_{in} = 25\ ℃$
Outlet	$\frac{\partial T}{\partial x}(y,L) = 0$ or $-n.q = 0$
Walls	$T(W,x) = T_{wall} = 70℃$

This system of equations was solved for a range of inlet velocities from 0.2 to 1 cm.s^{-1} and different values for the inlet width. The relationship between the critical length of the thermalizer, the average fluid velocity, and the width of the channel was then calculated using MATLAB. This result was compared with the second-order dependence of critical length on the velocity obtained from the analysis of the Graetz problem.

2.2.1.2 Graetz Problem and Critical Length of the Thermalizer

The Graetz Problem considers a steady-state heat transfer of a fluid in a channel[39]. The fluid enters with a temperature of T_0 and encounters walls with a temperature of T_{wall}. A 2D sketch of this system is shown in Figure 2.

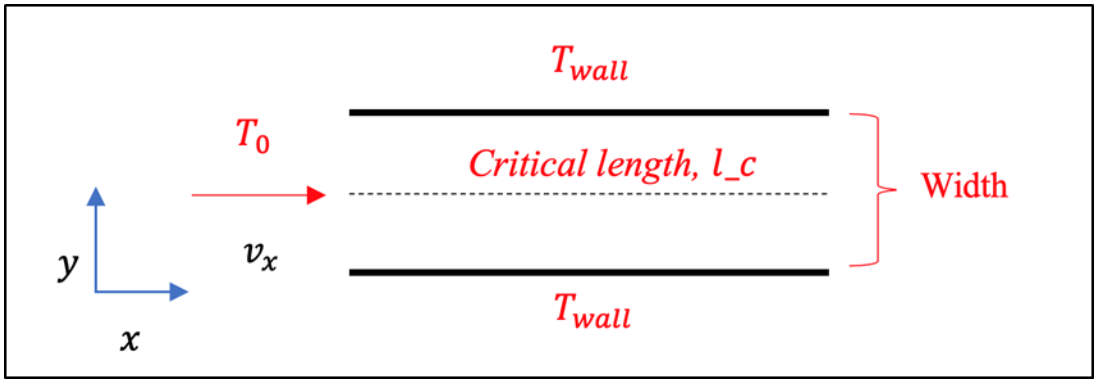

Figure 2: Schematic of the 2D Graetz problem showing the thermalizer channel with boundary conditions of T_0 as the temperature of the entering stream and T_{wall} as the temperature of the walls.

The energy balance equation in the cartesian frame was used to find the temperature profile.

$$\rho c_p \left(\frac{\partial T}{\partial t} + v_x \frac{\partial T}{\partial x} + v_y \frac{\partial T}{\partial y} + v_z \frac{\partial T}{\partial z}\right) = -\left(\frac{\partial q_x}{\partial x} + \frac{\partial q_y}{\partial y} + \frac{\partial q_z}{\partial z}\right) - \left(\frac{\partial \ln \rho}{\partial \ln T}\right)\frac{DP}{Dt} - (\tau : \nabla v) \quad (6)$$

In this equation, v_x, v_y and v_z are velocity in x, y, and z directions, and ρ and c_p were density and specific heat at constant pressure. In order to solve the problem, the following assumptions were applied:

- Fully developed laminar flow;
- Constant physical properties of the fluid/incompressible fluid (ρ, μ, k, c_p are constant);
- The two-dimensional problem in x and y direction which means $v_y = v_z = 0$ and velocity in the x-direction is non-zero;
- Temperature varies in *x* and *y* directions that resulting in $\frac{\partial T}{\partial z} = \frac{\partial q_z}{\partial z}$;
- Viscous dissipation term is ignored, which means $(\tau : \nabla v) = 0$;

The energy balance equation is then simplified to:

$$\rho c_p v_x \frac{\partial T}{\partial x} = \left(\frac{\partial q_x}{\partial x}\right) + \left(\frac{\partial q_y}{\partial y}\right) \quad (7)$$

$$\left(v_x \frac{\partial T}{\partial x}\right) = -\alpha \left(\frac{\partial q_x}{\partial x} + \frac{\partial q_y}{\partial y}\right) \quad (8)$$

and $\alpha = \frac{k}{\rho . c_p}$ is the thermal diffusivity of the fluid.

The velocity field is also assumed to have Poiseuille flow, where v_{max} is the maximum velocity at the centerline.

$$v_x(y) = v_{max}\left(1 - \left({}^{y}/_{W}\right)^2\right) \quad (9)$$

Boundary conditions for solving this equation are shown in Table 3.

Table 3: Boundary conditions of the Graetz problem.

Boundary	**Boundary Condition**
Inlet	$T(y, 0) = T_{in} = 25$ ℃
Centerline	$T\ (0, x)$ is finite or $\frac{\partial T}{\partial y}(0, x) = 0$
Walls	$T(W, x) = T_{wall} = 70$℃

The reduced energy balance equation becomes:

$$v_0\left(1-\left({}^{y}/_{W}\right)^2\right)\left(\frac{\partial T}{\partial x}\right) = -\alpha\left(\frac{\partial^2 T}{\partial x^2}+\frac{\partial^2 T}{\partial y^2}\right) \quad (10)$$

It is also required to de-dimensionalize the variables in the governing equation. The dimensionless variables were defined as:

$$\theta = \frac{T-T_{wall}}{T_0-T_{wall}} \quad (11)$$

$$Y = \frac{y}{W} \quad (12)$$

$$Z = \frac{x}{W.Pe} \quad (13)$$

$$Pe = \frac{W.v_0}{\alpha} \quad (14)$$

Where Z is the dimensionless length, w is the width of the channel, and Pe is the Peclet number. From the two last dimensionless variables, the critical length of the thermalizer can be obtained by substituting the value of Z at θ=0.99 such that:

$$z = Z(\theta).w.Pe = \frac{Z(\theta).w^2.v_0}{\alpha} \quad (15)$$

This equation shows that the critical length of the channel does not change with the wall temperature. However, it varies linearly with the velocity of the fluid and quadratically with the width of the inlet channel.

2.2.2 Mass Transport in the Mixer

The mixing between two or more flowing liquids depends primarily on the angle between inlets conduits, the geometry of the conduits, and velocity of flow. The angle between inlets was 180^o in T-junction (Figure 1A), cross-flow (Figure 1B), and cell-sorter (Figure 1C) designs to provide maximum hydrodynamic mixing. The H-shaped design (Figure 1D) has parallel inlets connecting the mixer such that there is no pressure-driven flow inside the mixer. Therefore, the angle between the inlets does not affect the mixing primarily governed by diffusion. In the case of multi-inlet

cyclone mixer design (Figure 1E), the number of equally spaced inlets determines the angle between them such that the inlet streams are tangential to the mixer, which creates a cyclone.

In the case of T-junction, cross-flow, cell-sorter, and cyclone mixer designs, the critical lengths of mixer required to attain 99% of average composition were determined by solving continuity and Navier-Stokes equations for varying width of the square conduit and average velocity. Since mixing in an H-shaped design is driven by counter-diffusion. The average composition is attained at the center of the mixer; therefore, the critical length is the same as the mixer length.

For designing the mixer, the design parameter chosen is the critical length, defined as the length at which the outlet stream from the mixer attains the homogeneous concentration, which assures homogenous supersaturation for crystallization. This critical length is considered the length at which the concentration reaches 99% of the well-mixed solution. The concentration profile is calculated from solving the transport of diluted species coupled with the Navier-Stokes equations for laminar flow. The mole balance equation for the transport of diluted species is given as:

$$\frac{\partial c_i}{\partial t} + \nabla.(N_i) = 0 \tag{16}$$

where N_i is defined as:

$$N_i = -D_i \nabla c_i + u c_i \tag{17}$$

In equation 17, c_i is the concentration of solute, and D_i is the diffusion coefficient of the solute. Following assumptions were made to simplify and solve this equation:

- The two-dimensional problem in x and y direction;
- The system has convective as well as diffusive fluxes;
- Diffusion coefficient D_i is assumed to be constant in the system;

Equation 18 shows the simplified mass balance equation.

$$\frac{\partial c_i}{\partial t} - D_i \nabla^2 c_i + (u.\nabla) c_i = 0 \tag{18}$$

The appropriate boundary conditions for the mass balance equation are listed in Table 4.

Table 4: Boundary conditions of the mass balance equation

Boundary	**Boundary Condition**
Inlet	The concentration of o-ABA (solute) in the solvent stream is 1 mol.m^{-3}, and in the antisolvent stream is 0 mol.m^{-3}.
Outlet	$-n.D_i\nabla c_i = 0$
Walls	No flux boundary condition ($-n.N_i = 0$)

This system was solved for different velocities in the range of 0.2 to 1 cm.s^{-1} and different values for the inlet width to obtain the critical length of the mixer.

2.2.3 Trajectories of Crystals in the Diffuser

The microfluidic devices shown in Figure 1 were also assessed computationally and experimentally for their ability to trap crystals, which is necessary to measure the nucleation and growth rates using an optical microscope. The designs in Figure 1 have a stagnation zone (marked red) in the diffuser section where the crystals can be trapped for dynamic measurement. First, the trajectories of crystals in the diffuser were computed by solving the Navier-Stokes equation coupled with Langevin's equation involving drag, Brownian, and gravitational forces. In solving for crystal trajectories, identical spherical crystals of 500 μm size were released uniformly at the end of the mixer where the solution is supersaturated. The average distance of the crystals from the stagnation point was obtained from the trajectories of crystals. Next, the Langevin equation was solved coupled with the Navier-Stokes equation to obtain the trajectories of crystals within each of these geometries. In this part, all forces were applied to the crystals to evaluate their trajectories in the diffuser. Crystal trajectories showed whether these crystals flow out from the

device or stay inside the trap zone. By considering the appropriate external forces, the Langevin equation was solved :

$$\frac{d(m_p V)}{dt} = F_t \tag{19}$$

where m_p is the mass of the crystal, V is the velocity vector of the crystal, and F_t is the sum of external forces, including drag force, Brownian force, and gravitational force. The drag force is given as:

$$F_d = \frac{1}{\tau_P} m_P (u - v) \tag{20}$$

where τ_P is the characteristic time scale of crystal motion

$$\tau_P = \frac{\rho_P \, d_P^2}{18\mu} \tag{21}$$

d_p is the diameter of crystal, ρ_P is the density of the crystal, and μ is the average viscosity of the water-ethanol solution. Properties of the crystals are also defined based on the o-ABA used for the experiments. The other external force is the Brownian force, given as:

$$F_B = \zeta \sqrt{\frac{12\pi k_B \mu T r_P}{\Delta t}} \tag{22}$$

where ζ is the Gaussian random number with zero mean and unit variance, k_B is the Boltzmann constant, μ is the viscosity, T is the temperature, and Δt is the time interval for trajectories.

The third force is the gravitational force (in the z-direction) included in the Navier-Stokes equation below.

$$\rho(u.\nabla)u = \nabla[-\mathrm{pl} + \mu(\nabla u) + (\nabla u)^{\mathrm{T}})] + \underline{F} \tag{23}$$

The implemented boundary conditions for this system are listed in Table 5.

Table 5: Boundary conditions for particle trajectories simulations.

Boundary	Boundary Condition
Inlet	Release time: after $5(s)$; Initial position; Density: 10 particles per release
Outlet	Disappear; $q = NaN$
Walls	Bounce; $v = v_c - 2\,(n.v_c)n$

2.3 Materials and Methods

2.3.1 Materials

The crystalline Form-I of o-aminobenzoic acid (o-ABA) or anthranilic acid (Sigma-Aldrich, chemical purity ≥98 %) was used for screening studies. The solutions for crystallization studies were made using deionized water (Sigma-Aldrich, 18 MΩ-cm) as a solvent and ethanol (Sigma-Aldrich, ACS 99.8%) as antisolvent. The reported solubility data of o-ABA in the water-ethanol from Jiang et al. was used in this study[40].

2.3.2 Fabrication of the Microfluidic Device

The 3D designs of the microfluidic device shown in Figure 1 were created using SolidWorks® (2018, Dassault Systems) and printed using stereolithography (SLA) 3D printer (Form2, Formlabs Inc., USA; Viper^{TM} SLA® system, Agile Manufacturing Inc., USA). The dimensions of all 3D-printed devices shown in Figure 1 are listed in Table 6. Here, W×H is the cross-section of the channels, and L is the length of the channels.

Table 6: Dimensions of 3D-printed microfluidic devices in Figure 1.

Device	Thermalizer	Mixer	Diffuser
T-junction	$L = 10\ mm$ $W = 1mm$ $H = 1mm$	$L = 10\ mm$ $W = 1mm$ $H = 1mm$	$L = 21\ mm$ $W = 1mm$ $H = 1mm$
Cross-flow	$L = 10\ mm$ $W = 1mm$ $H = 1mm$	$L = 10\ mm$ $W = 1mm$ $H = 1mm$	$L = 21\ mm$ $W = 1mm$ $H = 1mm$
Cell-sorter	$L = 10\ mm$ $W = 1mm$ $H = 1mm$	$L = 10\ mm$ $W = 1mm$ $H = 1mm$	$L = 10\ mm$ $W = 1mm$ $H = 1mm$ $D = 3\ mm$
H-shaped	$L = 10\ mm$ $W = 1mm$ $H = 1mm$	$L = 1\ mm$ $W = 1mm$ $H = 1mm$	$L = 10\ mm$ $W = 1mm$ $H = 1mm$
Cyclone Mixer	$L = 10\ mm$ $W = 1mm$ $H = 1mm$	$D = 4\ mm$ $H = 4\ mm$	$L = 10\ mm$ $W = 1mm$ $H = 1mm$

In this table, length is denoted as L, width is denoted as W, height is denoted as H, and diameter is denoted as D.

The Form 2 printer, as shown in Figure 3B, utilizes Clear FLGPCL02 resin activated by 405 nm laser to print optically clear microfluidic devices with 150 μm of lateral and 25 μm of axial resolutions. The Clear (FLGPCL02) resin is chemically resistant to various solvents, including ethanol and water. First, the exterior of the 3D-printed microfluidic device was washed for 20 minutes in isopropyl alcohol (IPA) (90%, Sigma-Aldrich) using Form Wash (Formlabs Inc., USA) to remove the residual resin. Next, the interior channels of the 3D-printed device were washed separately by injecting IPA using a syringe. The post-washed, 3D-printed devices were finished by removing supports and curing for 20 minutes using a commercial ultraviolet lamp. Finally, the

optical transparency of the 3D-printed microfluidic device was improved by wet-sanding using 400 to 12000 grit pads followed by spray painting of resin. Alternatively, the crystallization compartment of the microfluidic devices can be left open from the top and sealed separately with the glass coverslip for maximum transparency. A 3D-printed microfluidic device is shown in Figure 3C.

2.3.3 Experimental Setup

Figure 3D shows the experimental setup for polymorph and morphology screening of o-ABA grown via antisolvent crystallization in a continuous-flow microfluidic device at room temperature with water as antisolvent and ethanol as solvent. The microfluidic device was placed on the temperature-controlled stage of the optical microscope (Olympus BX53M, Olympus America Inc.). The dissolved o-ABA[41] in ethanol and pure water were pumped separately into the microfluidic device using programmed syringe pumps (NE-4000, New Era Pump System Inc.).

The o-ABA-ethanol solution and pure water flow rates were adjusted to achieve desired supersaturations (S = 1.2, 1.9, and 2.5). The inlets of the microfluidic device were connected with one-way check valves to avoid backflow from the mixer. The time-lapse images of the crystallization compartment were recorded using a built-in color camera (LC 30, Olympus America Inc.) of the optical microscope under the reflected light mode, which was also processed using MATLAB (MATLAB 9.3, The MathWorks Inc.) to measure growth rates and particle size distribution. The polymorphs of o-ABA at different supersaturations (S = 1.2, 1.9, and 2.5) were identified using (i) distinct morphological features such as Form-I had prismatic morphology whereas Form-II takes needle-like morphology, and (ii) X-ray diffraction (XRD) experiments on Scintag XDS 2000 with Cu Kα radiations. The polymorphs of o-ABA crystals obtained in the continuous-flow microfluidic device at those supersaturations were compared with a 96-well

crystallizer. Alternatively, the crystals can be harvested from the crystallization compartment by uncovering the glass coverslip to identify polymorphs using either XRD or Raman spectroscopy.

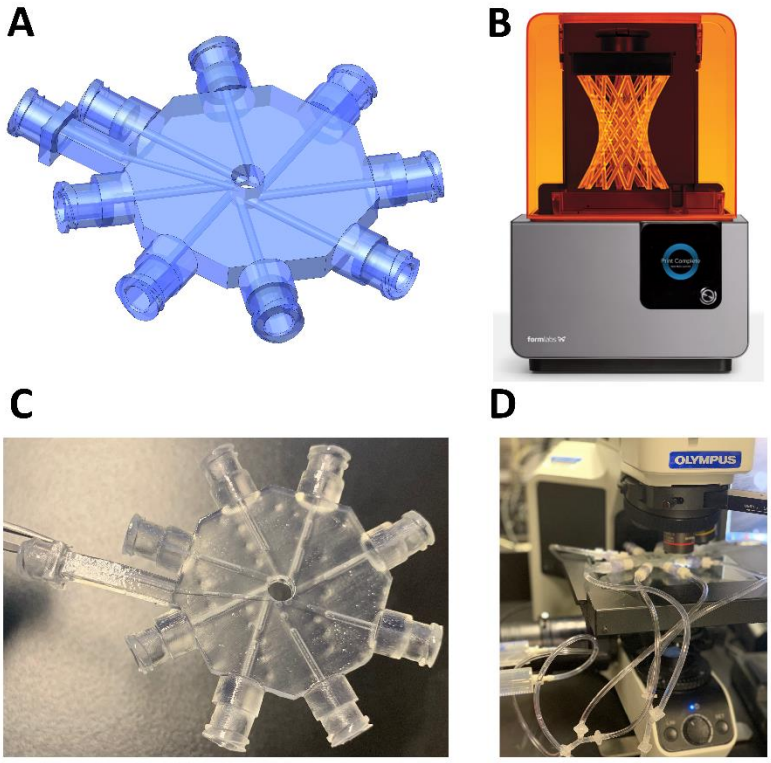

Figure 3: (A) Computer-aided design of the cyclone mixer shown in Figure 1D; (B) Form 2 SLA 3D printer used for printing of microfluidic device; (C) Final finished, 3D-printed cyclone mixer; (D) Cyclone mixer device placed on a temperature-controlled optical microscope and connected with tubes carrying solution and antisolvent through the check valves using a syringe pump.

2.4 Results and Discussion

In the following, the analysis for five different types of microfluidic devices (shown in Figure 1) is presented to guide the selection and design of a continuous-flow, well-mixed, microfluidic device that can be used for screening of polymorphs and morphology in a controlled supersaturated environment.

2.4.1 Optimal Design of the Thermalizer

For the applications based on cooling crystallization, the solution enters the microfluidic device at a higher temperature and cools down as it passes through the thermalizer. Figure 4 shows the critical length of the thermalizer required to attain 99% of the prescribed wall temperature for

different widths of the square channel and the average velocity of the fluid. From the Graetz problem in the absence of the axial conduction in a circular channel, it is well-known that the critical length is proportional to the product of the radius of the channel and the Peclet number. Confirming this analytical result, the simulation results in Figure 4 show a similar trend, such as the critical length varies linearly with the average velocity and almost quadratically with the width of the square channel. The critical length (l_c) was simulated for a broad range of channel widths (w from 1 μm to 1000 μm) and a range of average velocities (v from 0.2 cm.s^{-1} to 1 cm.s^{-1}). The simulated data were fitted to obtain an approximate expression for the critical length:

$$l_T = 134.3\, w^{0.94} v^{1.96} \tag{24}$$

This equation can be used directly to design a thermalizer for various microfluidic applications involving heating or cooling of the fluid. Moreover, equation 24 shows that the critical length is independent of the inlet temperature of the fluid and the external temperature of the wall. This result allows variation of external wall temperature to obtain different supersaturation in the same microfluidic device.

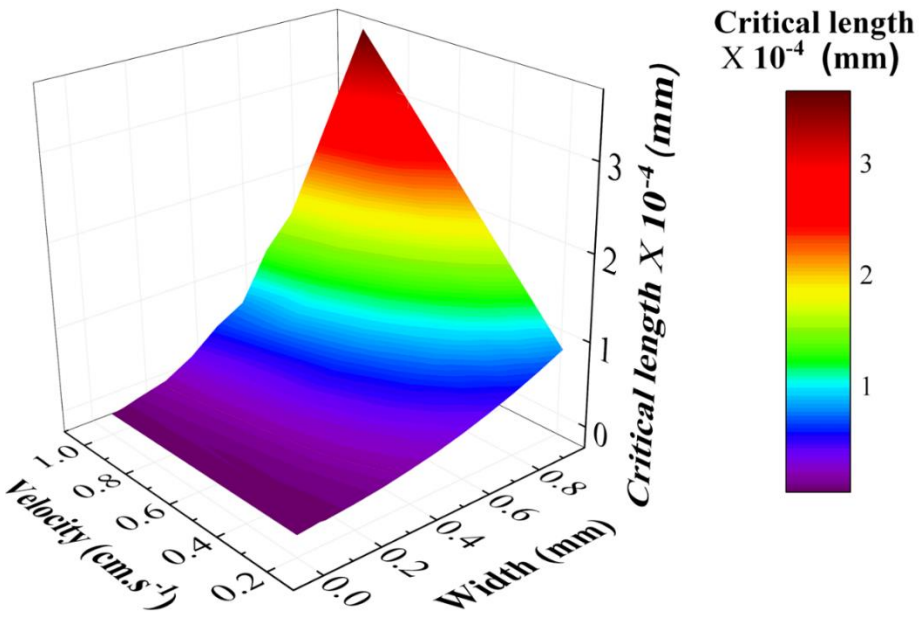

Figure 4: Dependence of the critical length of the thermalizer for entering fluid to attain 99% of the external wall temperature on the width of the square channel and the average velocity of the fluid. The critical length varies almost quadratically with the width and almost linearly with the average velocity.

2.4.2 Effectiveness of Mixing in Different Microfluidic Devices

The mixer in the microfluidic devices facilitates the mixing of solution and antisolvent to create a supersaturated environment for antisolvent crystallization. The mixer may follow the thermalizer when the effect of temperature and solvent composition are sought on the polymorphism and morphology of crystals. The micro-mixers considered in Figure 1 are passive and do not involve any external force to mix liquids as they may interfere with the crystallization process. The microfluidic devices shown in Figures 1A to 1C have a T-shaped passive mixer consisting of two inlets and one outlet. The variation of the critical length of a T-shaped passive mixer vs. the velocity of inlet streams and the width of the inlet channel is shown in Figure 5A. In such mixers, the flow is laminar, and streamlines do not cross over. As a result of this, mixing is not affected by the velocity of the flow. The streamlines and the concentration profile in a T-shaped passive mixer are shown in Figure 5B. Increasing the width of inlet channels increases the volume fraction of two unmixed streams entering the mixer, which requires a longer path for streams to mix passively. Therefore, the critical length of mixing (l_c) in the T-shaped passive mixer increases linearly with increasing the width. Equation 25 shows the relationship between the critical length of the mixer, average velocity, and the width of the mixer.

$$l_c = 3.57w^{0.99} \tag{25}$$

The other type of mixer is the diffusive mixer, as shown in Figure 1D, which relies on the counter-diffusion of the inlet streams to create supersaturation. Counter-diffusion crystallization was applied previously to grow macromolecule crystals that have longer induction time and slower growth kinetics[42]. Such diffusive mixers suffer from stable concentration gradients[42] causing supersaturation to vary across the length of the mixer and the longer time scale for the diffusion of solute. Figure 5C shows that the time scale of mixing increases quadratically with the increasing length of the diffusive mixer. When the time scale of crystallization is shorter than the time scale

of diffusion, the supersaturation variation will be much higher, causing inaccurate screening of polymorphs and morphology. The variation in the supersaturation and the time scale of diffusion can be reduced by using a sub-micrometer scale mixer. Figure 5D shows the streamlines of the fluids and the concentration profile in the H-shaped design based on counter-diffusion.

The third type of mixer considered here is the cyclone mixer (Figure 1E) that creates a rotational flow to mix the inlet fluids effectively. Figure 5E shows the mixing efficiency as a function of the height of the cyclone mixer with 4, 6, and 8 inlets. For a cyclone mixer of fixed height, the intensity of mixing will increase with increasing velocity and decreasing the radius of the mixer. The number of inlets and their diameters determine the minimum radius of the mixer. Figure 5F shows the concentration profile in the 8-inlet cyclone mixer for 0.8 cm s^{-1} of the average velocity of inlet fluids.

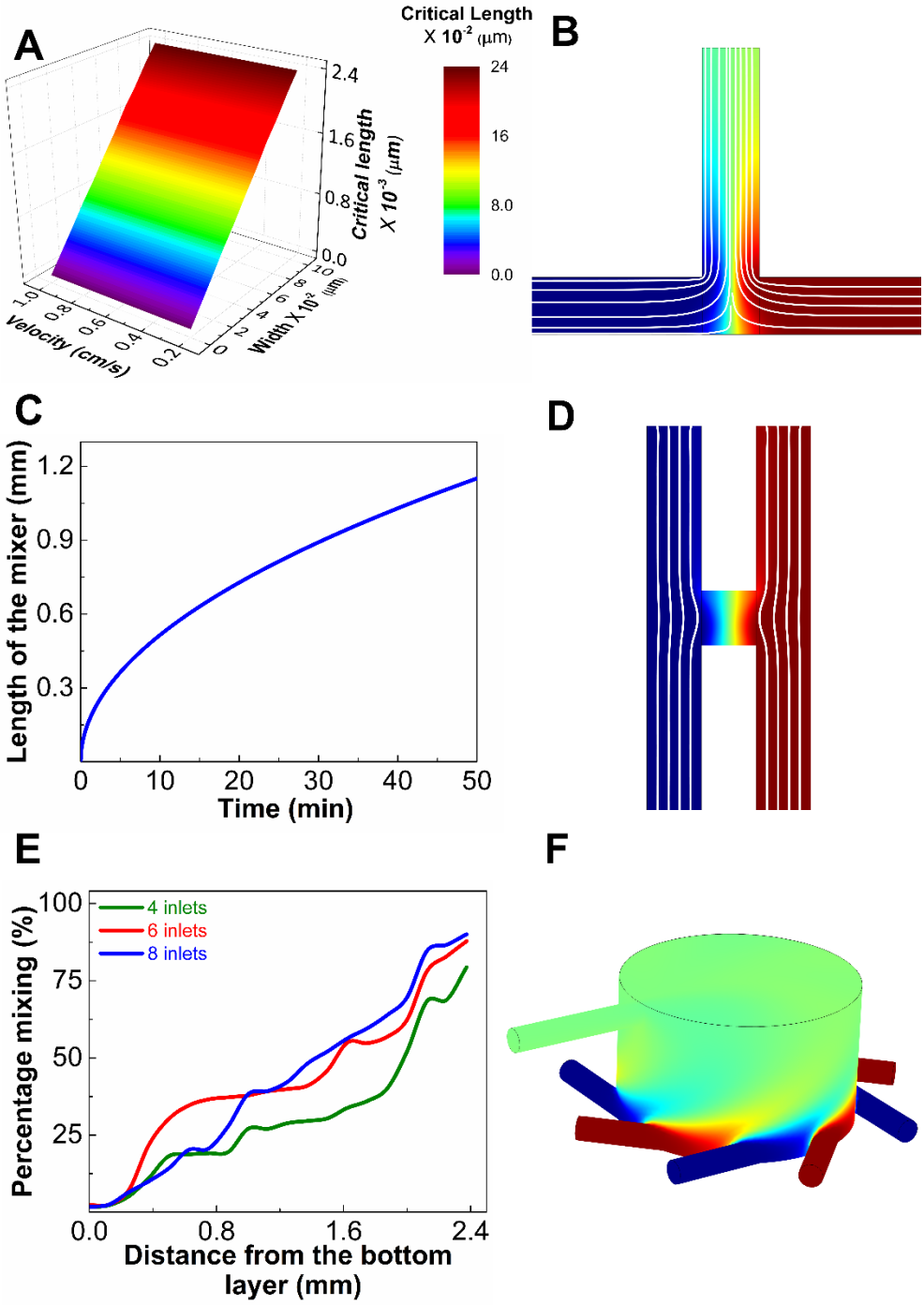

Figure 5: (A) Critical length of T-shaped passive mixer to attain 99% of average composition as a function of the average velocity of the inlet fluid and width of the inlet channel; (B) Steady-state concentration profile in a T-shaped mixer; (C) Time required for the counter-diffusion of solute for different lengths of the diffusive mixer, (D) Steady-state concentration profile in a diffusive mixer; (E) Percentage mixing in the cyclone mixer at different heights for 4, 6, and 8 inlets; (F) Steady-state concentration profile in a cyclone mixer.

2.4.3 Analysis of Trapping of Crystals in the Diffuser

The potential trap zones for the crystals are marked red in Figures 1A to 1E. These trap zones have near-zero velocities locally, allowing crystals to nucleate and grow at a fixed place surrounded by a constant supersaturated environment. Figure 6 shows the mean distance of crystals from the center of trap zones as a function of time for T-junction, cross-flow, cell-sorter, H-shaped, and cyclone mixer designs.

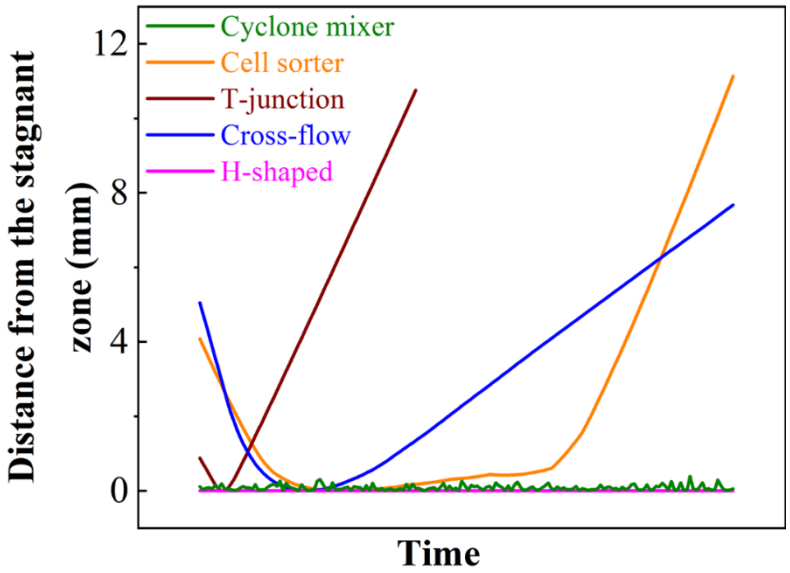

Figure 6: Average distance of crystals from the center of the stagnant zone as a function of time for T-junction, cross-flow, cell-sorter, H-shaped, and cyclone mixer designs. The crystals are released initially at the end of the mixer after inlet fluids are completely mixed. Thus the crystals move towards the stagnant trap zone but eventually deflected from the trap in T-junction, cross-flow, and cell-sorter designs. However, the crystals remained trapped in the H-shaped and cyclone mixer design.

Crystals were released at the end of the mixer length, and the mean distance from the trap zone was calculated. For T-junction, cross-flow, and cell-sorter designs, the crystals move initially towards the traps zone but eventually, their trajectories deflect away from the trap. To better understand the trajectories in all designs, the Stokes number is calculated. Stokes number is defined as the ratio of the characteristic time of the crystal motion to a characteristic time of the flow. The Stokes number is defined as:

$$Stk = \left(\frac{\tau_p U_0}{d_c}\right) \quad (26)$$

where U_0 is the average velocity of fluid, d_c is the characteristic diameter of the conduit, and τ_p is the characteristic time of the crystal motion, defined as:

$$\tau_p = \frac{\rho_p d_p^2}{18\mu} \quad (27)$$

Substituting values of density (2200 kg.m^{-3}), viscosity (0.00109 N.S.m^{-2}), and diameter (300μm), the characteristic time and Stokes number were calculated. In Table 7, the Stokes number of all microfluidic devices is summarized.

Table 7: Stokes number for different microfluidic devices.

Device	d_c	**Stokes Number**
T-junction	1 mm	1.1×10^{-2}
Cross-flow	1 mm	1.1×10^{-2}
Cell-sorter	1 mm	1.1×10^{-2}
H-shaped	1 mm	0
Cyclone Mixer	2 mm	5.5×10^{-3}

As shown in Table 7, the Stokes number for T-junction, cross-flow, and cell-sorter designs is close to 1.1 x 10^{-2}. Since the Stokes number is much less than one, the particles will be flowing along the streamlines. As a result of the lower Stokes number, if some crystals nucleate and grow in the trap zone, the other incoming crystals will knock them away from the trap zone. These simulations confirm that T-junction, cross-flow, and cell-sorter devices cannot trap crystals, and therefore, they are not suitable for the screening of crystals under continuous flow, which was further validated

experimentally. Although the lower Stokes number confirms that crystals are well dispersed in the bulk of the fluid, the crystals nucleating and growing near the wall where the fluid velocity is negligible can settle. The following formula can be used to calculate the settling velocity for the case when $Re \leq 2 \times 10^{5.27}$.

$$W_s = \frac{\upsilon}{d_p}\, d^{*3} \left[38.1 + 0.93\, d^{*\left(\frac{12}{7}\right)}\right]^{-\frac{7}{8}} \tag{28}$$

whereas υ is the fluid kinematic viscosity, d_p is the average size as 300 μm, and d^* is the dimensionless crystal diameter defined as:

$$d^* = \left(\frac{\Delta g}{\upsilon^2}\right)^{\frac{1}{3}} d_p \tag{29}$$

here $\Delta = \frac{\rho_s}{\rho} - 1$, and ρ_s and ρ are particle and fluid density, respectively, and g is the gravitational acceleration. To calculate the value for W_s the density and kinematic viscosity of ethanol: water (1:1) mixture at room temperature were considered. In Table 8, the maximum velocity of the fluid in the cyclone mixer is shown. The settling velocity was higher than the maximum velocity of the fluid in the cyclone mixer, which was obtained from COMSOL simulations.

Table 8: Maximum velocity in the cyclone mixer for different inlet velocities.

Inlet Velocity ($cm.s^{-1}$)	**Maximum Velocity ($cm.s^{-1}$)**
0.1	0.19412
0.2	0.38811
0.3	0.58197
0.4	0.7757
0.5	0.96929
0.6	1.1628
0.7	1.3561
0.8	1.5993
0.9	1.7423
1	1.93

Figure 7 also shows that crystals that grew in the H-shaped and cyclone mixer designs do not move away from the trap zone and can be confined in the mixer for a long time. The lower Stokes number for the H-shaped (Stk = 0) and cyclone mixer (Stk = 5.5×10^{-3}) confirm that crystals are dispersed in the fluid. However, the stagnant liquid zone in the mixer of the H-shaped device and at the bottom of the cyclone mixer will allow crystals to settle. Since the settling velocity of o-ABA crystals of average size 300 μm in 50:50 water-ethanol mixture is 2.83 $cm.s^{-1}$, all the crystals will settle in mixer volume where fluid velocity is less than the settling velocity. Therefore, the crystals grown in the mixer of H-shaped design and near the wall of the cyclone mixer will settle. The H-shaped designs have been previously demonstrated for counter-diffusion crystallization of proteins. Figure 7 shows the anti-solvent crystallization of o-ABA in the H-shaped design. The major issue with the H-shaped design is the variation of supersaturation in the mixer (see Figure 5D), which resulted in the various morphology of o-ABA crystals. Figure 7 shows the variation in morphology and number density of o-ABA crystals along the length of the mixer in the H-shaped

device. The average volume fraction of water was 0.5, corresponding to S = 1.9 at the center of the mixer. Since the supersaturation increases with increasing the volume fraction of water (antisolvent), the gradient in the volume fraction of water caused the gradient in supersaturation, which in turn, resulted in higher nucleation and growth of o-ABA on the right (water side) compared to the left (ethanol side). Due to variation in supersaturations, the crystal morphology and polymorphs varied in the mixer of the H-shaped device. Such variation could be minimized using a shorter mixer length.

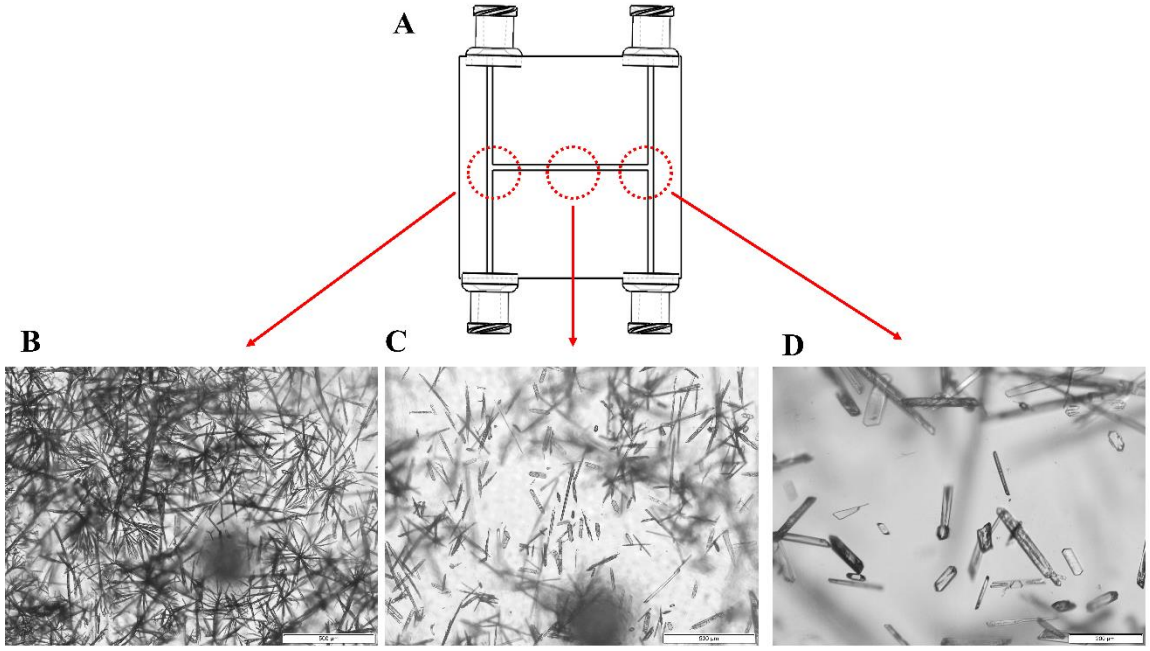

Figure 7: Schematic of the H-shaped design used for o-ABA crystallization at the supersaturation of 1.9. The optical images are obtained at three different locations in the passive mixer of the H-shaped design: (A) ethanol (solvent) side, (B) middle of the mixer, and (C) water (antisolvent) side. The variation in crystal number density and size along the mixer is due to the supersaturation gradient.

In contrast, the inlet fluids were homogeneously mixed in the cyclone mixer microfluidic, and crystals were trapped. The trapped crystals eventually settled at the bottom of the mixer and grew bigger. Due to the above reasons, the cyclone mixer design is better suited for screening crystal polymorphs and morphology at constant supersaturation maintained by continuous flow.

2.4.4 Screening of Polymorphs and Morphology using Continuous-Flow Cyclone Mixer versus a 96-Well Plate Batch Crystallizer

The screening of polymorphs and morphology of o-ABA was conducted using the novel cyclone mixer design and the conventional 96-well plate by varying supersaturation of o-ABA in a water-ethanol mixture. The o-ABA crystallizes into a stable Form-I of prismatic morphology at lower supersaturation ($S < 1.3$) and a metastable Form-II of needle-like morphology at higher supersaturation ($S > 1.8$). Figures 8A and B show prismatic morphology of For- I crystals and needle-like morphology of Form-II crystals grown for 60 seconds in a 96-well plate with initial supersaturation $S = 1.2$ and $S = 1.9$, respectively. Figure 8C shows the metastable Form-II crystals converting into Form-I crystals after 180 seconds in a 96-well plate. Figures 8D and 8E show Form-I and Form-II crystals grown for 60 seconds in the cyclone mixer design at constant supersaturation of $S = 1.2$ and $S = 1.9$, respectively. Figure 8F shows Form-II crystals even after 180 seconds of continuous crystallization. Cyclone mixer and 96-well plate designs initially showed Form-I and Form-II of o-ABA at lower and higher supersaturations. However, the metastable Form-II converted into stable Form-I in a 96-well plate due to the gradual depletion of supersaturation. In contrast, the cyclone mixer was consistently able to grow metastable Form-II at higher supersaturation. Form-I (shown in Figures 8A and 8D) and Form-II (shown in Figures 8B and 8E) are also confirmed in Figures 8G and 8H, respectively, by matching the measured XRD patterns with the standard XRD patterns of o-ABA.

The depletion of supersaturation in the 96-well plate also affects morphologies. Figure 8B shows shorter needle-like morphology of o-ABA, whereas Figure 8E shows a longer needle-like morphology of o-ABA at similar supersaturation. The depletion in supersaturation in the 96-well plate caused needle-like crystals to grow slower than the crystals at constant supersaturation in cyclone mixer design. This variation in morphology is the primary reason why screening results

from 96-well plates cause setbacks during the scale-up of crystallizers as they cannot provide accurate information on morphology and polymorphs.

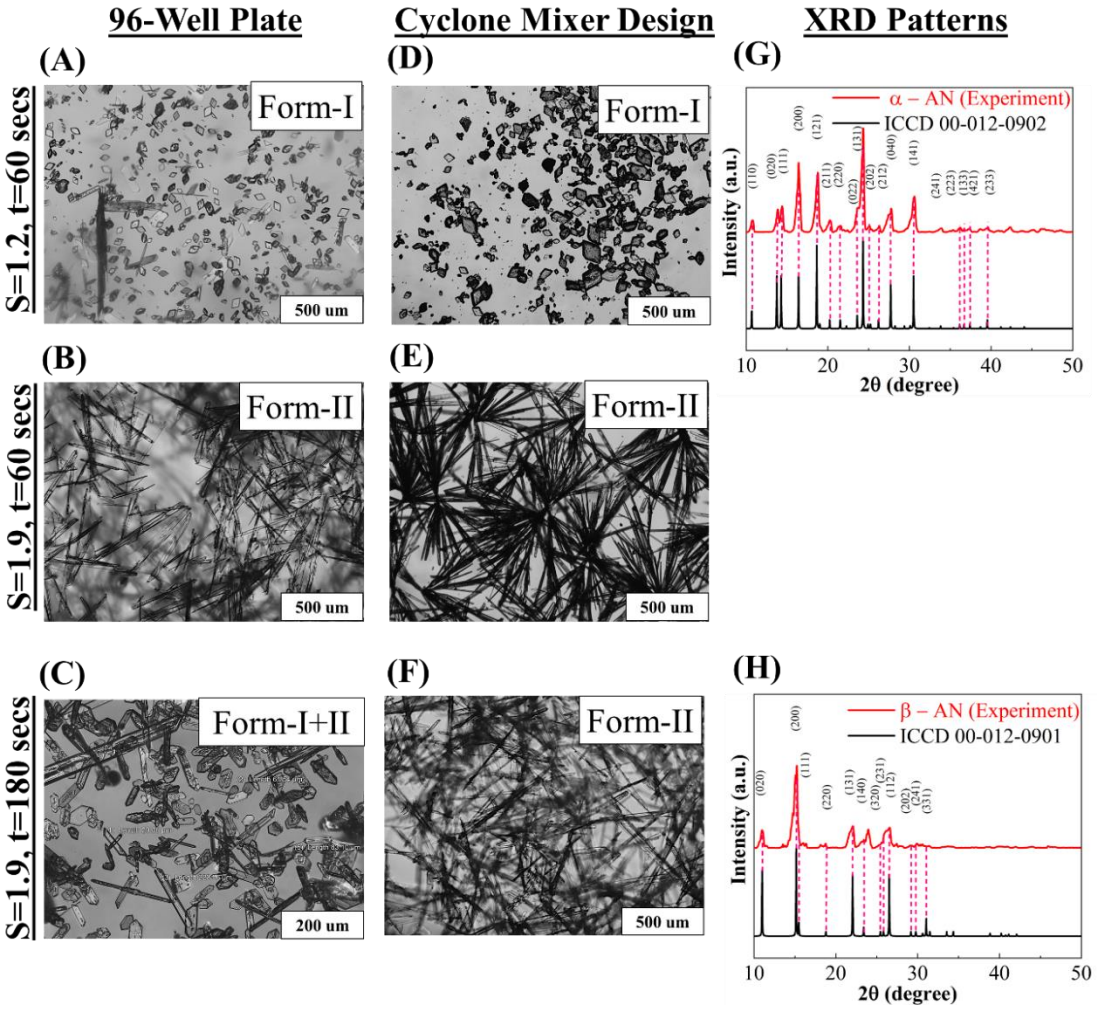

Figure 8: Comparative screening of polymorphs and morphologies of o-ABA obtained using a 96-well plate and cyclone mixer devices. (A) prismatic morphology of stable Form-I of o-ABA grown for 60 seconds in 96-well plate at initial supersaturation of 1.2; (B) Needle-like morphology of metastable Form-II of o-ABA grown for 60 seconds in 96-well plate at initial supersaturation of 1.9; (C) Conversion of needle-like morphology of Form-II to prismatic morphology of Form-I after 180 seconds in 96-well plate at initial supersaturation of 1.9; (D) Prismatic morphology of stable Form-I grown for 60 seconds in cyclone mixer at constant supersaturation of 1.2; (E) Needle-like morphology of metastable Form-II grown for 60 seconds in cyclone mixer at constant supersaturation of 1.9; (F) Needle-like morphology of metastable Form-II even after 180 seconds in cyclone mixer at constant supersaturation of 1.9; (G) XRD patterns for crystals in (A) and (D) confirming Form-I of o-ABA; and (H) XRD patterns for crystals in (F) confirming Form-II of o-ABA.

Figure 9 shows the screening results of o-ABA crystals at a higher supersaturation ratio of 2.5 in 96-well plate and cyclone mixer design. Initially, Form-II appeared in the 96-well plate (Figure 9A), then gradually transformed to Form-I (Figure 9B) after 5 minutes due to depletion of

supersaturation. In contrast, the cyclone mixer grew the metastable Form-II throughout the experiment (see Figure 9C and 9D). The polymorphs were confirmed with measured XRD patterns shown in Figure 9E.

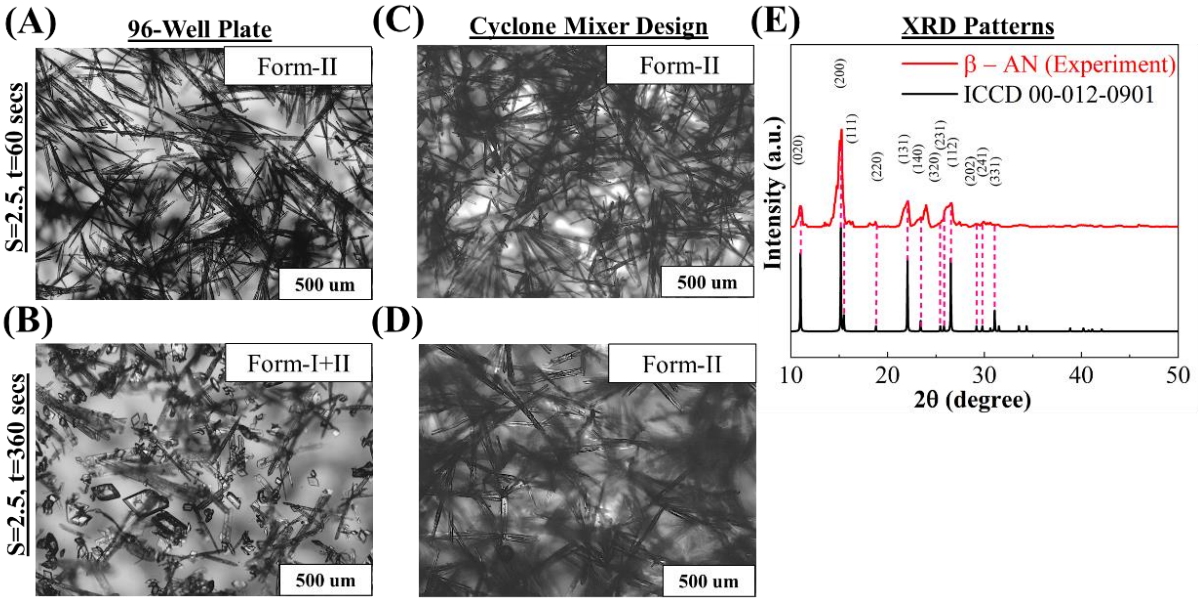

Figure 9: Screening of o-ABA crystals at a higher supersaturation ratio of 2.5 in 96-well plate and cyclone mixer. (A) Needle-like Form-I crystals were observed in the 96-well plate after 60 seconds; (B) Crystals in the 96-well plate after 360 seconds show some Form-II crystals transformed to Form-I (prismatic morphology). (C) Needle-like crystals of Form-I were observed in the cyclone mixer after 60 seconds; (D) More needle-like crystals were observed in the cyclone mixer after 360 seconds; (E) XRD patterns of extracted needle-like crystals confirming Form-II polymorph of o-ABA.

The dynamic evolution of crystal morphology can also measure face-specific growth rates at constant supersaturation using the cyclone mixer design. Time-lapsed images of growing crystals of o-ABA (Form-I) were taken to measure the face-specific growth rate. In Figure 10, an example of these measurements is shown.

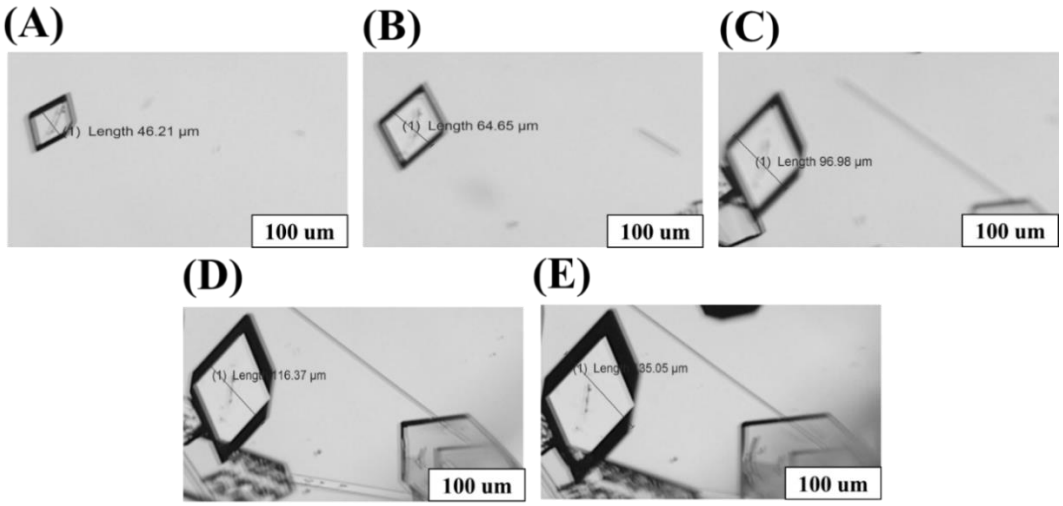

Figure 10: Time-lapsed images of o-ABA crystals (Form-I) taken every 30 seconds while growing at a supersaturation of 1.2 in a cyclone mixer. The distances between two parallel faces of o-ABA crystal are also reported in the images.

The measured growth rate of faces of o-ABA crystal (Form-I) at S = 1.2 is 0.63 $\mu m.s^{-1}$. The cyclone mixer is a robust platform that allows for continuous-flow, well-mixed microfluidic crystallization to screen polymorphs and morphologies of various materials. Since the crystals trapped inside the cyclone mixer grows continuously in a constant supersaturated environment, the entire mixer will eventually fill with the crystals to block the inlet channels for further crystallization. The crystallization in such a continuous-flow microfluidic device stops automatically without any external intervention. Figure 11 shows the size distribution of Form-I o-ABA crystals after 60 seconds at S =1.2 (see Figure 8B)

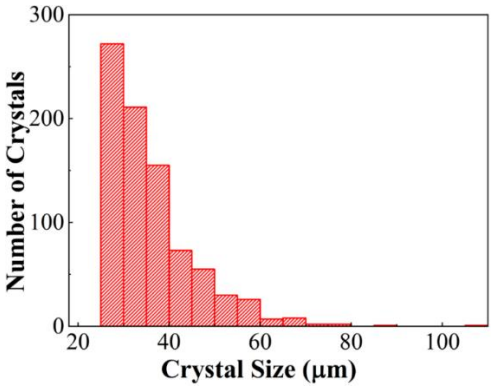

Figure 11: Size distribution of Form-I o-ABA crystals obtained after 60 seconds at S =1.2. This size distribution was obtained by processing crystals shown in Figure 8B.

2.5 Conclusion

Developing techniques for effective screening of crystal polymorphs and morphologies is essential to accelerate the discovery of novel crystalline materials. The current state-of-the-art techniques can simultaneously evaluate up to 1584 conditions using microtiter plates consisting of several compartments of volumes as low as one μL. Although these microtiter plates can be automated to screen ~10,000 conditions per day, the screening results are greatly influenced by the depletion of supersaturation in each compartment of the microtiter plate. The depletion in supersaturation often results in the conversion of metastable form into a stable form. In pharmaceutical industries, almost all the APIs have metastable forms that can convert rapidly into stable forms during screening via solution-mediated transformations (e.g., Ostwald Ripening). Therefore, an effective technique is required to keep supersaturation and other conditions constant during the analysis. Here we showed a robust technique to screen polymorphs and morphologies using a continuous-flow, well-mixed microfluidic crystallizer. Since the US Food & Drug Administration (FDA) supports critical research to spur innovation in continuous manufacturing, such a continuous-crystallization-based screening technique will also provide useful insights into crystallization kinetics applicable to continuous manufacturing.

Here we evaluated five different types of microfluidic devices such as T-junction, cross-flow, cell-sorter, H-shaped, and cyclone mixer to guide the selection and design of a continuous-flow, well-mixed, microfluidic device that can be used for screening of polymorphs and morphology in a controlled supersaturated environment. These devices typically consist of three sections – i) thermalizer for heating/cooling of entering solutions, ii) mixer for passive mixing solution and anti-solvent, and iii) diffuser with traps to isolate crystals from flowing solutions to enable measurement of growing crystals in a constant supersaturated environment. The key design equations for thermalizer (1) and mixer (2) were developed to identify optimal dimensions and

operating velocities for effective cooling and mixing fluids. Although the T-junction, cross-flow, and cell-sorter designs have stagnant zones to trap crystals, the simulation and experimental results show the continuous motion of crystals away from the trap due to the random collision of the trapped crystals with the inflowing crystals. Both H-shaped and cyclone mixer designs showed trapped crystals that grow continuously in a supersaturated environment maintained by the flowing solutions constantly. The H-shaped design has been used previously for counter-diffusion crystallization of macromolecules. However, crystals in the H-shaped mixer design are exposed to varying supersaturation affecting crystal morphology and polymorphs. The H-shaped design is still better for screening crystals with longer induction time and slower growth kinetics.

On the contrary, the cyclone mixer design has more uniform supersaturation allowing crystals to nucleate and grow while keeping them trapped inside the mixer. Thus, cyclone mixer design is ideal for screening metastable forms, which usually converts rapidly to stable forms in batch screening devices like microtiter plate and droplet-based microfluidic devices. This phenomenon is demonstrated in Figure 8, where the metastable Form-II of o-ABA gradually converts into the stable Form-I in a 96-well plate device. Also, the morphologies of crystals and their growth rates measured using a continuous-flow device are more accurate than the morphologies and growth rates obtained from a batch microtiter device at a similar supersaturation.

The proposed cyclone mixer device can be adapted into the existing microtiter plate by tangentially connecting inlet channels to the compartments of the microtiter plate and providing an outlet to every compartment. In addition, the volume, shapes, and interface of the compartment of cyclone mixer design can also be varied to study their effects on nucleation and growth under controlled supersaturation.

III. ADVANCED CONTINUOUS-FLOW MICROFLUIDIC DEVICE FOR PARALLEL SCREENING OF CRYSTAL POLYMORPHS, MORPHOLOGY, AND KINETICS AT CONTROLLED SUPERSATURATION

Reproduced from Ref. 61 with permission from Royal Society of Chemistry

3.1 Introduction

The continuous-flow, well-mixed microfluidic devices have emerged as an effective tool to screen crystal polymorph, morphology, size, and kinetics under controlled crystallization conditions such as supersaturation, temperature, and solvent composition[41]. These devices create cyclonic flow inside the microwell for uniform mixing of a solution while maintaining constant supersaturation. Such devices also overcome the limitations of existing platforms such as continuous flow, well-based, valve-based, and droplet-based microfluidic devices[43], which suffer from the depletion of supersaturation[41]. The continuous-flow microfluidic devices have also evolved to study material synthesis and biological processes under flow-controlled steady-state conditions[12,13]. Some applications of continuous-flow microfluidics include online characterization of nanoparticles[14], combinatorial screening of nanoparticles[44], parallel syntheses of nanoparticles[45], perfusion of cell culture[46], cell-sorting[47], and bioassays[13]. Specific to materials synthesis, most continuous-flow microfluidic devices utilize flow focusing, annular flow, or T/Y junctions to induce fast mixing followed by crystal nucleation and growth. In such flow configurations, the nucleated crystals move along the streamlines while consuming the solute and depleting the supersaturation in the flowing liquid that often leads to undesired morphologic and polymorphic changes. Maintaining constant supersaturation around the crystals in the flowing medium requires diverging crystals away from the streamlines and isolating them.

The rotational flow in the cyclone mixer allows crystals to be separated from the streamlines such that the crystals nucleating in the supersaturated solution can be trapped inside the vortex and grow under constant conditions. Such continuous-flow micromixers have been applied previously to screen crystal morphology, polymorphs, and kinetics with higher accuracy and reliability than microtiter plates[41]. However, these micromixers have not yet been integrated into microfluidic devices to conduct parallel or combinatorial screening for HT applications.

The parallel operation of microchannels is necessary to enable HT screening in continuous-flow microfluidic devices. There are two distinct approaches to automate such parallel, valve-controlled (active) and hydraulic-network-controlled (passive) approaches. The valve-controlled approach involves pressure-actuated valves for automated sampling, dilution, and mixing, which has been recently applied for parallel operation of eight microchannels for combinatorial screening of up to 648 conditions using six different chemicals in a couple of hours[14]. Such microfluidic devices can be fully automated and digitally controlled using computers. Another approach is passive control, where the primary solutions containing different chemicals are distributed and mixed in a split-flow pyramidal hydraulic network to create a range of conditions for parallel and combinatorial screening[48]. Any of these approaches can be applied to distribute chemicals in individual (single-inlet, single-outlet) microchannels in the device. However, the parallel connection and operation of micromixers that have multiple (up to eight) tangential inlets to create cyclonic flow have not been implemented yet. The design and implementation of such parallelly connected multi-inlets micromixers can have a transformative impact on developing robust materials discovery and screening platforms.

In this chapter, a continuous-flow microfluidic device consisting of fully integrated micromixers is designed, implemented, and evaluated for parallel screening of crystal morphology, polymorphs, and growth rates of crystals. Here we have engineered the previously reported design of a multi-

inlet, single-well microfluidic device[41] to develop a multi-well microfluidic device by consolidating the tangential inlets to eliminate geometric restriction for adjacent wells and the time lag between the inlet flow rates. The 3D-printed multi-well microfluidic device is first computationally evaluated and experimentally benchmarked against previously reported screening results of ortho-aminobenzoic acid (o-ABA)[41] and then implemented to screen polymorphs, morphologies, and growth rates of L-histidine crystals grown by anti-solvent crystallization. The multi-well microfluidic device is also used to measure the solubility of L-histidine.

3.2 Theoretical Methods

3.2.1 Design of the Merged-inlet Micromixer in Multi-Well Device

The alternate tangential inlets of the multi-inlet micromixer (Figure 12A) can be consolidated into the merged-inlet configuration (Figure 12B) for their arrangement into an array (Figure 12C) with fewer inlets to enable parallel screening. Without merging the inlets, an array of eight micromixers consisting of four inlets each will yield a total of 32 inlets requiring more pumps with increased difficulty to operate. Merging the alternate inlets decrease the total number of inlets to half; however, it requires a delicate balance of pressure drop between inlets to allow for uniform splitting of flow and mixing in the micromixer. One possible way to merge the alternate (non-neighboring) inlets is to connect them through a Y-junction while keeping them tangential to the micromixer. The Y-junctions for each pair of inlets have vertical offsets to avoid the intersection of inlet channels. Another requirement is to keep the path of both channels merged to be identical to maintain identical pressure drop along each inlet. Figure 12B shows the design of the merged-inlet micromixer with two merged-inlets and one outlet, where one merged-inlet can supply a mixture of an organic molecule (solute) and solvent, and the other merged-inlet includes antisolvent. Figure 12C shows the array of eight such micromixers with 16 merged-inlets and eight outlets. These inlets can be further consolidated using the hydraulic network, as shown in Figure

12D. The merged-inlets of micromixers are connected with three hydraulic networks. The top hydraulic network (blue shaded) allows variation in the solute concentration in each well:

- The hydraulic network in the bottom half (yellow colored) feeds antisolvent to the micromixers;
- The flow rates in these networks control the ratio of solvent to antisolvent in each well;
- The third hydraulic network (green shaded) removes excess crystals (or slurry) from the wells.

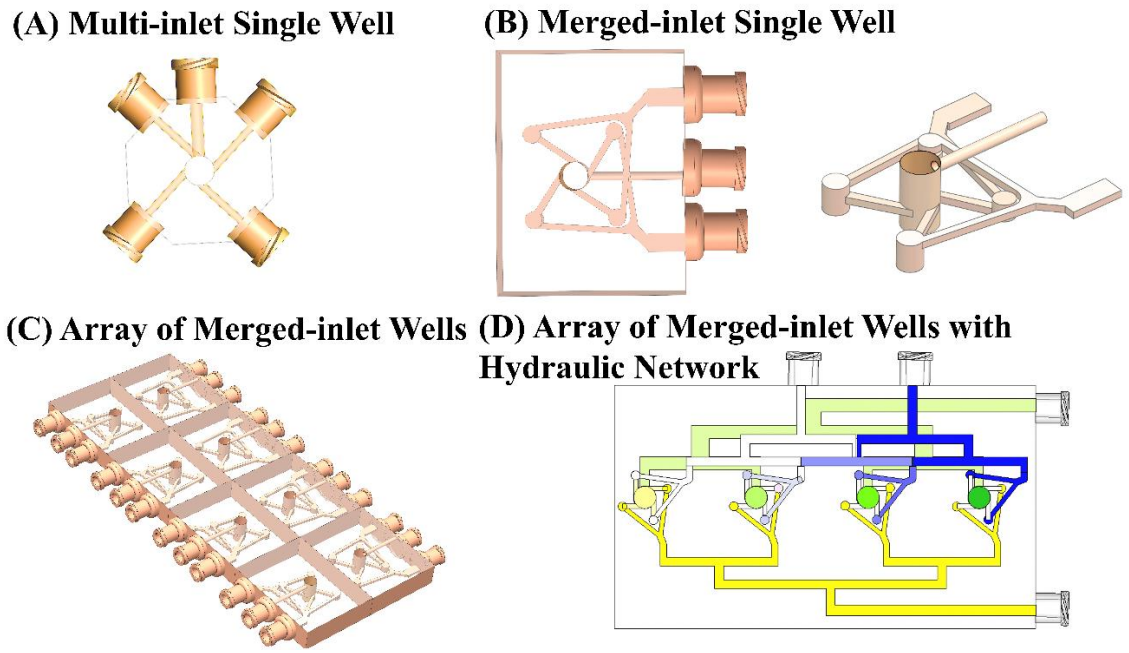

Figure 12: (A) A conventional multi-inlet micromixer with four inlets tangentially connected to the bottom layer of the cylindrical well and an outlet connected to the top layer of the well. This configuration of inlets and outlets creates cyclonic flow in the cylindrical well for efficient mixing of liquids and trapping nucleated crystals. (B) Merged-inlet design where alternate (non-neighboring) inlets are merged using a Y-junction such that all the ports are on one side of the device. The internal view shows the vertical offset in the Y-junction of merged inlets to avoid the intersection between channels. (C) An array of eight (4 x 2) merged-inlet micromixers for parallel screening application. Here, the separate inlets for solvent (8) and antisolvent (8) provide flexibility in changing solvent/antisolvent ratio and solute concentration in each well simultaneously. (D) 4 x 1 array of merged-inlet micromixers connected with three hydraulic networks. The top hydraulic network (blue shaded) on the upper half has two inlets coming from the north direction –one for the solution of solute and solvent and the other for pure solvent. The second hydraulic network (yellow colored) on the bottom half has an inlet for antisolvent coming from the east direction. The third hydraulic network (green shaded) located underneath the solvent feed (blue shaded) collects all the slurry from the micromixer and has an outlet located on the east side.

The dimensions of the merged-inlet single-well microfluidic device are shown in Figure 13 and summarized in Table 9.

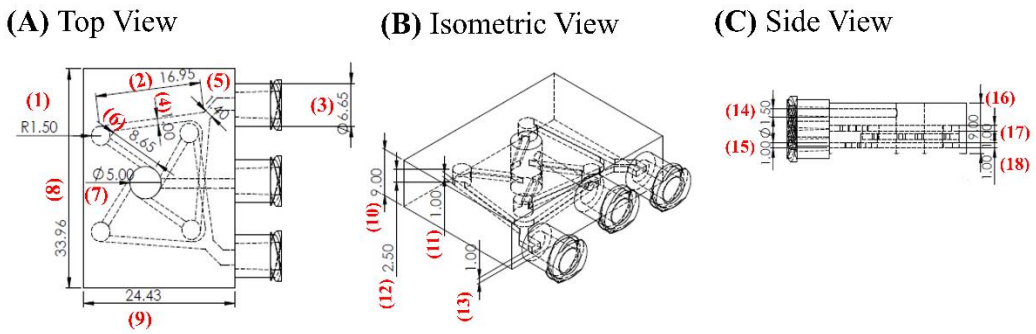

Figure 13: (A) Top view, (B) isometric view, and (C) side view of the merged-inlet single well with dimensions marked.

Table 9: Dimensions of the merged-inlet single well

Dimension	Value (mm)	Dimension	Value (mm)
1	1.5	9	24.43
2	16.95	10	9
3	6.65	11	1
4	1	12	2.5
5	1.4	13	1
6	8.65	14	1.5
7	5	15	1
8	33.96	16	9
9	24.43	17	1
10	9	18	1

This design was repeated eight times for designing the array of the merged-inlet wells, as shown in Figure 12C. In Figure 14, we have demonstrated the dimension of the array of the merged-inlet wells.

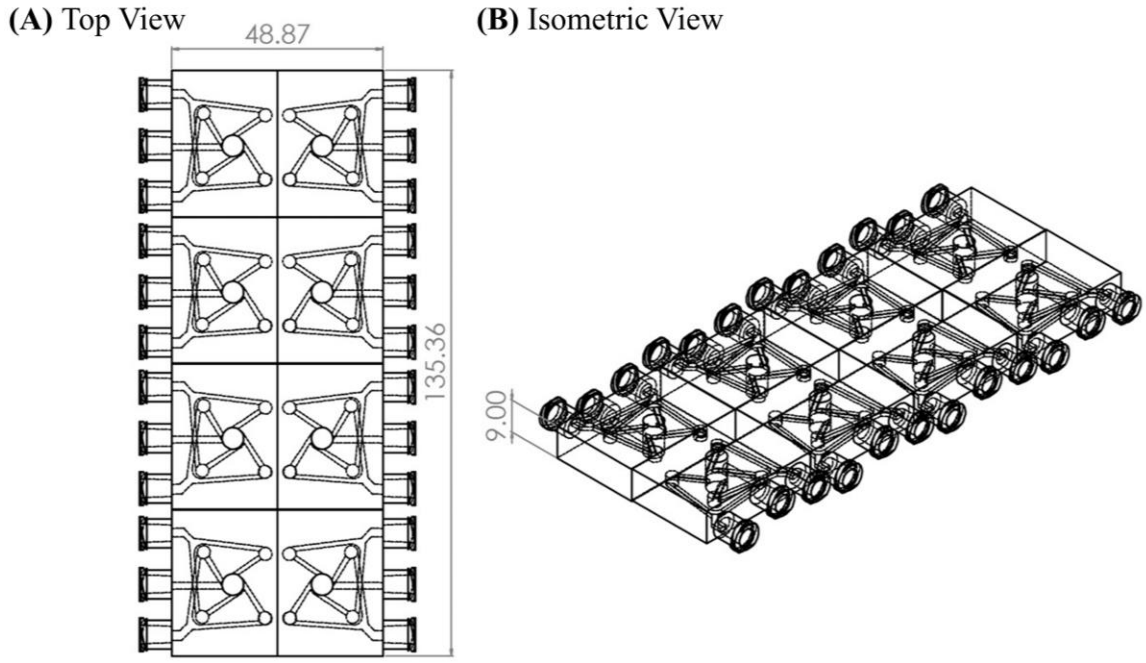

Figure 14: (A) Top view and (B) isometric view of the array of the merged-inlet wells with marked dimensions.

3.2.2 CFD Simulation of Merged-Inlet Device

The Navier-Stokes equation coupled with continuity equation to obtain the concentration profile from mixing pure streams of solvent (water) and antisolvent (ethanol). The solute was not considered in the simulation as its solubility is typically at least three orders of magnitude smaller than solvent and antisolvent concentration, which has a negligible effect on the mixing profile. The boundary conditions on inlets were set according to the entering flow rates of water and ethanol. The concentration-dependent viscosity and density of the water-ethanol mixture were considered in the model. The effectiveness of mixing in the merged-inlet micromixers is evaluated by calculating the velocity, pressure, and concentration profiles.

3.2.2.1 Laminar Flow Module: Equations and Boundary Conditions

The laminar flow module of COMSOL was used to calculate the velocity profile in the microfluidic mixer. The velocity and pressure profiles of the merged inlet microfluidic device were calculated using the time-dependent Navier-Stokes equation. The density and the viscosity were

defined for the mixture of ethanol and water. It was assumed that the fluid was incompressible, and the temperature was kept constant and equal to 298.15 K for all the simulations. The assigned boundary conditions are listed below and shown in Figure 15.

Boundary Conditions:

- Inlet 1: Q = 0.5 mL.min^{-1}
- Inlet 2: Q = 0.5 mL.min^{-1}
- Outlet: P = 1 atm

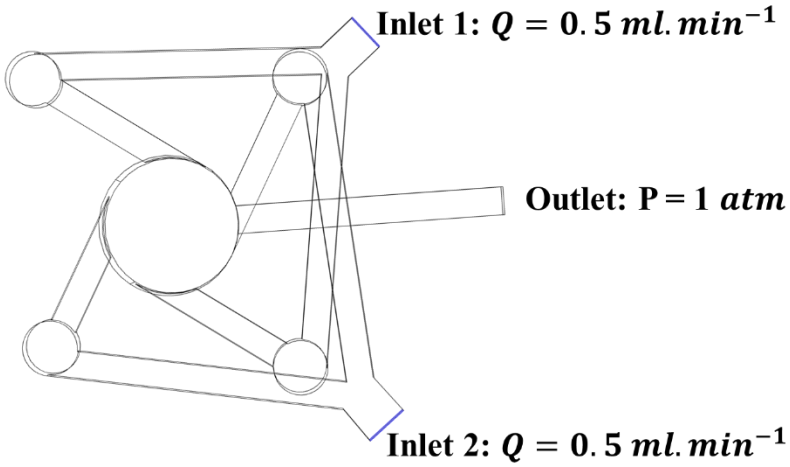

Figure 15: The top view of the merged inlet microfluidic mixer design with the assigned boundary conditions for the two inlets and one outlet in the laminar flow module.

3.2.2.2 Transport of Diluted Species Module: Equations and Boundary Conditions

The transport of the diluted species module is used to calculate the concentration profile in the microfluidic mixer. The time-dependent continuity equation solved is described as follows:

$$\rho \frac{\partial c_i}{\partial t} + \nabla . (-D_i \nabla c_i) + u . \nabla c_i = R_i \quad (30)$$

which includes both convection and diffusion for the transport mechanisms. Here ρ is the density, and u is the velocity of the fluid and comes from the laminar flow module. These two modules are coupled together, and the velocity profile is directly substituted into the continuity equation. The assigned boundary conditions for this model are listed below and shown in Figure 16:

Boundary Conditions:

- Inlet 1: $c_i = c_{0,i} = 0$ mol.m^{-3}
- Inlet 2: $c_i = c_{0,i} = 1$ mol.m^{-3}
- Outlet: $n.D_i \nabla c_i = 0$

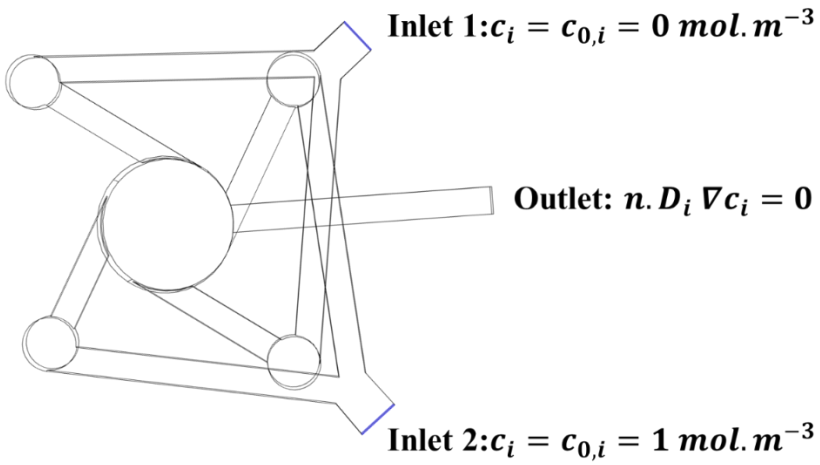

Figure 16: The top view of the merged inlet microfluidic mixer design with the assigned boundary conditions for the two inlets and one outlet in the transport of the diluted species module.

3.2.2.3 Model Parameters and Solver System of the CFD Simulations

In this study, we have simulated a coupled analysis of the laminar flow module and transport of the diluted species to evaluate the velocity pressure and concentration profile inside the microfluidic mixer. The 3D model for simulations was imported into the model from a Solid Work design. The design was further simplified by eliminating the sharp edges and smoothening the surfaces to enhance the mesh quality.

The free tetrahedral mesh was selected for the models. The tetrahedral mesh was selected for this study, and the details are provided in the following part:

- Maximum Element Size=3.42 mm
- Minimum Element Size=0.725 mm
- Maximum Element Growth Rate=1.3

- Curvature Factor=0.9
- Resolution of Narrow Region=0.4

The boundary meshes were set at level 2 with a stretching factor of 1.2 and a thickness adjustment factor of 5. The sharp edges of the corner were trimmed for the corners with angles in the range of 50^{o}-240^{o}. The elements were refined using a size scaling factor of 0.35.

The coupled equations of the Navier-Stokes and mass balance were solved in the stationary solver using linear solver "Algebraic Multigrid" (GMRES). The residual tolerance was set to 0.01 with 200 iterations and left preconditioning. Newton was selected as the non-linear method with a damping factor of 0.1 and tolerance as the termination technique. The relative tolerance was also kept at 0.001. The concentration-dependent viscosity and density of the water-ethanol mixture at room temperature were considered in model[49].

The boundary condition for the rest of the boundaries was set to wall condition = no-slip boundary condition ($u=0$). Finally, the coupled equations were solved using an iterative solver–Generalized Minimum Residual, combined with the Algebraic Multigrid method.

The residual tolerance was set to 0.01 with 200 iterations and left preconditioning. Newton's method was used for iterations with a damping factor of 0.1 and relative tolerance of 0.001.

3.3 Experimental Methods

3.3.1 Materials

The crystalline Form A (stable) of L-histidine and crystalline Form-I (stable) of o-aminobenzoic acid (o-ABA) (Sigma-Aldrich, chemical purity ≥98%) were used for parallel screening study and solubility measurements. The solutions for antisolvent crystallization studies were made using deionized water (Sigma-Aldrich, 18 MΩ cm) and ethanol (Sigma-Aldrich, ACS 99.8%).

3.3.2 Fabrication of Microfluidic Devices

The 3D designs of the microfluidic device shown in Figures 12B and 12C were designed in

SolidWorks® (2018, Dassault Systems) and then 3D-printed using a stereolithography (SLA) 3D printer (form 2, Formlabs Inc., USA). A clear FLGPCL02 resin activated by a 405 nm laser was used to 3D print optically clear microfluidic devices with 150 μm of lateral and 25 μm of axial resolutions. The clear resin is chemically resistant to various solvents, including ethanol and water. The printed devices were washed with IPA (90%, Sigma-Aldrich) bath for 20 minutes in the Form Wash (Formlabs Inc., USA) to remove the residues of the resin from the external surface. The interior channels of the 3D-printed device were washed separately by injecting IPA using a syringe. The post-washed 3D-printed devices were finished by removing supports and curing for 20 minutes using a commercial ultraviolet lamp. The optical transparency of the 3D-printed microfluidic device was improved by wet sanding using 400 to 12000 grit pads, followed by spray painting of resin. The top and bottom openings of the micromixers in the multi-well device (see Figure 18B) were sealed with polycarbonate films for optical clarity to image crystals under the microscope. The fabricated multi-well device is shown in Figure 18B.

3.3.3 Experimental Setup and Operation of Multi-Well Device

Figure 18A shows the experimental setup for parallel screening, which involves flow crystallization in a multi-well microfluidic device continuously monitored under the optical microscope (Olympus BX53M, Olympus America Inc.). This setup was first benchmarked to reproduce previously reported screening results for o-ABA and then applied to screen L-histidine morphology, polymorph, and growth rates for different solvent ratios, solute concentrations, and supersaturations. L-histidine was grown in a multi-well device using the antisolvent method implemented by mixing an aqueous L-histidine solution with pure ethanol (antisolvent) at room temperature (~20℃). The aqueous L-histidine solution and pure ethanol were pumped separately into each microwell in the multi-well device using programmed syringe pumps (NE-4000, New Era Pump System Inc.). The inlets are connected to one-way microfluidic check valves to prevent

backflow inside the channels. The solubility of L-histidine in the ethanol-water mixture was measured in the single merged-inlet device according to the procedure described in Section 3.3.4. The required concentration of L-histidine and the volume fraction of ethanol in the ethanol-water mixture were determined from the solubility curve to achieve desired supersaturation in the micromixer. For instance, a supersaturation of 2 corresponds to the solubility of 0.078 $mol.L^{-1}$ in 30 vol% ethanol achieved by feeding a 0.22 $mol.L^{-1}$ aqueous L-histidine solution at 0.7 $mL.min^{-1}$ and 100% ethanol at 0.3 $mL.min^{-1}$. Here the vol% is calculated based on the volume of pure ethanol and water mixed at room temperature (~20℃). Figure 32B shows the supersaturation in each well of the multi-well device labeled A to H. The supersaturations in wells A to D were controlled by varying concentrations of L-histidine in water fed while feeding ethanol at equal flow rates of 0.5 $mL.min^{-1}$ whereas the supersaturations in wells E to H were varied for fixed L-histidine concentration in water mixed with different flow rates of ethanol to achieve different vol% of ethanol in the mixer. The total flow rate of aqueous solution and ethanol was maintained at 1 $mL.min^{-1}$ in all the wells to have a similar residence time of supersaturated solution in the micromixers. The composition and flow rates of streams entering wells A to H are shown in Figure 17.

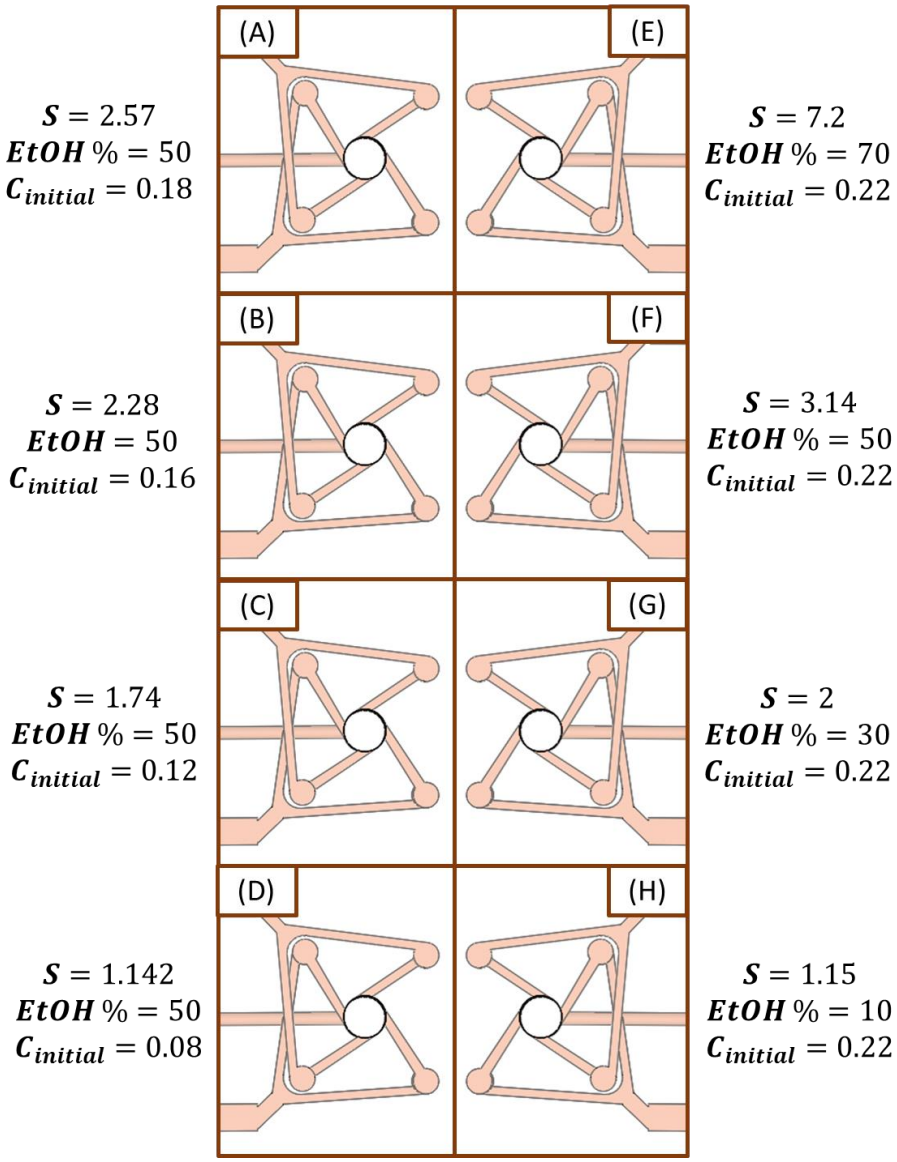

Figure 17: Array of the merged-inlets with marked experimental conditions.

Table 10: Details of experimental condition for the multi-well experiment

Samples	C_{Feed} (mol.L^{-1})	Ethanol Percentage (%)	C_{Mixer} (mol.L^{-1})	c*	SS	L-histidine Flow rate (mL.min^{-1})	Ethanol Flow rate (mL.min^{-1})
A	0.18	50	0.09	0.04	2.57	0.5	0.5
B	0.16	50	0.08	0.04	2.28	0.5	0.5
C	0.12	50	0.06	0.04	1.74	0.5	0.5
D	0.08	50	0.04	0.04	1.14	0.5	0.5
E	0.22	70	0.066	0.01	7.23	0.3	0.7
F	0.22	50	0.11	0.04	3.14	0.5	0.5
G	0.22	30	0.154	0.08	2	0.7	0.3
H	0.22	10	0.198	0.17	1.15	0.9	0.1

All the conditions in eight wells A-H were repeated thrice to obtain the error bars. The effective startup of a multi-well device is crucial for the consistent screening of crystallization. The multi-well device was first flushed with the aqueous solution of L-histidine to remove air from the channels and micromixers, and then ethanol was injected at a sufficiently higher total flow rate to attain steady concentration and flow profiles in a time duration much smaller than the induction time of the crystals. The induction time of L-histidine decreases with increasing vol% of ethanol and supersaturation, with the longest time reported of ~40 seconds[50]. Therefore, the startup time for this study was less than a few seconds. Since the startup time is close to the average residence time of the micromixer that has a volume of 0.8 mL, the initial total flow rate was set to 5 mL.min^{-1} for 10 seconds, followed by a steady flow rate of 1 mL.min^{-1} for 30 minutes. The microscopic images were recorded with a built-in color camera (LC 30, Olympus America Inc.). The time-

lapsed images were captured consecutively at an interval of 2 minutes on each well during the total crystallization time of 30 minutes.

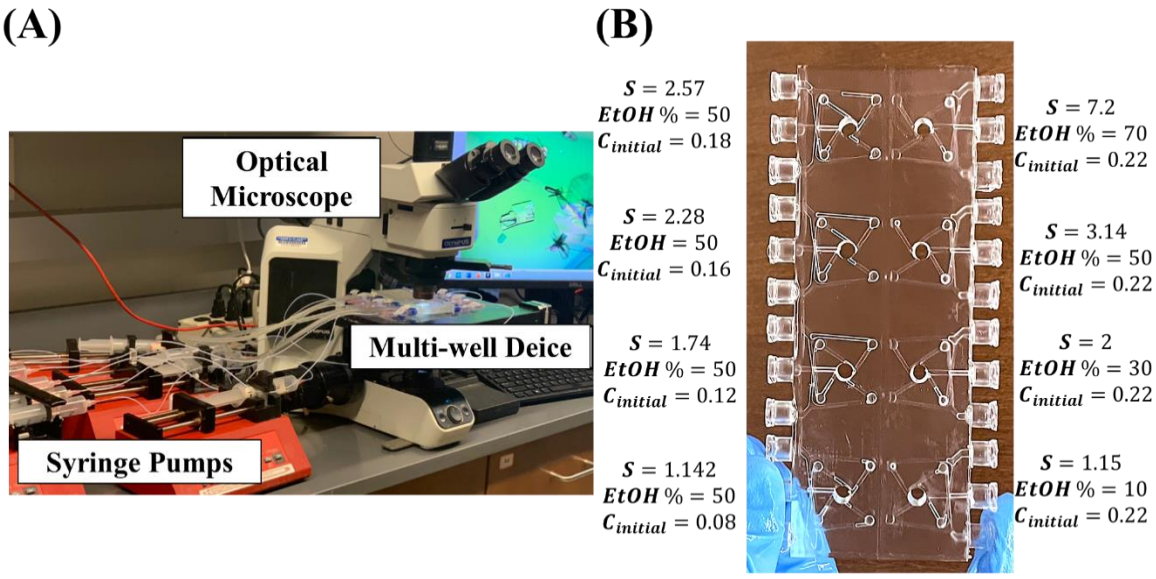

Figure 18: (A) Experimental setup for parallel screening. It involves syringe pumps pushing aqueous solution and antisolvent at a constant flow rate in a multi-well microfluidic device, continuously monitored under the optical microscope. (B) Picture of a 3D-printed multi-well device with wells labeled from A to H. The supersaturations in wells A to D were controlled by varying L-histidine concentration, and supersaturations of wells E to H were controlled by varying vol% of ethanol.

3.3.4 Solubility Measurement

The solubility data for o-ABA in the water-ethanol mixture was obtained from the literature[40,41]. The solubility of L-histidine in ethanol-water mixtures was measured at room temperature (20 ℃). The solubility measurements were conducted in the multi-inlet single well device (Figure 12A) by manipulating flow rates of four inlets, labeled as 1: pure ethanol, 2: pure water, 3-4: a joint inlet for a saturated solution of L-histidine in water, to observe nucleated crystals in a specific time interval. For example, the solubility at 50 vol% ethanol was measured by setting the flow rate of inlet-1 to 0.5 mL.min^{-1} initial flow rates of inlet-2 0.5 mL.min^{-1} and joint inlet-3 and 4 to 0 mL.min^{-1}. While keeping the total flow rate of inlet-2 and joint inlet-3 and 4 to 0.5 mL.min^{-1}, the flow rate of a saturated aqueous solution of L-histidine in the joint inlet had a stepwise increase until nucleated crystals were observed in one-minute time steps. The concentration of L-histidine in the

micromixer, calculated based on the flow rates of all inlets leading to the nucleation event, provides the solubility at a fixed ethanol vol%. Such a dynamic measurement of solubility is sensitive to the time interval for observation of nucleation during a stepwise increase in the flow rate of the joint inlet. The observed (or apparent) solubility decreases with increasing this time interval, where the solubility data obtained for 10 minutes interval matches well with the thermodynamic solubility[9,51]. The variation in solubility from 1 to 10 minutes observation interval can be interpreted as metastable zone width for nucleation. A more accurate estimation of solubility can be made by measuring solution composition for zero growth conditions[23].

3.3.5 Measurement of Growth Rates, Morphology, and Polymorphs

The time-lapsed images were processed to measure the size and shape distribution of crystals using image analysis in Olympus Stream Start. Details of image processing and analysis can be found in the literature[19]. The polymorphic forms of o-ABA and L-histidine were distinguished based on their distinct morphological forms. For several organic crystals, there are unique morphologies associated with different polymorphic forms that can be identified using the software MorphologyDomain[7,8]. Form-I of o-ABA has prismatic morphology, whereas Form-II takes needle-like morphology. The Form A (stable) of L-histidine has rod-like morphology, and Form-B (metastable) has plate-like morphology with dominant (100), (110), and (111) faces. Figure 19 shows the simulated crystals of Form-A and B from experimental samples[9,11,51].

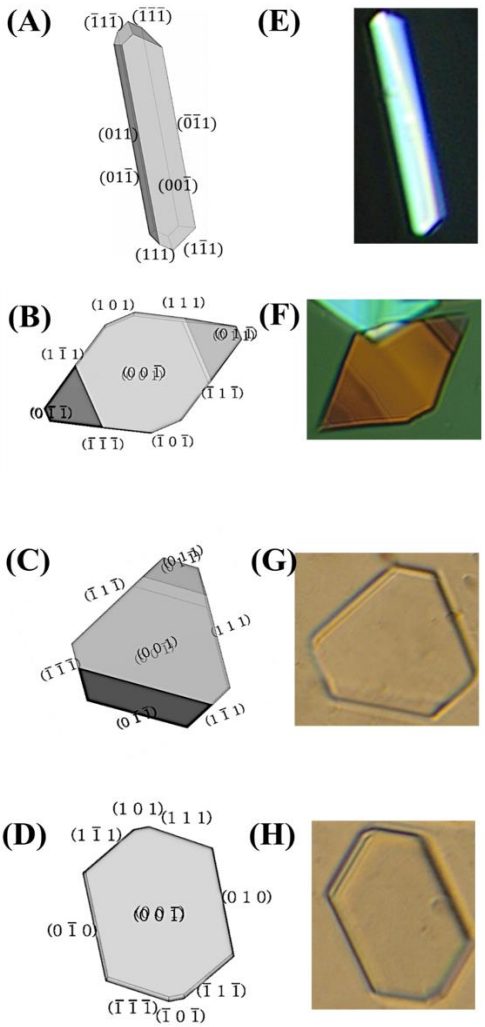

Figure 19: Crystal morphologies of Form-A and selected Form-B crystals of L-histidine with shown faces: (A) Predicted morphology of Form-A. (B), (C) and (D) Predicted morphology of Form-B. (E) Optical image of the Form-A crystals obtained experimentally. (F), (G) and (H) Optical images of the Form-B crystals were obtained experimentally.

The rod-like Form-A crystals were distinguished from the plate-like crystals of Form-B based on applying a cutoff of > 2 on the aspect ratio in the image analysis program. The percentage of Form-A was calculated based on the fraction of the area covered by the rod-like crystals. The polymorphic forms of L-histidine were also confirmed from X-ray diffraction (XRD) experiments on a Bruker D2 PHASER diffractometer using Ni-filtered Cu Kα radiation. For all samples, a step width 2θ of 0.2θ and a counting time of 5 seconds/step were used to enhance the signal-to-noise ratio.

3.4 Result and Discussion

3.4.1 Computational Results

3.4.1.1 Hydrodynamic Performance Analysis

As shown in Figure 12B (Internal view), the merged-inlet connections are shifted up and down from the plane of the four tangential inlets. Each inlet has an equal distance for end-to-end to ensure that the pressure drop in all four inlets is identical. The pressure drop is an important factor as the change in the pressure drop will change the velocity distribution. The effect of Y-junction in the merged-inlet single-well design on pressure drops difference between four tangential inlets is evaluated using CFD simulation. Also, its effect on the velocity profile in each inlet and mixing in the micromixer is evaluated computationally. Figure 20 shows the route where the pressure drop is calculated.

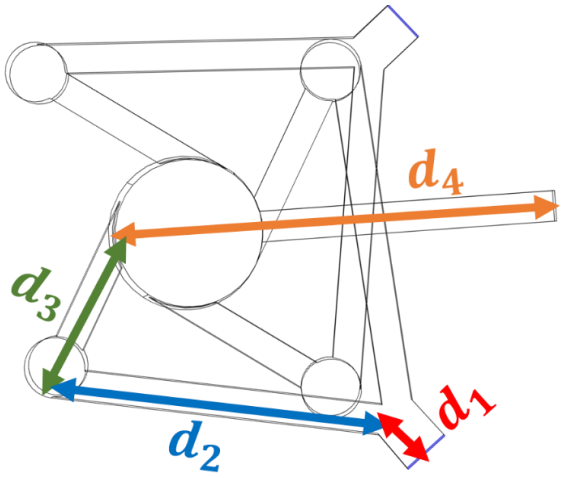

Figure 20: Top view of the merged-inlet single well with four arrows indicating the distance from the main inlets.

Since all the dimensions were kept identical for both major inlets, this distance is equal for all four tangential inlets.

$$Distance\ from\ the\ main\ inlet\ = d_1 + d_2 + d_3 + d_4 \quad (31)$$

3.4.1.2 Contour Pressure Profile for the Merged-inlet Single-Well Microfluidic Device

In addition to the pressure drop comparison shown in Figure 23B, we have shown the pressure

contour for the merged-inlet single-well microfluidic device. Figure 21 shows the isometric and top view of the pressure contours and confirms the identical pressure difference in all four inlets.

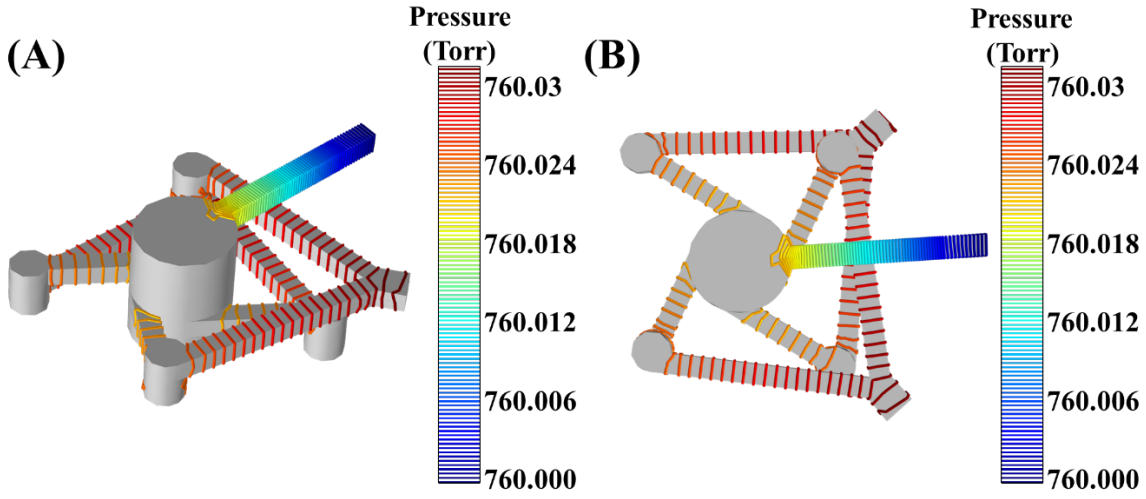

Figure 21: Contour pressure profile of the merged-inlet single-well microfluidic device: (A) Isometric view and (B) top view.

3.4.1.3 Velocity Profile for the Merged-Inlet Single-Well Microfluidic Device

In addition to the pressure profile, we have also computed and plotted the velocity profile of the merged-inlet single-well microfluidic mixer. Figure 22 shows that the velocity profile inside the merged-inlet single-well microfluidic device is identical, confirming that the flow distribution is not affected by merging the inlets using Y-junctions.

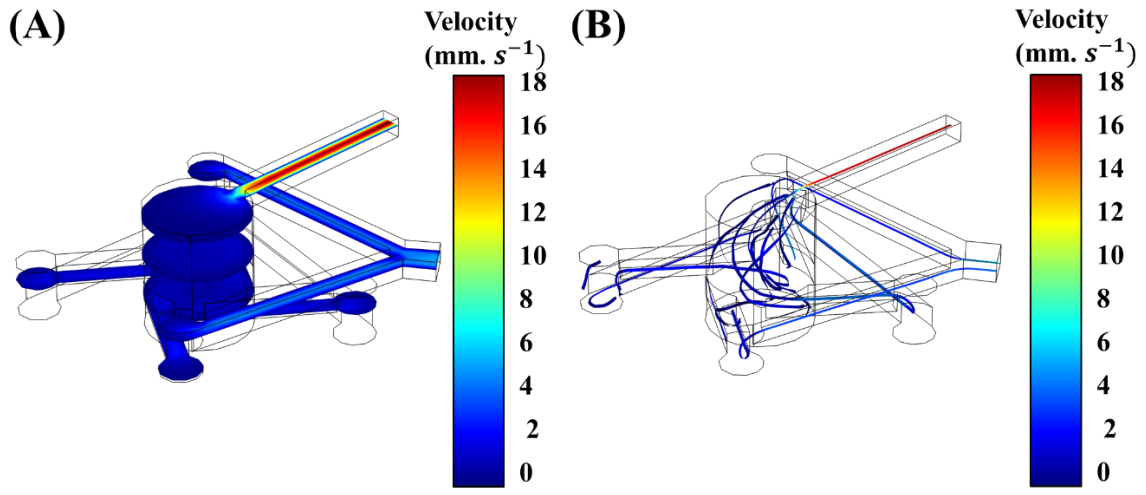

Figure 22: Velocity profile in the merged-inlet single-well microfluidic device (A) Streamlines inside the channels and mixer; (B) Average velocity at different vertical slices in the device.

3.4.1.4 Evaluation of the Mixing Index:

3.4.2 Pressure Variation and Mixing in the Merged-Inlet Device

The alternate inlets of the merged-inlet device are combined using a Y-junction to ensure an even split of flow and uniform pressure inside the micromixer. Figure 23A shows a decrease in the gauge pressure of ethanol flowing at 0.5 $mL.min^{-1}$ in inlets 1 and 3 and water flowing at 0.5 $mL.min^{-1}$ in inlets 2 and 4, entering into the mixer and leaving from the outlet of the device. The pressure change in the micromixer is within a few pascals and uniform across the cross-sectional planes. Figure 23B shows the gauge pressure drop along the axial direction starting from different inlets emerging from the Y-junction to the outlet. The pressure drop is identical in non-neighboring inlets, confirming identical flow rates in each pair of merged inlets.

The concentration distribution of ethanol and water as they are combined in the mixer at identical flow rates of 0.5 $mL.min^{-1}$ is shown in Figure 23C. Larger concentration gradients are observed near the inlets as compared to the central zone. These gradients are inevitable but can be reduced by increasing the number of inlets and the flow rates[41].

The mixing index is defined to evaluate the performance of the mixing in the merged-inlet single-well microfluidic device. The height of the mixer is divided into 20 parallel planes to calculate the mixing index. In each plane, the concentration profile was obtained from COMSOL, and then data was exported and post-processed in MATLAB. Next, the standard deviation of the concentration in each plane is calculated to obtain Mixing Index. The mixing index is defined as, where σ^2 is the variance of concentration in any cross-sectional plane and σ_0^2 is the variance in concentration of the bottom plane of the mixer.

$$Mixing\ Index = 1 - \left(\frac{\sigma^2}{\sigma_0^2}\right) \tag{32}$$

Figure 23D shows an increase in the mixing index of a cross-sectional plane of the mixer with increasing the distance from the bottom plane for 4-, 6-, and 8-inlet mixers.

The dynamic change in the mixing can be interpreted from the residence time distribution (RTD) of the mixer. In order to calculate the residence time distribution of the merged-inlet microfluidic mixer, the concentration at the outlet is recorded from t = 0 to t = 15 minutes at each flow rate. The flow rate varied from 0.1 to 1 with increments of 0.1 ($mL.min^{-1}$). Using MATLAB, these data were processed to calculate the average residence time and standard deviation at each flow rate. The outlet concentration at a different time $\bar{c}(t)$ is first divided by the initial concentration, which is set as 1 ($mL.min^{-1}$) :

$$F(t) = \frac{c\,\overline{(t)}}{c_0} \tag{33}$$

Here c(0) is the initial concentration, and $\bar{c}(t)$ is the average concentration at the outlet boundary. From here, the average residence time ($\overline{t}$) and the standard deviation (σ) were calculated as:

$$\overline{t} = \bar{t} = \int_0^\infty [1 - F(t)]dt \tag{34}$$

$$\sigma^2 = 2\int_0^\infty t[1 - F(t)]dt - \bar{t}^2 \tag{35}$$

The values of $\overline{t}$ and σ is calculated for each flow rate, and the results are shown in Figure 23E. Figure 23E shows the decrease in the average residence time and the standard deviation of RTD with the increasing total flow rate of the fluid. The dye experiments were also conducted to confirm efficient mixing of *(1-x)* $mL.min^{-1}$ of 15 $g.L^{-1}$ of aqueous dye solution with *x* $mL.min^{-1}$ of water. Figure 23F shows the concentration of diluted dye solution at the outlet of the merged-inlet device measured at 300 seconds for a varying percentage of added water.

In Table 11, the induction time for l-Histidine polymorphs for supersaturation above 1 and less than 10 are listed[52]. The induction time is compared with the calculated residence time for the merged-inlet device from figure 23E. As shown in Table 11, the average induction time for L-Histidine is around 9 seconds, while the residence time is between 20 to 73 seconds.

Table 11: Comparison of the induction time and residence time for L-Histidine polymorphs for the total flow rate of 1 ml.min^{-1}in the merged inlet device.

Induction time for L-histidine crystals for supersaturation between 1 to 10	Residence time for the total flow rate of 1 ml.min^{-1}
8.97 (s)	19.8 to 72.7 (s)

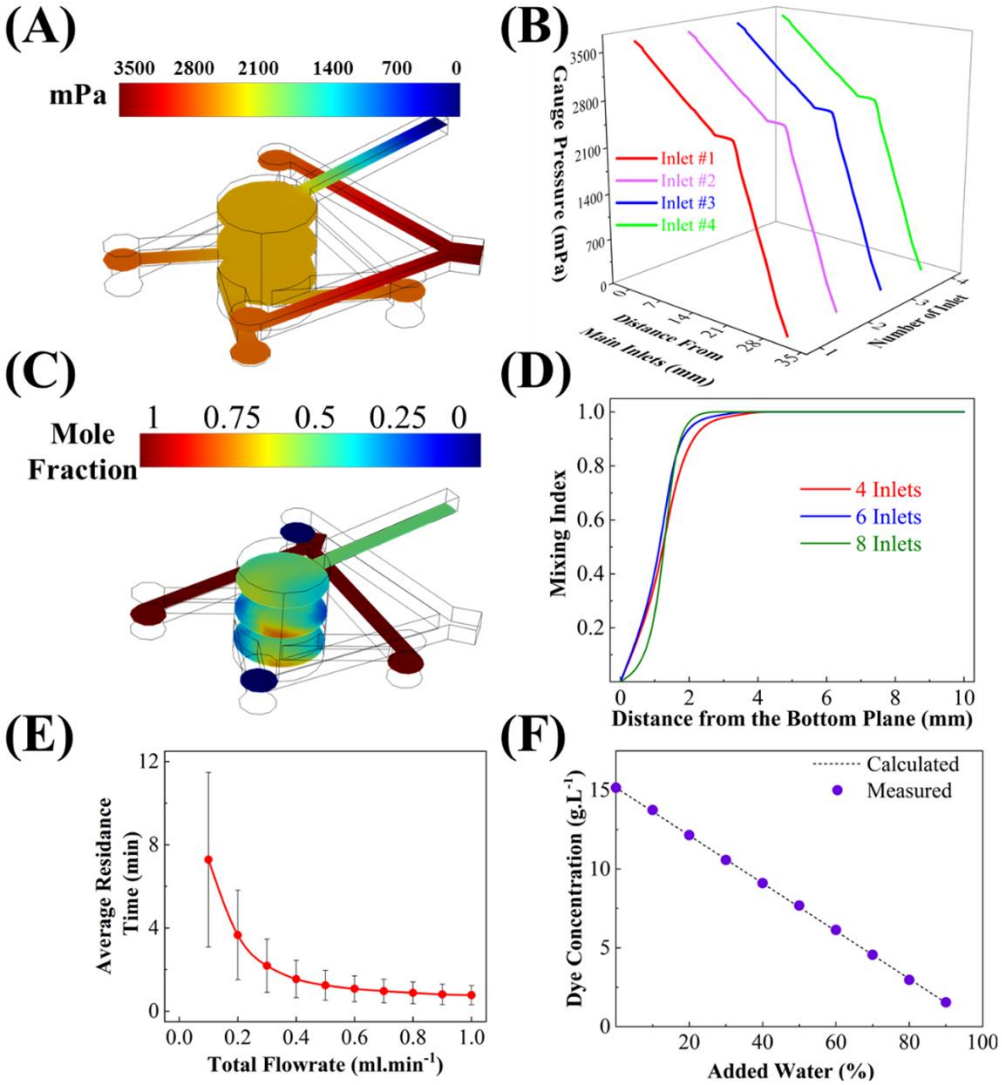

Figure 23: (A) Variation in the gauge pressure of ethanol-water mixture flowing upward in the micromixer for the inlet flow rate of 0.5 mL.min^{-1} for ethanol and 0.5 mL.min^{-1} for water. (B) Decrease in the gauge pressure along the axial direction of a channel for flow condition in (A). The pressure drop along each inlet is identical. (C) Variation in the mole fraction of ethanol in the mixer for the inlet flow rate of 0.5 mL.min^{-1} of ethanol and 0.5 mL.min^{-1}of water. (D) Increase of the mixing index in the cross-sectional planes from the bottom to the top surface for four-, six-, and eight-inlet micromixers. Almost homogeneous mixing is observed at a height greater than 1.8 mm. (E) Average residence time distribution and variance of the micromixer as a function of flow rate. (F) Verification of homogeneous mixing from dye experiment, where (1-x) mL.min^{-1} of 15 g.L^{-1} of aqueous dye solution is mixed with x mL.min^{-1} of water. Dilution of dye at the outlet with an increasing volume fraction of added water (x) matches the calculated values, confirming homogeneous mixing with no dead volume in the micromixer.

3.4.3 Solubility Measurements of Form-A of L-histidine in Different Ratios of Ethanol and Water at Room Temperature using Separated Inlets Microfluidic Mixer

In order to measure the solubility of Form-A of L-histidine in different ratios of ethanol and water, a saturated solution of L-histidine in the water at room temperature is prepared.

The four entering streams into the microfluidic mixer include two streams of saturated solution, one stream of pure solvent (water), and one stream of pure antisolvent (ethanol). The flow rate of the ethanol (Q_3) is initially set to the desired ratio and then kept constant with respect to the summation of the flow rates for the solution of L-his in water (Q_1) and pure water (Q_2) After that, starting from the highest ratio of the pure solvent, Q_1 is increased and consequently Q_2 is decreased. However, the summation of Q_1 and Q_2should remain constant. The point where crystals are formed within the microfluidic mixer is then considered the maximum point, and then the several ratios before that value are checked to obtain the values of the flow rates of all three streams and measure the solubility. Knowing the concentration of the L-histidine in the water, solubility is calculated as follows:

$$C_{eq} = \frac{c_{initial} \times Q_1}{Q_1+Q_2+Q_3} \quad (36)$$

3.4.4 Comparative Screening of Morphology and Polymorphs of o-ABA in Multi-Inlet versus Merged-inlet Device

The performance of the merged-inlet device is first benchmarked by reproducing reported data on morphology and polymorph screening of o-ABA[41]. Figures 24A to 24D show two different polymorphs of o-ABA Form-I at supersaturation 1.2 and Form-II at supersaturation 1.9 – obtained using the multi-inlet device (Figure 12A)[41]. The ability of micromixers to trap crystals and grow them under continuous feed allows consistent screening of metastable Form-II, which is not feasible in microtiter plates[41]. Figures 24E to 24H show similar results with the merged-inlet device, where Form-I and Form-II are identified at supersaturations 1.2 and 1.9, respectively. The

reproducibility of morphology and polymorphs in the merged-inlet device confirms its suitability for parallel screening applications using a multi-well device.

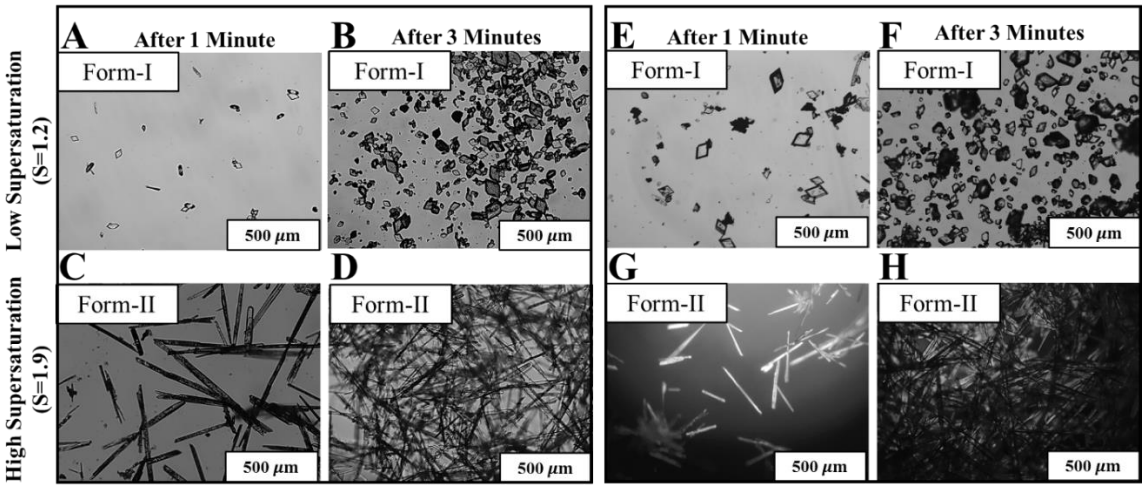

Figure 24: Comparison of morphologies and polymorphs of o-ABA at two different supersaturations in the multi-inlet device (A to D) and merged-inlet device (E to H). Both multi-inlet and merged-inlet devices show Form-I polymorph of prismatic morphology at supersaturation 1.2 (A and B, vs. E and F), and Form-II polymorph of needle-like morphology at supersaturation 1.9 (C and D, vs. G and H).

3.4.5 Parallel Screening of Morphology, Polymorphs, and Growth Rate of L-histidine using Multi-Well Device and 96-Well Microtiter Plate

The efficacy of the eight-well device (shown in Figure 18B) is evaluated here for parallel screening of morphology, polymorph, and growth rates of L-histidine via antisolvent crystallization. The concentration of L-histidine and vol% of ethanol in each well of the multi-well device are flow controlled to achieve different supersaturations. The composition in each well are labelled as A: $\sigma = 2.57$, 50 vol% ethanol, B: $\sigma = 2.28$, 50 vol% ethanol, C: $\sigma = 1.74$, 50 vol% ethanol, D: $\sigma = 1.14$, 50 vol% ethanol, E: $\sigma = 7.2$, 70 vol% ethanol, F: $\sigma = 3.14$, 50 vol% ethanol, G: $\sigma = 2.00$, 30 vol% ethanol, and H: $\sigma = 1.15$, 10 vol% ethanol. The supersaturation in wells decreases in the order E > F > A > B > G > C > H ≈ D. Figures 27 A-1, B-1, E-1, and F-1 show dominant plate-like morphology characteristic of Form-B (metastable) of L-histidine, whereas the rest other wells C-1, D-1, G-1, and H-1 show a few crystals of rod-like morphology of Form-A (stable) after 5 minutes in the multi-well device. Figure 27 A-2 to H-2 shows a much larger number

of crystals with similar morphological and polymorphic characteristics compared to A-1 to H-1 after 30 minutes. The rod-like crystals of Form-A are more evident in C-2, D-2, G-2, and H-2. The polymorphic forms of plate-like and rod-like crystals are also confirmed using the XRD pattern of both forms from the literature. (see Figure 25)

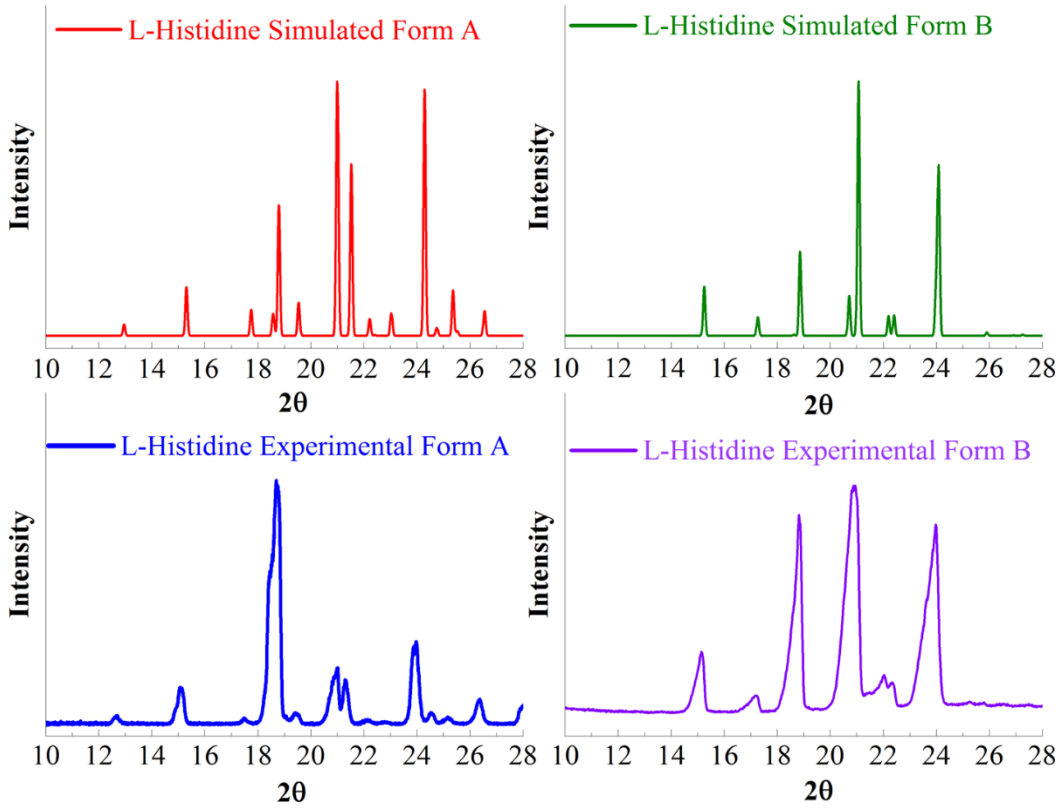

Figure 25: XRD patterns of L-histidine polymorphs: (A) Simulated Form-A; (B) Simulated Form-B; (C) Experimental Form-A; (D) Experimental Form-B.

The parallel screening performance of a multi-well device is compared with a 96-well plate. The right panels in Figures 27 A-3 to H-4 are optical micrographs of crystals grown under identical conditions in a 4x2 sub-array. Very few crystals can be seen in the first 5 minutes in wells A-3 to H-3, and the majority of these are rod-like crystals. After 30 minutes, larger crystals of mixed morphology and polymorphs are observed in wells A-4, B-4, E-4, and F-4, whereas the low-supersaturation wells C-4, D-4, G-4, and H-4 showed dominant, stable Form-A. Since the supersaturation in microtiter plates decreases as the crystals grow, a larger fraction of metastable

crystals can transform into stable crystals via Ostwald ripening which is the primary reason for the disappearance of plate-like crystals (metastable) in wells A-4, B-4, E-4, and F-4.

The percentage of stable Form-A (X_A) and the growth rates of (111) facets for different compositions in each well are obtained from image analysis (as described in section 3. 5). Figures 27A, B, and C show the variation in X_A and growth rates as a function of L-histidine concentration, vol% of ethanol, and supersaturation, respectively, for a multi-well device. Figure 27A shows the percentage of X_A decreases with increasing concentration of L-histidine in the mixer at fixed 50 vol% of ethanol, and it becomes negligible for concentration > 75 mM. However, the growth rate increases marginally with L-histidine concentration. Figure 27B shows a decrease in the percentage of X_A with increasing vol% of ethanol at a fixed L-Histidine concentration of 220 mM in the feed. The percentage of X_A is almost zero for > 50 vol% of ethanol. The combined effect of L-histidine concentration and vol% of ethanol can be represented as supersaturation, as shown in Figure 27C. While the percentage of Form-A drops sharply from supersaturation 1 to 2, the growth rate increases linearly from 0.010 to 0.015 $\mu m.s^{-1}$. The metastable Form-B dominantly occurs for supersaturation > 2.2, with growth rate increasing exponentially from 0.017 $\mu m.s^{-1}$ at supersaturation 2.2 to 0.04 μm/s at supersaturation 7. The growth rate data were obtained by taking time-lapse images from samples every five minutes. The change in the distance from face 111 was divided by the time difference. Here we have shown a sample of these calculations. In Figure 26, we have shown five pictures taken in 20 minutes for sample B (S=2.28).

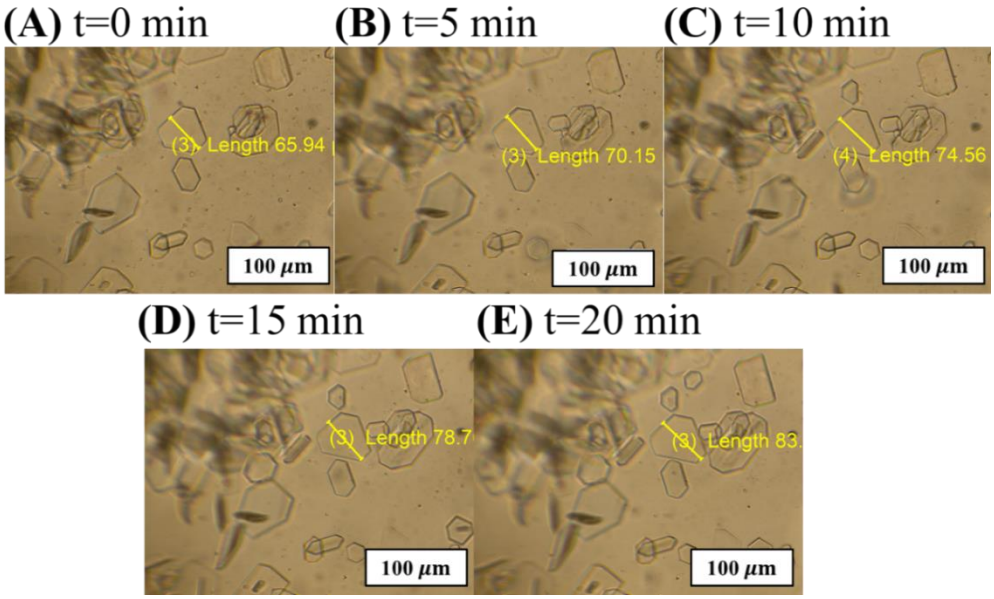

Figure 26: Time-lapse images from sample B (S=2.28) for 20 minutes. The t=0 is not the initial time of the experiments, and it is the time when the measurements started.

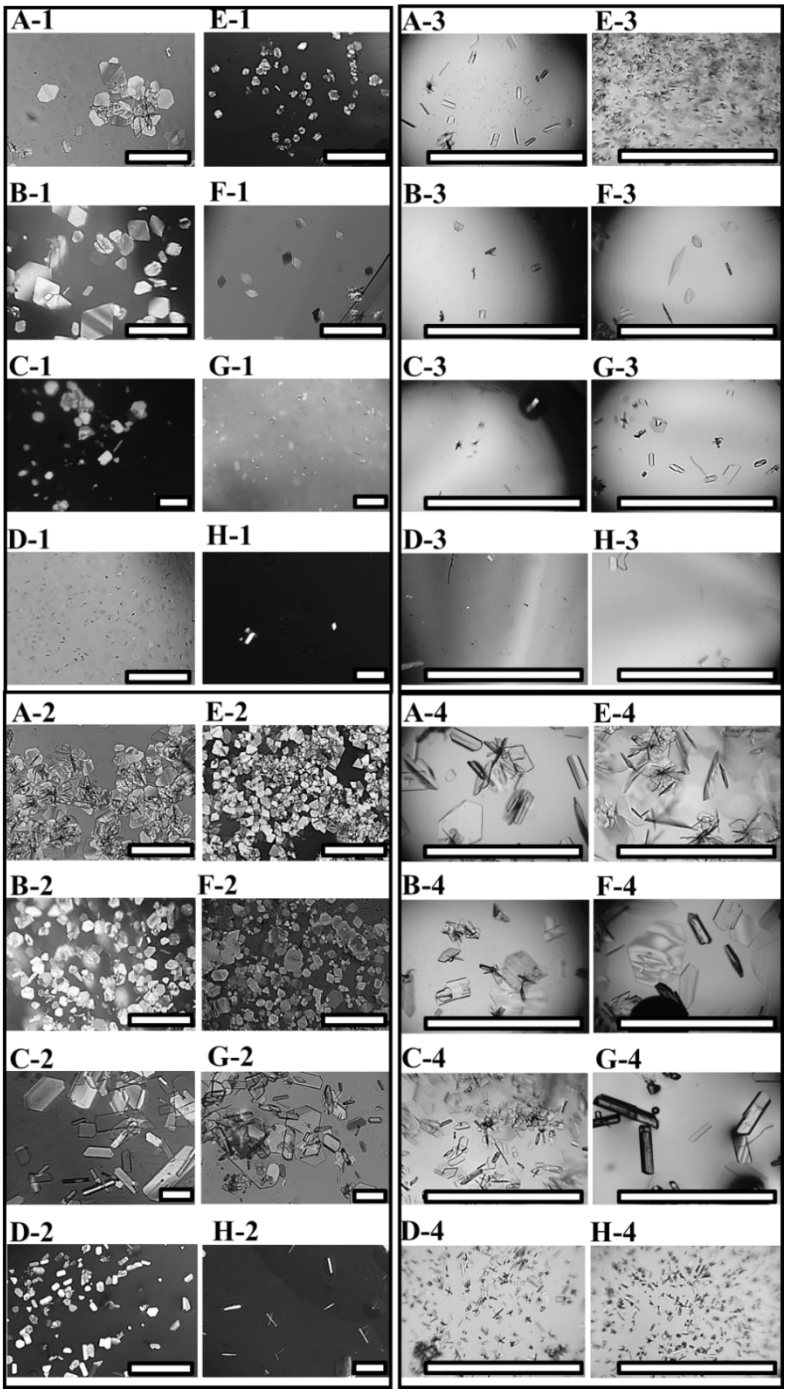

Figure 27: Screening of crystal morphologies and polymorphs of L-histidine crystals using the multi-well microfluidic device and the comparison of results with 96-well microtiter plate. Four panels of eight optical micrographs are arranged to compare the micrographs in the left panels (A-1 to H-1 (5 minutes), and A-2 to H-2 (30 minutes)) for the multi-well device with the micrographs in the right panels (A-3 to H-3 (5 minutes), and A-4 to H-4 (30 minutes)) for 96-well microtiter. The solution compositions for eight micrographs in each panel corresponds to the supersaturations (σ) and vol% ethanol shown in Figure 18B, such as A: σ = 2.57, 50 vol% ethanol, B: σ = 2.28, 50 vol% ethanol, C: σ = 1.74, 50 vol% ethanol, D: σ = 1.14, 50 vol% ethanol, E: σ = 7.2, 70 vol% ethanol, F: σ = 3.14, 50 vol% ethanol, G: σ = 2.00, 30 vol% ethanol, and H: σ = 1.15, 10 vol% ethanol.

Figures 28D, E, and F show the variation in X_A and growth rates as a function of L-histidine concentration, vol% of ethanol, and supersaturation, respectively, in the 96-well plate device. Although the microtiter plate qualitatively captures the trend in the percentage of X_A for varying concentrations, vol% of ethanol, and supersaturations, it overestimates the percentage of the stable form (X_A). The overestimation of stable form is due to the dissolution of metastable form that occurs when supersaturation decreases below the solubility of the metastable form. The depletion of supersaturation in microtiter plates greatly impacts the growth rate measurement, which constantly decreases over time and cannot be reliable.

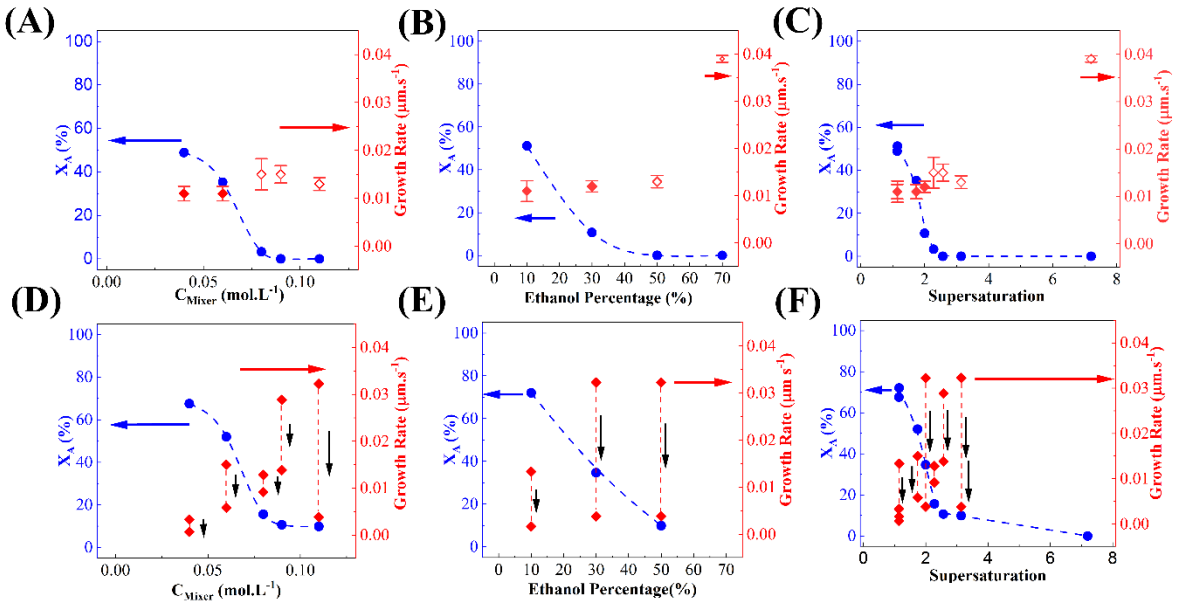

Figure 28: Variation in the percentage of Form -A (solid blue circles) and growth rates of (111) facet of Form-A (solid red diamonds) and Form-B (open red diamonds) of L-histidine with increasing (A) concentration of L-histidine (C_{Mixer}) in the multi-well device, (B) volume fraction of ethanol in the multi-well device, (C) supersaturation in the multi-well device, (D) concentration of L-histidine in the 96-well device, (E) volume fraction of ethanol in the 96-well device, and (F) supersaturation in the 96-well device. The black arrows in (D), (E), and (F) represent a decrease in the growth rate in 30 minutes due to depletion of supersaturation in the 96-well device. The red and blue arrows indicate y-axes for the growth rate and percentage of the stable form, respectively.

3.4.6 X-ray Diffraction Patterns of L-histidine Polymorphs

Figure 25 shows simulated and experimental XRD patterns for L-histidine pure Form-A and Form-B. The XRD of Form-A was taken directly for as-purchased L-histidine (Sigma-Aldrich, chemical

purity≥ 99%). The pure Form-B was prepared by cooling crystallization of a saturated solution of L-histidine at 70^{o}C.

Based on the subplots in Figure 25, we can conclude that the experimental spectra for both polymorphs match the simulated spectra. In the simulated XRD pattern, all the possible facets of the crystals exposed during scanning are shown. However, in the experimental XRD pattern, only the facets that are preferentially oriented are exposed. Also, a slight shift in the experimental XRD pattern compared to the simulated spectra for sample A can be due to the specimen displacement. It is a systematic peak position error due to the misalignment of the sample.

In Figure 25, we have dashed vertical lines to show the slight shifts in the major peaks for the experimental XRD pattern of L-histidine Form-A. After confirming the pure form of each polymorph, five mixtures of these pure forms were prepared with a total mass of 0.1 g. The total mass of the crystals was used in a 5 cm sample holder for obtaining the XRD pattern. In Figure 29, the spectra of these five samples and pure forms are shown in the order of increasing weight % of Form-B. There are two distinct peaks shown in Figure 25; one appears in Form-B but does not exist in Form-A (Figure 30A). The second peak appears in Form-A but not in Form-B. (Figure 30B). The intensities of these two peaks also vary with the percentage of Form-A.

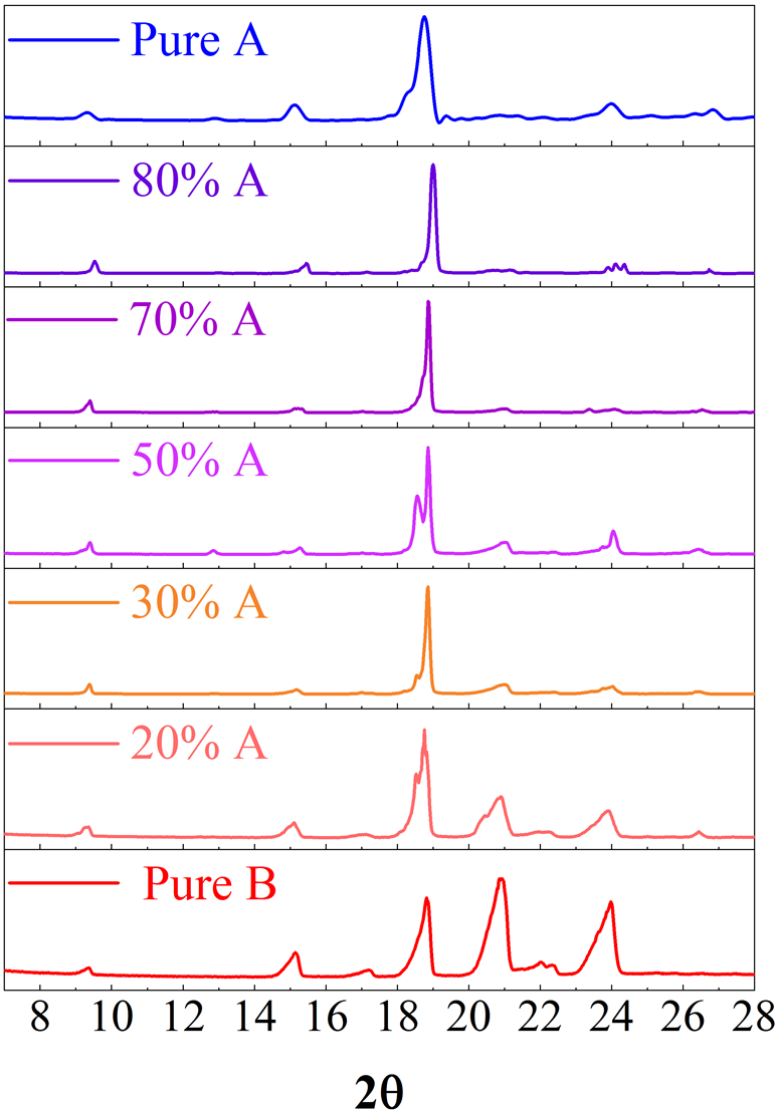

Figure 29: XRD pattern of mixtures of Form-A and B and their pure forms.

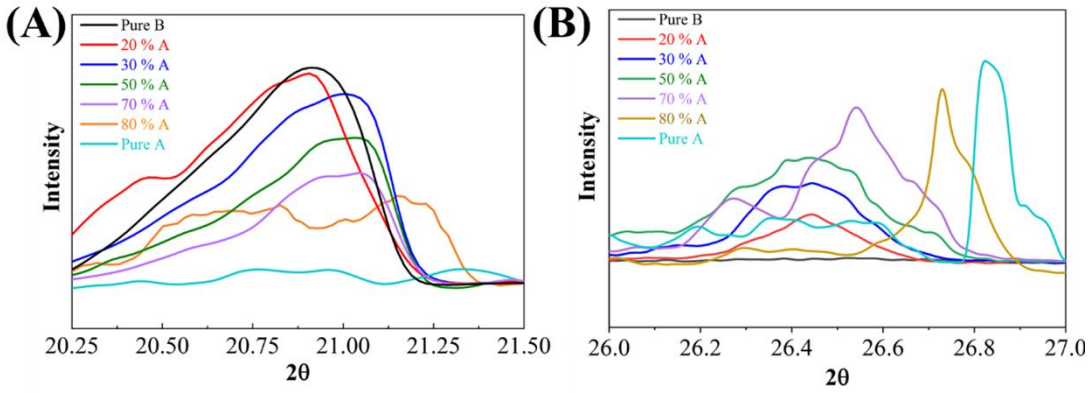

Figure 30: Variation in the intensity of characteristic peaks of (A) Form-B and (B) Form-A, with an increasing weight percentage of Form-A.

Figures 30A and 30B are magnified views from the selected peaks from Figure 29, and the target angle for the XRD measurement was from 8 to 28 degrees. The measured relative intensities of these characteristic peaks (From Figure 29) fit a linear relationship with respect to the weight percentage of Form-A L-histidine, as shown in Figure 31.

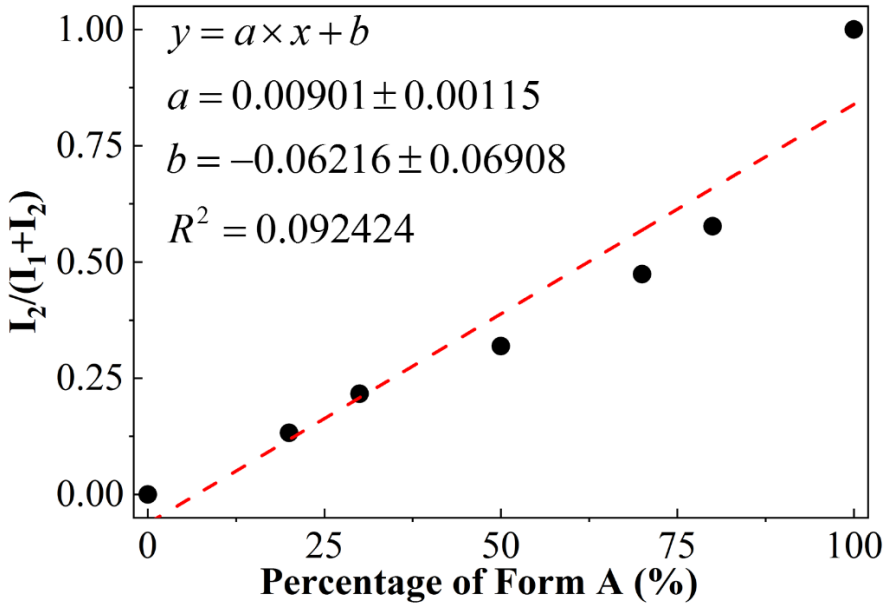

Figure 31: Calibration curve for the XRD pattern

3.5 Conclusion

An effective design of a continuous-flow, well-mixed, multi-well microfluidic device is presented here for parallel screening of crystalline materials at controlled conditions. The multiple tangential inlets of the micromixer are consolidated to make an array of wells without disrupting the cyclonic/vortex flow pattern inside the micromixers. A merged-inlet configuration utilizing Y-junctions effectively reduces the 32 inlets (four tangential inlets to each micromixer) in an array of eight micromixers to 16 inlets, which can be further reduced to three inlets using the hydraulic network. Reducing the total number of inlets reduces the number of pumps required for parallel screening using a multi-well device.

The identical pressure drops in non-neighboring, alternate inlets confirm uniform flow rates in

each inlet entering the micromixer. The negligible pressure drop in the micromixer and higher mixing index ensures homogeneous mixing of entering fluid, which is required to achieve homogeneous supersaturation rapidly in the micromixer. The average residence time of fluid can be controlled by varying the flow rates so that the startup time is much higher than the induction time of crystal nucleation, which is an important requirement to obtain reliable and reproducible data from such flow studies.

The impact of this multi-well device stems from its ability to conduct parallel screening and reduce the time required to evaluate multiple crystallization conditions. While the time required for sequential screening using a single well device increases linearly with several conditions, the parallel screening using a multi-well device can substantially reduce overall screening time. Here, we demonstrate screening of crystal morphology, polymorph, and growth rates of L-histidine for eight different conditions such as molar concentration, vol% of ethanol, and supersaturation in ~ 30 minutes. In contrast, the sequential screening would take 8x30 = 240 minutes to conduct a similar study. The effectiveness of the multi-well device is also compared with the traditional 96-well microtiter device to evaluate the impact of varying supersaturation in microtiter plates on screening results. In general, the microtiter plates overestimate the percentage of stable polymorph compared to metastable polymorph with large variations in the growth rates. At the same time, the continuous-flow multi-well device provides reliable and robust quantification of crystal polymorphs, morphology, and growth rates.

This design will eventually lead to the development of HT material screening devices that can trap varieties of crystalline materials and study them under controlled conditions.

IV. ON-THE-SPOT QUENCHING FOR EFFECTIVE IMPLEMENTATION OF COOLING CRYSTALLIZATION IN CONTINUOUS-FLOW MICROFLUIDIC DEVICE

4.1 Introduction

Cooling crystallization is a preferred separation technique in pharmaceutical, agrochemical, and wastewater treatment processes where dissolved species need to be removed selectively from a solution without adding external agents such as antisolvents, additives, pH, and modulators[53]. It can be implemented effectively if the solute has a significant solubility difference with respect to temperature. The necessary driving force, i.e., supersaturation, for the cooling crystallization is created by reducing the temperature of the solution towards a state of lower solubility. For such a crystallization process, it is essential to maintain a homogenous temperature of the solution and minimize the temperature gradients that are dominant around the entrance of flow crystallizers and on the walls of the batch crystallizers during cooling. Rapid cooling in conventional flow and batch crystallizers is typically achieved by implementing a convection cooling jacket with an external control system[54]. However, the temperature control strategies for microfluidics are quite different from conventional crystallizers due to space constraints and the miniaturized size of the device[55]. Different cooling techniques have been employed for microtiter and microfluidic systems (see Figure 32)[23]. Here the primary purpose of these techniques is to rapidly cool the entering hot solution in the microchannel or the initial hot solution in the microtiter to a lower temperature. One of the most common techniques is thermoelectric cooling using the Peltier device (see Figure 32A). It has been implemented to study nucleation of protein crystals in 400-well plates[56], screen nucleation kinetics of colloidal crystals[57], perform rapid PCR-based analysis[58]. Effective thermoelectric cooling requires higher thermal conductance of microfluidic devices.

However, most microfluidic devices are made of polymers with lower thermal conductivity. The higher thermal resistance of microfluidic devices and inefficient contact with the Peltier device often leads to entrance effects in continuous-flow microfluidic devices.

The other approach for local cooling is to use either endothermic mixing or reaction near the microchannel. Alternatively, phase change materials that transform from liquid phase to gas phase can cool down the microchannels (see Figure 32B)[17]. In such cooling schemes, the reduction in reaction rates due to depletion of reactants in the cooling channels can result in temperature gradients along the microchannels[16]. Alternatively, the coolants with higher specific heat capacities can be used to maintain a uniform temperature. Figure 32C shows a configuration of droplet-based microfluidic setup, which includes a long capillary tube immersed in a circulating cooling bath. In such systems, the droplets flowing in a continuous phase cool down via diffusive heat transfer. However, the temperature gradient within the capillary wall may result in a larger temperature variation along the tube. Therefore, this type of cooling is mainly applied to study slow nucleating crystals with longer induction time, such as proteins. Another cooling technique is convective mixing of hot and cold solutions to quench the hot solution. Figure 32D shows the example of convective mixing in a slug-flow tubular crystallizer, where concentrated hot and cold solutions are mixed in at T-junction and then pumped into the channels along with air to form slugs[59]. The achievable temperatures and concentration of the mixed stream are limited by the temperature and concentration ranges, respectively, of hot and cold solutions. A comparative analysis of these four cooling techniques to effectively reduce the temperature of inlet solution with minimum gradients is provided in Table 12.

Table 12: Comparative Analysis of Different Cooling Techniques

	Thermoelectric Cooling	**Endothermic Cooling**	**Convective Cooling**	**Cooling Via Mixing**
Temperature Gradient along the microchannel	• Low with conductive material and low thickness • High with materials with low conductivity and high thickness	Medium	Low	• Low with Proper insulation • High without insulation
Supersaturation along the microchannel	Not Constant	Not Constant	Not Constant	Not Constant

Although it is possible to reduce temperature gradients under certain conditions (see Table 12), the continuous depletion of solute due to nucleation and growth of crystals in the cooled channels results in a continuous variation of supersaturation. Additionally, faster nucleation and growth may also cause clogging of the microchannels. It is possible to vary the temperature along the cooled channels using a gradient generator to maintain constant supersaturation[60]. However, it is difficult to know a priori how much solute will be depleted in the microchannel and the required temperature to offset the drop in supersaturation. Therefore, an effective microfluidic device for cooling crystallization is required to reduce the temperature gradient, maintain constant supersaturation, and prevent clogging. Recent developments of the continuous-flow crystallization in microfluidic devices have enabled effective screening of crystal morphology, polymorph, size, and kinetic data under controlled conditions[41,61]. These microfluidic devices have cylindrical micromixers with tangential inlets of entering solution at the bottom, creating a cyclonic (or rotational) flow to trap nucleated crystals. The cyclonic solution flow in the micromixer provides uniform mixing and isothermal conditions to achieve constant supersaturations while allowing the steady growth of trapped crystals.

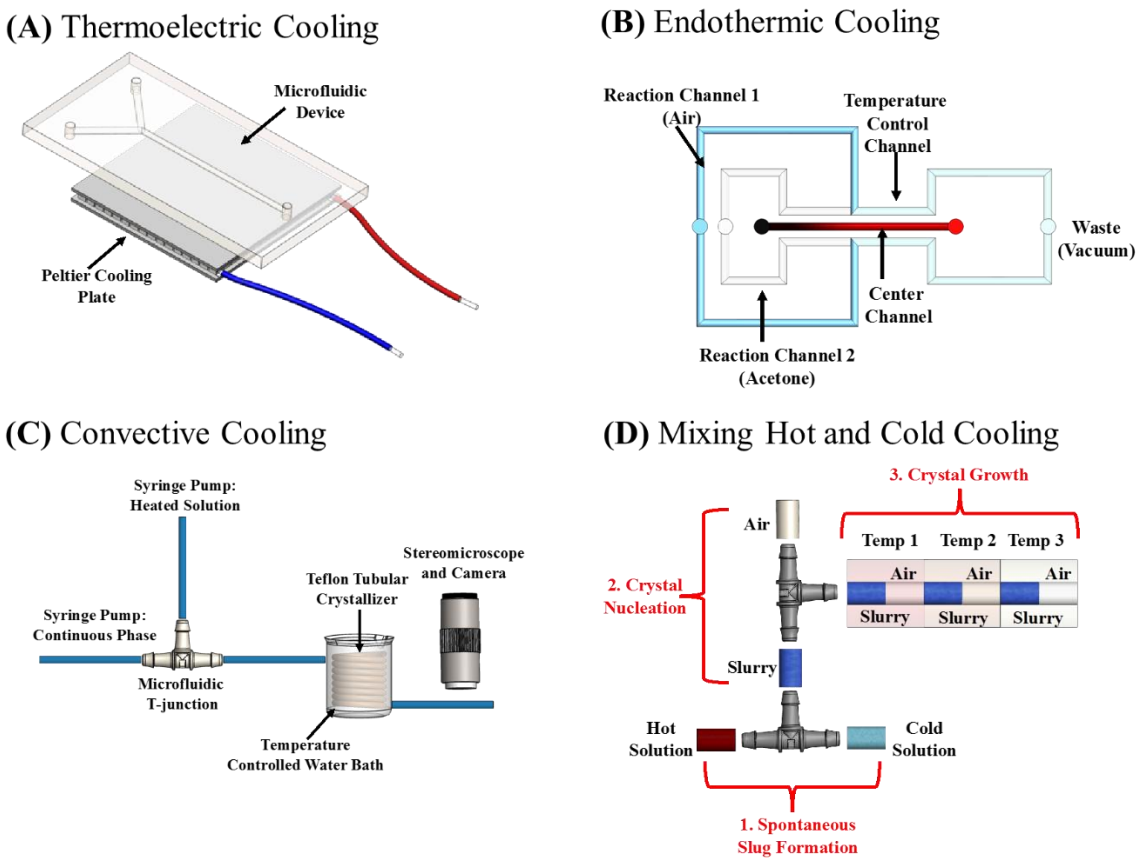

Figure 32: Different types of cooling techniques to study cooling crystallization in microfluidic devices: (A) thermoelectric cooling using Peltier device; (B) endothermic cooling using endothermic reaction or evaporation in cooling channels; (C) convective cooling using external cooling bath; and (D) convective cooling by mixing hot and cold streams.

This study aims at developing effective quenching strategies for these continuous-flow well-mixed microfluidic devices that will enable the screening of crystalline materials through cooling crystallization techniques[41]. Here, two different on-the-spot quenching strategies are introduced to cool down the inlet solution with minimum possible spatial gradient. The first strategy is inspired by jacketed mixed-suspension mixed-product removal reactors used for batch and semi-batch cooling crystallization in the larger scales. Here, a cooling jacket is implemented around the lower bottom of the microwell, where the inlets are located to quench the entering solution. The cooling jacket has a separate inlet and outlets to recirculate the coolant stream. The second on-the-spot quenching strategy involves the mixing of two separate saturated solutions of higher and lower temperatures. The mixed solution in the microwell attains a lower temperature than the entering

hot solution, thereby developing a steady supersaturation. The temperature profile is initially evaluated for both strategies at different flow rates and temperatures of entering solution and coolant and then assessed for the accessible range of supersaturations. The attainable temperature and supersaturation ranges are confirmed both experimentally and computationally. Finally, the microfluidic devices with and without cooling jackets are 3D-printed and then tested to screen the morphology, polymorph, and growth rate of L-glutamic acid crystals grown by cooling crystallization.

4.2 Theoretical Method

4.2.1 Design Consideration to Implement on-the-spot Quenching Techniques in Multi-inlet Micromixer Device

Here we evaluate two distinct quenching techniques to enable on-the-spot cooling in the multi-inlet micromixer device. The first technique is convective cooling that uses an external cooling jacket, and the second technique involves convective mixing of a hot and cold solution. While the latter scheme allows on-the-spot quenching of hot and cold solutions to attain equilibrium temperatures, the former scheme requires some additional design considerations to enable on-the-spot quenching. The residence time of solutions in these tiny micromixers (up to 4 mm height and 4 mm diameter) varies from a few seconds to a few minutes. As the hot solution enters the micromixer from the bottom and rises upward, it will continuously cool down without reaching a steady temperature and thus developing a large temperature variation inside the micromixer. It is nearly impossible to attain equilibrium temperatures in a fully jacketed micromixer with these residence times. Therefore, one of the design considerations is to have a shorter height of cooling jacket not exceeding the diameter of the inlet. This collar of the cooling jacket ensures that tangentially entering solutions are cooled as they are mixed in a cyclonic flow inside the mixer. The thermal insulation above the collar maintains the temperature of the cooling solution. Figure

33A shows the design of the micromixer with a collar of the cooling jacket. The coolant in the cooling jacket can be set to a sufficiently lower temperature for the entering hot solution to achieve the desired temperature. It depends on the design of the micromixer, thermal and physical properties of coolant, solution, and material of construction, which is discussed in the next section. In this cooling technique, the temperature and concentration of the cooling solution are independent of each other, allowing probing a wider range of supersaturations.

The second cooling technique does not require any cooling jacket if the insulation of the micromixer is efficient to maintain the temperature of the cooling solution. Here, the temperature of the mixed solution is lowered by mixing hot and cold solutions that are pre-saturated with solute. For efficient mixing, the hot and cold solutions are entered from the non-neighboring inlets of the micromixer to increase the contact area between hot and cold regions and eventually enhance the heat transfer. The equilibrium temperature of the mixed solution is a function of the flow rate and temperature of each stream. This type of cooling also dilutes the solute concentration in the hot feed, thereby limiting the range of attainable supersaturation in the micromixer.

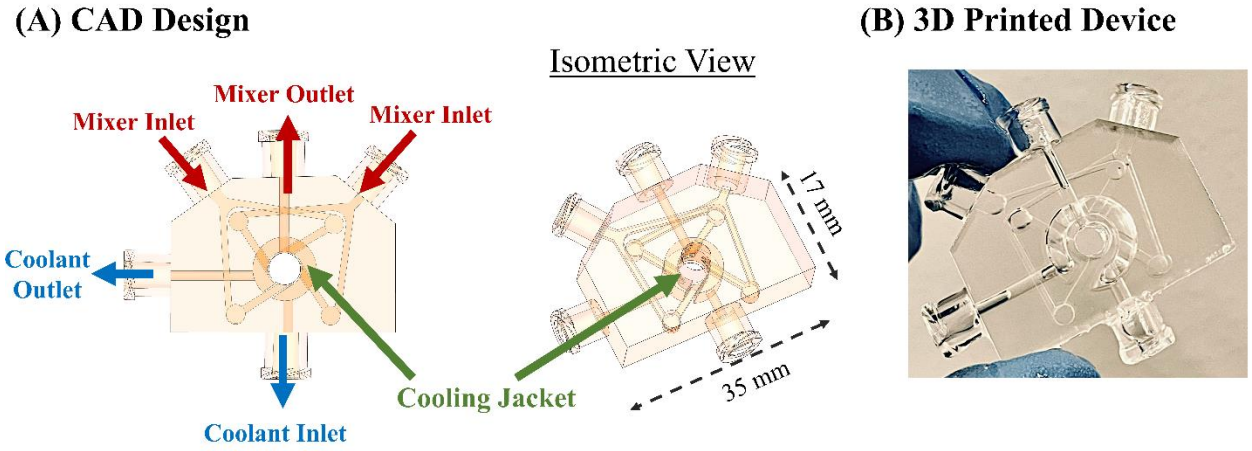

Figure 33: (A) CAD design of the jacketed micromixer; (B) 3D-printed jacketed micromixer device

4.2.2 Simulation of Temperature, Velocity, Concentration, and Supersaturation Profiles to Evaluate on-the-spot Quenching Techniques

The effectiveness of above mentioned on-the-spot quenching techniques is evaluated by calculating the temperature and supersaturation profiles in the micromixer. Convective cooling using external jacket: The dimensions of the micromixers with cooling jackets is provided in Figure 34.

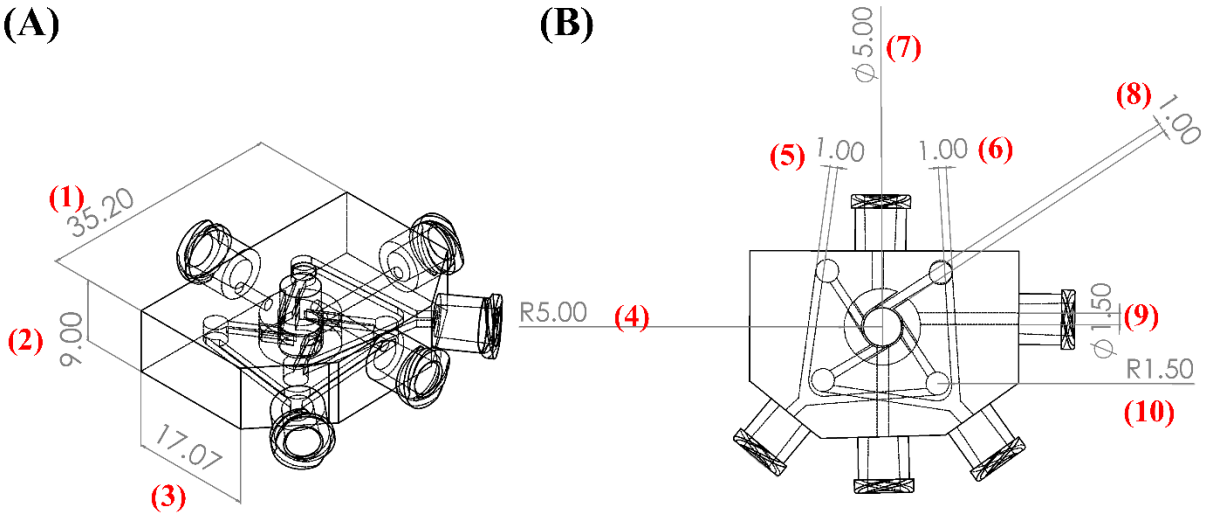

Figure 34: (A) Isometric view and (B) top view of the jacketed microfluidic mixer device with marked dimensions.

The CAD file for these designs was imported into COMSOL Multiphysics® and meshed using a free tetrahedral mesh of element size 0.207 to 1.15 mm and a curvature factor of 0.6. The maximum element growth rate and resolution of the narrow regions were set at 1.5 and 0.5, respectively. Navier-Stokes equation and the energy balance equation consisting of conduction and convection terms were solved simultaneously for the entering streams of water at different temperatures. The solute was not considered in the simulation as its solubility is typically at least three orders of magnitude smaller than solvent and has a negligible effect on the thermal and viscous properties of the solution.

4.2.2.1 Laminar Flow Module: Equations and Boundary Conditions

The boundary conditions at the inlets were set according to the entering flow rates and temperature of water in the micromixer and coolant (50 vol% ethylene glycol and water) in the jacket. The

boundary condition at the outlet was set to zero conductive flux for the energy balance equation and fixed ambient pressure for the Navier-Stokes equation. At the external surface of the device, Newton's law of cooling was applied using the heat transfer coefficient of stagnant air. The laminar flow module of COMSOL was used to calculate the velocity profile in the microfluidic mixer. The time-dependent Navier-Stokes equation solved is described as follows:

$$\rho \frac{\partial u}{\partial t} + \rho(u.\nabla)u = \nabla.[-p.I + \mu(\nabla u + (\nabla u)^T) + F \quad (37)$$

Where ρ and μ are temperature-dependent density, and the viscosity of water is assumed to be incompressible. Here the selected boundary conditions for the two temperature controlling strategies are listed.

- **Strategy 1: Cooling bath implementation:**

Figure 35A shows the isometric view of the imported 3D file of the jacketed microfluidic mixer device in the COMOSL Multiphysics for the simulation. In Figure 35B, the assigned boundary conditions for this system are shown and listed as:

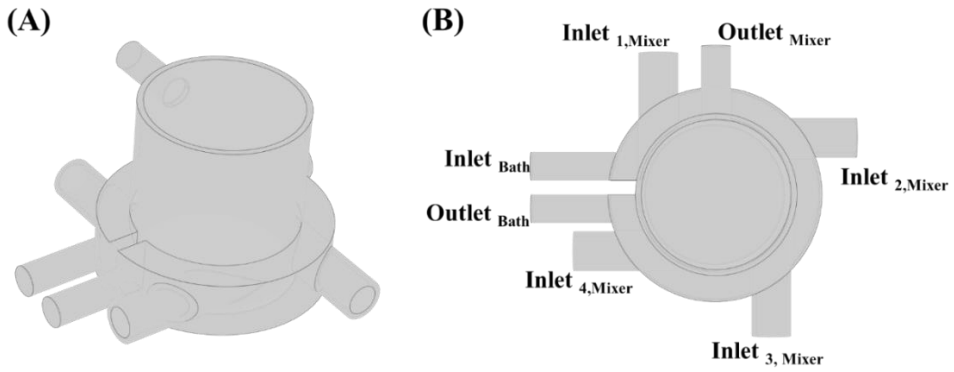

Figure 35: (A) Isometric view of the jacketed microfluidic device; (B) The top view of the jacketed microfluidic device with the assigned boundary conditions for the mixer and cooling bath in the cooling bath strategy.

Boundary Conditions:

- Inlet $_{1, Mixer}$ = Inlet $_{2, Mixer}$ = Inlet $_{3, Mixer}$ = Inlet $_{4, Mixer}$: Q_{Mixer} = 0.25 mL.min^{-1}
- Outlet $_{Mixer}$: P = 1 atm

- Inlet $_{\text{Bath}}$: Q_{Bath} = 10 mL.min^{-1}
- Outlet $_{\text{Bath}}$: P = 1 atm
- **Strategy 2: Mixing saturated hot and cold streams:**

Figure 36A shows the isometric view of the imported 3D file of the microfluidic mixer device in COMOSL Multiphysics for the simulation. In Figure 36B, the assigned boundary conditions for this system are shown and listed as:

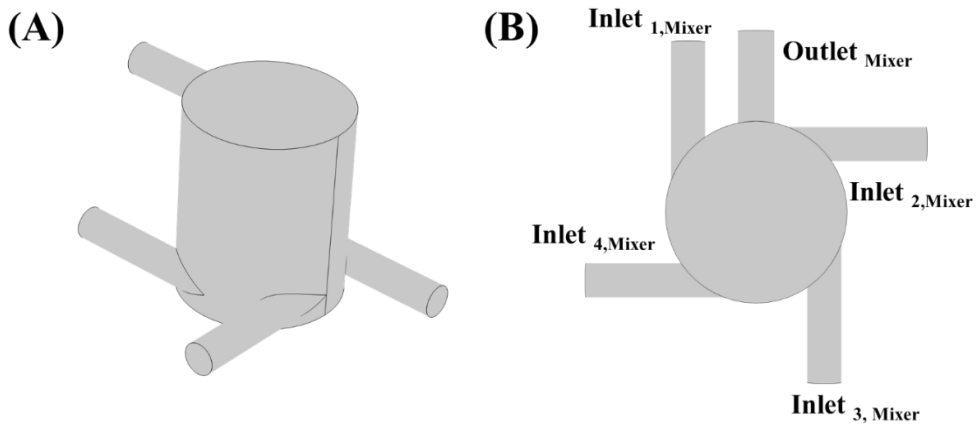

Figure 36: (A) Isometric view of the microfluidic mixer device; (B) The top view of the microfluidic mixer device with the assigned boundary conditions for the mixer in mixing hot and cold strategy.

Boundary Conditions:

- Inlet $_{\text{1, Mixer}}$ = Inlet $_{\text{3, Mixer}}$: Q_{Hot} = 0.25 mL.min^{-1}
- Inlet $_{\text{2, Mixer}}$ = Inlet $_{\text{4, Mixer}}$: Q_{Cold} = 0.25 mL.min^{-1}
- Outlet $_{\text{Mixer}}$: P = 1 atm

The laminar flow module is coupled with the heat transfer in solid and fluid module modules, and all the assigned temperatures conditions are listed in section 4.2.2.2.

4.2.2.2 Heat Transfer Module: Equations and Boundary Conditions

- **Strategy 1: Cooling bath implementation**

The heat transfer in the solids and fluids module is coupled with the laminar flow module to predict the equilibrium temperature profile in the microfluidic mixer device. As a result, the time-dependent energy balance equation is:

$$\rho c_P u.\nabla T + \nabla(-k\nabla T) = Q \quad (38)$$

where k is the thermal conductivity, ρ is the density and c_P is the heat capacity at constant pressure. Here, the bath walls are selected as the solid walls with PMMA selected as its material. The bath fluid and mixing fluids are also separated, and their boundary conditions are listed as:

- Inlet $_{1, Mixer}$ = Inlet $_{2, Mixer}$ = Inlet $_{3, Mixer}$ = Inlet $_{4, Mixer}$: $T_{Hot} = 70$ ℃
- Outlet $_{Mixer}$: $-n.q = 0$
- Inlet $_{Bath}$: $T_c = 20$ ℃
- Outlet $_{Bath}$: $-n.q = 0$

All other boundaries were set at the thermal insulation boundary.

- **Strategy 2: Mixing saturated hot and cold streams:**

The heat transfer in the fluids module is coupled with the laminar flow module to predict the equilibrium temperature profile in the microfluidic mixer device. The time-dependent energy balance equation is shown in equation 31. In Figure 36B, boundaries with certain conditions are indicated and listed as:

Boundary Conditions:

- Inlet 1, Mixer = Inlet 3, Mixer : $T_{Hot} = 70$ ℃
- Inlet 2, Mixer = Inlet 4, Mixer : $T_{Cold} = 20$ ℃
- Outlet Mixer: $-n.q = 0$

All other boundaries were set at the thermal insulation boundary.

The temperature-dependent viscosity and density of the water were also considered in the simulation.

4.2.2.3 Model Parameters of the Simulations

In this study, we have simulated a coupled analysis of the laminar flow module and heat transfer in solids and fluids to evaluate the velocity, pressure, and temperature profile inside the microfluidic mixer and the cooling jacket. The 3D model for simulations was imported into the model from a Solid Work design. The design was further simplified by eliminating the sharp edges and smoothening the surfaces to enhance the mesh quality. The free tetrahedral mesh was selected for the models. The tetrahedral mesh was selected for this study, and the details are provided in the following part:

- Maximum Element Size $= 1.15$ mm
- Minimum Element Size $= 0.207$ mm
- Maximum Element Growth Rate $= 1.5$
- Curvature Factor $= 0.6$
- Resolution of Narrow Region $= 0.5$

The discretized equations were solved using the parallel sparse direct solver (PARDISO) solver, and the residual tolerance was set to 0.01 with 100 iterations and tolerance termination technique. Newton's method was used for iterations with a damping factor of 0.1 and relative tolerance of 0.001. Since the solute concentration in the micromixer does not change, the calculation of supersaturation was only determined by the temperature profile. The exit temperature (T_e) of the solution from the mixer was calculated for a range of coolant temperatures (T_c), entering solution temperature (T_h), and total volumetric flow rate (Q_t) of solution. A dimensionless temperature (θ) was identified that combines all the temperatures as follows:

$$\theta = \frac{T_e - T_c}{T_h - T_c} \tag{39}$$

such that θ is only dependent on Q_t. The relationship between θ and Q_t for jacketed microwell device is unique and referred to as a calibration curve, which will be used later to determine the operating conditions of the microfluidic device.

Convective cooling by mixing hot and cold solutions: The dimensions of the micromixer are similar to the case above, except there is no cooling jacket. To effectively mesh the geometry, a free tetrahedral mesh of element size 0.207 to 1.15 mm and a curvature factor of 0.6. The maximum element growth rate and resolution of the narrow regions were set at 1.5 and 0.5, respectively. The governing equations and boundary conditions for the simulation of temperature and velocity are similar to the case above. Since the solute concentrations are very low in the solution, the temperature profile was assumed to be independent of the concentration profile. The concentration profile was simulated by solving the Navier-Stokes equation and the continuity equation. The boundary conditions at the inlets were set according to the entering flow rates and solute concentration in the hot and cold streams. The boundary condition at the outlet was set to zero diffusive flux for the continuity equation and fixed ambient pressure for the Navier-Stokes equation. The temperature-dependent viscosity and density of the water were also considered in the simulation. The discretized equations were solved using the PARDISO solver, and the residual tolerance was set to 0.01 with 100 iterations and tolerance termination technique. Newton's method was used for iterations with a damping factor of 0.1 and relative tolerance of 0.001. Supersaturation was then calculated using the simulated concentration and temperature profiles. The exit temperature (T_e) of the solution from the mixer was calculated for different values of entering cold solution temperature (T_C), entering hot solution temperature (T_h), and volumetric flow rate (Q_C) of cold solution for a constant total flow rate of 1 mL.min^{-1}. Similar to the first cooling technique, a dimensionless temperature (θ) was identified (eq 32), and a calibration curve of θ vs. Q_C was developed for a fixed total flow rate.

4.3 Materials and Experimental Method

4.3.1 Materials

The crystalline β-Form of L-glutamic acid (Sigma-Aldrich, chemical purity ≥98%) was used to screen polymorph, morphology, and growth rates during cooling crystallization. The solutions for cooling crystallization studies were made using deionized water (Sigma-Aldrich, 18 MΩ cm). A mixture of ethylene glycol-water (50% vol) was used to recirculate the coolant stream in a jacketed micromixer device.

4.3.2 Fabrication of the Microfluidic Device

The 3D design of the jacketed micromixer device shown in Figure 33A was designed in SolidWorks® (2020, Dassault Systems) and then 3D-printed using a stereolithography (SLA) 3D printer (Form 3, Formlabs Inc., USA). A clear FLGPCL02 resin activated by a 405 nm laser was used to 3D print optically clear microfluidic devices with 150 μm of lateral and 25 μm of axial resolutions. The 3D-printed devices were washed with isopropyl alcohol (IPA) (90%, Sigma-Aldrich) bath for 20 minutes in the Form Wash (Formlabs Inc., USA) to remove the residues of the resin from the external surface. The interior channels of the 3D-printed device and the circulation bath were washed separately by injecting IPA using a syringe to remove the uncured resins. The orientation for prints on the 3D printer stage was selected to minimize the contact of the supports with top and bottom surfaces. However, if necessary, the optical transparency can be improved by wet sanding using 400 to 12000 grit pads followed by spray painting of resin. The top and bottom openings of the micromixers in the multi-inlet device (see Figure 33B) were sealed with polycarbonate films for optical clarity to image crystals under the optical microscope. The fabricated multi-inlet device is shown in Figure 33B.

4.3.3 Experimental Setup and Operation of the Cooling Crystallization in the Microfluidic Device

Experimental Setup: The experimental setup for the continuous cooling crystallization of L-glutamic acid involves the multi-inlet micromixer device continuously monitored under an optical microscope (Olympus BX53M, Olympus America Inc.) to screen the morphology, polymorph, and growth rate of L-glutamic acid at different supersaturations. The aqueous solution of L-glutamic acid was pumped into the microfluidic device using two single-channel programmed syringe pumps (NE-1000, New Era Pump System Inc.). Two sets of syringe heating pad and heater were used to control the temperature of L-glutamic acid solutions to the desired temperature. Additionally, the heat loss from the syringe heating pads was measured to calibrate the syringe heater, compensate for the heat loss, and finally maintain the temperature of each solution at the set point. The foam protection wraps were also used to insulate the tubing that connects the syringes to the inlets of the microfluidic device. Both inlets were connected to the one-way microfluidic check valves to prevent backflow from the micromixer. A refrigerated recirculation cooling bath (ARCTIC A40, Thermo Fisher Scientific) was used to recirculate a mixture of ethylene glycol and water (50:50 vol ratio) as the coolant stream inside the cooling jacket.

Operation of the jacketed micromixer: A calibration curve that relates dimensionless exit temperature (T_e) with the total volumetric flow rate (Q_t) of the solution was first established computationally and then validated experimentally. The solubility data of L-glutamic acid[59,60] in water and the calibration curve were used to identify operating conditions to achieve specific supersaturations. For example, to obtain a supersaturation of $S = 2$ at T_e, the necessary concentration of entering solution was obtained as follows:

$$C = S \times C^*(T_e) \tag{40}$$

where C^* is the solubility of L-glutamic acid in water. Next, the total volumetric flow rate was chosen to achieve lower mean residence time and its variance. The total volumetric flow rate is 1 mL.min^{-1} was chosen that yields a mean residence time of 46.4 ± 27.5 seconds. The calibration curve was then used to obtain the value of dimensionless temperature for a given flow rate of 1 mL.min^{-1}. From the definition of θ (eq 32), the temperature of the entering solution (T_h) was calculated for a choice of coolant temperature (e.g. $T_c = 0℃$). The supersaturation can be varied by varying the concentration of entering the solution while keeping all other parameters fixed. A total of eight experimental conditions were explored using this cooling technique. Details of the selected flow rates, feed concentrations, and temperatures are provided in Table 13. These operating conditions are also illustrated in Figure 37. In Table 13, we have listed the flow rates and concentration of L-glutamic acid in water for the initial solution, mixer, and equilibrium condition. The supersaturation is calculated as:

$$S = \frac{C_{Mixer}}{C_{equ}} \tag{41}$$

For samples A to H, the concentration of the mixer is the concentration of the entering solution. In the case of the mixing approach, the concentration of mixer is the average concentration of hot and cold streams and is calculated as:

$$C_{mixer} = \frac{Q_{Hot} * C_{Hot} + Q_{cold} * C_{cold}}{Q_{Hot} + Q_{Cold}} \tag{42}$$

The C_{equ} or C^* is the concentration of the L-glutamic acid at the equilibrium temperature in the micromixer.

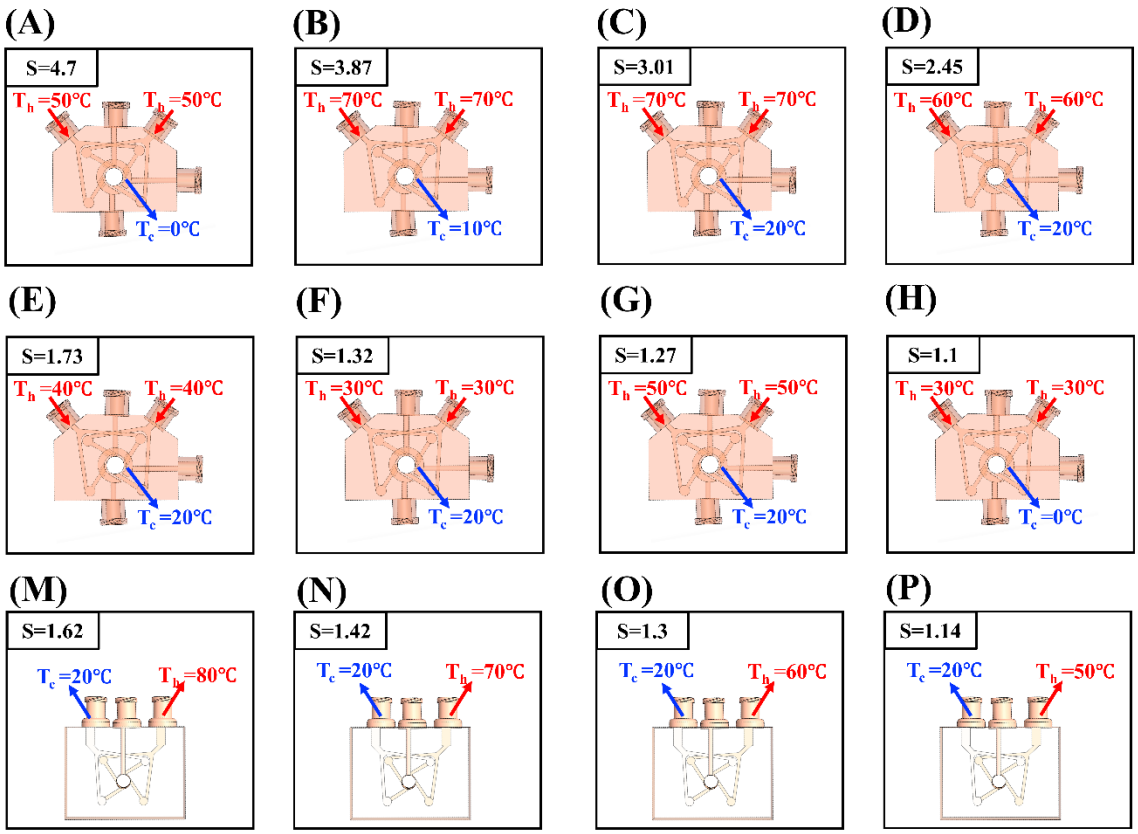

Figure 37: Experimental conditions for the cooling crystallization: (A), (B), (C), and (D) selected temperatures for cooling bath and saturated hot L-glutamic acid solutions in the cooling bath strategy; (E), (F), (G), (H) Selected temperatures for saturated hot and cold L-glutamic acid solutions in the mixing hot and cold strategy.

Table 13: Details of experimental condition for cooling crystallization of the L-glutamic acid.

Samples	**T_h (^oC)**	**T_c (^oC)**	**T_{equ} (^oC)**	**Q_{Total} (mL.min^{-1})**	**$C_{Initial}$ (mol. L^{-1})**	**C_{Mixer} (mol. L^{-1})**	**C_{equ} (mol. L^{-1})**	**S.S**
A	50	0	9.30	1	0.152	0.152	0.032	4.78
B	70	10	33.19	2	0.289	0.289	0.076	3.87
C	70	20	39.37	2	0.289	0.289	0.096	3.01
D	60	20	35.39	2	0.214	0.214	0.087	2.45
E	40	20	27.59	2	0.102	0.102	0.059	1.73
F	30	20	23.77	2	0.066	0.066	0.050	1.32
G	50	20	31.46	2	0.091	0.091	0.070	1.29
H	30	0	11.27	2	0.036	0.036	0.033	1.11
M	80	20	50.00	1	0.430	0.239	0.148	1.61
N	70	20	45.00	1	0.290	0.175	0.124	1.42
O	60	20	40.00	1	0.210	0.131	0.101	1.30
P	50	20	35.00	1	0.150	0.098	0.086	1.14

The effective startup of the jacketed micromixer is crucial for accurate screening of coocrystallization. Therefore, the micromixers and channels were first flushed with water to remove air. The coolant stream was then recirculated in the jacket for 15 minutes at a high flow rate of 10 mL.min^{-1} to ensure the device attains an equilibrium temperature. Next, the saturated solutions at a temperature T_h is pumped into the micromixer, and the flow rates at both inlets were set equal.

Operation of the non-jacketed micromixer with mixing hot and cold approach: A calibration curve that relates dimensionless exit temperature (θ) with the volumetric flow rate of entering cold

stream (Q_c) at a fixed total flow rate of 1 mL.min^{-1} was first established computationally and then validated experimentally. The solubility data of L-glutamic acid in the water, along with the calibration curve, was used to identify operating conditions to achieve specific supersaturations. Following protocol was used to attain specific supersaturation and temperature inside the micromixer. The solute concentration in the micromixer was obtained for the desired supersaturation (e.g., S = 1.3) and temperature (e.g. $T_e = 40$℃) using eq.33. Next, we set the flow rate of a cold solution, Q_c. The calibration curve (θ vs.Q_c) was then used to obtain the value of θ, which then yields a relation between T_h and T_c (eq.32). The entering hot and cold solutions were considered at their saturation limits, such that the concentration of the mixed solution in the mixer is:

$$C = \frac{C_h^* Q_h + C_c^* Q_c}{Q_t} \tag{43}$$

where C_h^* is the solubility of hot solution at T_h and C_c^* is the solubility of cold solution at T_c. Given the relation between T_h and T_c (eq.32), the eq.34 was then solved to obtain the necessary temperatures of hot and cold solutions. A total of four experimental conditions were explored using this cooling technique. Details of the selected flow rates, feed concentrations, and temperatures are provided in Figure 37 and summarized in Table 13.

The effective startup of the second cooling technique requires flushing the device with water to remove air from the channels and micromixer. Then an aqueous solution of the L-glutamic acid at low temperature is pumped in, and as it fills the micromixer, the high-temperature saturated stream is injected after that.

4.3.4 Measurements of Growth Rates, Morphology, and Polymorphs

The microscopic images were recorded with a built-in color camera using transmitted light mode(LC 30, Olympus America Inc.). The time-lapsed images were taken every 60 to 300 seconds to measure growth rates of L-glutamic acid crystals for around 10-30 minutes using OLYMPUS

Stream Start software. A longer measurement time was necessary at lower supersaturation. The time-lapsed images were processed using OLYMPUS Stream Start to measure the growth rate and the percentage of polymorphs of L-glutamic acid crystals. The polymorphic forms of L-glutamic acid were distinguished based on their distinct morphological forms.

The α-Form of the L-glutamic crystal is the metastable polymorph with prismatic shaped crystals, whereas the stable β-Form is shaped like needles. Therefore, the percentage of β-Form was calculated based on the fraction of the area covered by the needles.

The prismatic and needle shape morphologies of the α- and β-Forms of L-glutamic acid were also confirmed from X-ray diffraction (XRD) pattern obtained using a Bruker D2 PHASER diffractometer with Ni filtered Cu Kα radiation. A step width of 0.2 and a counting time of 5 seconds/step were used to enhance the signal-to-noise ratio for all the samples. Diffraction patterns of L-glutamic acid forms were compared with the literature to confirm the polymorphic form (see Figures 44).

4.4 Results and Discussion

4.4.1 Temperature Gradient Comparison for the Temperature Control Strategies

Figure 38A shows the steady-state temperature profile in a jacketed microfluidic device. The jacketed device was fed with coolant (50 vol% ethylene glycol in water) at 10℃ at 10 $mL.min^{-1}$ and the solvent (water) to the micromixer at 70℃ at 1 $mL.min^{-1}$.The flow rate of the coolant was high enough to keep the temperature of the jacket uniform. The temperature gradients start developing near the tangential inlets and enter the micromixer, where the solution temperature becomes uniform after 2 mm height from the bottom plan of the cooling jacket. Figure 38B shows the steady-state temperature profile in a microfluidic device without a cooling jacket. This device was fed with hot and cold water through non-neighboring inlets. The cold water at 10℃ and 0.5 $mL.min^{-1}$ is mixed with hot water at 70℃ and 0.5 $mL.min^{-1}$. The total flow rate of water in a

micromixer is similar to a jacketed device. However, in this case, the temperature gradient spans a larger height up to 2.75 mm from the bottom plane. This temperature gradient is independent of total flow rate or velocity and is mainly determined by heat diffusion between hot and cold streams. However, the span of temperature gradient in a jacketed device is mainly determined by the height of the jacket.

The temperature distributions in Figures 38A and 38B were compared using a thermal homogeneity index. The thermal homogeneity index at any horizontal plane of the micromixer is defined as:

$$Thermal\ Homogeneity\ Index = 1 - \frac{\sigma^2}{\sigma_0^2} \tag{44}$$

where σ^2 is the variance of the temperature in any cross-sectional plane and σ_0^2 is the variance of temperature at the bottom plane of the micromixer. Figure 38C shows that for a total flow rate of 1 mL.min^{-1}, a slightly lower temperature homogeneity index is observed in the micromixer with hot and cold mixing than the cooling jacket technique.

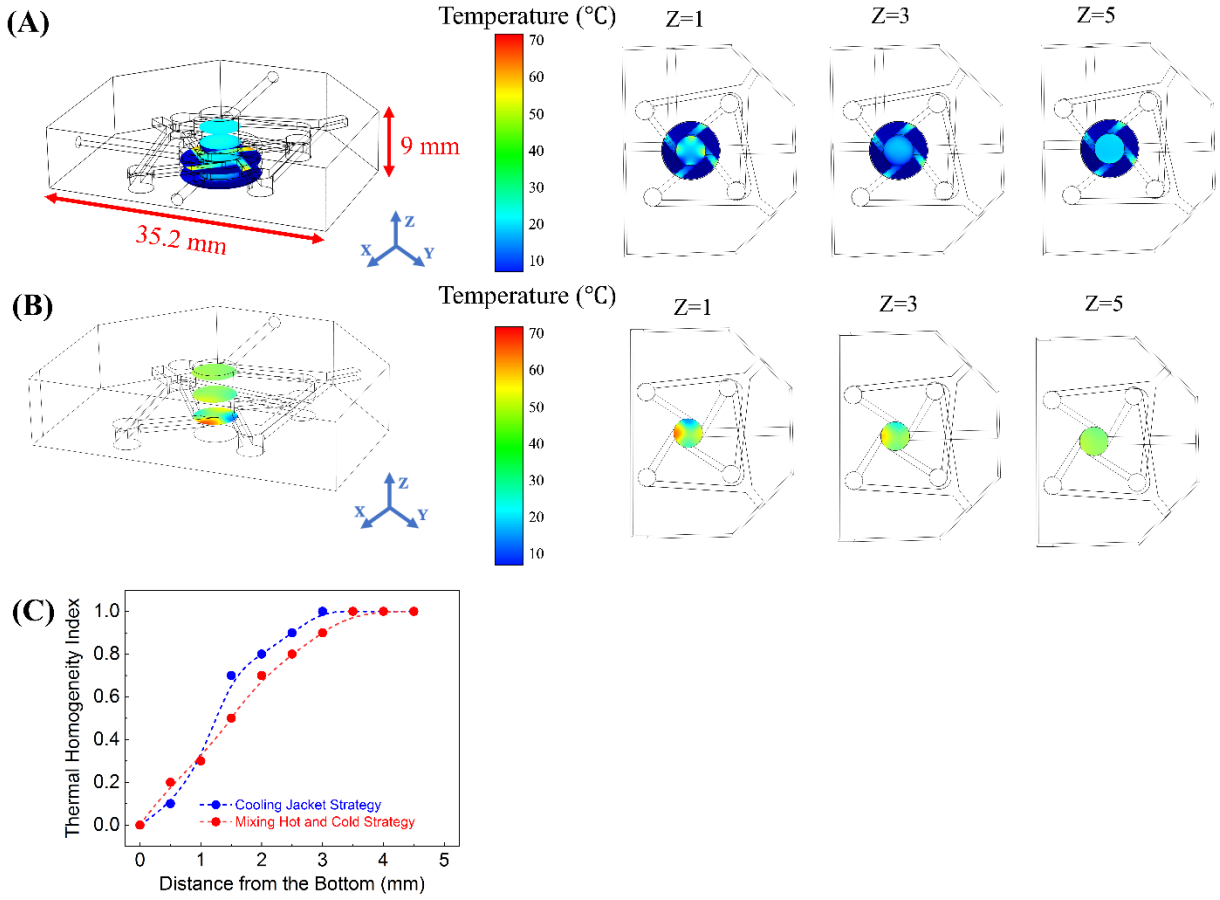

Figure 38: (A) Steady-state temperature profile in the jacket and micromixer for the cooling jacket approach. While the cooling jacket attains a uniform temperature, the temperature in the micromixer varies only up to the height of the jacket, followed by a uniform temperature profile.; (B) Steady-state temperature profile in the non-jacketed microfluidic device. The total flow rate was kept similar to the jacketed-microfluidic device. Larger temperature variation was seen along with the micromixer height; (C) Comparison of the variation in the thermal homogeneity from the bottom to the top surface of the micromixer.

4.4.2 Attainable Temperatures and Supersaturations in the Micromixer Device

The Navier-Stokes equation and the energy balance equation consisting of conduction and convection terms were solved simultaneously to calculate the average temperature of solution exiting micromixer as a function of coolant temperature and temperature and flow rates of inlet streams. These temperatures can be represented collectively as a dimensionless temperature (θ), see eq.1, which depends only on the total flow rate (Q_t) of the solution entering the jacketed micromixer. Figure 40A shows an increase in θ with increasing Q_t. The close agreement between experimental and simulation values of θ confirms the accuracy of simulation results. This plot was

used as a calibration curve to determine the necessary flow rate, the coolant temperature, and the temperature of the inlet solution to attain the desired temperature in the jacketed-microfluidic device (see details in section 4.3.3). A desired degree of supersaturation can be achieved by varying saturation concentration or temperature of the inlet solution. The solubility curve, therefore, determines the attainable range of supersaturation in such a cooling technique.

For the non-jacketed micromixer, the dimensionless temperature depends on the flow rate of hot and cold solutions entering the micromixer. Figure 40B shows a decrease with increasing the flow rate of cold solution for a fixed total flow rate of 1 mL.min^{-1} in the micromixer. A comparison of experimental and simulation values for different temperatures of the cold solution is provided in Figure 39. This plot was used as a calibration curve to determine the necessary flow rate and the temperature of cold and hot solutions to attain the desired temperature in the non-jacketed microfluidic device (see details in section 4.3.3). For example, θ is 0.5 for 0.5 mL.min^{-1} of the cold saturated stream at 10℃, and the equilibrium temperature will be 35℃.

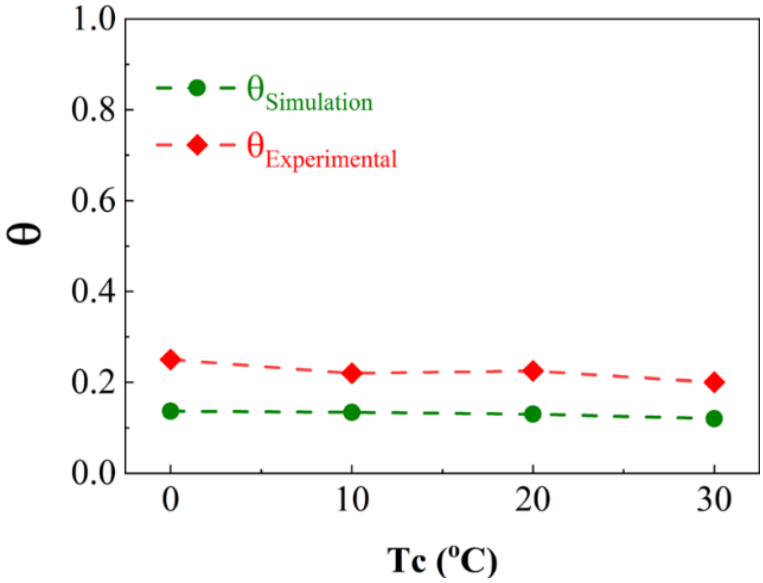

Figure 39: Comparison of the dimensionless temperature (θ) between simulated values and experimentally measured.

The simulation results for suggested temperature control strategies show that the input parameters (T_h, T_c, and Q_t) can be tuned to obtain the desired temperature inside the jacketed microfluidic device. However, when mixing hot and cold solutions, a limited range of equilibrium temperature is feasible over a wide range of input parameters. Figure 40C shows the attainable equilibrium temperature for different values of T_c and Q_c at a fixed total flow rate of 1 mL.min^{-1} and T_h of 70℃. Figure 40C is not specific to any compound but is used to calculate the attainable range of the supersaturation for the compound of interest. The accessible range of the supersaturation for the aqueous solution of L-glutamic acid is then obtained using solubility data and equilibrium temperature from Figure 40C. Figure 40D shows that the feasible range of supersaturation for the aqueous solution of L-glutamic acid ranges from 1.03 to 2.03. The highest supersaturation value is obtained when a saturated cold stream at 10℃ and a saturated hot stream at 70℃ are pumped into the mixer at 0.7 and 0.3 mL.min^{-1}, respectively.

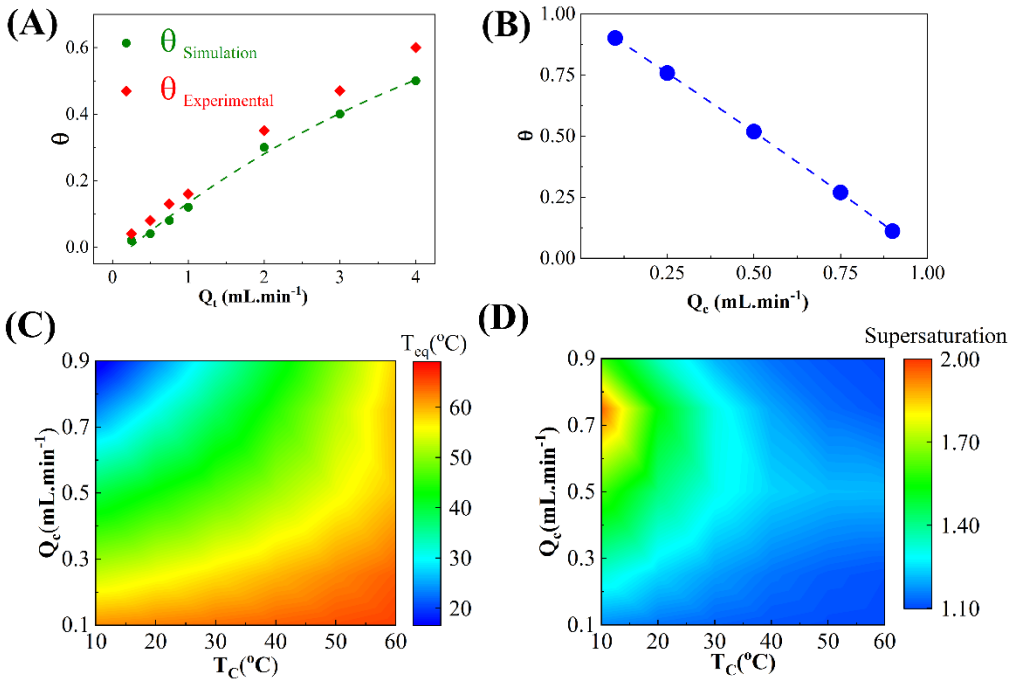

Figure 40: (A) Dimensionless temperature (θ) vs. the total flow rate of the micromixer for the cooling-jacket strategy; (B) Dimensionless temperature (θ) vs. the flow rate of the saturated cold stream for the mixing hot and cold strategy; (C) Equilibrium temperature for the microfluidic mixer in the mixing strategy for different flow rate and temperature of the cold stream at fixed T_h and Q_t; (D) Accessible range of supersaturation for the cooling crystallization of L-glutamic acid for the mixing strategy.

4.4.3 Screening of Morphology, Polymorphs, and Growth Rate of L-glutamic Acid using Two Different On-the-Spot Quenching Techniques

The efficacy of the two different on-the-spot quenching techniques – cooling jacket and mixing hot and cold solutions – for the microfluidic mixer is evaluated to screen morphology, polymorph, and growth rate of L-glutamic acid via cooling crystallization. In Figures 41A to H, the temperature of the micromixer is lowered down using the cooling jacket strategy. The flow rates of the recirculating coolant stream are set at 10 and 1 mL.min^{-1} For wells A, C, and H, the bath temperature is at 0℃, whereas wells B, D, E, F, and G, are set at 20℃. Therefore, the temperature and total flow rate of the saturated L-glutamic acid in wells A to H are set as **A**: Q_t= 1 mL.min^{-1} , $T_h = 70$℃, **B**: Q_t = 1 mL.min^{-1},$T_h = 60$℃, **C**: Q_t,= 1 mL.min^{-1}, $T_h = 50$℃, **D**: Q_t = 1 mL.min^{-1}, $T_h = 60$℃, **E**: Q_t= 1 mL.min^{-1} ,$T_h = 40$℃, **F**: Q_t = 1 mL.min^{-1} ,$T_h = 30$℃, **G**: Q_t = 1 mL.min^{-1} ,$T_h = 50$℃, **H**: Q_t = 1 mL.min^{-1} ,$T_h = 30$℃,. The equilibrium temperature for wells A to H is calculated from Figure 41A, and the imposed supersaturation in these wells is $A: \sigma = 4.7, B: \sigma = 3.87, C: \sigma = 3.01, D: \sigma = 2.45,, E: \sigma = 1.73,, F: \sigma = 1.32,, G: \sigma = 1.27,, H: \sigma = 1.1$. The supersaturation in these eight wells decreases in the order of $A > B > C > D > E > F > G > H$. Figures 41A to 4H show the optical images that are taken from these experimental conditions. The scale bar for all images is 200 μm. Figures 41A to 41C show the dominant prismatic morphology characteristic of α-Form (metastable) of L-glutamic acid. In Figure 41D, most crystals have prismatic morphology, which is the characteristic of the α-Form, but some plate shape crystals that represent the stable form (β-Form) are also observed. Figures 41I to 41P show optical images for cooling crystallization of aqueous solutions of L-glutamic acid, where the second temperature control strategy is implemented. The total flow rate of 1 mL.min^{-1} is set for all four wells, and the temperatures of saturated hot and cold streams are labeled in Figure 37. For

Wells M to P, the hot and cold temperatures are $A: T_h = 80℃, T_c = 20℃, B: T_h = 70℃, T_c = 20℃, C: T_h = 60℃, T_c = 20℃, D: T_h = 50℃, T_c = 20℃$.

The equilibrium temperature for wells M to P is calculated from Figure 40B, and the imposed supersaturation in these wells is M: $\sigma = 1.62, N: \sigma = 1.42, O: \sigma = 1.3, P: \sigma = 1.14$. Figure 41M shows a mixture of metastable α-Form with prismatic morphology and the plate shape morphology of the stable β-Form L-glutamic acid. In Figure 41N, most crystals have the plate shape morphology, which is the characteristic of the β-Form, but some metastable crystals are also detected. Figures 41O and 41P show that only the stable β-Form with the plate shape morphology is crystallized in wells O and P.

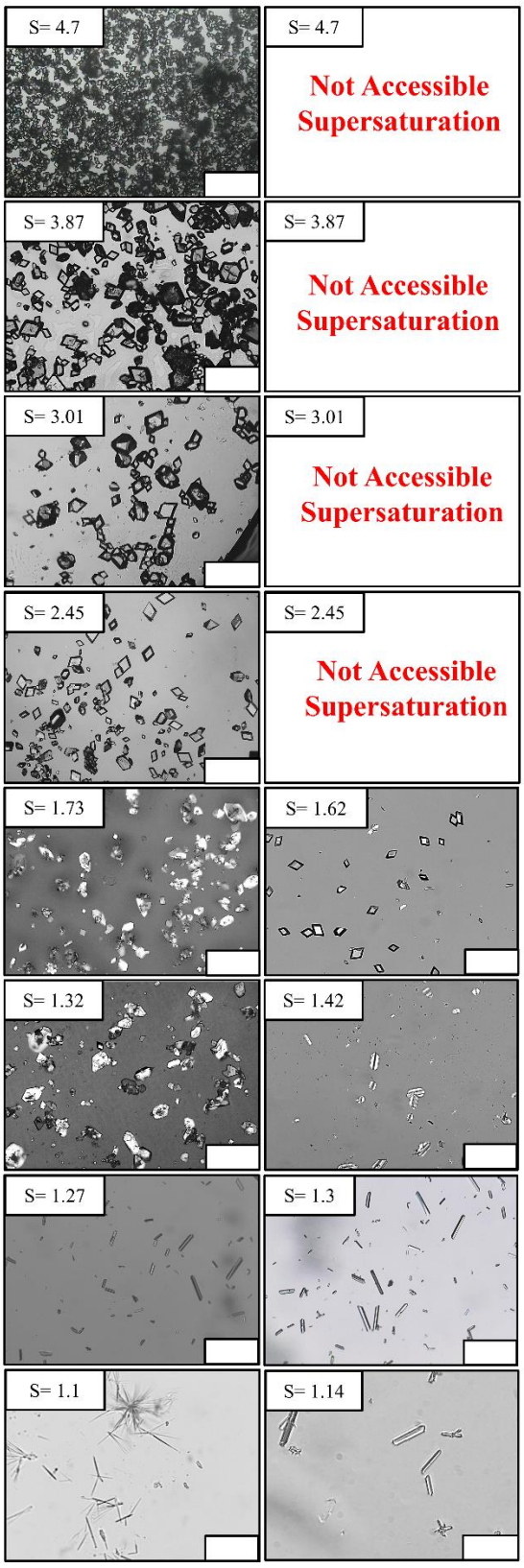

Figure 41: Micrographs of L-glutamic acid crystals obtained at different.

The percentage of stable β-Form (X_β) and the growth rates of (111) facet for each well are obtained from image analysis using OLYMPUS Stream Start. Figure 43A shows the variation in X_β as a function of supersaturation in the micromixer. The percentage of the stable form for very low supersaturations ($\sigma \leq 1.3$) is around 100%. It is then decreasing as the supersaturation is increased and becomes zero for at high supersaturations ($\sigma \geq 3$). The growth rates of L-glutamic acid crystals in wells A to P are measured from time-lapsed images taken in a period of 10 to 30 minutes. Figure 43B shows the measured growth rates as a function of supersaturation. Here, the equilibrium temperature for wells A to P is labeled next to each data point. In Figure 43B, the growth rate does not follow any trend vs. the supersaturation value since the equilibrium temperature is different for each data point. The measured growth rate is compared with the predicted growth rate for wells A to P. An example of the growth rate calculations is shown in Figure 42. The growth rate data were obtained by taking time-lapse images from samples every sixty seconds. The change in the distance from face 111 was divided by the time difference. Figure 42 shows a series of time-lapse images taken for sample C where the supersaturation is 3.01.

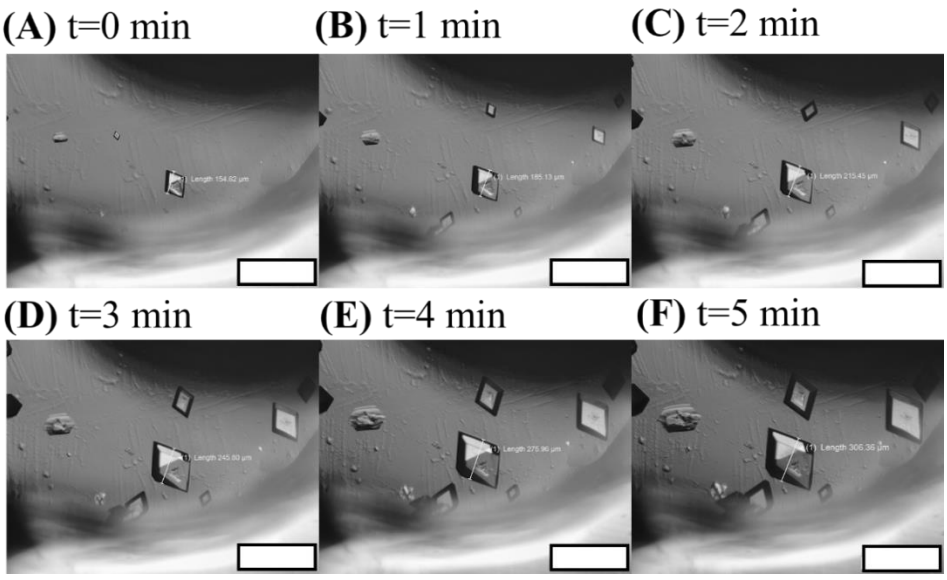

Figure 42: Time-lapse images from sample C (S=3.01) for 5 minutes. The t=0 is not the initial time of the experiments, and it is the time when the measurements started. (The scale bar is 500 μm)

Table 14: Growth rate measurements for sample C (S=3.01)

Time(s)	Size (μm)	GR ($\mu m.s^{-1}$)
0	154.62	0.5085
60	185.13	0.5053
120	215.45	0.5058
180	245.8	0.5026
240	275.96	0.5066
300	306.36	
Mean GR ($\mu m.s^{-1}$)		0.5058
SD		0.0019

The measured growth rates are compared with the predicted values that are calculated[62] from equation (4):

$$G_{B+S} = AT\ exp\left(-\frac{B}{T}\right)(S-1)^{\frac{2}{3}}\ exp\left(-\frac{C}{T^2 lnS}\right) \quad (45)$$

$A = 3.63 \times 10 - 4\ ms^{-1}K^{-1}$;

$B = 3.72 \times 10^3\ K$;

$C = 5.42 \times 10^4 K^2$

Comparing the measured and predicted growth rates confirms that the cooling bath approach and mixing hot and cold streams are valid approaches for performing continuous cooling crystallization using the microfluidic mixer device.

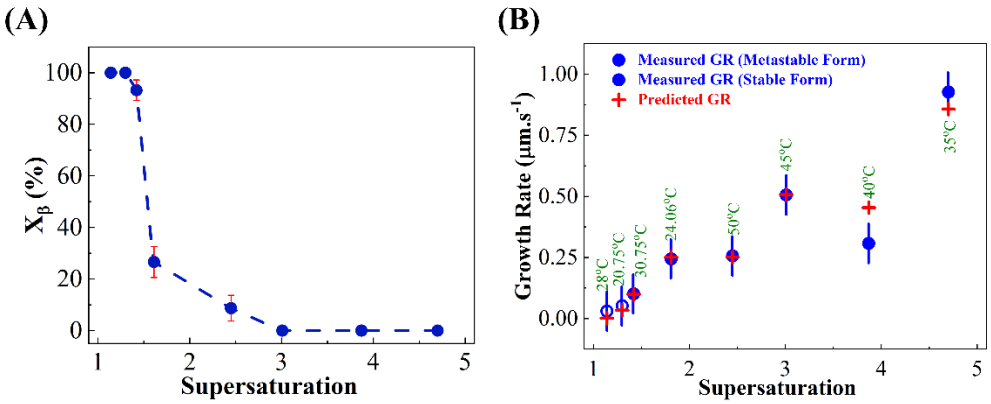

Figure 43: (A) Percentage of the stable polymorph (X_β) of L-glutamic acid at different supersaturation ratios; (B) Measured and predicted growth rate values of the L-glutamic acid crystals at different supersaturation ratios and equilibrium temperature.

4.4.4 X-ray Diffraction Patterns of L-glutamic Acid Polymorphs

Figure 44 shows simulated and experimental XRD patterns for pure α-Form and β-Form. The XRD of β-Form was taken directly for as-purchased L-glutamic acid (Sigma-Aldrich, chemical purity≥ 99%). The pure α-Form was prepared by cooling crystallization of a saturated aqueous solution of L-glutamic acid at 70℃.

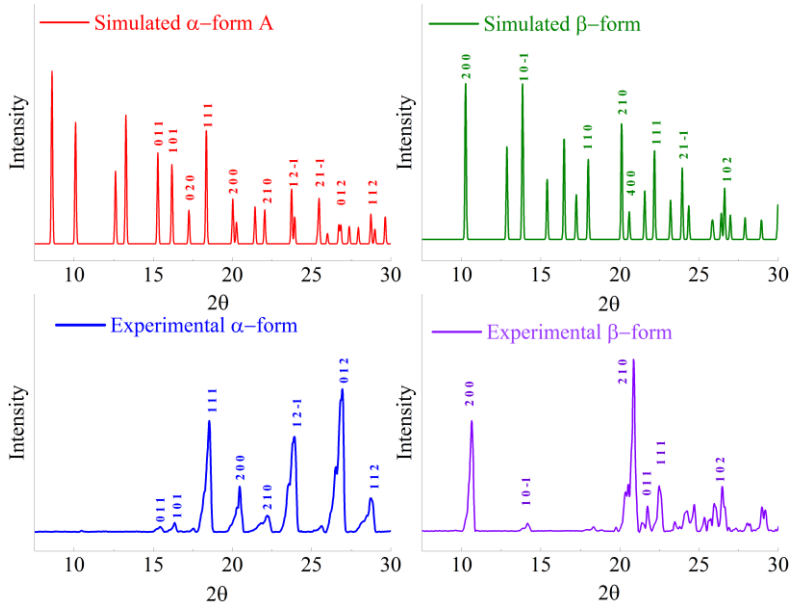

Figure 44: XRD patterns of L-glutamic acid polymorphs: Simulated : (A) α-Form and (B) β-Form; Experimental: (C) α-Form, and (D) β-Form.

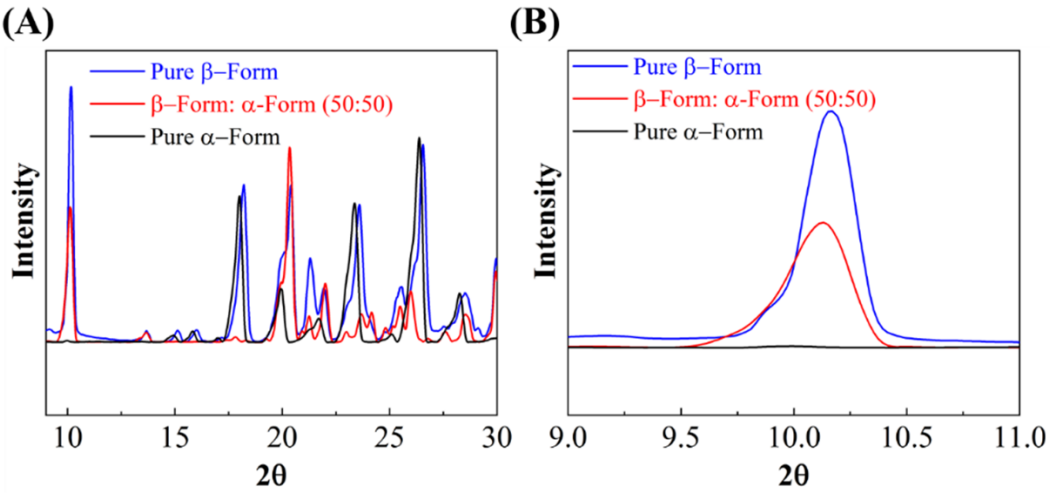

Figure 45: Variation in the intensity of characteristic peaks of β-Form with an increasing weight percentage of α-Form: (A) Full XRD pattern, (B) Magnified view of the characteristic peak of β-Form.

4.5 Conclusion

Effective implementation of cooling crystallization in a continuous-flow microfluidic device has been challenging primarily due to the development of large temperature gradients. These temperature gradients are dominant near the entrance of the microfluidic channel causing variations in supersaturation. Additionally, the depletion of supersaturation due to crystal nucleation and growth in the channel has prevented the successful evaluation of cooling crystallization in a continuous-flow microfluidic device. Here, two effective techniques to reduce temperature gradients in the microfluidic device are presented that involve on-the-spot quenching of entering solutions for continuous cooling crystallization at constant supersaturation. The first technique involves a collar of the cooling jacket around the micromixer, and the second technique utilizes mixing the hot and cold solution. The temperature gradients in the jacketed-microfluidic device are determined by the height of the jacket, which can be smaller than 1 mm, whereas the temperature gradients in the second technique are governed by the mixing efficiency of a hot and cold solution. The cooling jacket allows access to a full range of supersaturations based on the solubility curve. However, the attainable supersaturations in the hot-and-cold-mixing technique are significantly limited by the temperature and concentration difference between hot and cold streams. Based on these attributes of two different temperature control strategies, the cooling jacket technique is better suited to study higher supersaturations, and the hot-and-cold-mixing technique is preferred for targeting the lower range of supersaturations.

Here we demonstrate comparative screening of crystal morphology, polymorph, and growth rates of L-glutamic acid for eight different conditions employing both on-the-spot quenching approaches. The cyclonic flow in the micromixer allows the trapping of crystals and helps in attaining homogeneous temperature. The compact design of the jacketed and non-jacketed microfluidic device permits direct placement under an optical microscope to take time-lapse

images to measure morphology, polymorph, and growth rate. The maximum supersaturation attained is 4.7 in the cooling jacket technique, whereas the hot-and-cold-mixing technique could only screen supersaturations up to 1.6. Both cooling techniques effectively measure growth rates of L-glutamic acid crystals at given supersaturations and temperatures, which is in good agreement with the predicted values. These techniques also show a similar trend in the decrease of β-Form of L-glutamic acid crystals with increasing supersaturation.

In this section, we discussed the design rules to implement on-the-spot quenching in a continuous-flow microfluidic device and provided a solution to one of the challenges in studying cooling crystallization in such systems. These on-the-spot quenching techniques will have a transformative impact on the continuous-flow microfluidics for various healthcare and energy applications.

V. SNAP-ON ADAPTOR TO TRANSFORM MICROTITER PLATE INTO A CONTINUOUS-FLOW MICROFLUIDIC DEVICE FOR SCREENING OF CRYSTALLINE MATERIALS

5.1 Introduction

The advent of high-throughput (HT) crystallization technologies is vital to the discovery and development of pharmaceuticals as it helps capture the diversity of solid forms in the early phases of drug development. Polymorphism, which refers to different crystal forms of the same chemical composition, is considered the most important solid-state property in various applications. The HT crystallization screening systems allow the study and evaluation of diverse salt forms, co-crystals, hydrates, and solvates. The discovery and design of solid forms depend on the type of molecule, its physical property, and the challenges associated with the development processes.

The preferred solid form of a compound is generally the one with the highest thermodynamic stability. The stable form of the parent compound may demonstrate poor solubility or dissolution rate. Therefore, it is common to prepare salt forms of pharmaceutically acceptable acids and bases to improve the bioavailability of active pharmaceutical ingredients (APIs)[63-66]. Depending on the intended target property, there can be a wide range of polymorphic, solvated, or hydrated forms of pharmaceutical salts. The physicochemical properties of different salts, such as solubility, morphology, density, and physical and chemical stability of a single organic cation, can differ significantly. The HT solid form screening aims to determine the desired crystal form as a preventative measure against unwanted outcomes later in development. An HT screening device based on wells or vials is usually used to analyze the crystal structure of newly synthesized compounds and to discover possible crystal forms.

Microtiter plate assays are available with volumes ranging from 1mL to 1L and can assess up to 10,000 conditions per day[5]. Furthermore, the apparatuses for HT screening can be fully automated and allow for solid-state studies of crystals by either X-ray diffraction (XRD) or Raman spectroscopy[67,68].

With the advances of miniaturized systems, screening techniques have evolved to accommodate multiple experiments in a single device. Currently examined screening techniques resemble well-mixed batch crystallizers that are well-mixed. While the temperature and solvent composition can be maintained constant and controlled in batch systems, the concentrations vary. The crystal nucleation and growth in batch systems cause a decrease in solute concentration and thereby supersaturation, a driver for crystallization. Hence, the polymorphs, morphology, crystallization kinetics, and crystal size discovered during initial screening may not remain constant. Attempts have been made to facilitate continuous-flow screening by designing a complementary part for the existing HT batch systems. Murphy and coworkers previously developed a continuous-flow HT screening by designing a passive micro-assembly of a fluidic control[69]. Continuous flow polymerase chain reaction chips (FPCRs) were combined with twelve networks that distributed the same polymerase chain reaction (PCR) cocktail to eight different devices in each column. A double-sided hot embossing technique was used to fabricate the fluid-control and multi-well (MW) CFPCR chips. This combination utilizes the existing advantages of MicroCFPCR devices, including rapid reactions and reduced reagent consumption, in a continuous flow mode. In another study, Murphy and coworkers designed, configured, and fabricated continuous flow thermal arrays of reactors in a 96-device[70].

The dimensions for the nanoliter CFPCR were chosen using finite element analysis based on a series of thermo-fluidic models. With these HT 96 CFPCR devices, DNA samples could be amplified rapidly, providing results at the right time. The advancement of 3D printing has enabled

the direct printing of microfluidic devices. However, it is limited to oxygen-impermeable materials. Eddington et al. studied 3D printed microfluidic devices with gas-permeable PDMS membranes for an oxygen-control cell culture assay[71]. A 3D-printed device coupled with gas-permeable membranes was applied to a 24-well oxygen control device for standard multi-well plates. Using this device, they controlled four different oxygen levels and maintained six wells under each oxygen level. In the studies presented here, the capability of adding a control layer to existing HT systems proved to be beneficial. Novel continuous-flow microfluidic devices are implemented to avoid the conventional batch system issues by controlling supersaturation[72]. The novel systems allow for the evaluation of crystal polymorphs and morphology at controlled supersaturation. Microfluidic devices that utilize a continuous-flow mode of operations and enable controlled conditions are proven effective for determining the crystal polymorph, morphology, size, and kinetics[70,73-75]. This microfluidic mixer device creates cyclonic flow, ensuring uniform mixing and constant supersaturation inside the mixer[41]. This well-mixed continuous-flow microfluidic device technology enabled the parallel screening of crystalline materials at controlled conditions[61]. Even though multi-well microfluidic technology offers many advantages, the device still poses difficulties for HT screening (such as salt screening) that demands multiple flow handling equipment.

This study aims to develop a snap-on adaptor that can transform any microtiter plate assay into a continuous-flow microfluidic mixer with a minimum requirement of fluid handling systems. The snap-on adapter includes the design of the cyclone mixer, with the merged inlet design where each inlet enters into the cyclone mixer from two channels, providing homogeneous mixing for every well[76]. The inlets of the snap-on adapter can be connected to the flow distributor or concentration gradient generator (CGG)[77,78]. By offering different combinations of the flow distributor and CGG, the experimental design becomes more flexible. Moreover, the technology of 3D printing has

considerably eased the fabrication process of multilayer snap-on adaptors compared to conventional micro-fabrication techniques.

Here, a 24-well plate was converted into a snap-on microfluidic device that was evaluated to screen naproxen salt. Different types of naproxen salt forms were identified and characterized more rapidly and comprehensively using this HT technology. This study screened naproxen salts of sodium hydroxide, potassium hydroxide, pyridine, and arginine using different solvents listed as ethanol, methanol, isopropyl alcohol (IPA), and deionized (DI) water. The snap-on microfluidic device also provides means to harvest newly formed crystals after screening for further analysis. The harvested crystals can be characterized using optical microscopy, x-ray diffraction (XRD), and Fourier transformed infrared spectroscopy (FT-IR).

5.2 Theoretical Methods

5.2.1 Flow Distribution Strategies for Snap-on Adaptor Design

The 24-well plate assay was converted into a continuous-flow microfluidic mixer device using a snap-on adapter. The assembly of a 24-well plate with the snap-on microfluidic mixer includes two compartments that are connected using tubes, fittings, and one-way check valves. The first part is the snap-on adaptor inserted inside a 24-well plate assay (see Figure 46A). The second compartment of this system was a network of microchannels that distributed solutions into wells. Each well in the snap-on adaptor part had an identical configuration to the merged inlet microfluidic device, which had been previously developed[61]. The overall size of a single well and the merged connections was equal to the inner diameter of a single well in a 24-well plate assay. The snap-on microfluidic mixer device is shown in Figure 46A. Similar to the merged inlet design, each well had two major inlets indicated with red arrows in Figure 46D. The major inlets of each well were then connected to an array of microchannels responsible for distributing the solutions inside the microfluidic mixer device.

Here, two frequently used flow distribution designs were used to distribute the solutions into the snap-on adaptor microfluidic mixer device. Here, two commonly used flow distribution designs were used to distribute the solutions into the snap-on adaptor microfluidic mixer device. The first design is the flow distributor design that equally distributes the entering stream to four channels (see Figure 46E). The flow distributor design was used to connect a 4x4 sub-array of wells, as shown in Figure 46E. These sixteen wells were operated in a continuous-flow manner using only eight syringe pumps. The eight different solutions entering into these arrays resulted in sixteen different conditions. The remaining eight wells (the 2x4 sub-array) were operated using the flow distributor and CGG. The design of the CGG is shown in Figure 46F. In the CGG, two different solutions were pre-mixed to generate four different concentrations, each sent into different channels[78]. The detailed measurements and dimensions of the snap-on adaptor, flow distributor, and CGG are shown in Figures 47, 48, 49, and 50.

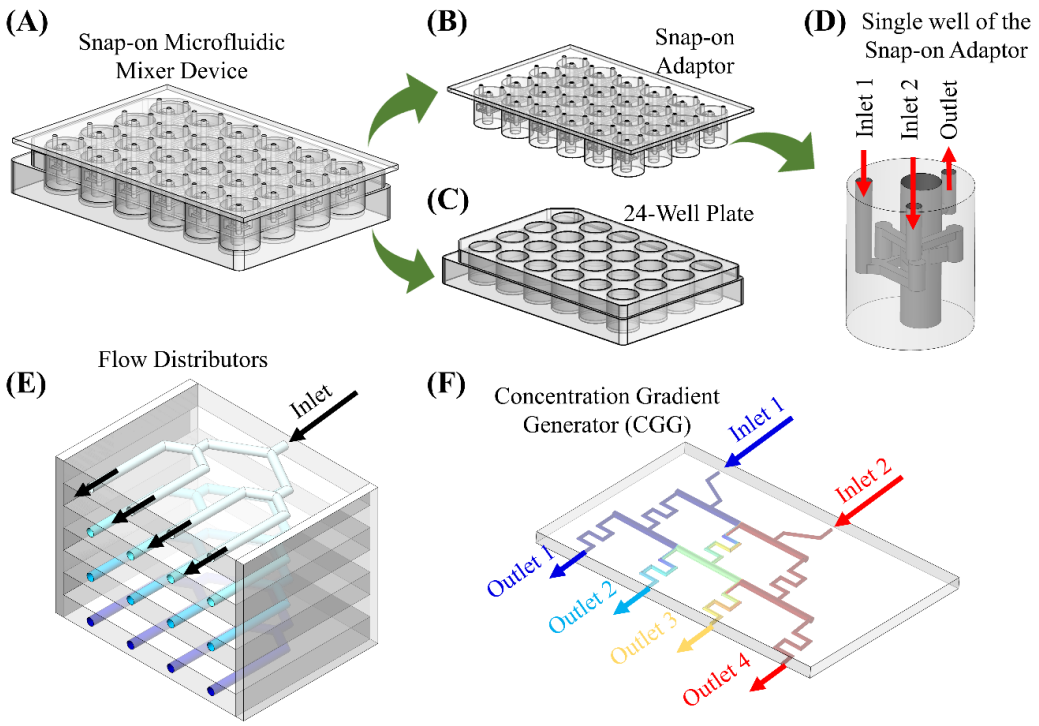

Figure 46: 3D design of an (A) 24-well plate snap-on microfluidic mixer device, (B) snap-on adaptor, and (C) 24-well plate assay; (D) Enlarged view of a single well of the snap-on adaptor; 3D design of (E) four sets of flow distributor in a stack, and (F) concentration gradient generator (CGG).

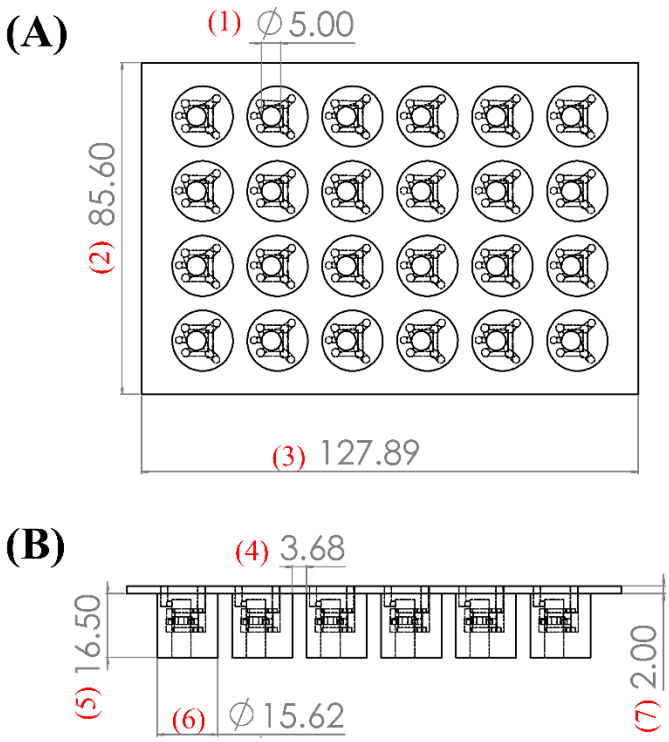

Figure 47: (A) Top view and (B) side view of the twenty-four well plate device.

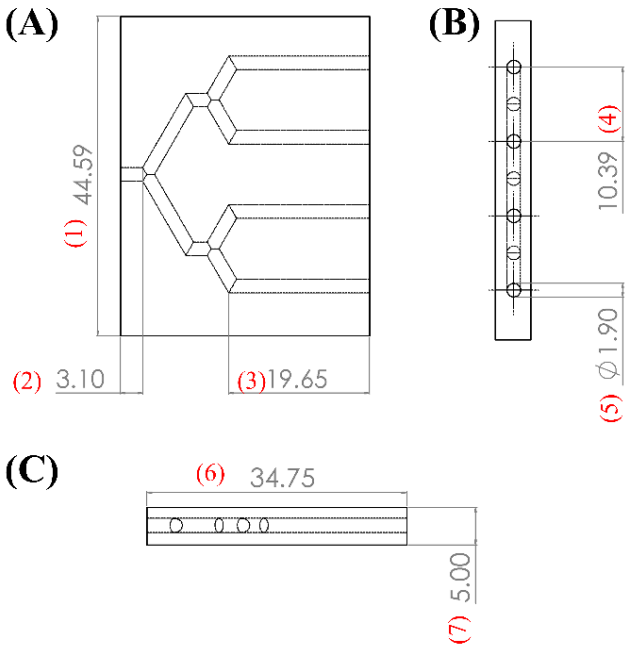

Figure 48: (A) Top view, (B) front view, and (C) side view of the flow distributor network.

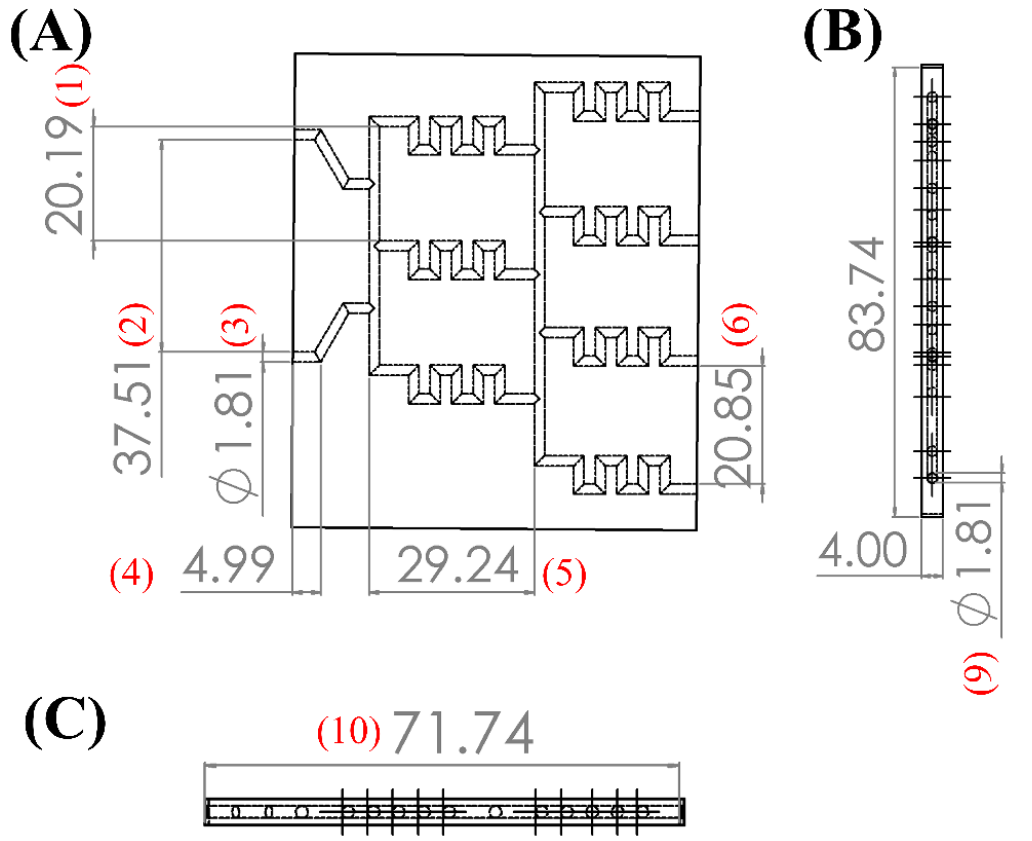

Figure 49: (A) Top view, (B) front view, and (C) side view of the concentration gradient generator network.

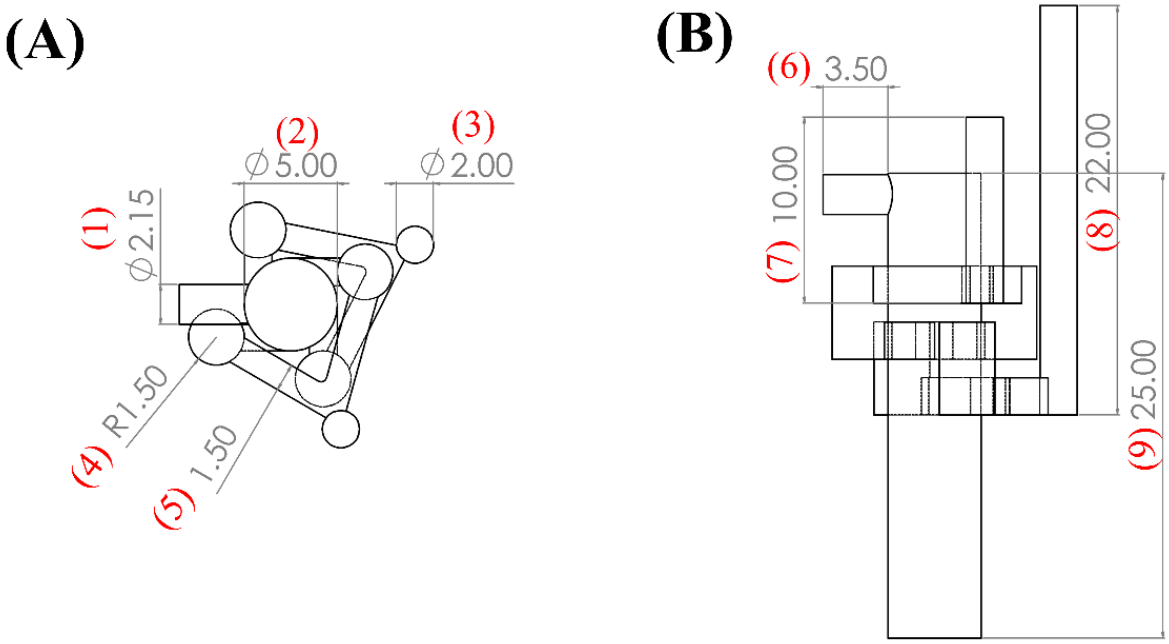

Figure 50: (A) Top view and (B) side view of the interior channels for a single well of the 24-well plate snap-on microfluidic device.

5.2.2 CFD Simulation of the Velocity and Concentration Profiles

The design of each well in the snap-on adaptor was similar to the design of the previously developed merged-inlet micromixers[61]. The effectiveness of mixing for each well was evaluated by calculating the velocity, pressure, and concentration profiles in the snap-on microfluidic mixer device. The CAD file for design for the inner channels and wells were imported in COMSOL Multiphysics® and meshed using a free tetrahedral mesh of element size 0.00789 to 0.00142 mm and a curvature factor of 0.6. The maximum element growth rate and the resolution of the narrow region were kept at 1.5 and 0.5 accordingly. Navier-Stokes equation coupled with continuity equation was solved to mix pure streams of API in the solvent (naproxen in ethanol) and salt former (SF) solution (NaOH in ethanol). Details of the CFD simulations are provided in section 5.2.2.1.

5.2.2.1 Laminar Flow Module: Equations and Boundary Conditions

The laminar flow module of COMSOL was used to calculate the velocity profile in the microfluidic mixer. The time-dependent Navier-Stokes equation solved is described as follows:

$$\rho \frac{\partial u}{\partial t} + \rho(u.\nabla)u = \nabla.[-p.I + \mu(\nabla u + (\nabla u)^T) + F \quad (46)$$

Where ρ and μ are density and the viscosity of water which is assumed to be incompressible. Here the selected boundary conditions for the 24-well plate snap-on microfluidic device are listed. Figure 51A shows the isometric view of the imported 3D file of the snap-on microfluidic mixer for the 4x4 sub-array in the COMOSL Multiphysics for the simulation. In Figures 51C, and 52D, the assigned boundary conditions for inlets and outlets of this system are shown and listed as:

Boundary Conditions:

- $Inlet_1$= $Inlet_2$: Q_{Mixer}= 4 mL.min^{-1}
- Outlet: P = 1 atm

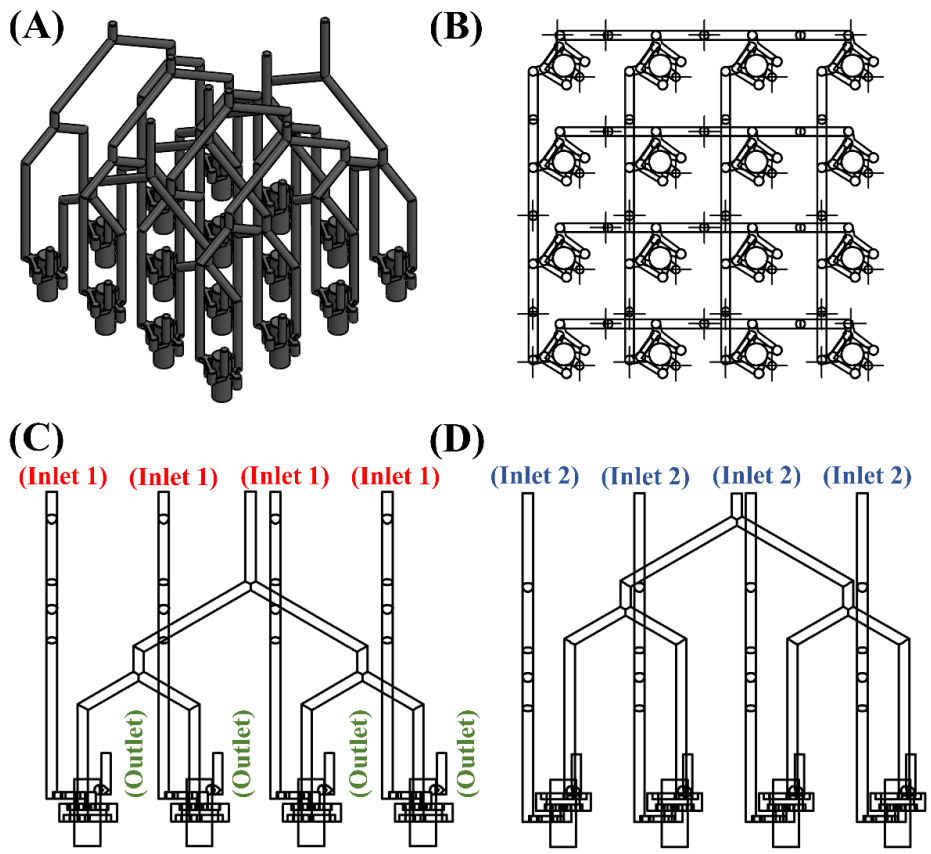

Figure 51: (A) The isometric view, (B) top view, (C) and (D) side views of the four-by-four part of the snap-on microfluidic mixer device with the assigned boundary conditions for the inlets and outlets (These figures show the designs used for COMSOL simulations).

In Figure 52, only wells selected for screening with flow distributor arrays are shown. This figure shows the interior channels of the 3D-printed object and is not used for 3D printing. Figure 52 shows the wells that were experimented with using a flow distributor and concentration gradient generator.

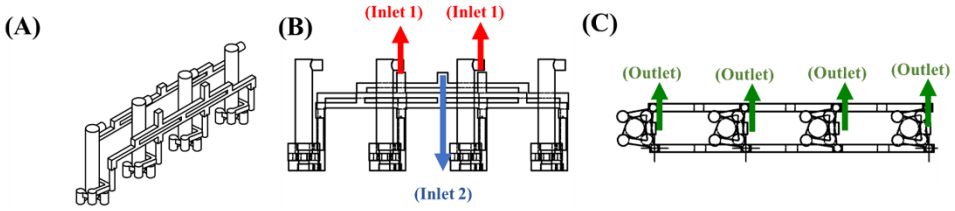

Figure 52: (A) The isometric view, (B) side view, (C) top view of the four-by-one part of the snap-on microfluidic mixer device with the assigned boundary conditions for the inlets and outlets (These figures show the designs used for COMSOL simulations).

5.2.2.2. Transport of Diluted Species Module: Equations and Boundary Conditions

The transport of the diluted species module is used to calculate the concentration profile in the snap-on microfluidic device. The time-dependent continuity equation solved is described as follows:

$$\rho \frac{\partial c_i}{\partial t} + \nabla.(-\mathrm{D_i}\nabla \mathrm{c_i}) + u.\nabla \mathrm{c_i} = \mathrm{R_i} \quad (47)$$

which includes both convection and diffusion for the transport mechanisms. Here ρ is the density, and u is the velocity of the fluid and comes from the laminar flow module. These two modules are coupled together, and the velocity profile is directly substituted into the continuity equation. The assigned boundary conditions for this model are listed below:

Boundary Conditions:

- Inlet $_1$:$c_i = c_{0,i} = 0$ mol.m^{-3}
- Inlet $_2$: $c_i = c_{0,i} = 1$ mol.m^{-3}
- Outlet: $n.D_i\nabla c_i = 0$

5.2.2.3 Model Parameters of the Simulations

In this study, we have simulated a coupled analysis of the laminar flow module and mass transfer in diluted species to evaluate the velocity, pressure, and concentration profile inside the patterned surface microfluidic mixer. The 3D model for simulations was imported into the model from a Solid Work design. The design was further simplified by eliminating the sharp edges and smoothening the surfaces to enhance the mesh quality. The free tetrahedral mesh was selected for the models. The tetrahedral mesh was selected for this study, and the details are provided in the following part:

- Maximum Element Size = 0.00789 m
- Minimum Element Size = 0.00142 m

- Maximum Element Growth Rate = 1.5
- Curvature Factor = 0.6
- Resolution of Narrow Region=0.5

The coupled equations of the Navier-Stokes and mass balance were solved in the stationary solver using the "MUMPS" solver. The residual factor was set to 1000 with 50 iterations. Newton was selected as the non-linear method with a damping factor of 0.1 and tolerance as the termination technique. The relative tolerance was also kept at 0.001.

5.3 Materials and Experimental Method

5.3.1 Materials

The crystalline naproxen (Sigma-Aldrich, chemical purity ≥98%) was used for the HT continuous-flow salt screening. The selected SFs for this study were sodium hydroxide (Sigma Aldrich), potassium hydroxide, pyridine, and L-arginine. All solvents used for salt screening were purchased from Sigma Aldrich with the following purities: Deionized water (Sigma-Aldrich, 18 MΩ cm), ethanol, methanol, 2-propanol (IPA).

5.3.2 Fabrication of the Snap-on Microfluidic Mixer Device

The 3D design of the snap-on adaptor for a 24-well plate assay shown in Figure 46B was designed in SolidWorks® (2020, Dassault Systems). A stereolithography (SLA) 3D printer (form 3, Formlabs Inc., USA) was used to print all parts. A clear FLGPCL02 resin activated by a 405 nm laser was used to 3D print optically clear microfluidic devices with 150 μm of lateral and 25 μm of axial resolutions. The 3D-printed parts were washed with IPA (90%, Sigma-Aldrich) bath for 60 minutes in the Form Wash (Formlabs Inc., USA) to remove the residues of the resin from the external surface. The generated support structures of the 3D-printed parts were loosened after the washing procedure, and their removal did not require much effort. All the interior channels of the

3D-printed device were washed separately by injecting IPA using a syringe followed by passing air from inlets to remove the uncured resins from all the channels. The careful selection of the layouts for prints on the 3D printer stage minimized the contact of the supports with top and bottom surfaces. However, if necessary, the optical transparency could be improved by wet sanding using 400 to 12000 grit pads followed by spray painting of resin. The bottom side of the snap-on adaptor part was kept open because it was sealed when inserted into the 24-well plate assay. Inner walls of each well in the 24-well plate assay were covered with a thin layer of resin. After plugging in the snap-on adaptor, the snap-on microfluidic device was cured and sealed. The top part of the snap-on adaptor was sealed separately by applying a thin layer of the resin around each opening and then putting small polycarbonate film. The top part was cured for around 10 minutes to seal all of the openings. The fabricated snap-on device adaptor is shown in Figure 54A.

5.3.3 Experimental Setup

Figure 54 shows the experimental setup for the salt screening of the naproxen using a 24-well plate assay coupled with the snap-on adaptor, flow distributor, and CGG. As shown in Figure 54A, the snap-on part was inserted into a 24-well plate assay, and then inlet connections on top were connected to output channels of the flow network externally. The separation of the connections from the snap-on part helps eliminate the possible disturbances to the system that might result in the pressure difference from the pump inlets to the outlets of each well. In addition, it allows for implementing the microfluidic one-way check valves before the major inlets of each well. Implementation of the one-way check valves guaranteed the equal distribution of flow into the outlet streams. The 24-plate assay was divided into two sub-arrays where different flow networks were used. The first sub-array included sixteen wells (a 4x4 sub-array) where every four wells on a single row or column were connected using one inlet. Thus, eight flow distributor arrays (see Figure 46C) were required for screening sixteen different conditions in the first sub-array.

Among these eight streams, four were naproxen solutions in different solvents: ethanol, methanol, IPA, and DI water. The other four inlets were ethanoic solutions of the different SF: sodium hydroxide, potassium hydroxide, pyridine, and arginine. Compared to the previously developed merged inlet microfluidic mixer design, the 4x4 sub-array of the snap-on microfluidic mixer device required one-fourth of the required pumps. The remaining eight wells of the microtiter plate were divided into two sets of the 4x1 sub-arrays. Details of the experimental condition for each of the twenty-four wells are provided in Figure 53 and Table 15. The parent compound solution is the Naproxen solution in different solvents: Ethanol, Methanol, IPA, and DI water. The SF solution is the ethanolic solution of Sodium hydroxide, potassium hydroxide, arginine, and pyridine.

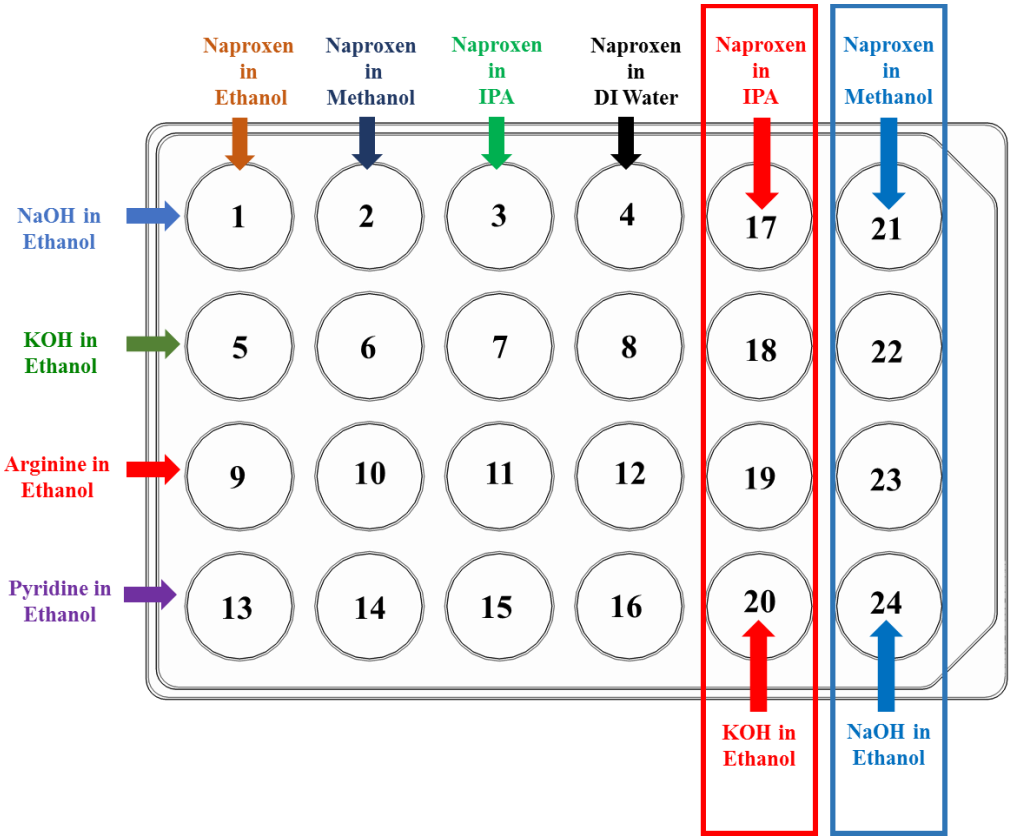

Figure 53: Details for the experimental conditions for the Naproxen salt screening. The entering solutions into each well are labeled.

Table 15: Molar concentration of the parent compound and SF solution entering each well for the naproxen salt screening.

Well	PC Concentration ($mol.L^{-1}$)	SF Concentration ($mol.L^{-1}$)	Well	PC Concentration ($mol.L^{-1}$)	SF Concentration ($mol.L^{-1}$)
1	0.2171	0.3750	**13**	0.2171	0.5057
2	0.2171	0.3750	**14**	0.2171	0.5057
3	0.2171	0.3750	**15**	0.2171	0.5057
4	0.0002	0.3750	**16**	0.0002	0.5057
5	0.2171	0.2674	**17**	0.2171	0.2674
6	0.2171	0.2674	**18**	0.2171	0.2674
7	0.2171	0.2674	**19**	0.2171	0.2674
8	0.0002	0.2674	**20**	0.2171	0.2674
9	0.2171	0.0861	**21**	0.2171	0.3750
10	0.2171	0.0861	**22**	0.2171	0.3750
11	0.2171	0.0861	**23**	0.2171	0.3750
12	0.0002	0.0861	**24**	0.2171	0.3750

A flow distributor and CGG were used in each 1x4 sub-array to screen concentration gradients of either the API or SF. For every 1x4 sub-array, three pumps were required since each CGG required two inflow at different concentrations, and each flow distributor needed one inflow. As shown in Figure 54, one-way check valves were installed at the outlet of the flow distributor, CGG, and the inlet of the snap-on adaptor. The snap-on adaptor was connected to the flow distributor and CGG using equal-length tubing for all inlets. Every single outlet stream was also collected separately for further analysis.

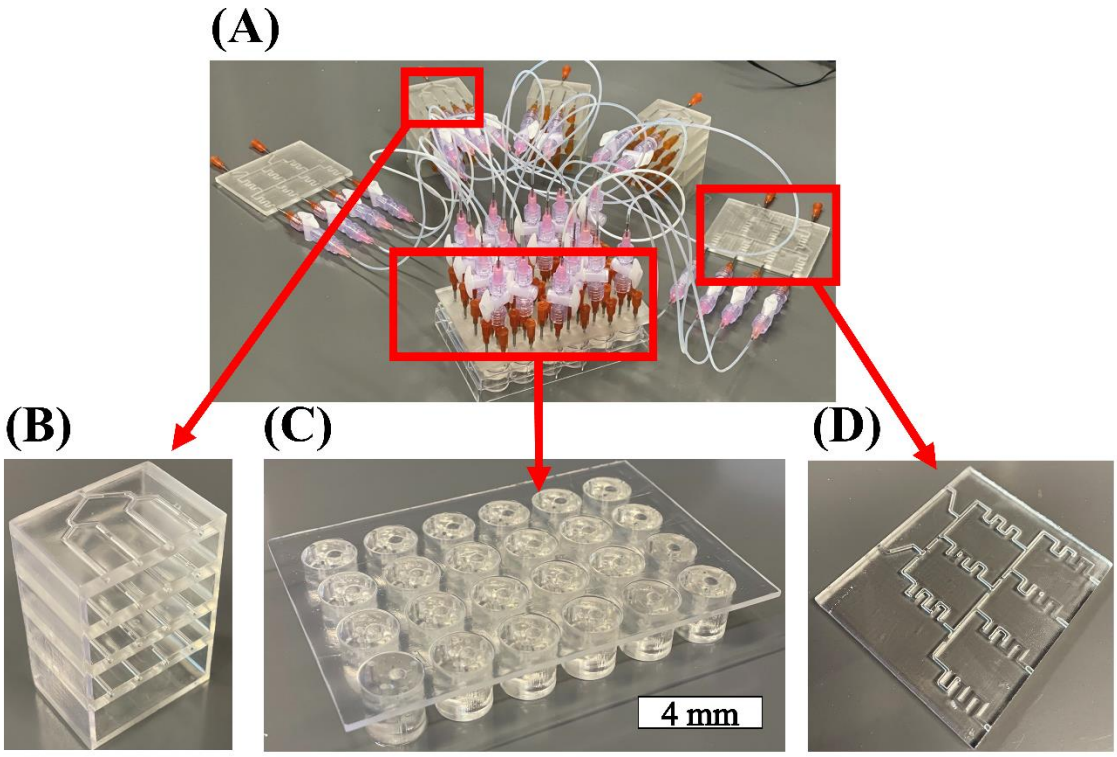

Figure 54: (A) Experimental setup for the snap-on microfluidic mixer device connecting flow distributor and CGG to the snap-on adapter; (B) Four sets of flow distributor arrays; (C) Snap-on adaptor showing snap-on adapter plugged into the 24-well plate assay; (D) Concentration gradient generator (CGG).

5.3.4 Characterization

Optical images of the naproxen salts were taken using an optical microscope (Olympus BX53M, Olympus America Inc.) The in-situ FT-IR measurements were done using an FT-IR Spectrometer INVENIO S coupled with a Pike demountable transmission flow cell. The XRD measurements were performed on a Scintag XDS 2000 diffractometer with Cu Kα radiation.

The kinetics of the dissolution rate measurement of the naproxen salts was investigated using electrochemical impedance spectroscopy (EIS) of the naproxen salts in water[79]. A three-electrode cell with Ag/AgCl as the reference electrode and Pt plates as counter and the working electrode to measure the solution resistance. The cell was initially filled with DI water, and then a known amount of each salt was added to it. The change in the solution resistance was measured vs. time and calibrated for the amount of the dissolved salts.

5.4 Results and Discussion

5.4.1 CFD Simulations for the Velocity and Concentration Profiles

The steady-state velocity and concentration profiles in the snap-on adapter are shown in Figures 55 and 56. The velocity profile of the 4x4 sub-array is shown in Figures 55A and 55B. Since it is necessary to obtain an equivalent level of mixing efficiency in each well, the goal is to evaluate the velocity profile in all sixteen wells when identical boundary conditions were applied at the main inlets for the API and SF solutions. Figures 55A and 55B show that applying these boundary conditions resulted in a similar velocity profile in the sixteen wells, preventing backflow. To better understand the velocity profile inside each well, the velocity profile inside one of the wells is shown in Figure 55C. The two streams of API solution and SF solution entered from the inlets 1 and 2 on the top are mixed in the cylindrical zone. The outlet connection was provided above both inlets. Using these velocity profiles, the concentration profile in the 4x4 array was calculated and shown in Figure 55D. Identical concentration profiles in all sixteen wells confirmed the identical mixing efficiencies across all the snap-on microfluidic mixer device wells. Figure 55E shows the enlarged view of the concentration profile of a single well for clarity.

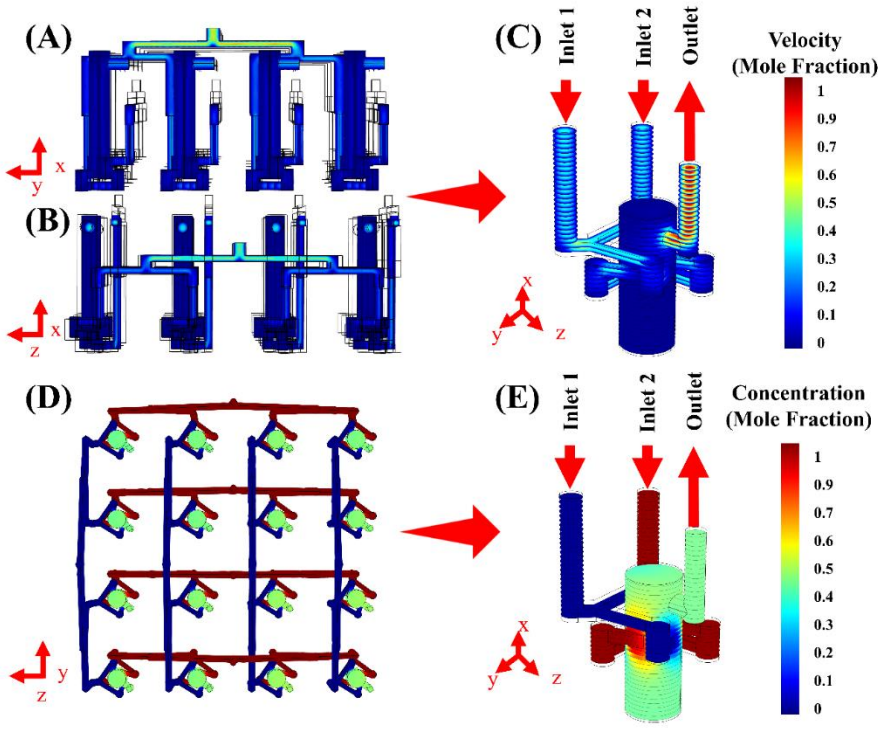

Figure 55: Steady-state velocity profile of a 4x4 sub-array of the 24-well plate snap-on microfluidic mixer device of (A) inlet 1, and (B) inlet 2;(C) Steady-state velocity profile of a single well in the 4x4 sub-array; Steady-state concentration profile of (D) a 4x4 sub-array of the 24-well plate snap-on microfluidic mixer device and (E) a single well in the 4x4 sub-array.

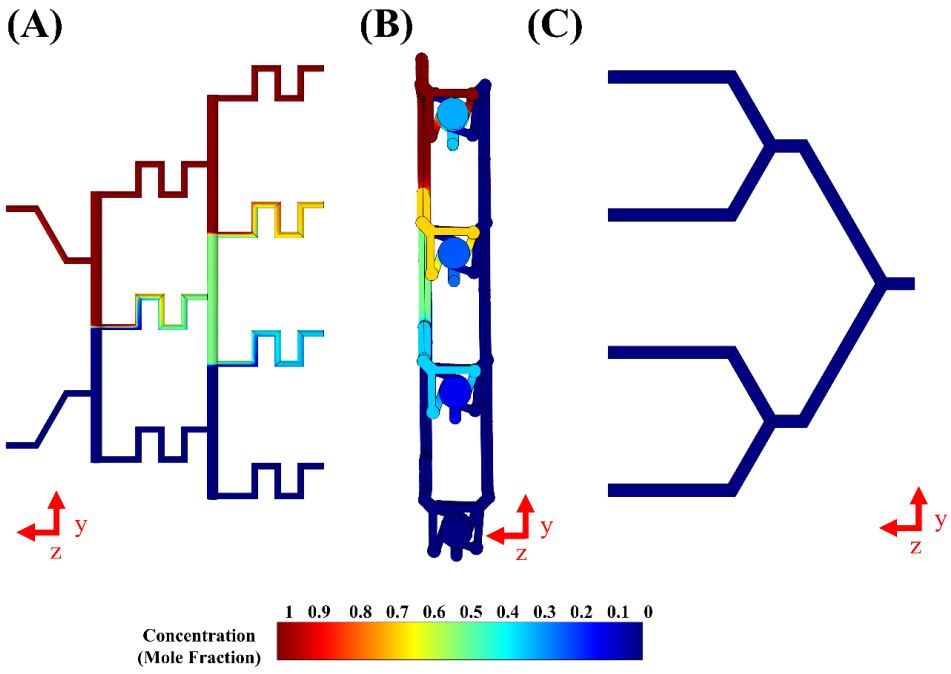

Figure 56: Steady-state concentration profile in the (A) CGG, (B) 4x1 sub-array of the 24-well plate snap-on microfluidic mixer device, and (C) flow distributor.

The concentration profile of the 4x1 sub-array is shown in Figure 56B. This sub-array required a combination of flow distributor and CGG. In Figure 56A, the concentration profile of the CGG is shown. Two streams with concentrations of 0 and 1 were pumped in and generated four streams with concentrations of 0, 0.25, 0.75, and 1. In Figure 56C, the concentration profile of a flow distributor is shown. Connecting the flow distributor and CGG to the 4x1 sub-array resulted in the concentration profile shown in Figure 56B.

5.4.2 Experimental Results

5.4.2.1 Optical Characterization of Naproxen Salts

The optical images of the naproxen salts formed in the 24-well plate snap-on microfluidic mixer device are shown in Figure 58. The results from the 4x4 sub-array are enclosed in the green square. The prepared naproxen solutions (in ethanol, methanol, IPA, and DI water) were distributed into the columns of the 4x4 sub-array. The SF solutions were also fed into the 4x4 sub-array using the flow distributor arrays. One flow distributor array was used to distribute the SF solutions into wells in each row. The continuous-flow screening of these sixteen conditions resulted in the formation of salts in 50% of the wells after 30 minutes of the screening. The most formed salt was sodium naproxen (see the wells on the first row). Sodium hydroxide dissolved in the ethanol reacted with all naproxen solutions (ethanol, methanol, IPA, and DI water) and formed naproxen sodium salt. The crystals formed with naproxen solution in ethanol had needle-shaped morphology and had a high aspect ratio. The sodium naproxen salt from the naproxen solution in IPA had more like a plate shape morphology and a lower aspect ratio than the previously discussed salts. The formation of naproxen salt from the naproxen solution in methanol resulted in very tiny crystals, and the morphology could not be reported using the optical images. The majority of the formed salts from an aqueous solution of the naproxen had plate-shaped morphology but were not uniform in size. Potassium salted out naproxen potassium in 75% of the wells. The formation of potassium

naproxen salts with the naproxen solutions in ethanol and methanol resulted in tiny crystals similar to sodium naproxen salts formed from the methanol solution of naproxen and sodium hydroxide. The morphology of these tiny crystals was not fully detected using the optical images, and the quantity of these formed salts was not enough for XRD. The naproxen solution in IPA formed plate-shaped crystals when mixed with sodium hydroxide and potassium hydroxide. The combination of naproxen in IPA and arginine or pyridine did not form any naproxen salts. The aqueous solution of naproxen only salted out in 25% of the conditions. As shown in Figure 58, a mixer of 2D, plate-shaped crystals, and agglomerated particles was formed where an aqueous solution of naproxen was mixed with sodium hydroxide. The arginine naproxen salt only formed when a naproxen solution in ethanol was used, resulting in small naproxen salts. Comparing the SFs according to the number of salts formed, the order was NaOH> KOH> L-arginine> pyridine. Arginine did not salt out naproxen in 75% of the wells, and pyridine was the only SF solution that did not salt out with naproxen in any conditions.

The red and blue boxes in Figure 57 show the optical images of the naproxen salts formed in two 4x1 sub-arrays of a 24-well plate. An ethanolic solution of potassium hydroxide was distributed into the four wells using a flow distributor for the wells shown in the red box. For the second inlet, two different concentrations of the naproxen solution in IPA were mixed distributed into these four wells using a CGG. As a result, the concentration of the SF was constant in all these four wells, while the concentration of naproxen solution in IPA was varied. As shown in Figure 57, potassium naproxen salt was formed in all four wells shown in the red box. As the concentration of naproxen increased, the yield and the aspect ratio of the plate-shaped salt crystals increased. The second 4x1 sub-array shown within the blue box had the same configuration for the solution distribution. The ethanolic sodium hydroxide solution was distributed into all four wells on the 6^{th} column using a flow distributor. For the second inlet, two different concentrations of the ethanolic solution of

naproxen were mixed in a CGG to distribute four different concentrations of the naproxen salts into the wells. The sodium naproxen salts formed in these wells had all needle-shaped morphology. The formation yield and aspect ratio of the crystals increased with the increment of the naproxen concentration.

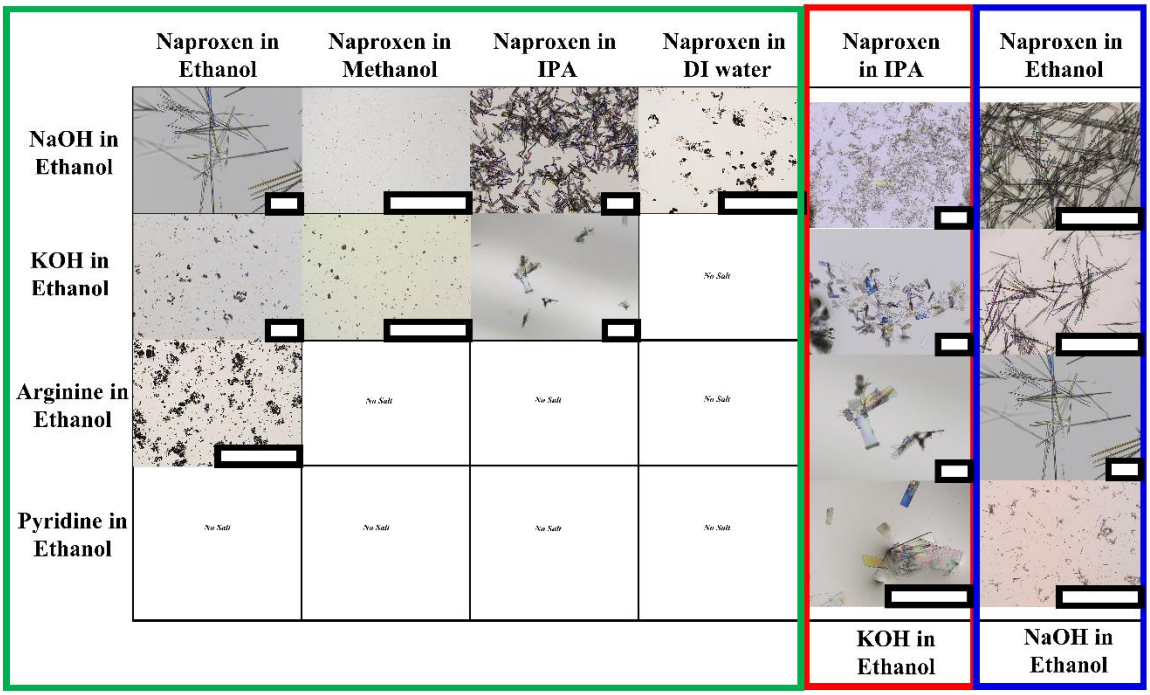

Figure 57: Optical images of naproxen salt screening in the snap-on microfluidic mixer device. The green box shows the 4x4 sub-array where one flow distributor was used for each column and row. The red and blue boxes each show a 4x1 sub-array where a combination of flow distributor and CGG were used to distribute the solutions in the wells. The wells where no crystal was formed are labeled as "No Salt."

5.4.2.2 Qualitative Screening of Naproxen Salts Using FT-IR

FT-IR analysis was performed to characterize the naproxen salts formed in the snap-on continuous-flow microfluidic mixer device. Figure 58A shows the FT-IR spectra of the three different crystallized naproxen salts, sodium naproxen, potassium naproxen, and arginine naproxen. These salts were formed from an ethanolic solution of naproxen and different SF solutions. While different naproxen salts were expected to show different spectra, naproxen sodium salts from different solutions show identical FT-IR spectra. Figure 58B shows the naproxen sodium salts formed from the reaction between an ethanolic solution of the sodium hydroxide and naproxen in

four different solvents listed as ethanol, methanol, IPA, and DI water. All four spectra show identical peaks, confirming the formation of naproxen sodium salts from these four wells.

Another FT-IR analysis was performed by studying the spectra of the potassium naproxen salts formed at different ratios of the naproxen and SF solution. Figure 58C shows that the four crystallized potassium naproxen salts have identical characterization peaks in their FT-IR spectra.

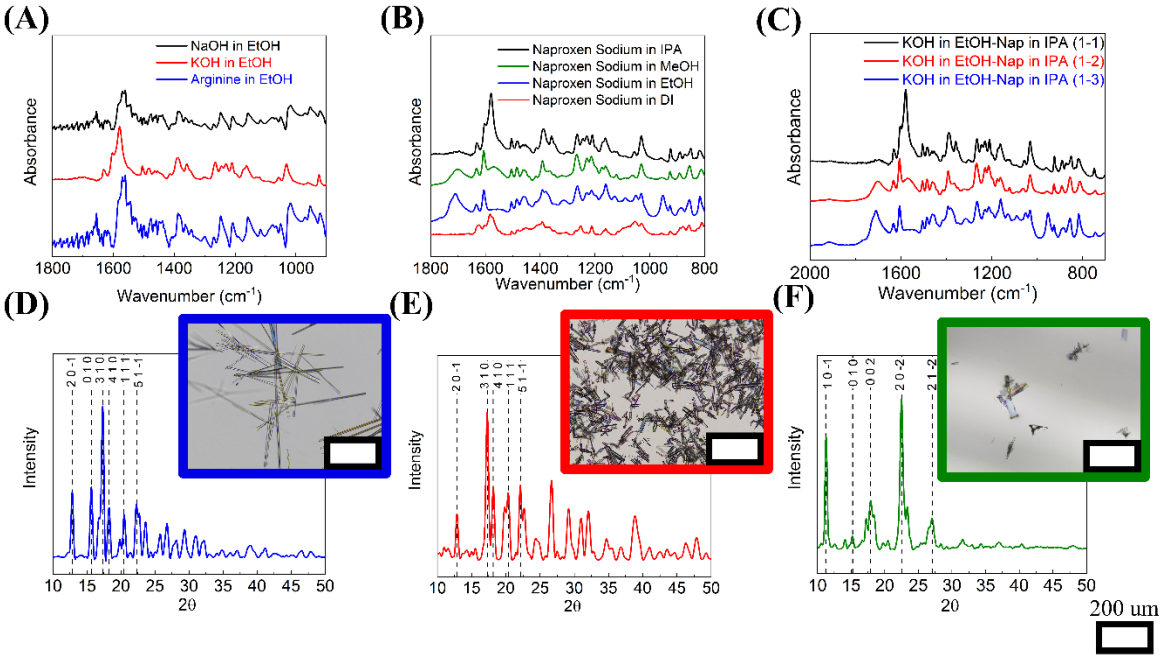

Figure 58: (A) FT-IR spectra of sodium, potassium, and arginine naproxen salts (B) FT-IR spectra of the naproxen sodium salts formed with sodium hydroxide in ethanol and naproxen in different solvents as listed: IPA, methanol, ethanol, and DI water; (C) FT-IR spectra of naproxen salts formed from potassium hydroxide in ethanol as SF and naproxen in IPA; XRD pattern of naproxen salts: (D) naproxen sodium formed from naproxen in ethanol and NaOH in ethanol; (E) sodium naproxen formed from naproxen in IPA and NaOH in ethanol; (F) naproxen sodium formed from naproxen in IPA and KOH in ethanol.

5.4.2.3 Dissolution Rate Measurements and XRD Analysis of Naproxen Salts

Among all the formed naproxen salts, only three of them had a high enough yield to salt out naproxen in a reasonable quantity. The rest of the wells had less naproxen salt formed inside, which was impossible to filter and dry for further analysis. From here, the sodium naproxen salt formed in naproxen solutions in ethanol and IPA and the potassium naproxen salt formed in IPA were filtered and dried for the XRD and crystal structure analysis and measurement of the dissolution rate. The XRD patterns of the salts with the highest yields are shown in Figures 58D, 58E, and

58F[80]. The needle-shaped crystals of naproxen sodium from ethanol and IPA solutions of naproxen showed similar XRD patterns. However, potassium naproxen with the plate shape morphology showed a different XRD pattern shown in Figure 58F.

The dissolution rate measurements were done from the EIS results. The amount of the salt initially is known. The resistance of the solution for the initial amount of the salt is recorded. After the complete dissolution of the salt, the resistance of the solution remains constant. In Figure 59, the amount of the dissolved salt is plotted vs. the resolution of the solution. The slope is then used to fit the resistance data vs. time.

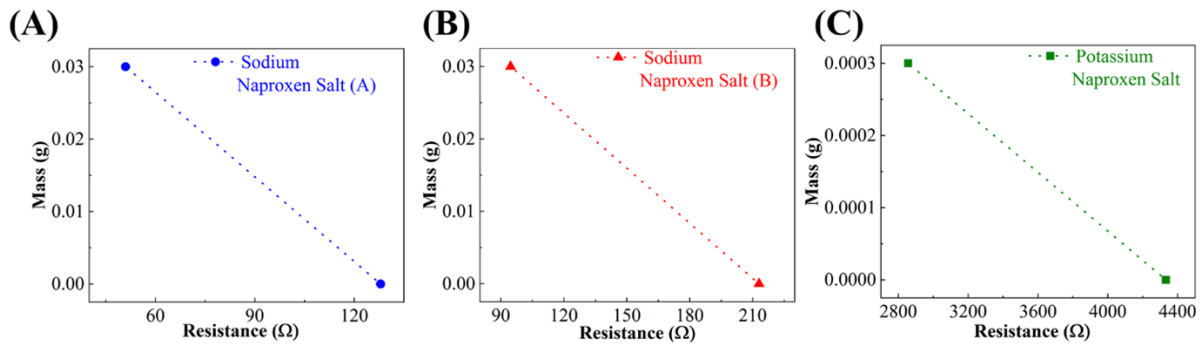

Figure 59: Dissolved mass of the naproxen vs. resistance of the solution for: (A) sodium naproxen formed in naproxen solution in ethanol, (B) sodium naproxen formed in naproxen solution in IPA, (C) potassium naproxen salt.

The dissolution rate of the three salts mentioned above was calculated using EIS. The change in the resistance of the pure water vs. time was measured for a known amount of added naproxen salt using a three-electrode cell. In Figure 60, the dissolved amount of salt vs. the time is shown for all three salts. The slopes of the fitted lines are reported as the dissolution rate and shown in Figure 60. The results showed that the sodium naproxen salts had significantly higher solubility compared to the potassium naproxen salt.

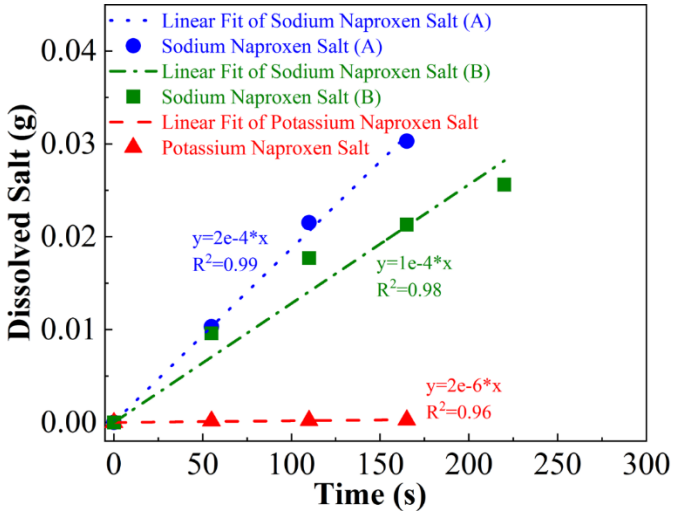

Figure 60: Dissolution rate comparison of naproxen salts: The fitted line for the blue circles shows the dissolution rate of sodium naproxen salt that was formed from an ethanolic solution of naproxen; the fitted line for the green squares shows the dissolution rate of sodium naproxen salt that was formed from naproxen in IPA; the fitted line for the red triangles shows the dissolution rate of potassium naproxen.

5.5 Conclusion

The effective and robust screening of possible crystal forms of newly synthesized drugs requires modifying the existing batch HT screening techniques to maintain stable solution conditions. The batch HT technologies involving microtiter assay suffer from depletion of the supersaturation inside the microwells due to crystal nucleation and growth. The screening results obtained under such varying solution conditions are often misleading. This study develops a novel snap-on adaptor, which converts a batch microtiter plate into a continuous-flow microfluidic mixer device. The continuous-flow HT technique enables effective and robust screening of crystal polymorph, morphology, size, and kinetics under controlled conditions. Here, the design of the snap-on adaptor is based on the previously developed continuous-flow microfluidic mixer that creates cyclonic flow in each well for efficient mixing and to capture crystals that can be easily harvested for characterization and further evaluation.

Here a snap-on adaptor is developed for a 24-well plate to enable continuous-flow salt screening of naproxen. The continuous-flow operation of the snap-on microfluidic mixer device requires implementing flow distribution networks to distribute solutions into all wells while minimizing the

number of pumps. Two types of flow distribution networks are introduced in this study to expand the capabilities of continuous-flow HT screening. The first is the flow distributor that can equally distribute a single entering stream into multiple channels (e.g., two, four, eight, sixteen). The second type of flow network is the concentration gradient generator (CGG). The CGG requires two entering streams of different concentrations that are split and mixed to obtain a range of the concentrations that can be fed to the snap-on adapter. Different combinations of these two types of distribution flow networks allow for different screening experiment designs. In this study, a 24-well plate assay is divided into two sub-arrays. The first one is a 4x4 sub-array of wells, and multiple flow distributors are implemented to screen sixteen different conditions.

First, naproxen is dissolved in four different solvents listed as ethanol, methanol, IPA, and DI water, and each is distributed into four wells with a flow distributor. Then four different SFs listed as sodium hydroxide, potassium hydroxide, arginine, and pyridine are dissolved in ethanol and distributed into the wells using flow distributors. On the remaining part of the 24-well plate assay, a combination of flow distributor and concentration gradient generator are used for every four wells to screen for different SFs and naproxen solution ratios. After the continuous-flow screening, optical images are taken from the crystallized salts in the wells. Naproxen is salted out in fifty percent of the conditions; however, not all salts have a high formation yield. Therefore, FT-IR analyses are done on the crystallized salts of naproxen to identify the formation of different salts. Among the crystallized salts, three have high formation yields where the quantity is enough for comparisons. These three salts are filtered and dried for XRD analysis and dissolution rate measurements. The dissolution rate of these salts is measured using the EIS technique. Resistance of the solution is measured over time as a function of salt concentration and correlated to calculate dissolution rate. The results show that the naproxen sodium salt has around two orders of magnitude higher dissolution rate than the potassium naproxen salt. The flexibility of snap-on adapters to fit different types of microtiter plates, in

combination with different types of flow distributors, provide opportunities to use the snap-on microfluidic device for a range of HT screening applications. These efficient HT screening techniques will have a transformative impact on material discovery and development for various healthcare and energy applications.

VI. MACHINE-LEARNING-DRIVEN, SENSOR-INTEGRATED MICROFLUIDIC DEVICE FOR MONITORING AND CONTROL OF SUPERSATURATION FOR AUTOMATED SCREENING OF CRYSTALLINE MATERIALS

6.1 Introduction

Microfluidics systems have demonstrated higher efficiency than conventional macroscale methods for employing fewer reagents and samples while achieving greater accuracies when handling fluids. In addition, these microscale systems allow for effective and precise simulation of physical processes in large-scale systems. The sensor technology has evolved significantly in the past few decades towards higher precision and miniaturization, which has benefited the development of fully integrated microfluidic systems. Sensors can enable the detection of low-concentration analytes in a complex, multi-component solution while allowing fast, continuous monitoring at a reasonable cost. Furthermore, sensors can readily adapt to microfluidic platforms because of their easy integration and straightforward fabrication technologies[81,82].

Process analytical technology (PAT) instrumentations are commonly used to monitor crystallization processes. The PAT sensors can implement various measurement techniques such as attenuated total reflectance Fourier-transform infrared (ATR-FTIR), focused beam reflectance measurement (FBRM), Raman spectroscopy, particle vision measurement (PVM), electrical capacitance tomography, electrical resistance tomography, and ultrasound tomography[83-88]. The optical PAT sensors based on refractive index measurement are often employed to quantify solute concentration in liquid solutions. Although the refractive index can show better resolution and detection limit for specific molecules in a solution, they can have limited application to multi-component mixtures.

Additionally, the stray light can affect the refractive index measurement, and prolonged exposure can cause photobleaching. Fiber optics can add flexibility to optical PAT sensors, where an optical glass fiber can seamlessly connect sensing elements[89,90]. They were used as refractometric sensors for the concentration measurement of APIs (Paracetamol) in crystallization processes. Despite their advantages, fiber optic sensors are costly and require precise installation methods and procedures. ATR-FTIR spectroscopy can also be used for online monitoring and control of the supersaturation in the crystallization of API. The primary and secondary crystal nucleation occurrence can be informed by supersaturation profiles coupled with crystal size data from the laser backscattering probe. The time-resolved ATR-FTIR spectra can be used to measure the evolution of solute concentration in a multi-component mixture during crystallization[15,91,92]. Some of the disadvantages of infrared sensors are due to their limited range for detection and the need for line of sight. In addition, infrared sensors cannot measure the data when blocked by crystals during measurements and have a slow data transmission rate[93]. The third PAT sensor for concentration measurement is the electrochemical sensor. They can be configured to have higher resolutions and implemented in confined spaces while requiring low power[94-96]. The electrochemical sensors have shown repeatable real-time data collection and processing with higher accuracy. Additionally, they have a low fabrication cost and can be integrated readily with miniaturized screening systems[97,98]. In this study, we develop a fully integrated continuous-flow microfluidic mixer that implements an electrochemical sensor to detect and measure the concentration (and supersaturation) of API during crystallization. This microfluidic device allows crystals to nucleate under controlled conditions and creates a vortex to capture crystals for measurement[41,61]. In this continuous-flow microfluidic system, screening of crystal polymorphs, morphology, and growth rates can be performed in a controlled supersaturated environment. This device has an advantage over previously reported continuous-flow microfluidic devices that suffer

from supersaturation variation in the downstream channels. Integrating an electrochemical sensor into the continuous-flow microfluidic device can bring unprecedented control to the screening of API crystals. The approach mentioned above is novel as the electrochemical sensors to measure supersaturation in microfluidic crystallization devices have not been developed yet. Such sensor-integrated microfluidic systems are much needed to automate micro-scale screening devices in the pharmaceutical industries[99]. Even though such systems can rapidly generate information about the supersaturation propensities of API crystals, predicting the supersaturation is still a challenge, and the researchers primarily rely on time-consuming experiments to observe supersaturation[100,101]. Synergistic incorporation of modern data-driven approaches such as machine learning (ML) with the high-throughput sensor-integrated microfluidic systems can aid in predicting the supersaturation, optimizing experimental conditions, and further accelerating screening of API crystals[101-103]. Hence, there is a need to develop a robust method combining high-throughput (HT) experimental determination of supersaturation and ML-driven prediction of supersaturation to rapidly screen API crystals. In this work, we first developed a protocol to evaluate various transition metals for their electrochemical sensitivity to detect compounds of interest using cyclic voltammetry (CV). The most sensitive electrode material was then selected for a screen-printed electrochemical sensor and integrated with the continuous-flow microfluidic mixer. The screen-printed electrochemical sensor was calibrated and benchmarked to detect L-histidine in a water-ethanol solution. L-histidine is an ideal candidate to evaluate the effectiveness of the electrochemical sensor, as it has both carboxylate and amine groups that are present in most APIs. The obtained experimental data from the electrochemical sensors were employed to develop a prediction model using ML algorithms[104]. Four of the most frequently used techniques - neural networks, support vector machine, random forest, and gradient boosting were tested to train and

test sets[105,106]. The prediction model was then applied to predict the supersaturation of the mixture from the anodic CV slopes obtained from the sensor.

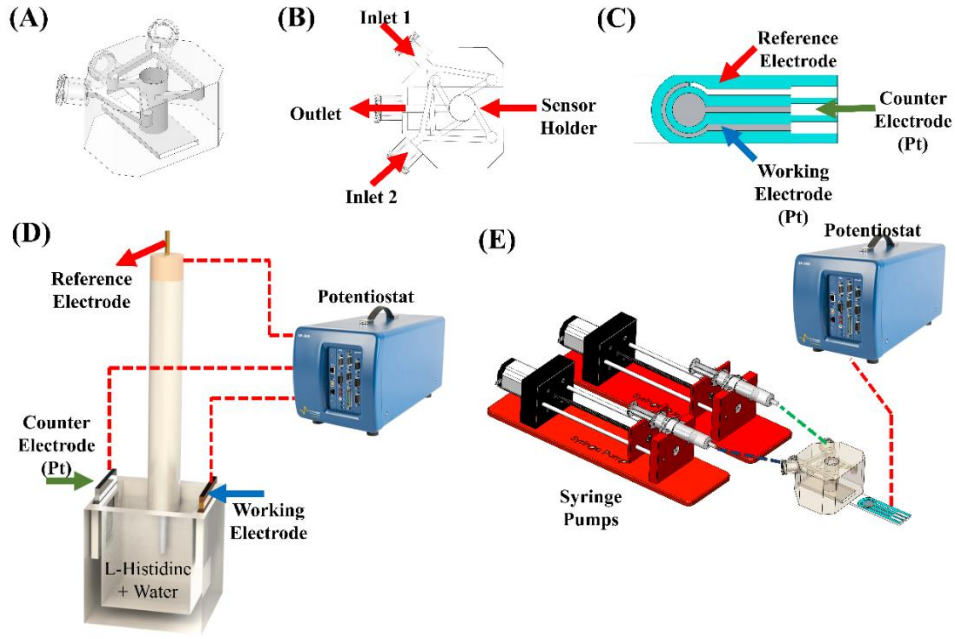

Figure 61: (A) Isotropic view of the sensor integrated microfluidic mixer device; (B) Top view of the sensor integrated microfluidic mixer with inlets and outlets shown marked. The rectangle marked as sensor holder is where the sensor is integrated inside the microfluidic device;(C) The integrated surface sensor with reference, working, and counter electrodes marked; (D) Experimental setup of batch cyclic voltammetry (CV) analysis; (E) Experimental setup of continuous flow sensor integrated microfluidic mixer device.

6.2 Theoretical Methods

6.2.1 Machine Learning Algorithms for Supersaturation Prediction Model

In this work, we implemented several ML algorithms-neural networks (NN), support vector machine (SVM), random forest (RF), and gradient boosting (GB)- using Scikit-learn ML library in Python 3.9.1. These ML algorithms were implemented to predict supersaturation in the continuous-flow microfluidic mixer at different experimental operating conditions[105].

The initial concentration of L-histidine in water, the ethanol to water ratio in the mixer (antisolvent ratio), and the distinct anodic CV slopes were the input parameters. The actual supersaturation was calculated using the solubility data reported in the literature[50,51]. Therefore, all algorithms were studied for supervised learning where the actual supersaturation for given ethanol to water ratio is

considered the output variable (i.e., ground truth). Since the input parameters are of different orders of magnitude, i.e., the concentration of L-histidine in water is in the range of 25-100 % of the saturation concentration at 25℃ while the CV slopes are in the order of 10-2-10-3, the individual input parameters were scaled using standard scaler as:

$$z = \frac{x-\mu}{\sigma} \tag{48}$$

Here z is the scaled parameter, x is the original unscaled parameter, μ is the average, and σ is the standard deviation of the parameter. The experimental dataset was divided randomly into a training set and testing set, and the performance of the algorithms was evaluated using the R^2coefficient defined as:

$$R^2 = 1 - \frac{\Sigma_i \left(s_{p,i} - s_{t,i}\right)^2}{\Sigma_i \left(s_{t,i} - \bar{s_t}\right)^2} \tag{49}$$

where s_p is the predicted supersaturation from the ML algorithms, s_t is the true value obtained from the literature[50,51], and $\bar{s_t}$ is the mean of the actual supersaturation for all the datasets under consideration. The hyperparameters of each of the was considered machine learning algorithms were optimized to give the best possible performance. Table 16 shows the list of hyperparameters and the range in which they are varied.

Table 16: Hyperparameters and the selected range of variation for the implemented ML algorithms.

ML Algorithm	Hyperparameters	Range
Neural Network (NN)	Nodes	1-100
	Hidden layers	1-2
	Activation function	Logistic, tanh, identity, rectified linear unit (relU)
	Convergence algorithm	Adams, LBFGS, SGD
	Learning rate	Constant, adaptive, inverse scaling
Support Vector Machine (SVM)	Kernel	Linear, polynomial, RBF, Sigmoid
	Margin parameter (C)	0.01-1000
	Regularization	Auto, scaled
Random Forest (RF) and Gradient Boosting (GB)	Number of estimators	1-100

6.3 Experimental Methods

6.3.1 Materials

The crystalline Form-A (stable) of L-histidine (Sigma-Aldrich, chemical purity ≥98%) was used for calibration measurements of the electrochemical CVs. In addition, deionized water (Sigma-Aldrich, 18 MΩ cm) and ethanol (Sigma-Aldrich, ACS 99.8%) were used as solvent and antisolvent for antisolvent crystallization studies. The screen-printed electrodes were purchased from Mettohm Inc. (Pt: DRP-550-U75)

6.3.2 Fabrication of Microfluidic Devices

The 3D designs of the sensor integrated microfluidic device shown in Figure 61A and 61B were designed in SolidWorks® (2018, Dassault Systems) and then 3D-printed using stereolithography (SLA) 3D printer (form 2, Formlabs Inc., USA). A clear FLGPCL02 resin activated by a 405 nm laser was used to 3D print optically clear microfluidic devices with 150 μm of lateral and 25 μm of axial resolutions. The clear resin is chemically resistant to various solvents, including ethanol and water. The printed devices were washed with isopropyl alcohol (IPA) (90%, Sigma-Aldrich) bath for 20 minutes in the Form Wash (Formlabs Inc., USA) to remove the residues of the resin from the external surface. The interior channels of the 3D-printed device were washed separately by injecting IPA using a syringe. The post-washed 3D-printed devices were finished by removing supports and curing for 20 minutes using a commercial ultraviolet lamp. The optical transparency of the 3D-printed microfluidic device was improved by wet sanding using 400 to 12000 grit pads, followed by spray painting of resin. The top opening of the sensor integrated microfluidic mixer was sealed with polycarbonate films for optical clarity.

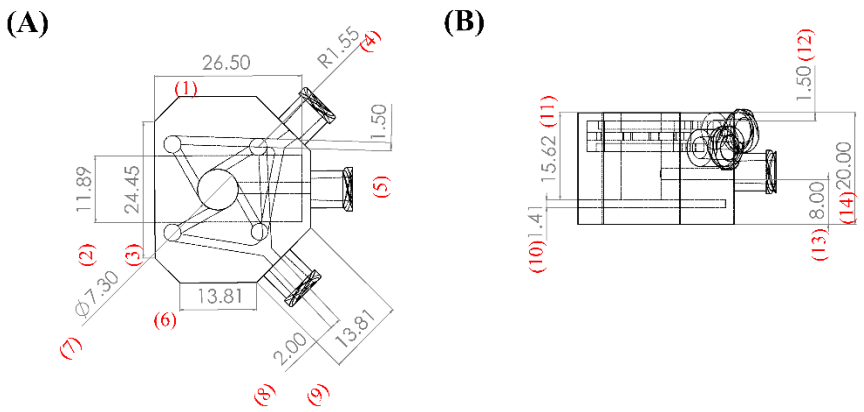

Figure 62: (A) Top view and (B) side view of the array of the sensor integrated microfluidic mixer device with marked dimensions.

6.3.3 Experimental Setup

Figure 61D shows the experimental setups used for the batch CV analysis to test various transition metals. A custom-made three-electrode cell was designed (see Figure 1D) to study the sensitivity of different metals. Transition metals foils of Ir, Ni, Ag, Pd, Zn, and Pt (>99.9% purity, ACI Alloys) were used for the electrochemical measurements. These metals were selected since they were the potential candidates because they are electroactive for organic molecules. The metal that showed the most sensitivity towards L-histidine in CV measurements was then chosen to be implemented as the sensor for the continuous-flow sensor-integrated microfluidic mixer. Metal plates were cut in size 1.5x1.5x0.1 cm and then mechanically polished using 1000 grit sandpaper followed by alumina suspensions of particle size 1, 0.3, and 0.05 um to achieve a mirror-like finish. The polished metals were sonicated in deionized (DI) water for 5 minutes to remove any residual suspension on their surface. The mechanically polished metals were used as the working electrodes, an Ag/AgCl micro-reference electrode (Innovative Instruments Inc.) was used as the reference, and a Pt strip (99.999% purity, ACI Alloys) was used as the counter electrode. Initially, four different concentrations of L-histidine in water (25%, 50%, 75%, and 100% of the saturated concentration at 25℃) were prepared. Then, 6 mL of a solution with a known concentration of L-

histidine in water was added to the three-electrode electrochemical cell and stirred at 200 rpm using magnetic stirring. The sensitivity of the transition metals towards L-histidine in a water-ethanol mixture was assessed by performing CV measurements on a Biologic SP-300 potentiostat. (see Figure 61D) CVs were performed in a wide range of potential (-1 to 1 V vs. Ref) on the six selected transition metals and four concentrated solutions at different scan rates of 10, 50, 100, 500, and 1000 $mV.s^{-1}$. The anodic CV slope of current vs. voltage was recorded as an indicator of the concentration of the L-histidine in water. Furthermore, the antisolvent (ethanol) effect was investigated by repeating the CV measurements for the solvent to antisolvent ratios of 1:1, 2:1, 3:1, and 4:1.

The selected metal from the batch CV analysis was then selected as the working electrode for the screen-printed electrode assembly. In a screen-printed electrode (Figure 61C), the circular zone (diameter~7 mm) must be in direct contact with the mixture for supersaturation measurements. The in-situ supersaturation measurement in a continuous-flow manner required coupling the screen-printed electrodes with the microfluidic device (see Figure 61E). The design of the novel continuous-flow microfluidic mixer was modified to integrate a screen-printed electrode in the bottom plane[107]. As shown in Figures 61A and 61B, the sensor was horizontally inserted into the continuous-flow microfluidic mixer to enable direct contact between the screen-printed electrode and mixture. Here, a wired connection was used to connect the screen-printed electrode to the potentiostat. A relatively narrower range of potential (-0.5 to 0.5 V vs. Ref) was applied for the continuous-flow CV measurements compared to the batch experiments to calibrate the platinum screen-printed electrochemical sensor. The experimental setup for the continuous-flow CV measurement is shown in Figure 61E. The two inlets of the continuous-flow sensor-integrated microfluidic mixer were connected to two syringe pumps containing aqueous L-histidine solution and ethanol (antisolvent). The CV measurements were performed for ten different antisolvent

ratios and four different concentrated solutions of L-histidine. The total flow rates of inlets were maintained at 1 $mL.min^{-1}$, and the percentage of each flow rate was changed to vary the volumetric antisolvent ratios.

For the initial benchmarking and validation, four aqueous solutions of L-histidine with initially unknown concentrations were prepared. The antisolvent crystallization was performed for a volumetric ratio of 50% for the antisolvent. The total flow rate was kept constant at 1 $mL.min^{-1}$, and each stream was pumped into the device at 0.5 $mL.min^{-1}$. Details of the unknown concentrated L-histidine solutions are provided in Table 17.

Table 17:Details of the Experimental Conditions for Calibration of the Pt Screen-Printed Electrochemical Sensor

AS %	Conc. [mol/L]	slope start	slope end	Δ_{slope}	SS	Normalized Δslope	Normalized SS
10	0.0632	0.018	0.01	0.006	0.3	0.44	0.25
10	0.1264	0.034	0.02	0.008	0.6	0.63	0.50
10	0.1897	0.046	0.03	0.009	0.9	0.73	0.75
10	0.2530	0.034	0.02	0.013	1.3	1.00	1.00
20	0.0632	0.019	0.01	0.007	0.4	0.33	0.25
20	0.1264	0.030	0.01	0.011	0.8	0.52	0.50
20	0.1897	0.035	0.02	0.014	1.3	0.70	0.75
20	0.2530	0.057	0.03	0.020	1.7	1.00	1.00
30	0.0632	0.023	0.01	0.011	0.5	0.40	0.25
30	0.1264	0.039	0.02	0.018	1.1	0.69	0.50
30	0.1897	0.036	0.01	0.019	1.6	0.57	0.75
30	0.2530	0.052	0.03	0.021	2.2	1.00	1.00
40	0.0632	0.019	0.01	0.009	0.7	0.27	0.25
40	0.1264	0.030	0.01	0.019	1.4	0.59	0.50
40	0.1897	0.053	0.02	0.030	2.1	0.93	0.75
40	0.2530	0.045	0.01	0.032	2.8	1.00	1.00
50	0.0632	0.023	0.01	0.012	0.9	0.34	0.25
50	0.1264	0.045	0.02	0.023	1.8	0.65	0.50
50	0.1897	0.047	0.01	0.029	2.7	0.82	0.75
50	0.2530	0.056	0.02	0.036	3.7	1.00	1.00
60	0.0632	0.018	0.01	0.008	1.1	0.23	0.25
60	0.1264	0.038	0.01	0.026	2.3	0.76	0.50
60	0.1897	0.044	0.01	0.029	3.5	0.88	0.75
60	0.2530	0.065	0.03	0.034	4.7	1.00	1.00
70	0.0632	0.017	0.00	0.009	1.4	0.31	0.32
70	0.1264	0.035	0.01	0.016	2.9	0.56	0.63
70	0.1897	0.047	0.02	0.020	4.4	0.70	0.95
70	0.2530	0.062	0.03	0.029	5.9	1.00	1.26
80	0.0632	0.019	0.01	0.007	1.8	0.25	0.40
80	0.1264	0.034	0.01	0.017	3.7	0.66	0.80
80	0.1897	0.039	0.01	0.020	5.6	0.77	1.20
80	0.2530	0.056	0.03	0.026	7.5	1.00	1.60
90	0.0632	0.019	0.01	0.008	2.4	0.37	0.53
90	0.1264	0.027	0.01	0.016	4.9	0.74	1.06
90	0.1897	0.038	0.01	0.019	7.4	0.85	1.58
90	0.2530	0.059	0.03	0.022	9.9	1.00	2.11

6.4 Results and Discussion

6.4.1 Evaluation of the Sensitivity of the Transition Metals Towards L-histidine Solution

The comparison of the sensitivity of the six selected transition metals is shown in Figure 63. The CV measurements were performed at two different scan rates of 100 and 1000 $mV.s^{-1}$, and the variation in the anodic CV slope between 0 and 1V vs. Ref was measured.

The anodic CV slope was chosen as an indicator of L-histidine concentration since the cathodic CV slope (0 to -1V vs. Ref) may be influenced by the evolution of hydrogen due to the reduction of water under negative potentials[108,109]. Linear regression was performed on CV slope vs. concentration to obtain the correlation coefficient (R^2) values, which are representative of the sensitivity of metals. The R^2 value implies that metals with a high correlation coefficient are better candidates for the electrochemical sensor than those with a low correlation coefficient. For the scan rate of 100 $mV.s^{-1}$, Ir metal showed the lowest sensitivity (R^2 values) among all the transition metals. Ni, Ag, Pd, and Zn showed sensitivities between 0.65 to 0.85 of tested conditions. Among all other metals, Pt had the highest sensitivity of ~0.98 toward L-histidine for all tested conditions. Maintaining higher sensitivity at higher scan rates is important for a quick and robust evaluation of analyte concentration. The sensitivity of all the metals increased at a higher scan rate of 1000 $mV.s^{-1}$. Pt and Ag were the most sensitive metals to detect L-histidine at higher scan rates. Since Pt was reliably able to sense the L-histidine concentration at both low and high scan rates, it was selected as the working electrode for the in-situ screen-printed electrochemical sensor for the continuous flow crystallization studies.

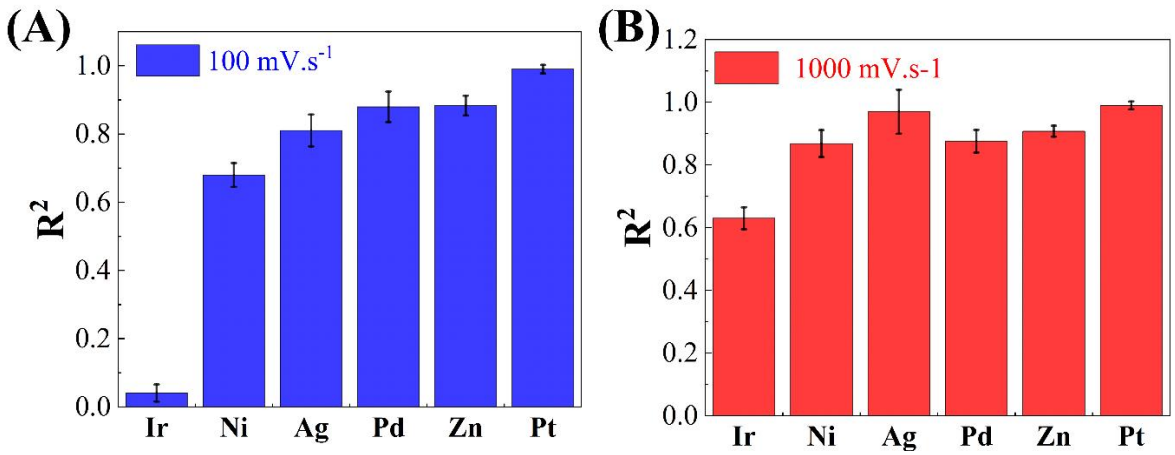

Figure 63: Comparison analysis for different metals for their sensitivity toward the aqueous solution of L-histidine in water at different scan rates: (A) 100 $mV.s^{-1}$ and (B) 1000 $mV.s^{-1}$.

6.4.2 Calibration of the Platinum-based Screen-Printed Electrochemical Sensor

The calibration of the Pt screen-printed electrochemical sensor was performed with ten different ratios of solvent (water) to antisolvent (ethanol) and four different concentrations of the L-histidine. CVs were performed in the continuous-flow sensor-integrated microfluidic mixer (Figure 61E) in the range of -0.5 to 0.5V. For the batch CV measurements, the anodic slope from 0 to 1V was selected as the sensitivity criterion for sensors; however, screen-printed electrochemical sensors do not have a high surface area, unlike their bulk counterparts, and application of higher potentials may result in damaging the sensor; therefore, the anodic slope between 0 to 0.5V was used instead. It is imperative to understand the effect of the antisolvent concentration on the supersaturation, and hence, for a fixed flow rate of 1 $ml.min^{-1}$, the volumetric antisolvent ratio was changed from 10% to 90%. Initially, the aqueous L-histidine solution was only pumped in the microfluidic mixer, and the CV measurement was initiated. Upon adding the antisolvent stream, a transition in the CV was observed, indicating the change of the supersaturation (See Figure 64). These transitions are dependent on both L-histidine concentration and the antisolvent to solvent ratio. Figures 64A, 64B, 64C, and 64D represent the change of the anodic slopes for four different concentrations of the L-histidine solutions at 50% of volumetric

antisolvent ratio. The starting CV cycle represents the steady-state CV for the aqueous solution L-histidine, and the end cycle represents the steady-state cycle for the mixture of the solvent and antisolvent stream. As shown in Figure 64, the change in the anodic slope became more significant as the concentration of L-histidine in water increased. The change of the anodic slope (Δ_{slope}) of these two steady-state cycles is then used to calculate the supersaturation of L-histidine inside the microfluidic mixer. All measured steady-state anodic slopes are provided in Table 17.

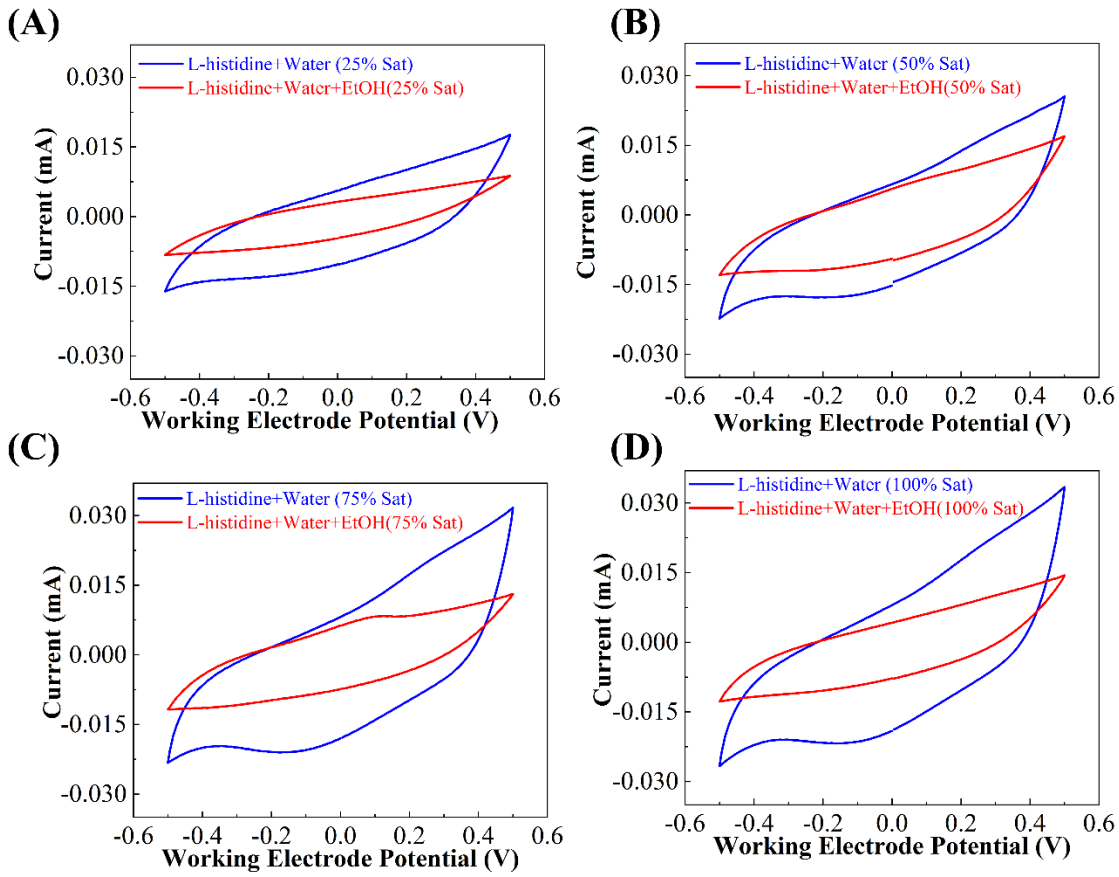

Figure 64: Cyclic voltammetry measurements for 50% of antisolvent solution (Ethanol) for the continuous flow system. Here the initial cycle shows the stable CV for the aqueous solution of L-histidine. The end cycle shows the steady-state CV after the addition of the antisolvent stream for different concentrations of L-histidine in water: (A) 25% of the saturated solution; (B) 50% of the saturated solution; (C) 75% of the saturated solution; (D) 100% of the saturated solution.

Empirical estimation of the supersaturation during the antisolvent crystallization of L-histidine requires a known ratio of antisolvent to solvent in which the crystallization occurs. Using the anodic CV slopes of the experimentally determined supersaturation from Table 17, a heat map

shown in Figure 65A is presented to back-calculate the supersaturation of the solution. A maximum supersaturation is attainable at every antisolvent ratio when a 100% saturated aqueous solution of L-histidine is used. Therefore, at every antisolvent volumetric ratio, the rest of the anodic CV slopes were normalized using the calculated anodic CV slope obtained from the experiments with the 100% saturated aqueous solution of L-histidine at 25^{o}C. Similarly, the supersaturation values at any given L-histidine concentration and antisolvent to solvent ratio are normalized against the maximum supersaturation at 100% L-histidine concentration for a given volumetric antisolvent ratio. These normalized data plotted as the heat map shown in Figure 65A also indicate the Pt sensor performance. An ideal sensor is expected to be responsive to the API concentration only; therefore, the heat map calibration curve must show completely horizontal color gradients implying that the sensor is unaffected by the presence of the antisolvent and is exclusively dependent on the concentration of the API in the microfluidic device. Figure 65A suggests that this Pt-based screen-printed electrochemical sensor shows almost ideal behavior, further corroborating the choice of Pt as a suitable sensor candidate. Table 17 includes the maximum attainable supersaturation value and the anodic slopes for different antisolvent ratios. From Figure 65A and Table 17, the unknown supersaturation during the continuous-flow antisolvent crystallization can be calculated. First, the obtained anodic CV slope should be normalized according to the volumetric ratio of the antisolvent. Then using Figure 65A, the normalized supersaturation is calculated and converted to the actual supersaturation using Table 17.

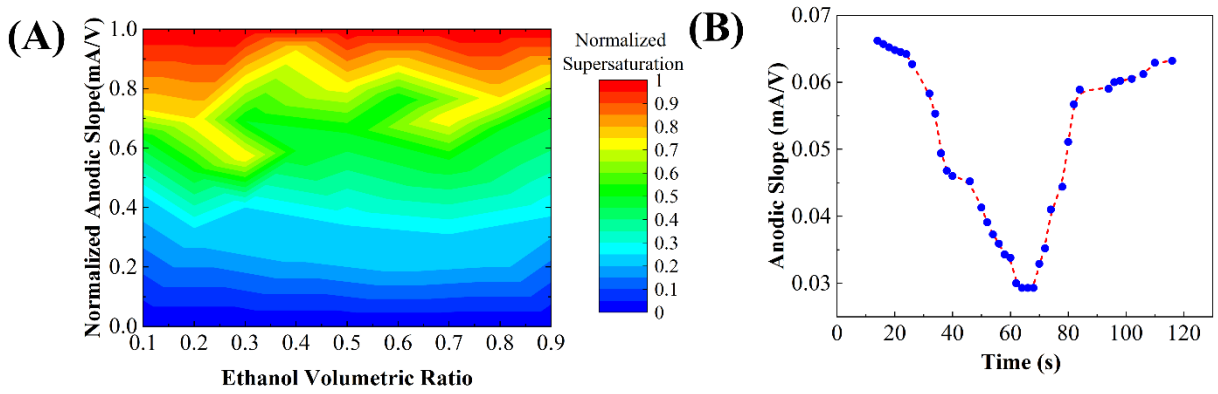

Figure 65: (A) Calibration heat map for calculating the supersaturation of antisolvent crystallization of L-histidine; (B) The change of the anodic slope vs. time for the case of supersaturation depletion when the continuous flow system is changed to batch.

6.4.3 Experimental Validation of the Screen-Printed Electrochemical Pt Sensor in the Sensor-Integrated Continuous-Flow Microfluidic Mixer

The screen-printed Pt electrochemical sensor with the provided calibration curve shown in Figure 65A was tested under two different circumstances to validate its accuracy.

In the first set of the validation analysis, four aqueous L-histidine solutions with various intermediate concentrations (i.e., L-histidine concentrations that were not used in calibration experiments) were prepared. First, the antisolvent crystallization experiments with a 50% volumetric antisolvent ratio were performed, and the anodic CV slopes were measured. Next, the measured anodic CV slopes were normalized with the maximum attainable CV slope obtained for a 50% volumetric antisolvent ratio. Finally, the normalized supersaturation values were obtained from Figure 65A and converted into the actual supersaturation. Table 18 shows the measured supersaturation, actual concentration, and calculated supersaturation from the solubility curve of L-Histidine for all four samples.

Table 18: The comparison of the measured supersaturation vs. the calculated supersaturation for the validation experiments of the sensor integrated continuous-flow microfluidic device.

Sample	Measured Supersaturation	Concentration [mol. L^{-1}]	Calculated Supersaturation	Error (%)
A	3.15	0.2150	3.14	0.2
B	2.37	0.1644	2.4	1.3
C	1.67	0.1138	1.66	0.3
D	1.3	0.0885	1.28	1.2

In the second validation experiment, the effect of the crystallized particles during the crystallization on the sensor was studied. The antisolvent crystallization of aqueous solution of L-histidine was performed for a 50% ratio of the antisolvent, and after the anodic CV slope became stable, the pumps were stopped. The change of the flow condition from continuous into batch resulted in the supersaturation depletion in the cylindrical zone, and therefore, the anodic CV slope increased again. The observed trend for the change of the anodic CV slopes proved that the integrated electrochemical sensor detects the dissolved L-histidine content, and the slopes can be correlated to calculate the supersaturation value. The change of the anodic CV slopes vs. time is shown in Figure 65B. Here, the anodic CV slopes decrease as the antisolvent and solvents get mixed inside the microfluidic mixer device and eventually attain a stable slope. As the pump is turned off, the supersaturation depletion happens inside the mixer, and the crystals inside the well will grow by consuming the dissolved L-histidine in the mother liquor. As the supersaturation deviates from the stable value, the anodic CV slopes increase as well. These validation experiments confirm the potential of the integrated electrochemical sensor for the detection of supersaturation.

6.4.4 ML Analysis and Supersaturation Prediction Model

ML models are created to predict supersaturation in the continuous-flow microfluidic mixer device. Such models are crucial for high-throughput screening of pharmaceutical compounds as a

robust ML model can predict supersaturation faster than an actual physical measurement. In this work, four different ML algorithms- neural networks (NN), support vector machine (SVM), random forest (RF), and gradient boosting (GB)- were trained for supervised learning to predict the supersaturation in the continuous-flow microfluidic mixer. Figure 66 shows the performance of each of these algorithms in predicting supersaturation.

The experimental datasets were given to each algorithm to train the models for supersaturation detection. The dataset included supersaturation value and anodic CV slopes for four different concentrations of L-histidine solutions (25%, 50%, 75%, and 100% of the saturated concentration at 25℃)) and ten antisolvent volumetric ratios (0.1 to 0.9). The change of the anodic CV slope measured between 0 and 0.5V was taken as a distinct observable parameter since the current in that range shows the most sensitivity toward the change in the feed conditions. The dataset was randomly split into 70-30% training and testing datasets, respectively. In Figure 66, the training dataset and test datasets are indicated with blue and red circles, respectively. The training dataset was used to train the ML algorithms, and the testing dataset was used to check the accuracy of the prediction of the ML algorithms.

Furthermore, to altogether remove the bias of the original dataset, a new dataset with eight different experiments with entirely different conditions from the original ones was created and tested in each of the ML algorithms. These data points are shown with green triangles in Figure 66. As can be seen from Figures 66A, 66B, and 66D, neural networks (NN), support vector machine (SVM), and gradient boosting (GB) show a good correlation between the actual and the predicted supersaturation values, while random forest (RF) delivers the least performance amongst all.

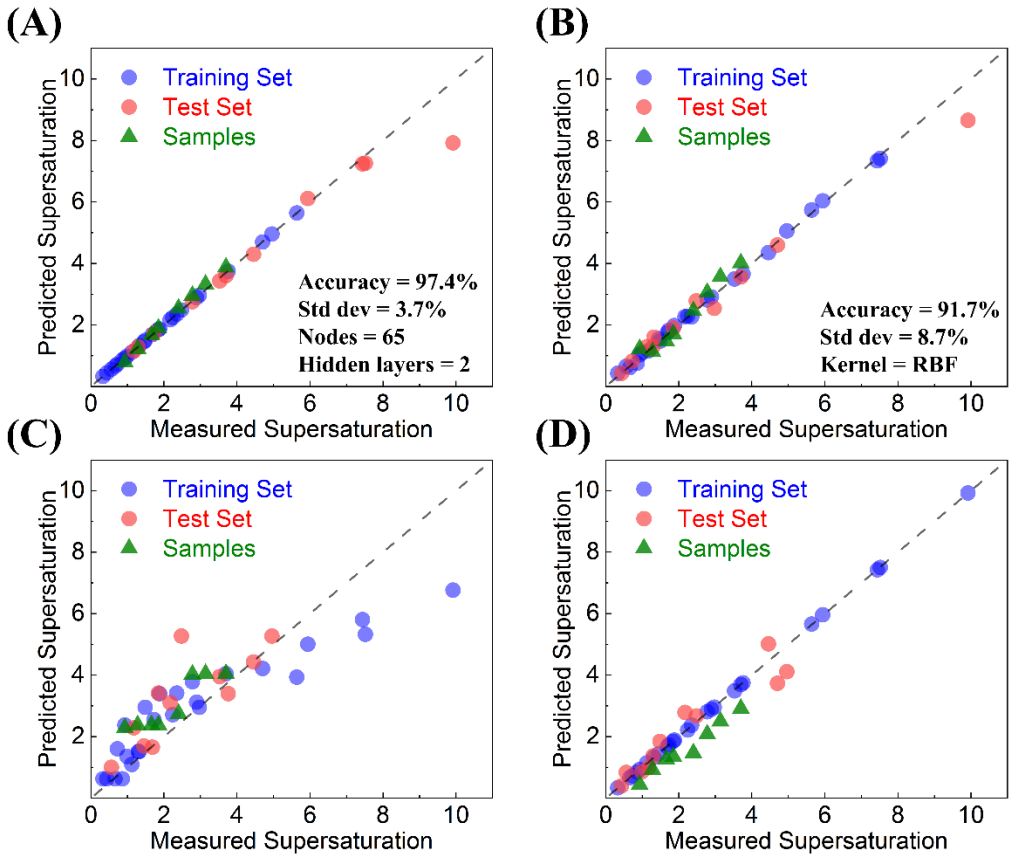

Figure 66: Performance of machine learning algorithms in predicting supersaturation of the antisolvent crystallization of L-histidine: (A) neural network, (B) support vector machine, (C) random forest, (D) gradient boosting.

In Table 19, the accuracy and standard deviation of each of the machine learning algorithms are summarized. The neural network algorithm had the highest accuracy (greater than 97 +/- 4%). Support vector machine and gradient boosting also showed more than 90% accuracy, but the standard deviation for these algorithms was too high, which indicated that these algorithms are not reliable for predicting the supersaturation of L-histidine.

Table 19: Comparison of the performance of ML algorithms for the supersaturation prediction in the continuous-flow microfluidic mixer device for antisolvent crystallization of L-histidine.

Algorithm	Accuracy (%)	Standard deviation (%)
Neural Network	97.425	3.682
Support Vector Machine	91.698	8.679
Random Forest	79.673	23.057
Gradient Boosting	90.784	8.037

The most optimized model of the neural network algorithm selected for the supersaturation prediction had two hidden layers (65 nodes each). This model showed an excellent prediction of supersaturation in the range of 0-8 but deviated from the norm at higher supersaturation greater than eight. Operating the continuous flow sensor integrated microfluidic mixer for higher is not feasible due to the high L-histidine crystallization rate inside the wells. At very high supersaturations, the microfluidic mixer is filled, and the channels are clogged with crystals. The crystals completely block the interface of the sensor with the mother liquor and prevent the sensor from further analysis. The results from ML support the reliability of the continuous flow sensor integrated microfluidic mixer to predict supersaturation during an antisolvent crystallization. Three out of four of the most common ML algorithms were able to predict the supersaturation with acceptable accuracy, which corroborates the robustness of this fast-response screen-printed electrochemical sensor-based microfluidic device.

6.5 Conclusion

The current process of marketing a new drug after the invention of an active pharmaceutical ingredient (API) molecule takes around ten years and costs billions of dollars. A significant portion of that decade is invested in process development, where companies screen different polymorphic forms of APIs and develop robust processes to manufacture the stable form with the acceptable physical properties to turn that into tablets. Commercial microtiter plates used for screening run into a problem due to depletion of supersaturation (driver for crystallization), which is the primary reason for setbacks during the scaleup and technology transfer to manufacturing API. Real-time monitoring is challenging but pivotal for data acquisition on crystal nucleation and growth. The invention of microfluidic devices with integrated sensors helps pharmaceutical companies comply with an FDA initiative to move from batch-based production to continuous manufacturing, spur advancements in drug production, and lower costs. The in-situ monitoring along with automated

microfluidic platforms are executed to regulate crystallization processes. Therefore, developing and integrating a nondestructive sensor with microfluidic devices in a continuous flow manner is of great importance. One of the most used techniques is the ATR-FTIR technique which continuously collects spectra during crystallization. These sensors have limited detection ranges and require a line of sight. Electrochemical sensors, however, can provide real-time data collection at high accuracy. The cost of fabrication is much lower for the electrochemical sensors, and they can be integrated within microfluidic systems quite easily.

In this study, an electrochemical sensor integrated continuous-flow microfluidic mixer is developed to measure the supersaturation during the antisolvent crystallization of L-histidine. The sensor is calibrated with different concentrations of an aqueous solution of L-histidine and ten different antisolvent volumetric ratios. The CV analysis was done for all the experiments, and the anodic CV slopes were recorded. The data were normalized for fixed volumetric ratios of antisolvent and presented as a heat-map. The data were then imported for a machine learning analysis, where four of the most used techniques were implemented to train a prediction model. NN, SVM, RF, and GB were tested for a different train set and test sets, and among all neural network prediction models showed the highest accuracy. From this prediction model, the supersaturation of an aqueous L-histidine solution with an unknown concentration is predicted.

VII. In-Line Detection of Liquid-Liquid Phase Separation Boundaries using a Turbidity-Sensor-Integrated Continuous-Flow Microfluidic Device

7.1 Introduction

Liquid-liquid phase separation (LLPS) or oiling out is the appearance of a second liquid phase prior to crystallization[110,111]. The formation of the second phase is due to the differences in component polarities, which results in a miscibility gap. Thermodynamically, phase separation occurs when the Gibbs free energy of mixture ($\Delta G_{mixture}$) is less than zero; however, in mixtures exhibiting LLPS, $\Delta G_{mixture}$ reaches a minimum value at two compositions where the phase separation occurs. These two compositions represent the binodal points of the mixture where each species has equal chemical potential in both phases[111]. Once reaching the binodal points, the system enters a metastable zone and has to overcome an energy barrier to initiate a new phase. When this energy barrier is overcome, the metastable zone ends as two compositions called spinodal points. Spinodal points mark the beginning of the unstable zone in which the mixture divides into two phases and crystals are formed. LLPS is most likely to be observed in the vicinity of the binodal points because detection of the spinodal points demands precise control on rapid changes in process conditions, which may not be feasible in a crystallization[112]. LLPS has several adverse effects, including a significant reduction in crystallization rate and formation of impurities due to aggregation[113-115].

Moreover, LLPS eliminates the possibility of altering the particle morphology[113] and size distribution[116]. Therefore, LLPS should be fully understood and prevented to avoid its negative consequences during scale-up manufacturing. Some of these consequences include the contamination of reactors, which can result in batch termination and material losses, or the sticking of the oil phase to the reactor, which results in demand for higher energy for agitation[116].

LLPS boundaries or binodal can be determined by monitoring the occurrence of the second liquid phase in a mixture using either the static light scattering methods or measuring the turbidity induced by the dispersed phase[117]. Various process analytical techniques (PATs), such as FBRM, PVM, turbidity, and ATR UV/vis, have been employed to detect the LLPS boundaries. An FBRM is a probe-based measurement that measures the changes in the particle counts or chord length distribution (CLD) that is determined by the number, size, and shape of particles. These probes are directly inserted into the crystallizer, eliminating the need for sample dilution and offering fast, online, and in-situ measurements. However, the direct immersion of probes into the crystallizer is challenging as the small particles accumulate on the probe of the FBRM and block the measurment[118-120]. The particle vision measurement (PVM) technique implements a high-resolution video microscope and multiple laser beams to light up the measurement area to show the crystals passing against the window[117]. Fiber-optic probes are more robust and cost-effective than FBRMs due to their simpler design. In situ video microscopy (such as particle vision and measurement (PVM) or Easy Viewer) is normally coupled with the aforementioned measuring tools. Similar to FBRM, the accumulation of the particles on the detection window is one of the shortcomings of the PVM technique. Consequently, it results in low-quality images and requires cleaning after every run, which is not ideal for high-throughput (HT) screening[121]. The attenuated total reflectance ultraviolet/visible (ATR UV/vis) spectroscopy technique measures the kinetics of the supersaturation and de-supersaturation through the occurrence of the transient wave in the slurry. Since the radiated wave does not interact with crystals, the measurement indicates the concentration of solutes[112]. Fiber optic turbidity probes can also be implemented to study LLPS by indicating the turbidity change in the solution due to the formation of the second liquid phase[122]. . In addition, fiber-optic probes are more robust and cost-effective than FBRMs due to their simpler design. In-situ video microscopy (such as PVM or Easy Viewer) is usually used in combination

with these measurement tools to improve the accuracy of measurements. Moving toward HT screening systems, continuous-flow microfluidic devices have shown great potentials for various crystallization applications such as antisolvent, cooling, or reactive crystallizations[123,124]. However, continuous-flow microfluidic devices have not been previously implemented for detecting the LLPS boundaries as the integration of the existing probes with the miniaturized devices is not feasible due to their size scale or the cost of fabrication.

On the other hand, integrating microfluidic devices with turbidity sensors such as fiber optics and photosensitive sensors is feasible as these sensors do not need to be immersed in the mixture. Over the past decade, continuous-flow microfluidic devices have been recognized for their potential for HT screening, resulting in their integration with different sensors and feedback control systems. In this study, an easy-to-adapt and affordable photosensitive turbidity sensor was developed and integrated into a novel continuous-flow microfluidic device for detecting the LLPS boundaries[41,61]. The turbidity sensor consists of a photodiode as the detector and an infrared LED light that provides the light source. The infrared LED and photodiode are used to create our turbidity sensor, which can measure turbidity indirectly[125]. The turbidity is determined by measuring the scattered light by droplets formed in the mixture and the amount of light absorbed by the emitter[126]. As the composition of the mixture reaches binodes, the mixture gets turbid, and the magnitude of the scattered light is changed. Despite the fast detection of the turbid solution, the binodes are reported at the steady-state condition when the mixture becomes homogeneous[122]. Besides being cost-effective, LLPS detection with this photosensitive turbidity sensor can be complemented by the addition of in-situ video microscopy and the placement of the continuous-flow microfluidic device under an optical microscope. Here we studied the LLPS boundaries for the ternary system of β-alanine-water-IPA at room temperature and β-alanine-water-ethanol at 50^{o}C in the turbidity-sensor-integrated microfluidic device[115,127].

7.2 Theoretical Methods

7.2.1 Design of the Turbidity-Sensor-Integrated Continuous-Flow Microfluidic Device

The 3D design of a novel continuous-flow microfluidic device was modified to integrate a photosensitive sensor. The photosensitive sensor included a light-dependent resistor (LDR) (see Figure 67A) and a light-emitting diode (LED) (see Figure 67C). The LED and LDR were placed on opposite sides of the mixture, facing each other through a clear path. Two small squares were cut on the opposing sides of the cylindrical mixing zone to create a clear path between the LED and LRD. The cut surfaces were then covered with a polycarbonate film using clear resin as the glue to allow light to pass through the micromixer and reach the detector. As shown in Figure 67B, two holders were separately printed for LED and LRD and attached to the polycarbonate film. The four inlets of the continuous-flow microfluidic device were located on the bottom of the device, and the outlet was kept perpendicular to the light path. Figure 67E shows the top view of the sensor-integrated continuous-flow microfluidic device with the directional arrows for the inlet and outlet streams.

7.2.2 Detection of the LLPS Boundaries using Turbidity-Sensor-Integrated Continuous-Flow Microfluidic Device

The turbidity of the solution is monitored over the different compositions of the mixture with the turbidity-sensor-integrated continuous-flow microfluidic device to determine the LLPS boundaries. The composition of the microfluidic device is varied by changing the ratio of flow rates of streams carrying solvent, antisolvent, and API solution. The four inlets of the microfluidic device included streams of the saturated β-alanine solution, pure solvent, and pure antisolvent. The total flow rate is maintained constant for all measurements, and the compositions in which the mixture became turbid were reported as the LLPS boundaries. The volumetric flow rates were

recorded, and the mass fraction of each component was calculated to plot the ternary phase diagram.

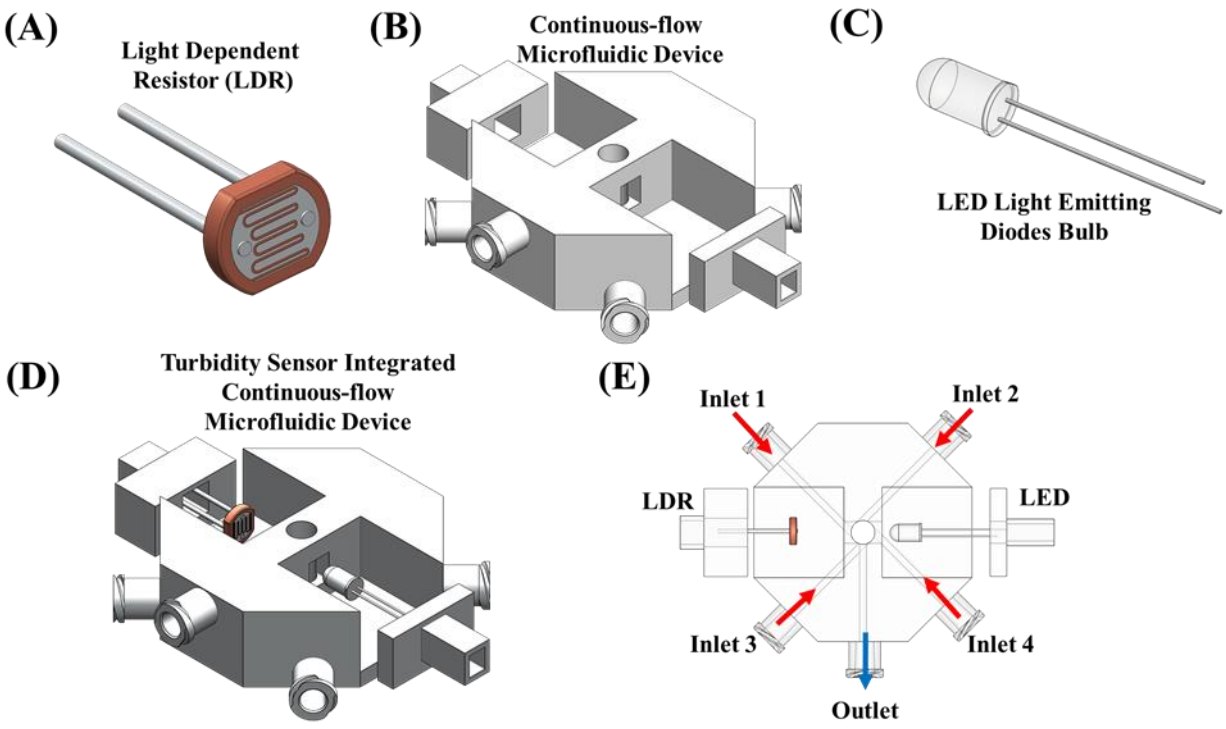

Figure 67:3D design of the (A) light-dependent resistor (LDR); (B) contiguous-flow microfluidic device, and (C) Light-emitting diodes bulb (LED); (D) Isometric view of the Turbidity sensor integrated continuous-flow microfluidic device, and (E) top view of the Turbidity sensor integrated continuous-flow microfluidic device.

7.3 Materials and Experimental Method

7.3.1 Materials

The stock β-alanine (Sigma-Aldrich, chemical purity ≥98%) was used to detect oiling out boundaries. Deionized water (Sigma-Aldrich, 18 MΩ cm), 2-propanol (IPA) (Sigma Aldrich), and ethanol (Sigma Aldrich) were used as the solvent.

7.3.2 Fabrication of the Turbidity Sensor Integrated with the Continuous-Flow Microfluidic Device

The 3D design of the sensor integrated continuous-flow microfluidic device shown in Figure 67 was designed in SolidWorks® (2020, Dassault Systems). A stereolithography (SLA) 3D printer (form 3, Formlabs Inc., USA) was used to print all parts. A clear FLGPCL02 resin activated by a

405 nm laser was used to 3D print optically clear microfluidic devices with 150 μm of lateral and 25 μm of axial resolutions. The 3D-printed parts were washed with IPA (90%, Sigma-Aldrich) bath for 60 minutes in the Form Wash (Formlabs Inc., USA) to remove the residues of the resin from the external surface. The generated support structures of the 3D-printed parts were loosened after the washing procedure, and their removal did not require much effort. All the interior channels of the 3D-printed device were washed separately by injecting IPA using a syringe followed by passing air from inlets to remove the uncured resins from all the channels. The careful selection of the layouts for prints on the 3D printer stage minimized the contact of the supports with top and bottom surfaces. However, if necessary, the optical transparency could be improved by wet sanding using 400 to 12000 grit pads followed by spray painting of resin. The top and bottom sides of the continuous-flow microfluidic device were kept open during the print and then sealed (see Figure 67). A thin layer of the resin is put around the opening, followed by a thin polycarbonate film. Then it was cured in the Form Cure (Formlabs Inc., USA) for around 10 minutes. On the sides, the openings were first covered by a thin polycarbonate film (same as top and bottom), and then the holders for LDR and LED were attached to the film using the curing technique. These openings allowed for the light to pass through the well and go through the photoresist.

7.3.3 Experimental Setup

Figure 68B shows the experimental setups used to detect the LLPS boundaries using the turbidity-sensor-integrated microfluidic device. In addition to using the turbidity sensor for detecting the LLPS boundaries, an optical microscope (Olympus BX53M, Olympus America Inc.) was also used in parallel to enable video microscopy measurements and observe the formation of oil droplets in the mixer. One dual-channel (NE-4000, New Era Pump System Inc.) and two single-channel programmed syringe pumps (NE-1000, New Era Pump System Inc.) were used to pump

the solutions into the microfluidic device. For all measurements at higher temperatures, the entering streams were heated using syringe heating pads and a heater. The foam protection wraps were also used to insulate the tubing that connects the syringes to the inlets of the microfluidic device. Additionally, a heating jacket was provided around the mixing zone to maintain the temperature of the mixer.

Operational Procedure of the Continuous-Flow Microfluidic Device: According to Figure 2A, the four streams entering the microfluidic device are two streams of a saturated solution of β-alanine (Q_2), one stream of the pure solvent (water) (Q_3), and one stream of the pure antisolvent (IPA) (Q_1). By mixing the pure water and IPA, gas bubbles arise in the mixture[128], which creates a partially turbid solution. To avoid this issue and prevent the false detection of the LLPS boundaries, pure water and IPA were pre-mixed and degassed at ratios of 90:10 and 10:90 and then used as the solvent and antisolvent streams. The total flow rate in the mixture is maintained at 1 mL.min^{-1} and Q_1 is changed from 0 to 0.8. The experiments started with the lowest value for the Q_1 (Q_1= 0 mL.min^{-1}) and highest value of Q_2 (Q_1= 1 mL.min^{-1}). Since the total flow rate is maintained at 1 mL.min^{-1}, Q_3 was 0 mL.min^{-1}. From here, Q_1 was increased with a step size of 0.1 mL.min^{-1}. At every value of Q_1, while Q_2 and Q_3 were decreased and increased respectively to detect the compositions in which the solution became turbid. The compositions where the oil droplets appeared within the micromixer were considered as the LLPS boundaries. Each composition that resulted in a turbid solution was given a five-minute wait time to ensure the system was at the steady-state condition.

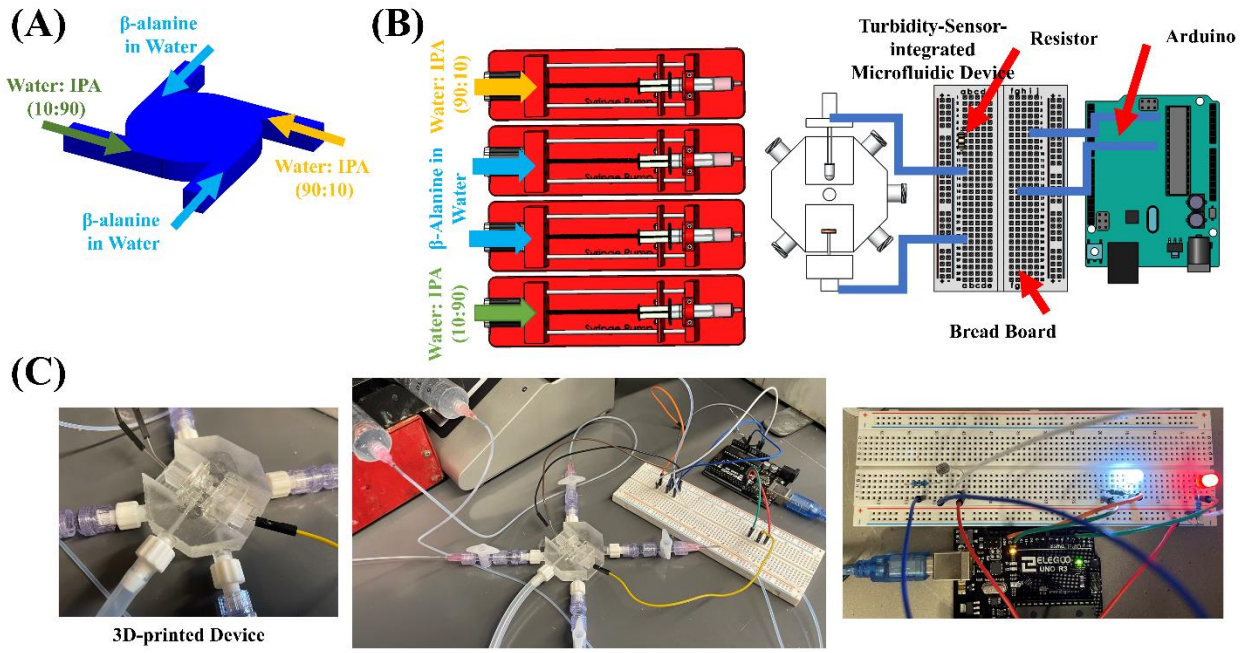

Figure 68: (A) 3D sketch of the microfluidic mixer with labeled entering streams; (B) 3D-printed sensor integrated microfluidic device; (C) 3D sketch of the experimental setup of the turbidity sensor integrated microfluidic device for LLPS measurement.

Detection of Oiling Out Boundaries using Turbidity Sensors and in-situ Video Microscopy:

The turbidity sensor was built on an open-source microcontroller board-Arduino, Uno. The Arduino board has 14 digital input/output pins and six analog input pins. One digital and one analog pin were utilized to build the sensor. An LED in series with a 220 resistor was connected to a digital input pin of the Arduino board that serves as a constant source of light for the sensor. The photoresistor in series with a ten resistor was connected to an analog pin that converted the voltage drop across the photoresistor into integers between 0 and 1023. The sensor was programmed with the Arduino Integrated Development Environment (IDE) using a C-based program code to show the integer output of the signal received by the photoresistor. The photoresistor was placed directly in the light path of the LED to maximize the signal-to-noise ratio. The signal received by the photoresistor was monitored with a data transfer rate of 9600 bits per second where the clear solution in the microfluidic device would show a steady high response of value >500, and any introduction of turbidity in the path between the LED and the photoresistor

would reduce the response to a value <250. The in-situ video microscopy method for detecting LLPS was performed under an optical microscope ((Olympus BX53M, Olympus America Inc.). A 5X lens was used to observe a larger portion of the mixing well under the optical microscope and record the formation of oil droplets.

7.4 Results and Discussion

7.4.1 Calibration of the Turbidity Sensor Calibration for Detection of LLPS in β-Alanine−Water−Isopropanol System

Five different volumetric ratios of IPA (x) were chosen to calibrate the photosensitive sensor. The range of signal change was recorded for $0.1 < x < 0.9$ where the saturated solution of β-alanine, IPA: water (x:1-x), and IPA: water (1-x:x) were pumped into the sensor integrated device[115,129,130]. The total flow rate of the device was maintained constant, and Q_1 and Q_2 were kept equal. Then the flow rate of the β-alanine solution (Q_2) was gradually increased, and the response of the sensor was recorded. At a certain composition, the solution was turbid the signal was changed. The measurements were repeated for different x equal to 0.1, 0.25, 0.5, 0.75, and 0.9, as shown in Figure 69A. From here, 300 to 500 was selected as the optimum detection range and implemented in the Arduino code.

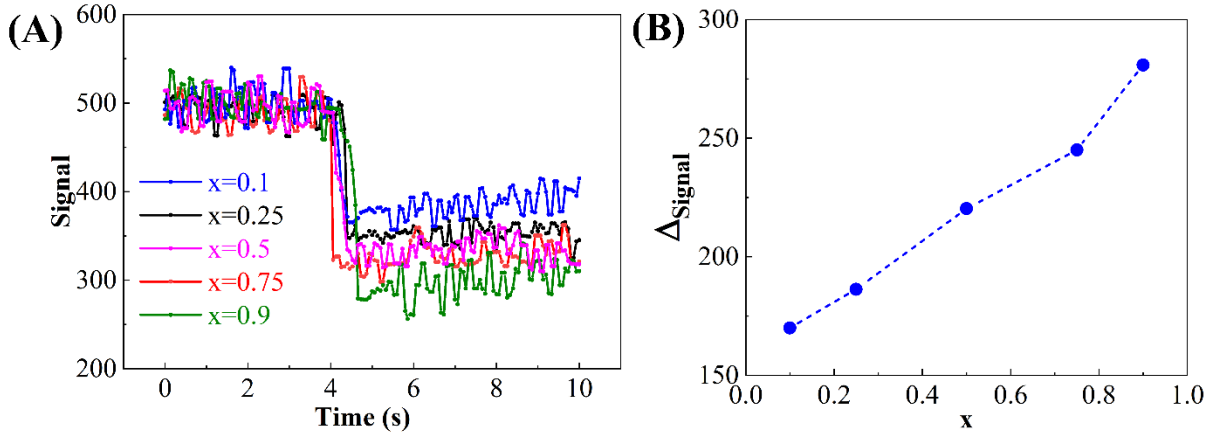

Figure 69: Detection of oil droplets within the microfluidic mixer using the turbidity sensor for different volumetric ratios of IPA: (A) signal vs time, and (B) change of the sognal vs volumetric ratios of IPA.

7.4.2 Ternary Phase Diagram and LLPS Boundary of β-Alanine−Water−IPA at 25℃

Figure 70 shows the LLPS boundaries on the ternary phase diagram of the β-alanine-water-isopropanol system. The LLPS boundaries were detected using both turbidity sensor and optical microscopy techniques. As shown in Figure 70, the data points from both methods match the reported values in the literature, yet the turbidity-sensor-integrated continuous-flow device predicted the oiling out boundary more precisely and confidently. The final values for the selected flow rates are listed in Table 20. These flow rates were used to calculate the mass fraction of β-alanine, water, and Isopropanol. For example, the flow rate of β-alanine was set at 0.1 $mL.min^{-1}$. At this flow rate, Q_3 was initially set at zero, and Q_2 was at 0.9 $mL.min^{-1}$. At this composition, the solution remained clear; therefore, Q_3 was gradually increased at a point where the mixture became turbid. The flow rates Q_2 and Q_3 at this were 0.88 and 0.02 $mL.min^{-1}$ accordingly. These flow rates were then used to calculate the mass fraction of each component in the mixture (see Table 20) Figure 70 shows the detected LLPS boundaries for the two measurement techniques and the reported data from the literature[131]. The orange circles show the data points obtained from the turbidity-sensor-integrated continuous-flow microfluidic device, and the blue circles show data points obtained from the video microscopy technique. The comparison between the results from both methods proves the reliability of the turbidity-sensor-integrated microfluidic device for detecting the LLPS boundaries. Implementation of the sensor will significantly ease the measurement and enable the integration of feedback control systems.

Table 20:Operational Flow-conditions for the LLPS boundary using the turbidity-sensor-integrated continuous-flow microfluidic device.

Q_3 $(mL.min^{-1})$	Q_2 $(mL.min^{-1})$	Q_1 $(mL.min^{-1})$	X_{Water}	$X_{\beta-Alanine}$	X_{IPA}
0.11	0.87	0.02	0.5369	0.3917	0.0715
0.21	0.55	0.24	0.5738	0.2649	0.1613
0.32	0.34	0.37	0.5797	0.1680	0.2524
0.41	0.25	0.34	0.5359	0.1313	0.3328
0.51	0.16	0.29	0.4732	0.0909	0.4359
0.61	0.12	0.27	0.4271	0.0670	0.5059
0.69	0.07	*0.24*	0.3789	0.0401	0.5810
0.83	0.04	0.13	0.2680	0.0237	0.7082

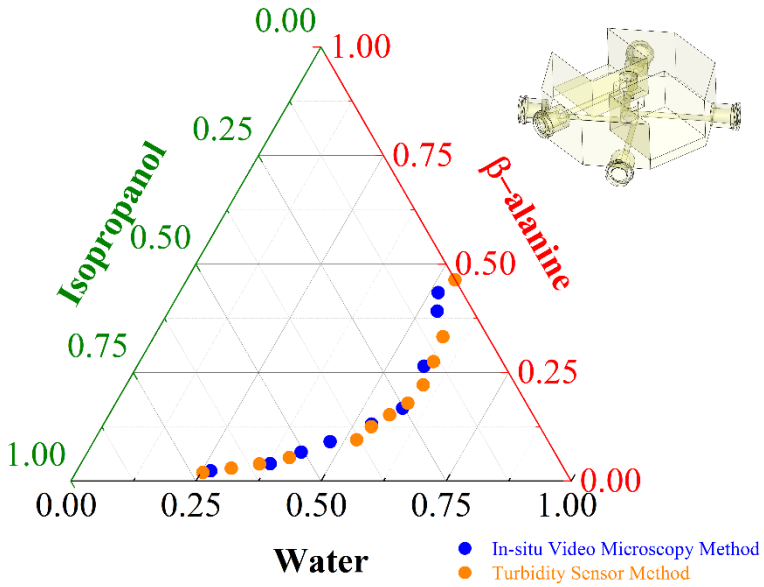

Figure 70: Ternary phase diagram showing LLPS boundaries β-alanine, water, and IPA system. The axes represent the mass fraction of β-alanine, water, and IPA, respectively. In this diagram, the liquid-liquid phase boundary is shown for the two detection methods. The orange circles are data points obtained from the turbidity-sensor-integrated continuous-flow microfluidic device, and the blue circles show the data points obtained from the in-situ video microscopy method.

7.4.3 Ternary Phase Diagram and LLPS Boundary of β-Alanine−Water−Ethanol at 50℃

The turbidity-sensor-integrated continuous-flow microfluidic device was next used to detect the LLPS boundary at 50℃. for the β-alanine-water-ethanol[132]. Here, a heating jacket was added around the mixing zone to maintain the temperature of the entering streams at 50℃. The entering

solutions were pre-heated using syringe heaters and heating pads. Additionally, all tubes and connections were covered using isolation foams. The same procedure explained in section 7.4.2 was repeated for the β-alanine-water-ethanol, and the flow rates where the sensor detected the turbid solutions were recorded. The flow rates were then used to calculate the mass fractions of each component and plot the LLPS boundaries. Figure 71 shows the LLPS boundaries for the ternary system of β-alanine-water-ethanol at 50℃.

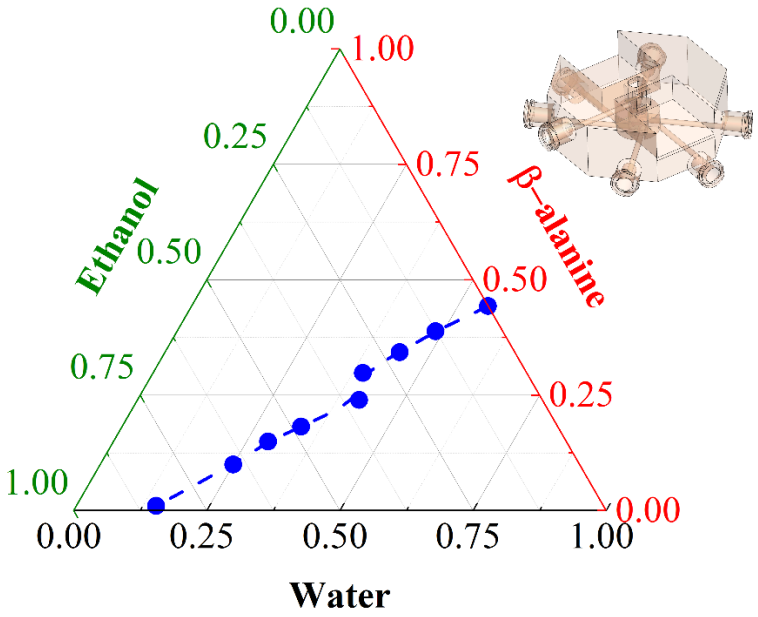

Figure 71: Ternary phase diagram showing LLPS boundaries β-alanine, water, and ethanol system. The liquid-liquid phase boundary was obtained from the turbidity-sensor-integrated continuous-flow microfluidic device.

7.5 Conclusion

Liquid-liquid phase separation (LLPS) occurs in many pharmaceutical molecules, fine chemicals, and proteins, where a dispersed phase and a continuous phase are formed from a single-phase solution. LLPS is an unwanted phenomenon that negatively affects crystal purity and complicates scale-up processes. The detection of LLPS boundaries allows crystallization procedures to be designed more precisely. The LLPS boundaries are detected using different PATs such as FBRM,

fiber optics, and in-situ video microscopy. However, detecting the LLPS boundaries is limited in microscale systems due to the lack of potential detection tools integrated with these microscale systems. While most FBRM probes can not be easily integrated within the microfluidic systems, fiber optics and other turbidity sensors are better options for integration with microfluidic devices. Here we illustrate the design of a photosensitive turbidity sensor integrated with a continuous-flow microfluidic device to detect the LLPS boundaries. The turbidity sensor includes a photodiode as the detector (LRD) and an infrared light (LED) as the light source. In this study, the turbidity-sensor-integrated continuous-flow microfluidic device was evaluated to detect the LLPS boundaries for the ternary system of β-alanine-water and IPA at room temperature and β-alanine in water-ethanol at 50℃.

VIII. PATTERNED-SURFACES MICROFLUIDIC DEVICES FOR RAPID SCREENING OF METAL-ORGANIC FRAMEWORKS YIELDS INSIGHTS INTO POLYMORPHISM AND NON-MONOTONIC GROWTH

8.1 Introduction

Fundamental studies and bottom-up synthesis of metal-organic frameworks (MOFs) are increasingly pursued in materials science and engineering[133-135]. MOFs are a class of chemical compounds that form networks of metal nodes and organic linkers[136]. As a result of the unique repeated pattern of this unit cell, MOFs have shown outstanding properties that make them suitable for various applications. Co-existing crystallinity and high porosity of MOFs are primary reasons for the increasing attention toward this class of materials[137]. Another critical feature of these porous structures is their high stability and flexibility in designing new structures[138]. So far, thousands of MOFs have been designed and synthesized for different applications[139], such as gas storage[140-142], separation[143-146], adsorption[147-149], and catalytic application[150,151].

Moreover, MOFs have been used as sensors[152-155], LEDs[156], and conductive magnets because of the existing metal nodes in their structures[157-160]. Their high porosity also has made them very suitable candidates for drug delivery applications. In addition, multiple studies demonstrate their high effectiveness in solving a wide range of industrial and environmental problems involving capturing and treating liquid effluents and greenhouse gas emissions[148,161].

MOFs are synthesized by solvent-mediated synthesis, electrochemical depositions[162-164], ball milling[165,166], and sonochemical techniques[167,168]. Hydro/solvothermal synthesis is the most conventional route for most of the discovered MOFs[169-171]. However, electrochemical deposition, ultrasonic, and microwave synthesis are preferred due to their higher effectiveness and yield.

Most of these experimental syntheses are employed in batch operational mode, which is straightforward for early-stage exploration. However, despite facilitating the discovery of the novel structures and compositions of MOFs, batch operations suffer from significant drawbacks such as low energy efficiency, lack of flexibility for in-situ monitoring, and tuneability of the final product. In addition, batch syntheses demand harsh experimental conditions and extensive synthesis times while not providing a reliable kinetic and thermodynamic understanding of the product formation and growth rate.

Acquiring a comprehensive understanding of nucleation and growth kinetics is advantageous in broadening synthesis strategies like 2D film formation and cross-linking polymers[172,173] and understanding the influence of the orientation of metal ligands and organic linkers on the final size and morphology. A controlled synthesis approach of MOFs allows to tune in their physical and chemical properties and maximize their applicability toward their highest potential. Continuous-flow synthesis benefits from enhanced mass and heat transfer and allows for real-time monitoring and mechanistic studies. They have shown promising results for fine-tuning crystal size and morphology, self-assembly of higher-ordered structures, and integrating control-feedback systems. As a result of the inherent difficulty in the batch synthesis of MOFs at pilot scales, continuous processing strategies integrated with heaters and fluid control elements are implemented for the pilot-scale production. Before scaling up a process to the pilot scale, it is crucial to optimize the processing conditions to obtain the desired product attributes. The current screening procedure of a single processing condition can take up to three days of reaction and post-processing procedures such as washing and drying. Some of the extensively studied MOFs such as MIL-53, HKUST-1, ZIF-8, and UIO-66 have very high processing times (48-72 hours) in batch during the initial period of the discovery phase. Microreactors are significant assets for screening in the early stages of development and optimizing the synthesis conditions. The high rates of heat

and mass transfer in the small reaction volumes of the micro-reactors enable easy manipulation and rapid HT screening of the reaction parameters and allow for studying their influences on the crystal attributes[174-177]. However, the crystallization mechanism and its effect on the properties of MOFs are not yet fully elucidated, but the interface is becoming crucial in controlling the process[174].

De Vos and coworkers showed that MOFs synthesis and design could be performed in a droplet-based microfluidic device. They developed a T-junction microreactor to create droplets of an aqueous solution containing metal ions and organic ligands, resulting in a spherical water-oil interface over the droplets. Using organic and inorganic precursors with different solubilities induced a self-completing growth mechanism, leading to the formation of hollow spheres and a layer of MOF over the interface[178]. The droplet-based microfluidic device used in another study by Kim et al. demonstrated the continuous and ultrafast synthesis of MOF crystals and composites. Optical micrographs of the MOF droplets revealed the rapid crystallization in the continuous-flow reactor due to enhanced mass and heat transfer[179].

Walton and Lester et al. utilized a counter-flow reactor to mix MOF precursors with high-temperature water flow right before the inlet. By mixing the two flows directly, the temperature rose rapidly, resulting in the rapid growth of MOFs in a few seconds.

Furthermore, the concentration of the precursor solutions and the hot water temperature could be adjusted to control MOFs crystal size[174,180]. Developing continuous-flow reactors that are more efficient at mixing requires innovative concepts and tools. In addition, a practical, HT, continuous-flow production of ordered porous materials requires new scaling-up strategies that consider both transport characteristics and crystallization characteristics.

This study aims to develop a continuous-flow synthesis approach that eliminates the need for harsh experimental conditions and provides kinetics of MOF synthesis under controlled conditions.

Here, a 3D-printed patterned-surface microfluidic mixer device is developed for in-situ measurement of morphology and growth, coupled with time-resolved Fourier transformed infrared (FT-IR) spectroscopy to provide a fundamental understanding of the reaction kinetics. Implementation of this novel 3D-printed patterned microfluidic device allows for controlling the reaction conditions while preventing the decay of the concentration of reactants during nucleation and growth. In this study, the previously developed continuous-flow microfluidic mixer device was modified to include a patterned surface at the bottom to compensate for the low settling velocities of the nano-sized crystals[41]. In general, nano-sized patterns are known to enhance nucleation and decrease the induction time. However, the implemented patterned surfaces in this study had 100 and 200 μm diameters and decreased the induction time due to an increase in surface area[181]. Additionally, the higher surface area of the implemented patterned surface increases the heterogeneous nucleation and enhances the capture of HKUST-1 crystals within the microfluidic mixer device. Here, we studied the effect of the solvent system and pH on the reactive crystallization of archetypical HKUST-1 MOF[182,183].

The proposed continuous-flow setup was placed under an optical microscope, allowing for in-situ measurements of the growth kinetics. However, the synthesis procedure can result in nano-sized HKUST-1 crystals that are below the resolution of the optical microscope. Also, the rapid nucleation of new particles can make the solution inside the microfluidic mixer device opaque and hard to image. To resolve these potential problems, we developed a comprehensive study for the growth measurements of HKUST-1 crystals. Initially, a time-resolved FT-IR analysis was performed to discover a region of the residence time where nucleation was minimized, and the growth of the crystals was favored. Then, the selected residence time was employed for measuring the growth of seeded HKUST-1 crystals in the patterned microfluidic mixer. These results demonstrated effective strategies that are essential and transferable for screening MOFs and

similar classes of compounds.

8.2 Theoretical Methods and Screening Strategy

8.2.1 CFD Simulation of the Patterned Microfluidic Mixer Devices

The patterned surfaces were coupled with a recently developed microfluidic mixer device[41,61] to effectively screen the influence of the reaction parameters on crystal attributes such as morphology, polymorph, and size distribution. The patterns increase the available surface area for the reaction and surface roughness and increase the density of captured crystals[181]. Despite their advantages, patterned surfaces can negatively affect the mixing efficiency if the aspect ratio of the pattern height to the mixer diameter is large. Computational modeling of the patterned-surface microfluidic mixer device helps to understand the effect of patterns on the mixing efficiency. The influence of the above-mentioned patterned surfaces on homogenous mixing was evaluated by calculating the velocity and concentration profile in the micromixer. Here, the effect of patterned surfaces on mixing efficiency was assessed for patterns with different sizes. The dimensions of the micromixers with patterned surfaces are provided in Figure 74. The CAD file for the 3D design of the device, shown in Figure 73A, was imported in COMSOL Multiphysics® and meshed using a free tetrahedral mesh of element size 0.207 to 1.15 mm and a curvature factor of 0.6. The maximum element growth rate and resolution of the narrow regions were set at 1.5 and 0.5, respectively. Navier-Stokes equation was coupled with mass balance equation and solved to measure the mixing efficiency vs. the height of the mixer for different patterns.

The solute (e.g., metal-ligand and linker) was not considered in the simulation because its solubility is typically at least three orders of magnitude smaller than solvent and has a negligible effect on the mixing profile.

8.2.1.1 Laminar Flow Module: Equations and Boundary Conditions

The laminar flow module of COMSOL was used to calculate the velocity profile in the microfluidic mixer. The time-dependent Navier-Stokes equation solved is described as follows:

$$\rho \frac{\partial u}{\partial t} + \rho(u.\nabla)u = \nabla.[-p.I + \mu(\nabla u + (\nabla u)^T) + F \quad (50)$$

Where ρ and μ are density and the viscosity of water which is assumed to be incompressible.

Here the selected boundary conditions for the patterned surface microfluidic device are shown below. Figure 72 shows the isometric view of the imported 3D file of the microfluidic mixer device in the COMOSL Multiphysics for the simulation. In Figure 72, the assigned boundary conditions for this system are shown and listed as:

Boundary Conditions:

- Inlet $_{1, Mixer}$ = Inlet $_{2, Mixer}$: Q_{Mixer} = 0.5 mL.min^{-1};
- Outlet $_{Mixer}$: P = 1 atm;

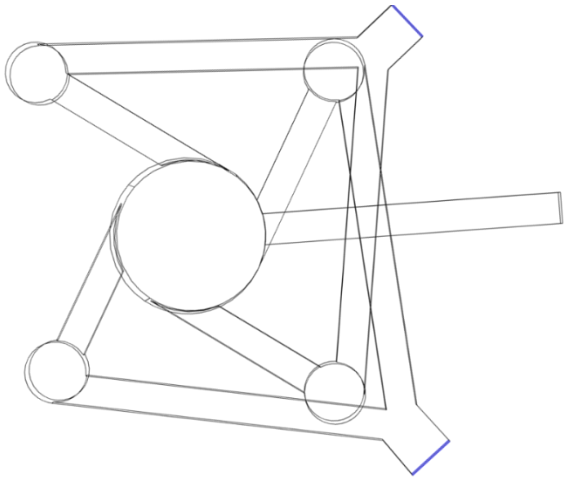

Figure 72: The top view of the patterned-surface microfluidic mixer device with the assigned boundary conditions for the mixer. (Patterns are located on the bottom surface)

8.2.1.2 Transport of Diluted Species Module: Equations and Boundary Conditions

The transport of the diluted species module is used to calculate the concentration profile in the microfluidic mixer. The time-dependent continuity equation solved is described as follows:

$$\rho \frac{\partial c_i}{\partial t} + \nabla.(-\mathrm{D_i}\nabla \mathrm{c_i}) + u.\nabla \mathrm{c_i} = \mathrm{R_i} \quad (51)$$

which includes both convection and diffusion for the transport mechanisms. Here ρ is the density, and u is the velocity of the fluid and comes from the laminar flow module. These two modules are coupled together, and the velocity profile is directly substituted into the continuity equation. The assigned boundary conditions for this model are listed below:

Boundary Conditions:

- Inlet $_{1,\ \mathrm{Mixer}}$: $c_i = c_{0,i} = 0$ mol.m^{-3}
- Inlet $_{2,\ \mathrm{Mixer}}$: $c_i = c_{0,i} = 1$ mol.m^{-3}
- Outlet $_{\mathrm{Mixer}}$: $n.D_i \nabla c_i = 0$

8.2.1.3 Model Parameters of the COMSOL Simulations

This study simulates a coupled analysis of the laminar flow module and mass transfer in diluted species to evaluate the velocity, pressure, and concentration profile inside the patterned surface microfluidic mixer. The 3D model for simulations was imported into the model from a SolidWorks design. The design was further simplified by eliminating the sharp edges and smoothening the surfaces to enhance the mesh quality. The free tetrahedral mesh was selected for the models. The tetrahedral mesh was selected for this study, and the details are provided in the following part:

- Maximum Element Size $= 1.15$ mm
- Minimum Element Size $= 0.207$ mm
- Maximum Element Growth Rate $= 1.5$
- Curvature Factor $= 0.6$
- Resolution of Narrow Region $= 0.5$

The coupled equations of the Navier-Stokes and mass balance were solved in the stationary solver using the “PARDISO” solver. The residual tolerance was set to 0.01 with 100 iterations and left

preconditioning. Newton was selected as the non-linear method with a damping factor of 0.1 and tolerance as the termination technique. The relative tolerance was also kept at 0.001. The temperature-dependent viscosity and density of the water were considered in the model.

8.2.1.4 Area Enhancement Factor for the Patterned Surface Microfluidic Devices

The presence of the patterns on the bottom side of the device increases the existing surface area for the heterogeneous reaction. Here the enhanced area is calculated and divided by the area of the bottom surface when no pattern exists. This ratio is called Area Enhancement Factor and is measured for all six patterns. Here $N_{Pattern}$ is the total number of patterns.

$$Area\ Enhancment\ Factor = F_{AE} = \frac{N_{Pattern} \times (\pi D_{Pattern} L + 2\frac{\pi D_{Mixer}^2}{4})}{\frac{\pi D_{Mixer}^2}{4}} \quad (52)$$

In Table 21, we have listed the area enhancement factor for all six patterns.

Table 21: Area Enhancement factor for all six patterned surfaces

Pattern Shape	Inscribed Circle Diameter (mm)	F_{AE}
Circular	0.1	1.6
Circular	0.2	1.1
Squared	0.1	1.9
Squared	0.2	1.3
Hexagonal	0.1	1.9
Hexagonal	0.2	1.3

8.2.2 Experimental Evaluation of the Effect of Solvents and pH on Polymorphism and Size of HKUST-1 Crystals

Precise control of the size distribution of MOFs maximizes their functionality. MOFs had shown enhanced CO_2 reduction and adsorption properties when the crystals had narrow size distributions. Furthermore, continuous-flow synthesis provides a significant hold on controlled nucleation and

growth. Therefore, the primary focuses of this study were enabling continuous-flow synthesis of HKUST-1 for effective control of the morphology, size distribution, and growth kinetics.

In MOFs synthesis, the selection of solvent systems is a major concern since varying solvents change the morphology and particle size distribution of the final product. Furthermore, the coordination of metal ligands and organic linkers is under the direct or indirect influence of the solvent system[184]. The solvent can exist within the metal ions and organic linker network, or it can appear as a guest molecule within the final lattice structure of the MOFs. In this study, we selected two solvent systems for the synthesis of HKUST-1 crystals. The first system had ethanol as the solvent for the metal-ligand (copper nitrate) and organic linker (trimesic acid, TA), while for the second solvent system, copper nitrate was dissolved in the DI water. The effect of solvent selection on the final morphology, size, and uniformity was compared for both solvent matrices.

Another experimental factor that affects the morphology and size distribution of the MOFs is the pH. In MOFs synthesis, the extent of deprotonation of the organic ligand or generation of the OH- ligand due to a pH change affects the reaction[184-186]. The change in the pH increases the connectivity of the polycarboxylate ligand to the metal ion and favors the reaction. The effect of pH on the crystal size and dimensionality was studied using acetic acid and pyridine as the acidic and basic modulators, respectively.

Table 22: Details for the precursor solutions for the effect of the solvent experiments.

Sample	Cu/TA (mol)	Solvents
A	1.5	Both solvents Ethanol
B	1.5	Ethanol: Water (0.3:1)

Experimental details of the pH variation studies using acidic and basic modulators are provided in Table 23. In the final study, a comprehensive analysis was performed to obtain kinetic data and measure the non-monotonic growth rate of HKUST-1 crystals.

Table 23: Details for the precursor solutions for the effect of the pH.

Sample	Cu/TA (mol)	Solvents	Modulator
Acidic	1.5	Both solvents Ethanol	Acetic Acid
Neutral	1.5	Both solvents Ethanol	-
Basic	1.5	Both solvents Ethanol	Pyridine

8.2.3 Understanding the Growth Kinetics of HKUST-1 Crystals

The growth kinetics of HKUST-1 crystals was studied using time-resolved FT-IR and in-situ optical microscopy. The importance of residence times in each performed study is critical in determining the optimal conditions for controlled synthesis. The precursor solutions were initially reacted in a tubular flow reactor at different residence times, and the spectra of the reacted solutions were recorded over time. Different intensities of peaks corresponding to the reactants and the product provided an understanding of the rate of reactant consumption and product formation. An ideal residence time range where the nucleation was not detected was obtained through time-resolved FT-IR. These conditions were observed to allow crystal growth but not initiate nucleation. Subsequently, the continuous-flow growth measurements were performed using a microfluidic mixer device connected to the syringe pump and placed under an optical microscope. HKUST-1 crystals were attached to the bottom surface of the microfluidic mixer and exposed to precursor solutions at different residence times. Snapshots of crystals were captured, and the growth rates were measured accordingly.

8.3 Materials and Experimental Methods

8.3.1 Materials

Copper (II) nitrate trihydrate (Sigma-Aldrich, puriss. p.a., 99-104%) and benzene-1,3,5-tricarboxylic acid known as trimesic acid (TA) (Sigma-Aldrich, chemical purity~ 95%) were used for the continuous-flow reactive crystallization of HKUST-1. The selected solvents for reactive

crystallization studies were deionized water (Sigma-Aldrich, 18 MΩ cm), ethyl alcohol (Sigma-Aldrich, 200 proof, ACS reagent, ≥99.5%), and acetic acid (Sigma-Aldrich, glacial, Reagent Plus®, ≥99%). All these materials were used without further purification.

8.3.2 Fabrication of the Patterned-Surface Microfluidic Mixer Device

The 3D design of the patterned-surface microfluidic mixer device, shown in Figure 73A, is designed in SolidWorks® (2020, Dassault Systems). These patterned-surface microfluidic mixer devices were fabricated using 3D printing technology. The patterned surfaces were located on the bottom of the microfluidic mixer devices and consisted of the extruded boss circular, square, or hexagons shapes with a diameter of 100 to 200 μm. The microfluidic devices in the previous studies were fabricated using Form 3 (Formlabs Inc, SLA 3D printer). However, these small patterns were not captured with a Form 3 3D printer and required an ultra-high-resolution 3D printer. Therefore, the devices without patterns were 3D-printed on a Form 3 printer. The patterns were printed separately on a 10 m series printer of the Boston Microfluidic Fabrication (BMF). The ten series 3D printer has ultra-high resolutions and can precisely print these small patterns. For fabricating the microfluidic mixer device without patterns, the clear FLGPCL02 resin activated by 405 nm laser to 3D print optically clear microfluidic mixer devices with 150 μm of lateral and 25 μm of axial resolutions. The 3D-printed devices are washed with isopropyl alcohol (IPA) (90%, Sigma-Aldrich) bath for 20 minutes in the Form Wash (Formlabs Inc., USA) to remove the residues of the resin from the external surface.

The interior channels of the 3D-printed devices were thoroughly washed by injection of IPA with a syringe to ensure complete removal of the uncured resins. The top and bottom surfaces of the 3D-printed device might need smoothing steps if the layout of the supports is not carefully selected. In this case, wet sanding using 400 to 12000 grit pads followed by spray painting of resin is suggested. The 3D-printed patterns were printed using HTL (BMF Inc) resin, a high-performance

engineering material. These patterns were attached to the microfluidic mixer devices using clear FLGPCL02 resin and curing it in the Form Cure. (Formlabs Inc., USA). The top opening of the patterned microfluidic mixer devices was sealed with polycarbonate films for optical clarity to image crystals under the microscope. The fabricated patterned microfluidic mixer device is shown in Figure 73C.

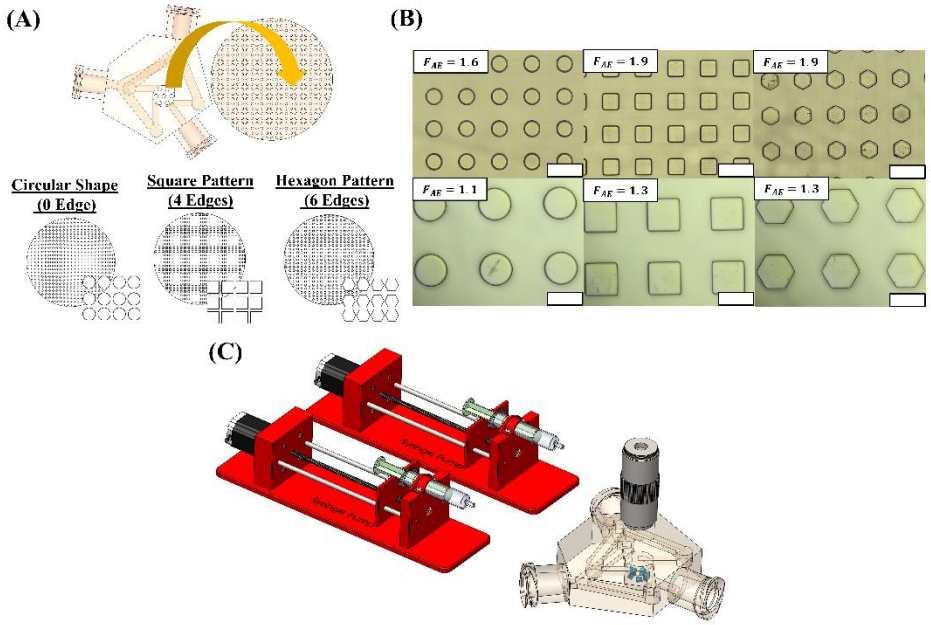

Figure 73: (A) Patterned-surface microfluidic mixer device with three different types of patterns: circular, square, and hexagonal shapes; (B) Optical images of the patterned surfaces and their area enhancement factor (F_{AE}); (C) Experimental setup for the reactive crystallization and growth rate measurement of HKUST-1.

The 3D design and details of measurements of these patterns are provided in Figure 74.

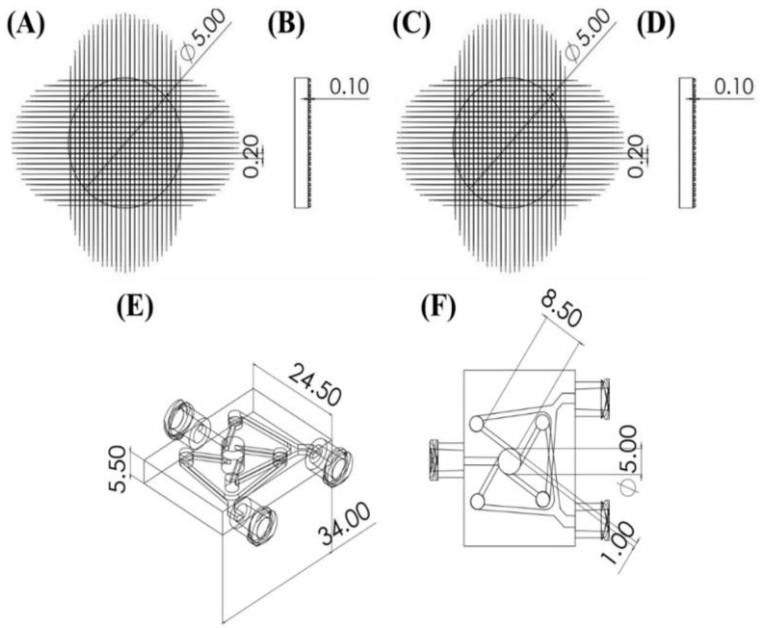

Figure 74: (A) Top view and (B) side view of the 100μm size patterned surface with marked dimensions; (C) Top view and (D) side view of the 200 μm size patterned surface with marked dimensions; (E) Isometric view and (F) top view of the microfluidic mixer device with open top and bottom side with marked dimensions.

8.3.3 Experimental Setup

The experimental setup for the reactive crystallization of HKUST-1 using a patterned microfluidic mixer device is shown in Figure 73C. First, the device was placed under an optical microscope (Olympus BX53M, Olympus America Inc.) to monitor the formation of HKUST-1 crystals. Next, the precursor solutions of the synthesis of HKUST-1 were pumped into the microfluidic device using a dual-channel programmed syringe pump (NE-4000, New Era Pump System Inc.). The outlet stream was also collected in a sealed beaker for analysis. This study investigated the effect of solvent selection for the precursor solutions and the addition of pH modulators. The two precursors for the synthesis of HKUST-1 were copper nitrate trihydrate and benzene-1,3,5-tricarboxylic acid, known as trimesic acid (TA), and both are soluble in ethanol while TA is insoluble in water. The metal precursor solution was prepared in pure ethanol and pure DI water to study the effect of solvent on the final crystals. The effect of pH on HKUST-1 crystals was also studied by adding acidic and basic modulators to the precursor solutions.

Here, a novel method was developed for the growth rate measurements of HKUST-1 crystals. This method included two complementary studies. The first study was an in-situ time-resolved FT-IR for understanding the kinetics of the formation of HKUST-1 crystals. The experimental setup for the time-resolved studies on FT-IR is shown in Figure 73C. Two 30 mL syringes are filled with solutions of copper nitrate and TA in ethanol. A dual-channel syringe pump (NE-4000) is used to pump the precursor solutions into the flow cell. As shown in Figure 78A, a pike demountable transmission flow cell has only one inlet and one outlet. Therefore, a T-junction is used right before the inlet to mix the reactant solutions before entering the flow cell. Here, the residence time for the system was calculated based on the total volume of the tubing, T-junction, and flow cell, which is around 0.8 mL.

The second study of the growth rate measurements required the synthesis of large HKUST-1 crystals. Large seeds of HKUST-1 crystals were essential to visualize growth under an optical microscope. These crystals are prepared by a solvothermal synthesis reported in the literature[187]. The two precursor solutions were initially prepared with 0.49 gr of copper nitrate trihydrate dissolved in 3 mL DI water and 3 mL of DMF, and 0.24 g of benzene-1,3,5-tricarboxylic acid dissolved in 3 mL of ethanol and 12 mL of glacial acetic acid. These two solutions were mixed and kept in a furnace at 55°C for three days. The crystallized HKUST-1 crystals were then harvested, washed, and soaked in ethanol for three days. Next, a square piece of polycarbonate film (2cm x 2cm) was covered with double-sided tape and dipped into HKUST-1 crystal slurry for one minute. The tape was then washed with ethanol and dried at 70 °C for two minutes on a hot plate. After that, the polycarbonate film was glued to the bottom of the microfluidic mixer device using clear resin (FLGPCL02) and cured for five minutes using Form Cure. (Formlabs Inc., USA). The microfluidic mixer device with the seeded crystals was located under an optical microscope (Olympus BX53M, Olympus America Inc.) and connected to a dial channel syringe pump.

Identical precursor solutions used for the in-situ FT-IR study were passed over the seeded crystals on the bottom surface of the microfluidic mixer device. The selected flow rates for the second study were adjusted according to the obtained residence time from the time-resolved experiments. The growth rate of the seeded crystals was measured by taking time-lapsed images.

8.3.4 Characterization

Optical images of HKUST-1 crystals were taken using an optical microscope (Olympus BX53M, Olympus America Inc.) The morphologies of the synthesized HKUST-1 crystals were characterized using a Scanning electron microscope, SEM Hitachi S-4800. The particle size distribution of the HKSUT-1 crystals was measured using a Malvern dynamic laser scattering device. In these measurements, the smaller the particle is, the more rapid the Brownian motion becomes. All ex-situ and in-situ time-resolved FT-IR measurements were performed using an FT-IR Spectrometer INVENIO coupled with a pike demountable transmission flow cell. The X-ray diffraction (XRD) measurements were performed on a Scintag XDS 2000 diffractometer with Cu Kα radiation.

8.4 Results and Discussion

8.4.1 Computational Results

The equilibrium concentration profiles for different patterns in the microfluidic devices are shown in Figures 75A and 75B. These patterned-surface microfluidic mixer devices were compared in terms of mixing efficiency and ability to capture HKUST-1 crystals. The mixing efficiency of different patterns was compared by calculating the mixing index, which is defined as where σ^2 and σ_0^2 are the concentration variance in any cross-sectional plane and the bottom plane of the micromixer, respectively. Figures 75A and 75B show that the mixing index decreased for identical flow conditions and concentrations as the height of the patterns increased. Here the concentration profile of three planes in the microfluidic mixer device with patterns of 100 and 500 μm are shown.

The presence of the patterns hindered the flow movement and resulted in low velocity within the height of the patterns. The smaller the velocity gets near the patterned surface, the lower the convective mixing becomes. Therefore, the mixing index decreased, and the equilibrium concentration profile was delayed inside the microfluidic mixer. The equilibrium concentration profiles of the bottom plane for the 100 and 500 μm pattern height are shown in Figures 75C and 75D. The device with patterns of 100 μm height has a larger surface area of the homogeneous concentration profile than the microfluidic mixer device with patterns of 500 μm.

On the other hand, these patterns acted like pores that captured HKUST-1 crystals inside them and grew them over time. Therefore, an optimum height for the patterns increases the capture yield and does not sacrifice the mixing efficiency. As shown in Figure 75E, patterns with heights of less than 100 μm have a mixing index profile similar to devices with no pattern surfaces. However, for patterns with a height greater than 200 μm, the mixing index profile deviates significantly from the no-pattern case. All six patterned surfaces were tested under identical experimental conditions. After 30 minutes, these patterns were compared for the final amount of crystals captured within them. As shown in Figure 75F, the number of captured crystals increased with increasing edges, whereas the most coverage was for the pattern with hexagons. Also, for identical pattern shapes, the number of crystals increased with increasing the pattern density. For example, patterns with a diameter of 100 μm captured more crystals than the 200 μm diameters.

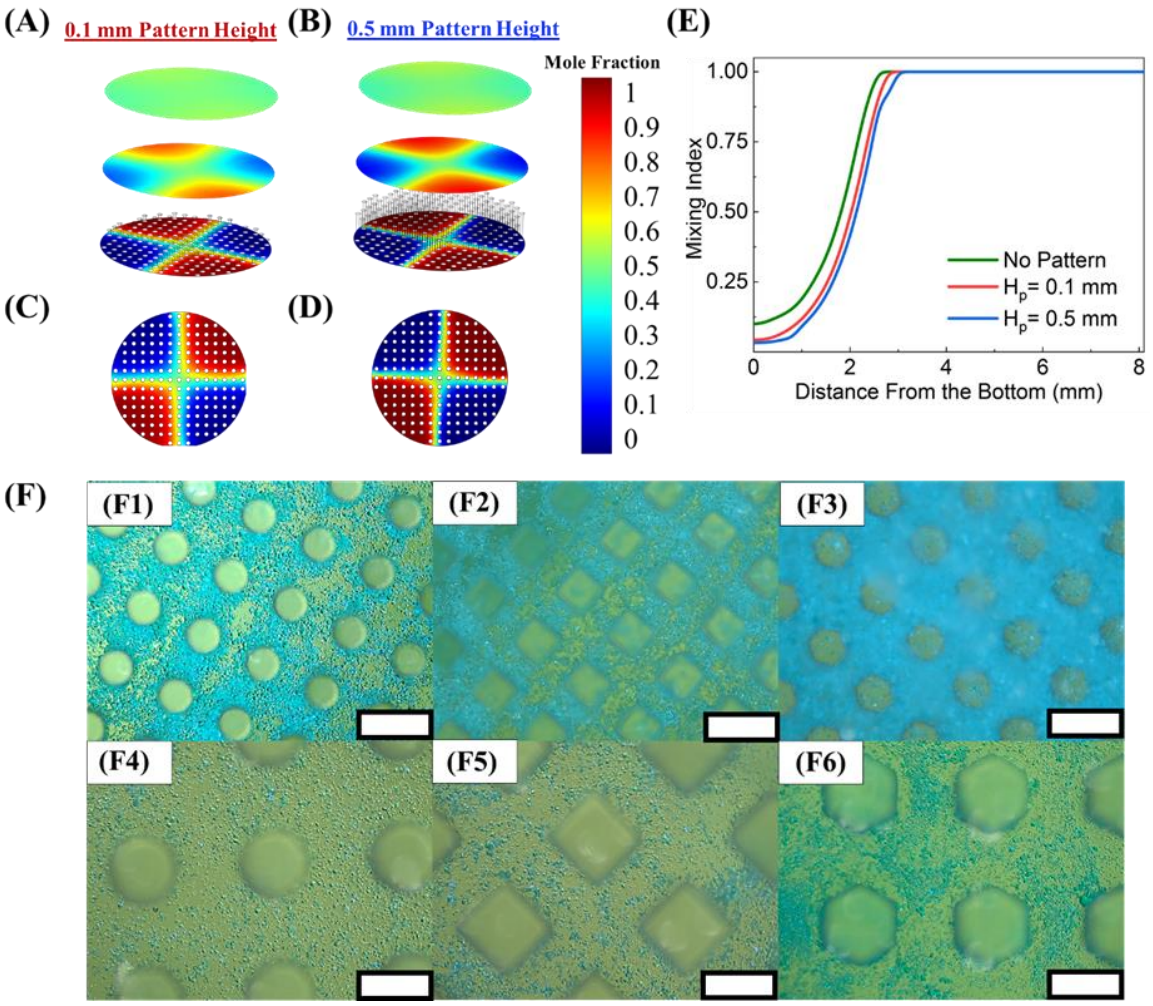

Figure 75: Equilibrium concentration profile inside the patterned-surfaces microfluidic mixer device with pattern heights of (A) 100 μm and (B) 500 μm; Equilibrium concentration profile of the bottom plane (top view) for the patterned-surface microfluidic mixer device with pattern heights of (C) 100 μm and (D) 500 μm pattern height; (E) Comparison of the concentration mixing index for microfluidic mixer devices with 100 µm, 500 μm and without patterns; (F) Captured crystals within the patterned-surfaces with 100 μm and 200 µm diameters. (Figures F1 to F3 are circular, square, and hexagonal patterns of a size of 100 μm. Figures F4 to F6 are circular, square, and hexagonal patterns of a size of 200 μm.)

8.4.2 Effect of the Solvent System on HKUST-1 Crystals

The significant influence of the solvent selection on the crystal structure of HKUST-1 crystals is shown in Figure 76. The selected solvent affects the coordination of the Cu atoms and changes the growth direction of the crystal. Here, when the organic linker precursor was dissolved in ethanol, HKUST-1 crystals were formed (Figure 76A). However, the hydrated HKUST-1 crystals shown in Figure 76B were formed when the solvent system was changed into the ethanol-water mixture (copper nitrate was dissolved in ethanol for non-hydrated HKUST-1 and dissolved in DI water for

the hydrated rod-shaped crystals). The optical and SEM images of HKUST-1 crystals were taken after completing the post-synthesis steps, including filtration, washing, and vacuum drying. The presence of the water resulted in HKUST-1 polymorphism, and some of the HKUST-1 crystals transformed from octahedral shapes to elongated rod-shaped crystals. As shown in Figures 76A and 76B, the particle size distribution of the crystals is also a function of the solvent selection. HKUST-1 crystals formed in pure ethanol have narrow particle size distribution; however, the particle size distribution is wider for a solvent composition of a 50:50 mixture of ethanol and water (see Figure 76B).

Figures 76D and 76E demonstrate the crystal structures of the octahedral and rod-shaped crystals from the reported structures in the literature[188]. The lattice parameters for each structure are listed in Figures 76D and 76E. Figure 76E shows the FT-IR spectra of HKUST-1 and hydrated HKUST-1. For the hydrated HKUST-1 crystal, the O-H stretching from hydrogen bonds is a broad peak centered around 3300 cm-1. There was no such vibration for HKUST-1 crystals synthesized in the presence of pure ethanol.

In Figure 76F, the XRD spectra of these two-crystal structures are confirmed with the existing database. From here, the simulated morphology of both forms was calculated using WinXmorph software (see Figures 76G and 76H).

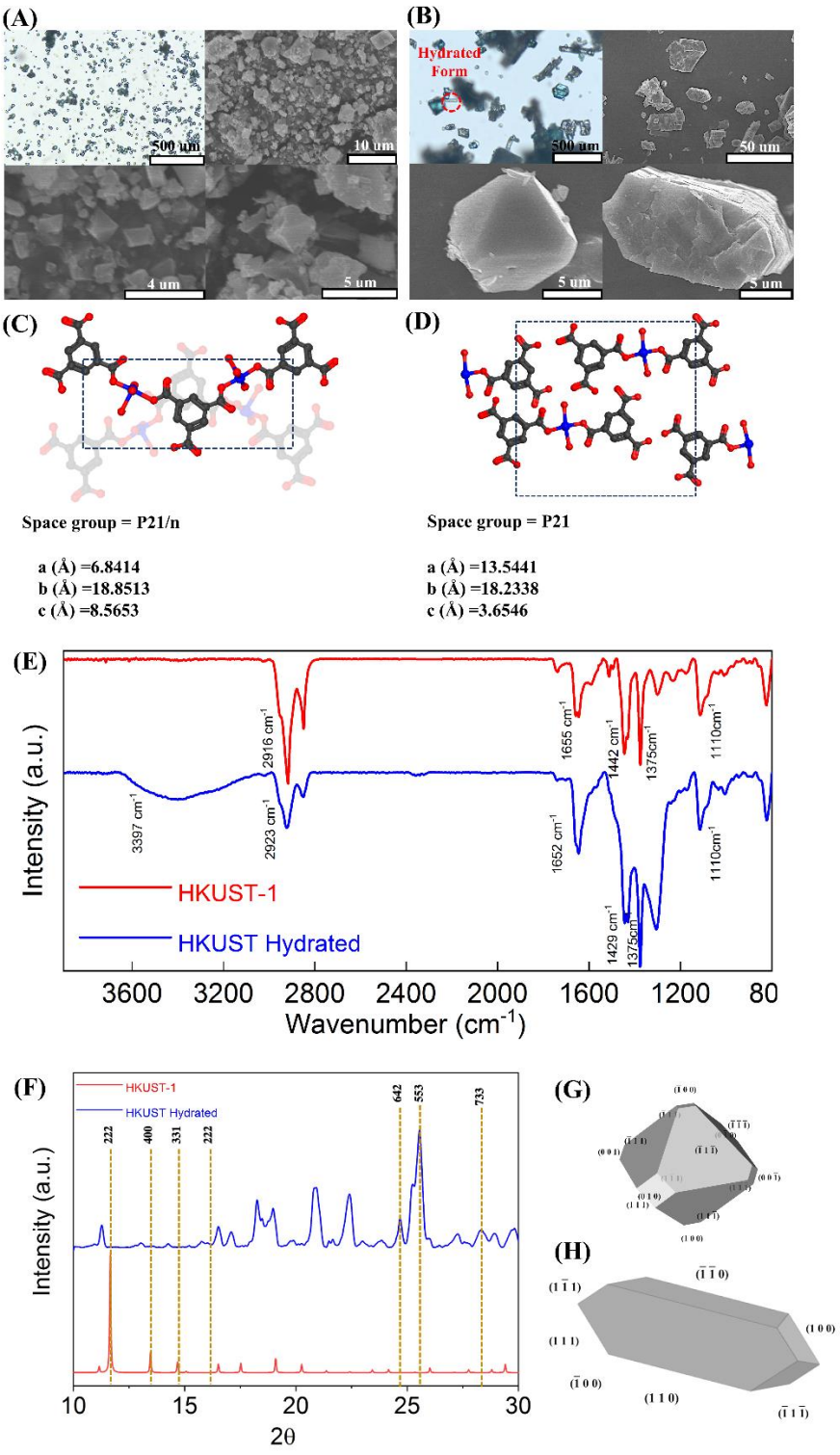

Figure 76: Optical and SEM images of the (A) non-hydrated HKUST-1 crystals formed from precursor solutions dissolved in ethanol and (B) hydrated HKUST-1 crystals formed from precursor solutions dissolved in an ethanol-water mixture (50:50); Crystal structure of (C) non-hydrated HKUST-1 crystals and, (D) hydrated HKUST-1 crystal; (E) FT-IR spectra for the non-hydrated and hydrated HKUST-1 crystals; (F) XRD pattern of the non-hydrated and hydrated HKUST-1 crystals; Simulated morphology of the (G) non-hydrated octahedral and (H) hydrated rod-shaped HKUST-1 crystals from Winmorph.

8.4.3 Effect of pH on the Particle Size Distribution

The influence of pH on the synthesis of inorganic and organic coordination compounds is well studied in crystallization[184-186]. The pH of the mixture affects the protonation and deprotonation of polycarboxylate groups and the attachment of the organic linker to the metallic ligands. In this study, acetic acid and pyridine were used as acidic and basic modulators. The details of the concentration of precursor solutions are provided in section 4.2. Here ten mol equivalents of the TA of acetic acid (acid modulator) and pyridine (basic modulators) were added to the organic linker solution (TA in ethanol) in the respective studies.

The effect of the pH on the morphology and size distribution of HKUST-1 crystals is shown in Figure 77.

Figures 77A, 77B, and 77C show the SEM images of HKUST-1 crystals in the presence of the acidic modulator, no modulator, and basic modulators. The crystals synthesized in the presence of the basic modulator had an octahedral morphology (see Figure 77C), which is similar to HKUST-1 crystals synthesized without adding any modulators (see Figure 77B). However, HKUST-1 crystals formed in the acidic solution had less dimensionality and a round-shape morphology. Therefore, it is concluded that the dimensionality of HKUST-1 crystals was enhanced by adding the basic modulators. However, the growth was prohibited after the crystals reached an average size of 1-2 μm. Figure 77D shows that both acidic and basic modulators decreased the average size of the crystals to around 1.5 μm and narrowed the particle size distribution. All obtained experimental samples were thoroughly washed with ethanol and vacuum dried for more than 12 hours before the XRD measurements. As shown in Figure 77E, the XRD pattern of HKUST-1 crystals formed in acidic and basic environments matched with the reported and the theoretical spectra for HKUST-1 in the literature[189].

The benefit of modulators is significant for the fabrication of thin films of HKUST-1 for

electrochemical and other adsorption-intensive applications. From here, it is concluded that as the pH increases in the reaction mixture, the degree of connectivity for ligands increases and results in the formation of higher dimensions crystals.

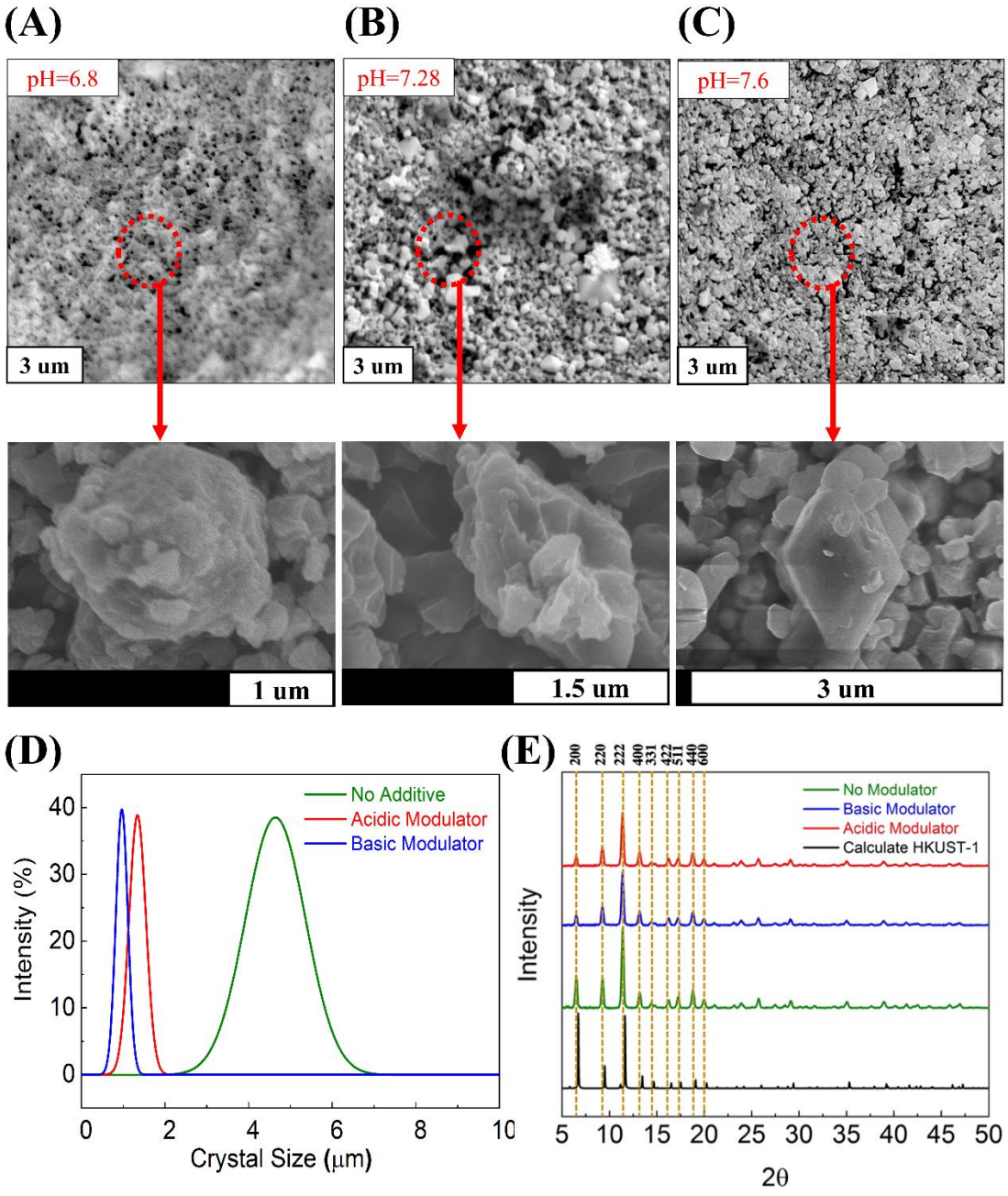

Figure 77: SEM images from HKUST-1 crystals synthesized in the presence of (A) the acidic modulator, (B) no modulator, and (C) the basic modulator; (D) particle size distribution of HKUST-1 crystals with no modulator, acidic, and basic modulator; (E) XRD patterns of HKUST-1 crystals with no modulator, acidic, and basic modulator compared with the calculated XRD pattern.

8.4.4 Feed-Forward Time-Resolved FT-IR for Kinetics Measurements of HKUST-1

Here we use FT-IR to obtain the reaction conditions for which the nucleation is minimum, and the growth of the crystals is favored. Figure 77D suggests that nucleation and growth are uncontrolled in the absence of modulators, leading to a broad crystal size distribution. However, even in the absence of modulators, tweaking the initial concentrations of the reactants favors the crystal growth over nucleation. Here, a time-resolved FT-IR was implemented to study the effect of different residence times on the growth rate measurements.

The residence time obtained from the time-resolved FT-IR analysis was utilized to study the growth rate measurements of the seeded HKUST-1 crystals inside the microfluidic mixer device. The experimental setup for the FT-IR studies is shown in Figure 78A. Similar to the previous studies, equimolar concentrations of precursor solutions were loaded onto the syringes. A T-junction was used to combine the two precursor solutions right before the inlet of the pike flow cell, which was being analyzed under FT-IR. Relative conversions of the reaction were obtained as a function of residence time by measuring the change in intensities of the reactant peaks since the concentrations of both the precursor solutions were significantly high when the reaction conversion was observed.

The reactant peaks were superimposed by HKUST-1 signature peaks, implying high nucleation rates. Lowering the concentrations of the precursors decreased the rate of the reaction. Therefore, the experiments were performed with lower concentrations (half and one-third of the initial solutions). Signals from the individual reactants implied that the reactant species were available to grow the seeded crystal (inside the microfluidic mixer device). Therefore, it was essential to screen the appropriate reactant concentrations and the residence times in the FT-IR transmission studies. A noticeable change in conversion is observed for 40mM reactant concentrations (one-third of the previous concentrations), and the reactant and product peaks are detected.

Figure 78B shows the spectra of the solution recorded at different residence times (τ). Few dominant peaks (around 1400 cm^{-1} and 1100 cm^{-1}) showed saturation since both reactants and the products contributed to this signal. In these spectra, the bond vibrations of C=O and Cu-N from precursor solutions are observed even in the absence of HKUST-1. Figures 78C and 78D are the expanded views of the C=O and Cu-N bonds from the spectra in Figure 78B. The solutions pumped for around six to seven minutes to obtain to the steady-state region. This linear increase in the intensity of reactant peaks in Figure 78E signifies a drop in conversion of the reaction with decreasing residence times, thereby implying a drop in nucleation rates. The obtained spectra indicated the presence of HKUST-1 from 600 to 700 cm^{-1} which is the signature of the Cu-O vibrations. However, there is some contribution by TA in that region. The contribution of TA was measured by calibrating the ratio of 1647 cm^{-1} and 672 cm^{-1} vibrations at different molar concentrations of the TA solution. The contribution of TA between 600-700 cm^{-1} was quantified by comparing the obtained peak intensities at 1647 cm^{-1} with the calibration curves. The respective intensities were subtracted between 672 cm^{-1} and 635 cm^{-1}, representing the formation of HKUST-1 with increasing residence times. The intensities of the reactant and products against residence time are plotted in Figure 78G. Since the absorbance can be directly related to concentration, the gradient was calculated to plot the dimensionless rates as a function of residence times. The increase in the rates with increasing residence time can be due to autocatalysis. The decrease in the rate at longer residence time is due to the depletion of reactant concentration.

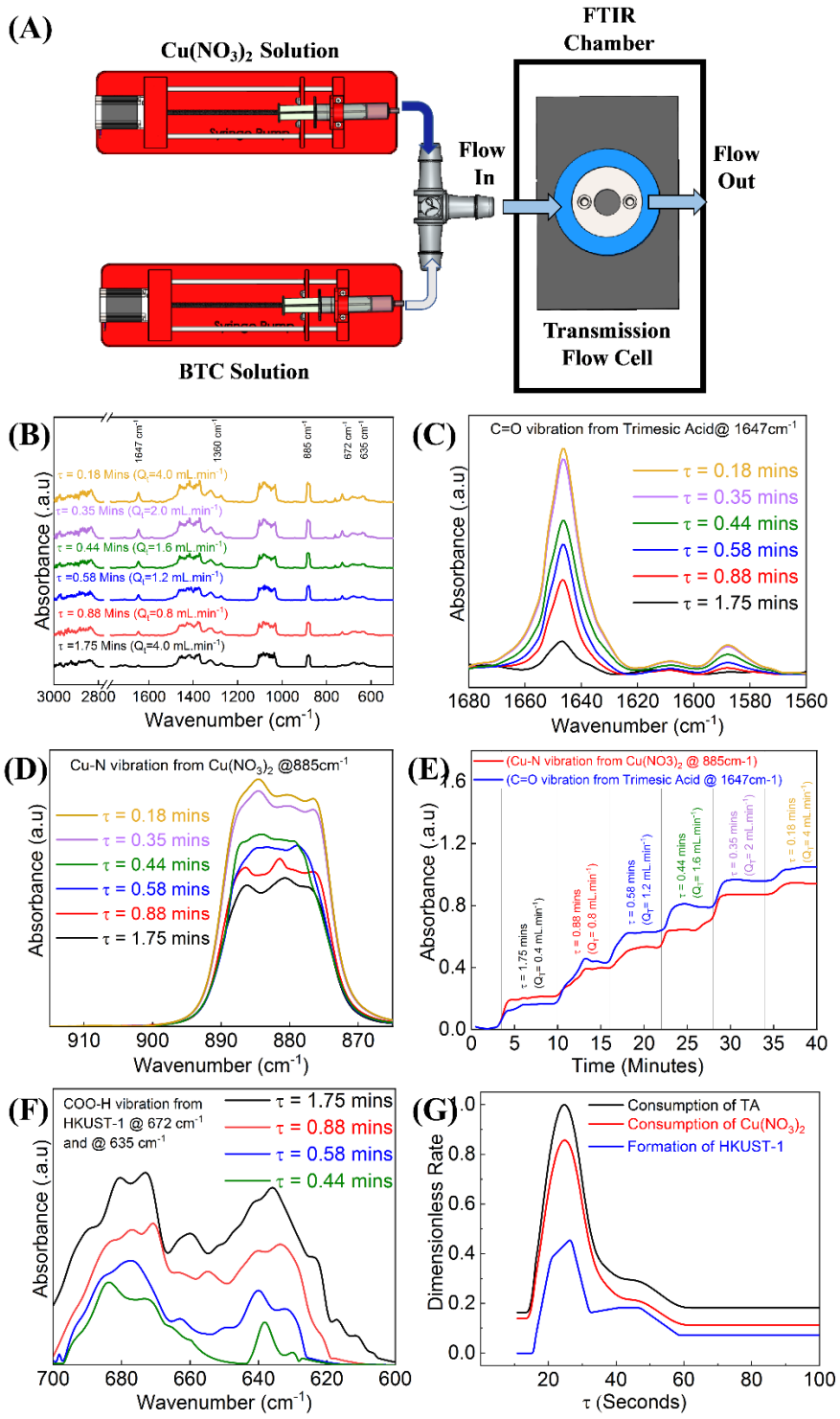

Figure 78: (A) Experimental setup used for the time-resolved FT-IR for kinetics measurements; (B) FT-IR spectra of solutions at different residence times; (C) Enlarged view of Cu-N vibration peaks at 729 cm-1 and 761 cm-1 ; (D) Enlarged view of C=O vibration peaks at 1647 cm-1 ; (E) absorbance of peaks from C=O and Cu-N vibrations vs. time for varying residence times; (F) Experimental growth rate of HKUST-1 crystals at different flow rates; (G) Dimensionless rate of reactant consumption and product formation as a function of residence time.

8.4.5 Growth Rate Measurement of HKUST-1 Crystals

The growth rate of seeded HKUST-1 crystals under continuous-flow conditions was obtained by measuring the size change of the crystals over time (see Figure 79A). The growth rate measurements were repeated for different residence times of the microfluidic mixer device, and the final results are shown in Figure 79B. The rates of HKUST-1 were obtained from FT-IR in Figure 79G. The growth rates in Figure 79B can be correlated by considering the relationship between the residence times and the reaction times. There was a steep rise in the growth rate of the seeded crystal between 0 to 6 seconds, which is obtained at residence times was much lower than the reaction time. Figure 79G confirms almost no reaction in such a short residence time. Therefore, it can be concluded that the growth of HKUST-1 is primarily due to the monomeric attachment of the metal ligand and linker to the crystal surface. The increase in the growth rate with increasing residence time can be due to the stabilization of the amorphous layer attached to the surface of MOF.

For residence times greater than 6 seconds, nucleation started, and a continuous decrease in the growth was observed. The growth was inhibited at longer residence times, as the precursor solutions inside the mixer reacted and HKUST-1 crystals were completely nucleated. The growth was dominant than the nucleation at lower residence times. As shown in Figure 79B, the maximum growth rate was measured for a residence time of around 7 seconds. At higher flow rates, the amorphous gel layer needed to grow crystals was disturbed and removed, which caused growth rates to decrease.

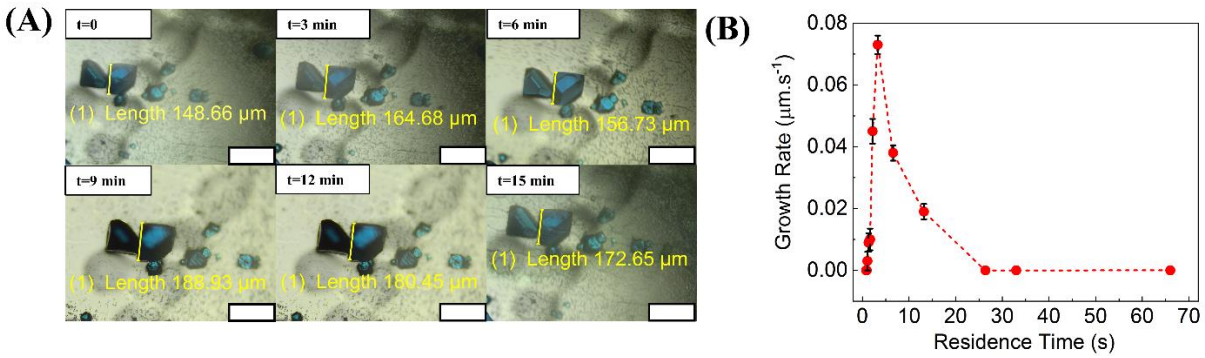

Figure 79: (A) Selected few time-lapsed images showing crystal growth for the seeded growth measurement of HKUST-1 crystals; (B) measured growth rates of HKUST-1 crystals vs. residence time of the microfluidic mixer device.

The rates obtained from FT-IR in Figure 78G and the measured growth rates in Figure 79B can be correlated by considering the relationship between the residence times and the reaction times. From Figure 79B, it is concluded that between residence time of 0 to 6 seconds, the residence time is much lower than the reaction time. After that, there is a sharp increase in the dimensionless rate, which shows the region where reaction time and residence time are approximately equal. Between 7 to 15 seconds, a moderate to high clearance of the reactants and HKUST-1 growth were observed due to monomeric addition. The system entered the nucleation regime at residence times exceeding the reaction times (15 seconds and above). As a result, the clearance rate of the reactant species from the flow cell decreased, which supports the observation of negligible growth of the seeded crystal.

8.5 Conclusion

Here, we demonstrated an innovative and effective approach to screen reactive crystallization conditions of HKUST-1 in a continuous-flow patterned microfluidic mixer device. The patterned surfaces promoted the crystal capture within the microreactor for further analysis. The small HKUST-1 crystals were trapped between the patterns on the bottom surface of the microfluidic mixer device and were harvested for polymorph and size measurements. The solvent composition and the pH are screened to investigate its effect on the polymorphism and size distribution of

HKUST-1 crystals. The selection of the water-ethanol solvent system resulted in the formation of hydrated HKUST-1 crystals with an elongated rod-shaped morphology among the octahedral HKUST-1 crystals. The formation of the rod-shaped crystals indicated the presence of water in the pores of the synthesized MOFs, as confirmed from the FT-IR analysis.

Additionally, the effect of pH on HKUST-1 crystals is evaluated by adding basic and acidic modulators to the precursor solutions. The results suggest that the addition of basic and acidic modulators decreases the particle size distribution. Furthermore, the SEM images of the samples suggested that adding the basic modulator enhanced the overall morphology of crystals, and crystals from the had sharp edges. The morphology of the sample formed with the basic modulator matched well with the known octahedral morphology of HKUST-1 crystals. In contrast, the acidic modular eliminated the sharp edges and resulted in more round-shape crystals (lowered the dimensionality of HKUST-1 crystals)

A two-step procedure for the growth rate measurements of HKUST-1 crystals in a continuous-flow microfluidic device is developed. An in-situ optical imaging system was coupled with a time-resolved FT-IR to obtain quantitative insights from the growth. The growth rate measurements for increasing residence time reveal the non-monotonic growth of HKUST-1 and the importance of amorphous layer stabilization and nucleation. Few studies have shown the effect of flow rates and residence times on the growth of seeded crystals. The studies require expensive tools such as in-situ transmission electron microscopy (TEM) and X-ray scattering (SAXS and WAXS) in addition to an extensive analysis time. These resources have limited availability; however, the alternative secondary tools developed here are readily available and can be utilized to obtain similar insights. In addition, the continuous-flow microfluidic mixer device adds the advantage of a minimal footprint. Therefore, it can be integrated with numerous analytical and spectroscopic instruments for in-situ monitoring and control. The microfluidic mixer device can be coupled with an external

heating element and feedback temperature control systems to screen reactive crystallization at high temperatures to advance this screening technology.

IX. FUNDAMENTAL INSIGHTS INTO THE MECHANISM OF MILLING USING THE CONTINUOUS-FLOW MICROFLUIDIC DEVICE

9.1 Introduction

Crystallization is one of the fundamental unit operations in drug manufacturing where the active pharmaceutical ingredient (API) is isolated and purified from the mother liquor. Solid-state properties such as particle size distribution and morphology significantly affect downstream processes such as filtration and quality of the drug substances. Therefore, several postprocessing techniques have been widely explored and implemented to reduce the size distribution of crystals to improve the critical quality attributes (CQAs). Sonication and milling are the two most commonly used methods for crystal breakage. There are two types of milling: wet and dry milling, and both use mechanical energy to break down the large crystals. Despite the relatively higher potential for scale-up, dry milling poses major drawbacks. The existence of an additional drying step in the dry milling procedure increases the overall costs of the operation.

Moreover, the cleaning of milling equipment causes product losses, thereby reducing the net yield. Additionally, the presence of both shear and tensile stresses during the dry milling increases the chance of crystal lattice deformation, leading to crystallinity reductions and crystal form conversions. By using the wet mill processes instead, the mentioned disadvantages are avoided. Ultrasonication tools are also powerful tools for tuning the particle size distribution and monitoring the crystal habit of an API. They enable manufacturing micron-sized particles while enabling dispersing and preventing agglomeration. Compared to the existing size reduction systems such as ball/bead mills and disc and jet mills, ultrasonication is well suited for generating micron and nano-sized particles.

In both wet milling and ultrasonication processes, the generation of fines is not desired and increases the PSD of the final product. Implementation of a fine dissolution step by adding a heat exchanger in line with the crystallizer helps remove the undesired fines. While coupling the fine dissolution step with the crystal breakage helps minimize the time and cost for post-processes, it requires a proper understanding of the heat transfer within the system.

Obtaining the breakage kernels requires understanding the effect of experimental parameters during wet milling or ultrasonication requires screening the PSD under different conditions. Continuous-flow crystallization helps speed up the screening procedures while using the minimum amount of APIs. Microfluidic devices have been previously used to study nucleation and growth mechanisms yet never explored for measuring the breakage kernels while using particle size reduction equipment. Studying the breakage kernels in the continuous-flow microfluidics demand coupling the micro-reactor with the size reduction equipment. Among all existing systems, ultrasonication has the greatest potential to be integrated with continuous-flow microfluidic devices. In this chapter, we have proposed integrating a sonication tool with the continuous-flow jacketed microfluidic device. Two different types of sonication tools are proposed for integration with the continuous-flow microfluidic system. One of them is the addition of a sonication tip into the cylindrical micro-mixer. A separate connection can be designed in the continuous-flow microfluidic mixer where the sonication microtip is inserted inside. Depending on the size of the microtip, the size of the micro-mixer needs to be adjusted. The second option for enabling the sonication in the micro-mixer is the integration of the continuous-flow microfluidic mixer with vibrating mini motor discs. These discs are connected to an Arduino board, and the vibration is controlled by using different types of resistors in the circuit. The mini vibrating motors can be integrated on the bottom surface of the microfluidic mixer, and the size of the micromixer can be adjusted according to the size of the selected vibrating mini motor.

In both of the proposed approaches, using the jacketed continuous-flow microfluidic mixer allows for proper control of the micro-mixer temperature and enables the dissolution of the fines. Unlike the measurement of the crystal growth, the breakage mechanism can not be optically observed in the microfluidic mixer. Therefore, the obtained PSD data can be employed in a prediction model, which assists us in obtaining the breakage kernel and further helps design the experiments to get to a certain PSD.

A general analytical solution for simple and complex kernels can be implemented to predict the particle and size and automate industrial applications. However, it is not very accurate since the solution does not include particles. On the other hand, there are instabilities with higher time scales in numerical techniques, and these solutions are often computationally expensive. Various techniques were used to solve the population balance, such as the method of moments, analytical solutions, discretization using fixed pivot and moving pivot technique, and Monte-Carlo. Due to the ubiquity of population balance equations, a novel analytical solution is needed to predict particle breakage in simple and complex kernels without losing accuracy and is stable across longer time scales. In the proposed model, different methods are investigated to solve the population balance equation, focused primarily on pure breakage, and discovered a predictive method to identify the eigenvectors of this problem and any problem with the same framework.

9.2 Conclusion and Future Prospects

In summary, this dissertation included the design and development of a continuous-flow microfluidic mixer device used for screening crystalline materials under controlled supersaturation. This microfluidic mixer device can be implemented for a different type of crystallization, such as antisolvent, cooling, and reactive. Temperature control approaches are discussed to enable screening at high temperatures, and patterned surfaces were integrated with this continuous-flow system to eliminate the need for harsh experimental conditions for reactive

crystallization of systems such as MOFs. This continuous-flow system is further developed for parallel screening of multiple conditions at a time. Moreover, the design of the micromixer is altered to create a snap-on adaptor that can convert the batch microtiter assays into continuous-flow systems. The snap-on adaptor paves the wave for HT screening of crystalline materials in a continuous-flow condition and does not demand many flow handling systems because of the designed flow distributors along with the snap-on adaptor device.

Moreover, this continuous-flow system is coupled with different types of sensors to precisely monitor the crystallization conditions. One of these sensors is the electrochemical sensor which can be integrated with the device to precisely measure the supersaturation in the micromixer. This sensor can be calibrated for any desired compound and further coupled with an ML model to predict the supersaturation value during the crystallization process. The second sensor is a photosensitive turbidity sensor that detects the formation of oil droplets and the occurrence of LLPS. This microfluidic device is a great asset for screening crystalline materials and has many potentials and applications. This development provides a good starting point for the automation of the continuous-flow HT screening systems. This snap-on adaptor can be integrated with different sensor types and be implemented for HT screening by using automation setups such as robotic hands, moving stage for the optical microscope, and control-feedback systems.

X. CONCLUDING REMARKS

The work presented in this dissertation focuses on fabricating continuous-flow microfluid devices for screening crystalline materials under controlled supersaturation. In **chapter 2,** different types of microfluidic de- vices such as the T-junction, cross-flow, cell sorter, H-shaped, and cyclone mixer were evaluated to select the desired design for a continuous-flow, well-mixed, microfluidic device that can be used for screening of polymorphs and morphology in a controlled supersaturated environment. The cyclone mixer device was selected as it was ideal for screening metastable forms, which usually convert rapidly to stable forms in batch screening devices, such as a microtiter plate and droplet-based microfluidic devices.

In **chapter 3**, the design of the developed continuous-flow system was modified to enable parallel screening of crystalline materials at controlled conditions. A merged-inlet configuration utilizing Y-junctions effectively reduces the number of inlets and creates an array of multiple tangential inlets of the micromixer.

In **chapter 4,** we presented two effective strategies for controlling the temperature of the continuous-flow microfluidic mixer device. The first strategy involved the implementation of a cooling jacket around the cylindrical mixing zone. In the second strategy, two saturated streams, two different temperatures named hot and cold streams, are pumped into the microfluidic mixer where the equilibrium temperature of the mixer is lower than the entering. Here we demonstrated screening of crystal morphology, polymorph, and growth rates of L-glutamic acid for eight different conditions employing both temperature control approaches.

In **chapter 5**, we developed a novel snap-on adaptor that converted a batch microtiter plate into a continuous-flow microfluidic mixer device. The designed snap-on adaptor was developed for a 24-well plate assay and tested for continuous-flow salt screening of naproxen. The continuous-flow operation of the snap-on microfluidic mixer device requires implementing flow distribution networks to distribute solution into all wells while minimizing the number of pumps screening of crystal polymorph, morphology, size, and kinetics under controlled conditions.

In **chapter 6**, an electrochemical sensor was integrated with the continuous-flow microfluidic developed to measure the supersaturation during the antisolvent crystallization of L-histidine. The sensor is calibrated with different concentrations of an aqueous solution of L-histidine and ten different antisolvent volumetric ratios. The data were then imported for a machine learning analysis, where four of the most used techniques were implemented to train a prediction model. Neural network, support vector machine, random forest, and gradient boosting were tested for a different train set and test sets, and among all neural network prediction models showed the highest accuracy. From this prediction model, the supersaturation of an aqueous L-histidine solution with an unknown concentration is predicted.

In **chapter 7**, we illustrated the design of a photosensitive turbidity sensor integrated with the continuous-flow microfluidic device, which is intended to detect oiling out boundaries coagulant process. A turbidity sensor was built using a photodiode as the detector and an infrared LED light as the light source. This sensor was then integrated into our previously developed continuous-flow microfluidic device to determine the Liquid−liquid equilibrium boundaries.

In **chapter 8**, we demonstrated an innovative and effective approach for screening the reactive crystallization of HKUST-1 in a continuous-flow patterned-surface microfluidic device. The patterned surfaces promoted the crystal capture within the microreactor for further analysis. The

small HKUST-1 crystals were trapped between the patterns on the bottom of the microfluidic mixer device and were harvested for screening form and size. Here, we laid out the effects of the solvent system and the pH of the solution on the HKUST-1 crystals.

In **chapter 9,** we discussed the potential of integration of sonication tools with the continuous-flow microfluidic device and developing a novel solution to the population balance equation for the breakage problem during sonication and milling. This solution can be implemented in a prediction model for predicting crystal PSDs. Furthermore, this model can be applied for a continuous-flow microfluidic device coupled with a sonication tool for continuously breaking the crystals.

APPENDIX A. PRINT PERMISSIONS

According to the Royal Society of Chemistry, Lab on Chip journal permission should be requested for the use of the whole article or chapter except if reusing it in a thesis. Since this document is a P.h.D thesis, there is not any need for permission. Attached is the screenshot of the journal statement and the flowchart indicating the need for permission in the necessary cases.

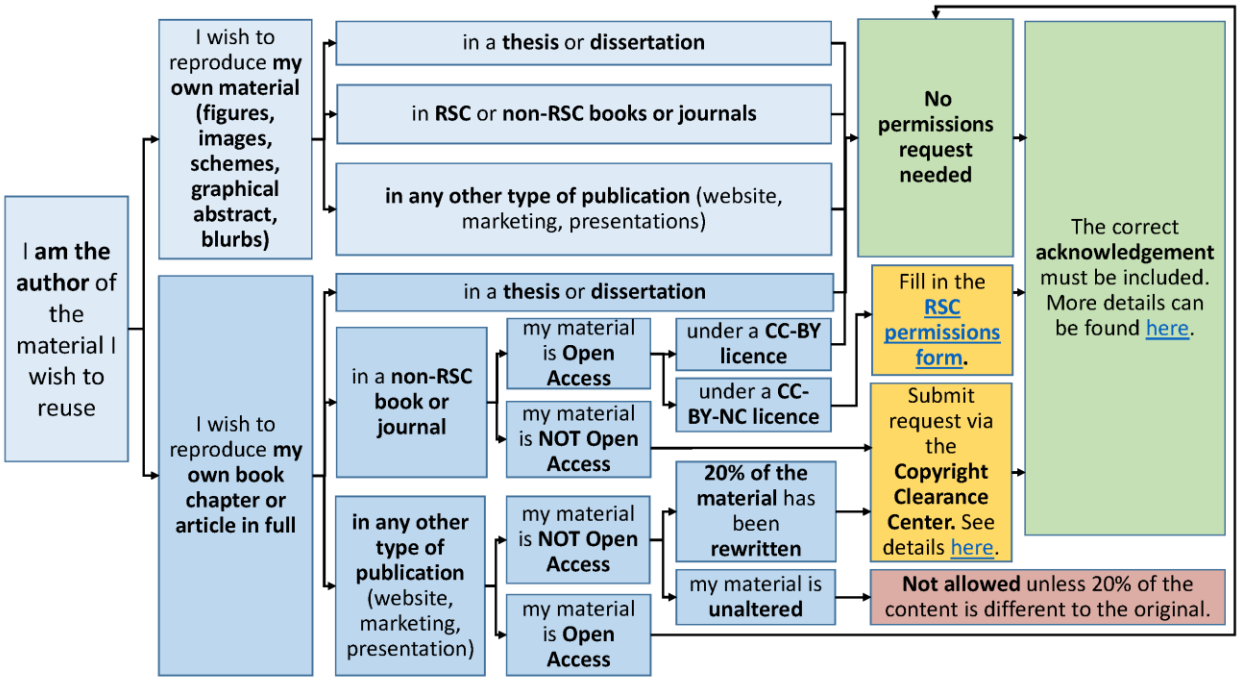

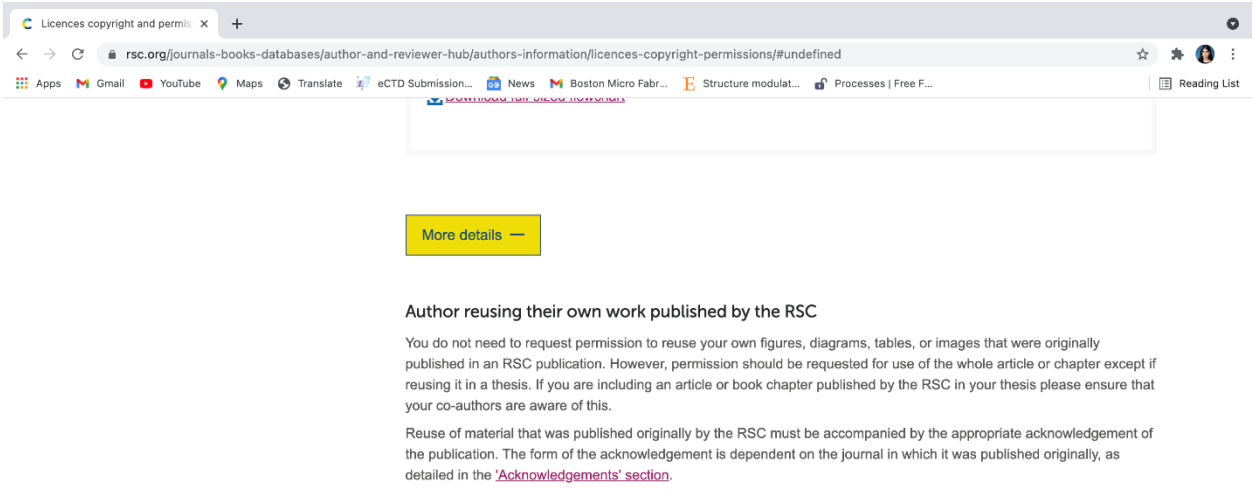

REFERENCES

1. Myerson, A.: *Handbook of industrial crystallization*; Butterworth-Heinemann, 2002.
2. Lu, J.; Rohani, S.: Polymorphism and crystallization of active pharmaceutical ingredients (APIs). *Current Medicinal Chemistry* **2009**, *16*, 884-905.
3. Taylor, D.: The Pharmaceutical Industry and the Future of Drug Development. In *Pharmaceuticals in the Environment*; The Royal Society of Chemistry, 2016; pp 1-33.
4. Van Eerdenbrugh, B.; Baird, J. A.; Taylor, L. S.: Crystallization Tendency of Active Pharmaceutical Ingredients Following Rapid Solvent Evaporation—Classification and Comparison with Crystallization Tendency from Under cooled Melts. *Journal of Pharmaceutical Sciences* **2010**, *99*, 3826-3838.
5. Bevan, C. D.; Lloyd, R. S.: A high-throughput screening method for the determination of aqueous drug solubility using laser nephelometry in microtiter plates. *Analytical chemistry* **2000**, *72*, 1781-1787.
6. Singh, M. R.; Chakraborty, J.; Nere, N.; Tung, H. H.; Bordawekar, S.; Ramkrishna, D.: Image-Analysis-Based Method for 3D Crystal Morphology Measurement and Polymorph Identification Using Confocal Microscopy. *Crystal Growth & Design* **2012**, *12*, 3735-3748.
7. Singh, M. R.; Verma, P.; Tung, H.-H.; Bordawekar, S.; Ramkrishna, D.: Screening crystal morphologies from crystal structure. *Crystal growth & design* **2013**, *13*, 1390-1396.
8. Singh, M. R.; Ramkrishna, D.: A comprehensive approach to predicting crystal morphology distributions with population balances. *Crystal growth & design* **2013**, *13*, 1397-1411.
9. Kitamura, M.: Crystallization behavior and transformation kinetics of L-histidine polymorphs. *Journal of chemical engineering of Japan* **1993**, *26*, 303-307.
10. Wantha, L.; Punmalee, N.; Flood, A. E.: Influence of Solvents on Solution-Mediated Polymorphic Transformation of the Polymorphs of L-Histidine. *Chemical Engineering & Technology* **2019**, *42*, 1505-1511.
11. Wantha, L.; Flood, A. E.: Growth and Dissolution Kinetics of A and B Polymorphs of L-Histidine. *Chemical Engineering & Technology* **2015**, *38*, 1022-1028.
12. Zhao, Q.; Cui, H.; Wang, Y.; Du, X.: Microfluidic platforms toward rational material fabrication for biomedical applications. *Small* **2020**, *16*, 1903798.
13. Valencia, P. M.; Farokhzad, O. C.; Karnik, R.; Langer, R.: Microfluidic technologies for accelerating the clinical translation of nanoparticles. *Nature nanotechnology* **2012**, *7*, 623-629.
14. Wang, H.; Liu, K.; Chen, K.-J.; Lu, Y.; Wang, S.; Lin, W.-Y.; Guo, F.; Kamei, K.-i.; Chen, Y.-C.; Ohashi, M.: A rapid pathway toward a superb gene delivery system: programming structural and functional diversity into a supramolecular nanoparticle library. *ACS nano* **2010**, *4*, 6235-6243.
15. Borissova, A.; Khan, S.; Mahmud, T.; Roberts, K. J.; Andrews, J.; Dallin, P.; Chen, Z.-P.; Morris, J.: In situ measurement of solution concentration during the batch cooling crystallization of l-glutamic acid using ATR-FTIR spectroscopy coupled with chemometrics. *Crystal Growth and Design* **2009**, *9*, 692-706.
16. Guijt, R. M.; Dodge, A.; van Dedem, G. W.; de Rooij, N. F.; Verpoorte, E.: Chemical and physical processes for integrated temperature control in microfluidic devices. *Lab on a Chip* **2003**, *3*, 1-4.
17. Maltezos, G.; Rajagopal, A.; Scherer, A.: Evaporative cooling in microfluidic channels. *Applied physics letters* **2006**, *89*, 074107.
18. Byrn, S. R.; Pfeiffer, R. R.; Stowell, J. G.: Solid-State Chemistry of Drugs, ; SSCI. *Inc.: West Lafayette, IN* **1999**, 243-245.

19. Singh, M. R.; Chakraborty, J.; Nere, N.; Tung, H.-H.; Bordawekar, S.; Ramkrishna, D.: Image-analysis-based method for 3D crystal morphology measurement and polymorph identification using confocal microscopy. *Crystal growth & design* **2012**, *12*, 3735-3748.
20. Federsel, H. J.: Facing chirality in the 21st century: approaching the challenges in the pharmaceutical industry. *Chirality: The Pharmacological, Biological, and Chemical Consequences of Molecular Asymmetry* **2003**, *15*, S128-S142.
21. Ramkrishna, D.; Singh, M. R.: Population balance modeling: current status and future prospects. *Annual review of chemical and biomolecular engineering* **2014**, *5*, 123-146.
22. Chakraborty, J.; Singh, M. R.; Ramkrishna, D.; Borchert, C.; Sundmacher, K.: Modeling of crystal morphology distributions. Towards crystals with preferred asymmetry. *Chemical Engineering Science* **2010**, *65*, 5676-5686.
23. Singh, M. R.; Nere, N.; Tung, H.-H.; Mukherjee, S.; Bordawekar, S.; Ramkrishna, D.: Measurement of polar plots of crystal dissolution rates using hot-stage microscopy. Some further insights into dissolution morphologies. *Crystal growth & design* **2014**, *14*, 5647-5661.
24. Singh, M. R.; Ramkrishna, D.: Dispersions in crystal nucleation and growth rates: Implications of fluctuation in supersaturation. *Chemical Engineering Science* **2014**, *107*, 102-113.
25. Gardner, C. R.; Almarsson, O.; Chen, H.; Morissette, S.; Peterson, M.; Zhang, Z.; Wang, S.; Lemmo, A.; Gonzalez-Zugasti, J.; Monagle, J.: Application of high throughput technologies to drug substance and drug product development. *Computers & chemical engineering* **2004**, *28*, 943-953.
26. Almarsson, Ö.; Hickey, M. B.; Peterson, M. L.; Morissette, S. L.; Soukasene, S.; McNulty, C.; Tawa, M.; MacPhee, J. M.; Remenar, J. F.: High-throughput surveys of crystal form diversity of highly polymorphic pharmaceutical compounds. *Crystal growth & design* **2003**, *3*, 927-933.
27. Fogg, M. J.; Wilkinson, A. J.: Higher-throughput approaches to crystallization and crystal structure determination. Portland Press Ltd., 2008.
28. Lee, A. Y.; Lee, I. S.; Dette, S. S.; Boerner, J.; Myerson, A. S.: Crystallization on confined engineered surfaces: A method to control crystal size and generate different polymorphs. *Journal of the American Chemical Society* **2005**, *127*, 14982-14983.
29. Davey, R. J.: Pizzas, polymorphs and pills. *Chemical communications* **2003**, 1463-1467.
30. Maeki, M.; Yamazaki, S.; Pawate, A. S.; Ishida, A.; Tani, H.; Yamashita, K.; Sugishima, M.; Watanabe, K.; Tokeshi, M.; Kenis, P. J.: A microfluidic-based protein crystallization method in 10 micrometer-sized crystallization space. *CrystEngComm* **2016**, *18*, 7722-7727.
31. Diao, Y.; Harada, T.; Myerson, A. S.; Hatton, T. A.; Trout, B. L.: The role of nanopore shape in surface-induced crystallization. *Nature materials* **2011**, *10*, 867-871.
32. Diao, Y.; Helgeson, M. E.; Siam, Z. A.; Doyle, P. S.; Myerson, A. S.; Hatton, T. A.; Trout, B. L.: Nucleation under soft confinement: role of polymer–solute interactions. *Crystal growth & design* **2012**, *12*, 508-517.
33. Guha, S.; Perry, S. L.; Pawate, A. S.; Kenis, P. J.: Fabrication of X-ray compatible microfluidic platforms for protein crystallization. *Sensors and Actuators B: Chemical* **2012**, *174*, 1-9.
34. Teshima, Y.; Maeki, M.; Yamashita, K.; Miyazaki, M.: A method for generating a metastable crystal in a microdroplet. *CrystEngComm* **2013**, *15*, 9874-9877.
35. Thorson, M. R.; Goyal, S.; Gong, Y.; Zhang, G. G.; Kenis, P. J.: Microfluidic approach to polymorph screening through antisolvent crystallization. *CrystEngComm* **2012**, *14*, 2404-2412.
36. Goyal, S.; Thorson, M. R.; Zhang, G. G.; Gong, Y.; Kenis, P. J.: Microfluidic approach to cocrystal screening of pharmaceutical parent compounds. *Crystal growth & design* **2012**, *12*, 6023-6034.

37. Horstman, E. M.; Goyal, S.; Pawate, A.; Lee, G.; Zhang, G. G.; Gong, Y.; Kenis, P. J.: Crystallization optimization of pharmaceutical solid forms with X-ray compatible microfluidic platforms. *Crystal Growth & Design* **2015**, *15*, 1201-1209.
38. Bhamidi, V.; Lee, S. H.; He, G.; Chow, P. S.; Tan, R. B.; Zukoski, C. F.; Kenis, P. J.: Antisolvent crystallization and polymorph screening of glycine in microfluidic channels using hydrodynamic focusing. *Crystal Growth & Design* **2015**, *15*, 3299-3306.
39. Papoutsakis, E.; Ramkrishna, D.; Lim, H. C.: The extended Graetz problem with Dirichlet wall boundary conditions. *Applied Scientific Research* **1980**, *36*, 13-34.
40. Jiang, S.; ter Horst, J. H.; Jansens, P. J.: Concomitant polymorphism of o-aminobenzoic acid in antisolvent crystallization. *Crystal Growth and Design* **2008**, *8*, 37-43.
41. Coliaie, P.; Kelkar, M. S.; Nere, N. K.; Singh, M. R.: Continuous-flow, well-mixed, microfluidic crystallization device for screening of polymorphs, morphology, and crystallization kinetics at controlled supersaturation. *Lab on a Chip* **2019**, *19*, 2373-2382.
42. García-Ruiz, J. M.: Counterdiffusion methods for macromolecular crystallization. *Methods in Enzymology* **2003**, *368*, 130-154.
43. Puigmartí-Luis, J.: Microfluidic platforms: a mainstream technology for the preparation of crystals. *Chemical Society Reviews* **2014**, *43*, 2253-2271.
44. Fraikin, J.-L.; Teesalu, T.; McKenney, C. M.; Ruoslahti, E.; Cleland, A. N.: A high-throughput label-free nanoparticle analyser. *Nature nanotechnology* **2011**, *6*, 308-313.
45. Kim, Y.; Lee Chung, B.; Ma, M.; Mulder, W. J.; Fayad, Z. A.; Farokhzad, O. C.; Langer, R.: Mass production and size control of lipid–polymer hybrid nanoparticles through controlled microvortices. *Nano letters* **2012**, *12*, 3587-3591.
46. Brennan, M. D.; Rexius-Hall, M. L.; Elgass, L. J.; Eddington, D. T.: Oxygen control with microfluidics. *Lab on a Chip* **2014**, *14*, 4305-4318.
47. Shields IV, C. W.; Reyes, C. D.; López, G. P.: Microfluidic cell sorting: a review of the advances in the separation of cells from debulking to rare cell isolation. *Lab on a Chip* **2015**, *15*, 1230-1249.
48. Dertinger, S. K.; Chiu, D. T.; Jeon, N. L.; Whitesides, G. M.: Generation of gradients having complex shapes using microfluidic networks. *Analytical Chemistry* **2001**, *73*, 1240-1246.
49. Galletti, C.; Arcolini, G.; Brunazzi, E.; Mauri, R.: Mixing of binary fluids with composition-dependent viscosity in a T-shaped micro-device. *Chemical Engineering Science* **2015**, *123*, 300-310.
50. Roelands, C. M.; Jiang, S.; Kitamura, M.; ter Horst, J. H.; Kramer, H. J.; Jansens, P. J.: Antisolvent crystallization of the polymorphs of L-histidine as a function of supersaturation ratio and of solvent composition. *Crystal growth & design* **2006**, *6*, 955-963.
51. Wantha, L.; Punmalee, N.; Sawaddiphol, V.; Flood, A. E.: Effect of Ethanol on Crystallization of the Polymorphs of L-Histidine. *Journal of Crystal Growth* **2018**, *490*, 65-70.
52. Wantha, L.: Determination of Nucleation and Growth Mechanisms of the B Polymorph of L-Histidine by Induction Time Measurement. *Chemical Engineering & Technology* **2016**, *39*, 1289-1294.
53. Mersmann, A.: *Crystallization technology handbook*; CRC press, 2001.
54. Nagy, Z. K.; Braatz, R. D.: Advances and new directions in crystallization control. *Annual review of chemical and biomolecular engineering* **2012**, *3*, 55-75.
55. Miralles, V.; Huerre, A.; Malloggi, F.; Jullien, M.-C.: A review of heating and temperature control in microfluidic systems: techniques and applications. *Diagnostics* **2013**, *3*, 33-67.
56. Galkin, O.; Vekilov, P. G.: Direct determination of the nucleation rates of protein crystals. *The Journal of Physical Chemistry B* **1999**, *103*, 10965-10971.

57. Gong, T.; Shen, J.; Hu, Z.; Marquez, M.; Cheng, Z.: Nucleation rate measurement of colloidal crystallization using microfluidic emulsion droplets. *Langmuir* **2007**, *23*, 2919-2923.
58. Yang, J.; Liu, Y.; Rauch, C. B.; Stevens, R. L.; Liu, R. H.; Lenigk, R.; Grodzinski, P.: High sensitivity PCR assay in plastic micro reactors. *Lab on a Chip* **2002**, *2*, 179-187.
59. Jiang, M.; Zhu, Z.; Jimenez, E.; Papageorgiou, C. D.; Waetzig, J.; Hardy, A.; Langston, M.; Braatz, R. D.: Continuous-flow tubular crystallization in slugs spontaneously induced by hydrodynamics. *Crystal growth & design* **2014**, *14*, 851-860.
60. Kim, S.; Kim, H. J.; Jeon, N. L.: Biological applications of microfluidic gradient devices. *Integrative Biology* **2010**, *2*, 584-603.
61. Coliaie, P.; Kelkar, M. S.; Langston, M.; Liu, C.; Nazemifard, N.; Patience, D.; Skliar, D.; Nandkishor, N.; Singh, M. R.: Advanced Continuous-Flow Microfluidic Device for Parallel Screening of Crystal Polymorphs, Morphology and Kinetics at Controlled Supersaturation. *Lab on a Chip* **2021**.
62. Schöll, J.; Lindenberg, C.; Vicum, L.; Brozio, J.; Mazzotti, M.: Precipitation of α L-glutamic acid: determination of growth kinetics. *Faraday Discussions* **2007**, *136*, 247-264.
63. Semin, D. J.; Jona, J.; Peterson, M. L.; Zanon, R.: Salt Screening and Selection. *Burger's Medicinal Chemistry and Drug Discovery* **2003**, 381-400.
64. Neau, S. H.: Pharmaceutical salts. In *Water-Insoluble Drug Formulation*; CRC Press, 2008; pp 431-450.
65. Gupta, D.; Bhatia, D.; Dave, V.; Sutariya, V.; Varghese Gupta, S.: Salts of therapeutic agents: chemical, physicochemical, and biological considerations. *Molecules* **2018**, *23*, 1719.
66. Fernández Casares, A.; Nap, W. M.; Ten Figás, G.; Huizenga, P.; Groot, R.; Hoffmann, M.: An evaluation of salt screening methodologies. *Journal of Pharmacy and Pharmacology* **2015**, *67*, 812-822.
67. Trietsch, S. J.; Israëls, G. D.; Joore, J.; Hankemeier, T.; Vulto, P.: Microfluidic titer plate for stratified 3D cell culture. *Lab on a Chip* **2013**, *13*, 3548-3554.
68. Thorson, M. R.; Goyal, S.; Schudel, B. R.; Zukoski, C. F.; Zhang, G. G.; Gong, Y.; Kenis, P. J.: A microfluidic platform for pharmaceutical salt screening. *Lab on a Chip* **2011**, *11*, 3829-3837.
69. Park, D.; Wang, H.; Chen, P.; Park, T.; Kim, N.; You, B.; Nikitopoulos, D.; Soper, S.; Murphy, M.: Passive micro-assembly of a fluidic control chip and a multi-well continuous flow PCR chip for high throughput applications. In *Proceedings of 14th international conference on miniaturized systems for chemistry and life sciences*, 2010; pp 1226-1228.
70. Chen, P.-C.; Park, D. S.; You, B.-H.; Kim, N.; Park, T.; Soper, S. A.; Nikitopoulos, D. E.; Murphy, M. C.: Titer-plate formatted continuous flow thermal reactors: Design and performance of a nanoliter reactor. *Sensors and Actuators B: Chemical* **2010**, *149*, 291-300.
71. Brennan, M. D.; Rexius-Hall, M. L.; Eddington, D. T.: A 3D-printed oxygen control insert for a 24-well plate. *PLoS One* **2015**, *10*, e0137631.
72. Simone, E.; McVeigh, J.; Reis, N. M.; Nagy, Z.: A high-throughput multi-microfluidic crystal generator (MMicroCryGen) platform for facile screening of polymorphism and crystal morphology for pharmaceutical compounds. *Lab on a Chip* **2018**, *18*, 2235-2245.
73. Park, D. S.-W.; Chen, P.-C.; You, B. H.; Kim, N.; Park, T.; Lee, T. Y.; Datta, P.; Desta, Y.; Soper, S. A.; Nikitopoulos, D. E.: Titer plate formatted continuous flow thermal reactors for high throughput applications: fabrication and testing. *Journal of Micromechanics and Microengineering* **2010**, *20*, 055003.
74. Park, D.; Chen, P.-C.; You, B.; Kim, N.; Park, T.; Datta, P.; Desta, Y.; Soper, S.; Nikitopoulos, D.; Murphy, M.: Optimization of Geometry for Continuous Flow PCR Devices in a

Titer Plate-Based PCR Multi-Reactor Platform. In *ASME International Mechanical Engineering Congress and Exposition*, 2007; Vol. 4305; pp 113-118.
75. Lai, B. F. L.; Lu, R. X. Z.; Huyer, L. D.; Kakinoki, S.; Yazbeck, J.; Wang, E. Y.; Wu, Q.; Zhang, B.; Radisic, M.: A well plate–based multiplexed platform for incorporation of organoids into an organ-on-a-chip system with a perfusable vasculature. *Nature Protocols* **2021**, *16*, 2158-2189.
76. Ding, X.; Mu, Y.: Digital Nucleic Acid Detection Based on Microfluidic Lab-on-a-Chip Devices. *Lab-on-a-chip fabrication and application* **2016**, 125.
77. Xie, S.; Wu, J.; Tang, B.; Zhou, G.; Jin, M.; Shui, L.: Large-area and high-throughput PDMS microfluidic chip fabrication assisted by vacuum airbag laminator. *Micromachines* **2017**, *8*, 218.
78. Sweet, E.; Yang, B.; Chen, J.; Vickerman, R.; Lin, Y.; Long, A.; Jacobs, E.; Wu, T.; Mercier, C.; Jew, R.: 3D microfluidic gradient generator for combination antimicrobial susceptibility testing. *Microsystems & Nanoengineering* **2020**, *6*, 1-14.
79. Cachet, C.; Ganne, F.; Maurin, G.; Petitjean, J.; Vivier, V.; Wiart, R.: EIS investigation of zinc dissolution in aerated sulfate medium. Part I: bulk zinc. *Electrochimica acta* **2001**, *47*, 509-518.
80. Kim, Y.-s.; Rousseau, R. W.: Characterization and solid-state transformations of the pseudopolymorphic forms of sodium naproxen. *Crystal growth & design* **2004**, *4*, 1211-1216.
81. Tong, J.; Doumbia, A.; Turner, M. L.; Casiraghi, C.: Real-time monitoring of crystallization from solution by using an interdigitated array electrode sensor. *Nanoscale horizons* **2021**.
82. Rodríguez-Ruiz, I.; Radajewski, D.; Charton, S.; Phamvan, N.; Brennich, M.; Pernot, P.; Bonneté, F.; Teychené, S.: Innovative high-throughput SAXS methodologies based on photonic lab-on-a-chip sensors: Application to macromolecular studies. *Sensors* **2017**, *17*, 1266.
83. Heinrich, J.; Ulrich, J.: Application of Laser-Backscattering Instruments for In Situ Monitoring of Crystallization Processes–A Review. *Chemical engineering & technology* **2012**, *35*, 967-979.
84. Kuentz, M.: Drug supersaturation during formulation digestion, including real-time analytical approaches. *Advanced drug delivery reviews* **2019**, *142*, 50-61.
85. Tacsi, K. l.; Gyürkés, M.; Csontos, I. n.; Farkas, A.; Borbás, E.; Nagy, Z. K. f.; Marosi, G. r.; Pataki, H.: Polymorphic Concentration Control for Crystallization Using Raman and Attenuated Total Reflectance Ultraviolet Visible Spectroscopy. *Crystal Growth & Design* **2019**, *20*, 73-86.
86. Rao, G.; Aghajanian, S.; Koiranen, T.; Wajman, R.; Jackowska-Strumiłło, L.: Process monitoring of antisolvent based crystallization in low conductivity solutions using electrical impedance spectroscopy and 2-D electrical resistance tomography. *Applied Sciences* **2020**, *10*, 3903.
87. Gao, Z.; Rohani, S.; Gong, J.; Wang, J.: Recent Developments in the Crystallization Process: Toward the Pharmaceutical Industry. *Engineering* **2017**, *3*, 343-353.
88. Luo, Y.-H.; Tu, Y.-R.; Ge, J.-L.; Sun, B.-W.: Monitoring the crystallization process of methylprednisolone hemisuccinate (MPHS) from ethanol solution by combined ATR-FTIR-FBRM-PVM. *Separation Science and Technology* **2013**, *48*, 1881-1890.
89. Soares, L.; Novais, S.; Ferreira, A.; Frazão, O.; Silva, S.: Detection of the Crystallization Process of Paracetamol with a Multi-Mode Optical Fiber in a Reflective Configuration. *Sensors* **2020**, *20*, 87.
90. Soares, L.; Cruz, P.; Novais, S.; Ferreira, A.; Frezão, O.; Silva, S.: Application of a Fiber Optic Refractometric Sensor to Measure the Concentration of Paracetamol in Crystallization Experiments. *IEEE Instrumentation & Measurement Magazine* **2021**, *24*, 36-40.

91. Liotta, V.; Sabesan, V.: Monitoring and feedback control of supersaturation using ATR-FTIR to produce an active pharmaceutical ingredient of a desired crystal size. *Organic Process Research & Development* **2004**, *8*, 488-494.
92. Derdour, L.; Fevotte, G.; Puel, F.; Carvin, P.: Real-time evaluation of the concentration of impurities during organic solution crystallization. *Powder technology* **2003**, *129*, 1-7.
93. McGrath, M. J.; Scanaill, C. N.: Sensing and sensor fundamentals. In *Sensor Technologies*; Springer, 2013; pp 15-50.
94. Ramachandran, R.; Leng, X.; Zhao, C.; Xu, Z.-X.; Wang, F.: 2D siloxene sheets: A novel electrochemical sensor for selective dopamine detection. *Applied materials today* **2020**, *18*, 100477.
95. Srikanth, S.; Mohan, J. M.; Raut, S.; Dubey, S. K.; Ishii, I.; Javed, A.; Goel, S.: Droplet based microfluidic device integrated with ink jet printed three electrode system for electrochemical detection of ascorbic acid. *Sensors and Actuators A: Physical* **2021**, *325*, 112685.
96. Liu, J.; Zhang, Y.; Jiang, M.; Tian, L.; Sun, S.; Zhao, N.; Zhao, F.; Li, Y.: Electrochemical microfluidic chip based on molecular imprinting technique applied for therapeutic drug monitoring. *Biosensors and Bioelectronics* **2017**, *91*, 714-720.
97. Nesakumar, N.; Kesavan, S.; Li, C.-Z.; Alwarappan, S.: Microfluidic electrochemical devices for biosensing. *Journal of Analysis and Testing* **2019**, *3*, 3-18.
98. Senel, M.; Dervisevic, E.; Alhassen, S.; Dervisevic, M.; Alachkar, A.; Cadarso, V. J.; Voelcker, N. H.: Microfluidic electrochemical sensor for cerebrospinal fluid and blood dopamine detection in a mouse model of Parkinson's disease. *Analytical Chemistry* **2020**, *92*, 12347-12355.
99. Löffelmann, M.; Mersmann, A.: A new method for supersaturation measurement: Idea, implementation and results. *International Journal of Modern Physics B* **2002**, *16*, 391-398.
100. Hancock, B. C.: Predicting the crystallization propensity of drug-like molecules. *Journal of pharmaceutical sciences* **2017**, *106*, 28-30.
101. Ghosh, A.; Louis, L.; Arora, K. K.; Hancock, B. C.; Krzyzaniak, J. F.; Meenan, P.; Nakhmanson, S.; Wood, G. P. F.: Assessment of machine learning approaches for predicting the crystallization propensity of active pharmaceutical ingredients. *CrystEngComm* **2019**, *21*, 1215-1223.
102. Wicker, J. G. P.; Cooper, R. I.: Will it crystallise? Predicting crystallinity of molecular materials. *CrystEngComm* **2015**, *17*, 1927-1934.
103. Raccuglia, P.; Elbert, K. C.; Adler, P. D. F.; Falk, C.; Wenny, M. B.; Mollo, A.; Zeller, M.; Friedler, S. A.; Schrier, J.; Norquist, A. J.: Machine-learning-assisted materials discovery using failed experiments. *Nature* **2016**, *533*, 73-76.
104. Sundararaj, A.; Ravi, R.; Thirumalai, P.; Radhakrishnan, G.: Artificial neural network applications in electrochemistry-A review. *Bulletin of Electrochemistry* **1999**, *15*, 552-555.
105. Meng, Y.; Lan, Q.; Qin, J.; Yu, S.; Pang, H.; Zheng, K.: Data-driven soft sensor modeling based on twin support vector regression for cane sugar crystallization. *Journal of food engineering* **2019**, *241*, 159-165.
106. Moraru, A.; Pesko, M.; Porcius, M.; Fortuna, C.; Mladenic, D.: Using machine learning on sensor data. *Journal of computing and information technology* **2010**, *18*, 341-347.
107. Antuña-Jiménez, D.; González-García, M. B.; Hernández-Santos, D.; Fanjul-Bolado, P.: Screen-printed electrodes modified with metal nanoparticles for small molecule sensing. *Biosensors* **2020**, *10*, 9.
108. Xiang, C.; Weber, A. Z.; Ardo, S.; Berger, A.; Chen, Y.; Coridan, R.; Fountaine, K. T.; Haussener, S.; Hu, S.; Liu, R.: Modeling, simulation, and implementation of solar-driven water-splitting devices. *Angewandte Chemie International Edition* **2016**, *55*, 12974-12988.

109. Ali-Löytty, H.; Louie, M. W.; Singh, M. R.; Li, L.; Sanchez Casalongue, H. G.; Ogasawara, H.; Crumlin, E. J.; Liu, Z.; Bell, A. T.; Nilsson, A.: Ambient-pressure XPS study of a Ni–Fe electrocatalyst for the oxygen evolution reaction. *The Journal of Physical Chemistry C* **2016**, *120*, 2247-2253.
110. Kiesow, K.; Tumakaka, F.; Sadowski, G.: Experimental investigation and prediction of oiling out during crystallization process. *Journal of crystal growth* **2008**, *310*, 4163-4168.
111. Deneau, E.; Steele, G.: An in-line study of oiling out and crystallization. *Organic process research & development* **2005**, *9*, 943-950.
112. Van Lindt, J.; Bratek-Skicki, A.; Nguyen, P. N.; Pakravan, D.; Durán-Armenta, L. F.; Tantos, A.; Pancsa, R.; Van Den Bosch, L.; Maes, D.; Tompa, P.: A generic approach to study the kinetics of liquid–liquid phase separation under near-native conditions. *Communications Biology* **2021**, *4*, 77.
113. Takasuga, M.; Ooshima, H.: Control of crystal size during oiling out crystallization of an api. *Crystal growth & design* **2014**, *14*, 6006-6011.
114. de Albuquerque, I.; Mazzotti, M.: Crystallization process design using thermodynamics to avoid oiling out in a mixture of vanillin and water. *Crystal growth & design* **2014**, *14*, 5617-5625.
115. Zhang, X.; Wei, Z.; Choi, H.; Hao, H.; Yang, H.: Oiling-Out Crystallization of Beta-Alanine on Solid Surfaces Controlled by Solvent Exchange. *Advanced Materials Interfaces* **2021**, *8*, 2001200.
116. Lu, J.; Li, Y.-P.; Wang, J.; Ren, G.-B.; Rohani, S.; Ching, C.-B.: Crystallization of an active pharmaceutical ingredient that oils out. *Separation and purification technology* **2012**, *96*, 1-6.
117. Duffy, D.; Cremin, N.; Napier, M.; Robinson, S.; Barrett, M.; Hao, H.; Glennon, B.: In situ monitoring, control and optimization of a liquid–liquid phase separation crystallization. *Chemical engineering science* **2012**, *77*, 112-121.
118. Bhamidi, V.; Abolins, B. P.: A thermodynamic approach for the prediction of oiling out boundaries from solubility data. *Processes* **2019**, *7*, 577.
119. Adlington, N. K.; Black, S. N.; Adshead, D. L.: How to use the lasentec FBRM probe on manufacturing scale. *Organic Process Research & Development* **2013**, *17*, 557-567.
120. Zhao, H.; Xie, C.; Xu, Z.; Wang, Y.; Bian, L.; Chen, Z.; Hao, H.: Solution crystallization of vanillin in the presence of a liquid–liquid phase separation. *Industrial & engineering chemistry research* **2012**, *51*, 14646-14652.
121. Simon, L. L.; Pataki, H.; Marosi, G. r.; Meemken, F.; Hungerbühler, K.; Baiker, A.; Tummala, S.; Glennon, B.; Kuentz, M.; Steele, G.: Assessment of recent process analytical technology (PAT) trends: a multiauthor review. *Organic Process Research & Development* **2015**, *19*, 3-62.
122. P. U. Siahaan, A.; Silitonga, N.; Iqbal, M.; Aryza, S.; Fitriani, W.; Ramadhan, Z.; Tharo, Z.; ., R.; Hidayat, R.; D. T. P. Nasution, M.; Ikhwan, A.; Azhar, Z.; Irwan Dwitama Harahap, M.: Arduino Uno-based water turbidity meter using LDR and LED sensors. *2018* **2018**, *7*, 5.
123. Dignon, G. L.; Zheng, W.; Kim, Y.; Mittal, J.: A High-Throughput Approach to Phase Separation of Disordered Proteins. *Biophysical Journal* **2019**, *116*, 350a.
124. Stender, E. G.; Norrild, R. K.; Larsen, J. A.; Jensen, H.; Buell, A.: Capillary flow experiments (Capflex) for thermodynamic and kinetic characterization of protein LLPS at high throughput. **2021**.
125. Mulyana, Y.; Hakim, D.: Prototype of water turbidity monitoring system. In *IOP Conference Series: Materials Science and Engineering*; IOP Publishing, 2018; Vol. 384; pp 012052.

126. Komiyama, R.; Kageyama, T.; Miura, M.; Miyashita, H.; Lee, S.: Turbidity monitoring of lake water by transmittance measuresment with a simple optical setup. In *2015 IEEE SENSORS*, 2015; pp 1-4.
127. Sun, M.; Tang, W.; Du, S.; Zhang, Y.; Fu, X.; Gong, J.: Understanding the roles of oiling-out on crystallization of β-alanine: unusual behavior in metastable zone width and surface nucleation during growth stage. *Crystal Growth & Design* **2018**, *18*, 6885-6890.
128. Basařová, P.; Pišlová, J.; Mills, J.; Orvalho, S.: Influence of molecular structure of alcohol-water mixtures on bubble behaviour and bubble surface mobility. *Chemical Engineering Science* **2018**, *192*, 74-84.
129. Sun, M.; Du, S.; Chen, M.; Rohani, S.; Zhang, H.; Liu, Y.; Sun, P.; Wang, Y.; Shi, P.; Xu, S.; Gong, J.: Oiling-Out Investigation and Morphology Control of β-Alanine Based on Ternary Phase Diagrams. *Crystal Growth & Design* **2018**, *18*, 818-826.
130. Choi, H.; Wei, Z.; You, J. B.; Yang, H.; Zhang, X.: Effects of Chemical and Geometric Microstructures on the Crystallization of Surface Droplets during Solvent Exchange. *Langmuir* **2021**, *37*, 5290-5298.
131. Sun, M.; Du, S.; Chen, M.; Rohani, S.; Zhang, H.; Liu, Y.; Sun, P.; Wang, Y.; Shi, P.; Xu, S.: Oiling-out investigation and morphology control of β-alanine based on ternary phase diagrams. *Crystal Growth & Design* **2018**, *18*, 818-826.
132. Zhang, X.; Wei, Z.; Choi, H.; Hao, H.; Yang, H.: Oiling-Out Crystallization of Beta-Alanine on Solid Surfaces Controlled by Solvent Exchange. *Advanced Materials Interfaces* **2021**, *8*, 2001200.
133. Li, Y. S.; Bux, H.; Feldhoff, A.; Li, G. L.; Yang, W. S.; Caro, J.: Controllable synthesis of metal–organic frameworks: From MOF nanorods to oriented MOF membranes. *Advanced Materials* **2010**, *22*, 3322-3326.
134. Yuan, S.; Feng, L.; Wang, K.; Pang, J.; Bosch, M.; Lollar, C.; Sun, Y.; Qin, J.; Yang, X.; Zhang, P.: Stable metal–organic frameworks: design, synthesis, and applications. *Advanced Materials* **2018**, *30*, 1704303.
135. Butova, V. V. e.; Soldatov, M. A.; Guda, A. A.; Lomachenko, K. A.; Lamberti, C.: Metal-organic frameworks: structure, properties, methods of synthesis and characterization. *Russian Chemical Reviews* **2016**, *85*, 280.
136. Zhou, H.-C.; Long, J. R.; Yaghi, O. M.: Introduction to metal–organic frameworks. *Chemical reviews* **2012**, *112*, 673-674.
137. Allendorf, M. D.; Stavila, V.: Crystal engineering, structure–function relationships, and the future of metal–organic frameworks. *CrystEngComm* **2015**, *17*, 229-246.
138. Aljammal, N.; Jabbour, C.; Chaemchuen, S.; Juzsakova, T.; Verpoort, F.: Flexibility in metal–organic frameworks: A basic understanding. *Catalysts* **2019**, *9*, 512.
139. Pettinari, C.; Marchetti, F.; Mosca, N.; Tosi, G.; Drozdov, A.: Application of metal−organic frameworks. *Polymer International* **2017**, *66*, 731-744.
140. Ma, S.; Zhou, H.-C.: Gas storage in porous metal–organic frameworks for clean energy applications. *Chemical Communications* **2010**, *46*, 44-53.
141. Mason, J. A.; Veenstra, M.; Long, J. R.: Evaluating metal–organic frameworks for natural gas storage. *Chemical Science* **2014**, *5*, 32-51.
142. Schröder, M.: *Functional metal-organic frameworks: gas storage, separation and catalysis*; Springer, 2010; Vol. 293.
143. Denny, M. S.; Moreton, J. C.; Benz, L.; Cohen, S. M.: Metal–organic frameworks for membrane-based separations. *Nature Reviews Materials* **2016**, *1*, 1-17.
144. Zhao, X.; Wang, Y.; Li, D. S.; Bu, X.; Feng, P.: Metal–organic frameworks for separation. *Advanced Materials* **2018**, *30*, 1705189.

145. Li, J.-R.; Sculley, J.; Zhou, H.-C.: Metal–organic frameworks for separations. *Chemical reviews* **2012**, *112*, 869-932.
146. Krishna, R.: Methodologies for evaluation of metal–organic frameworks in separation applications. *RSC advances* **2015**, *5*, 52269-52295.
147. Maleki, A.; Hayati, B.; Naghizadeh, M.; Joo, S. W.: Adsorption of hexavalent chromium by metal organic frameworks from aqueous solution. *Journal of Industrial and Engineering Chemistry* **2015**, *28*, 211-216.
148. Liu, J.; Thallapally, P. K.; McGrail, B. P.; Brown, D. R.; Liu, J.: Progress in adsorption-based CO 2 capture by metal–organic frameworks. *Chemical Society Reviews* **2012**, *41*, 2308-2322.
149. Li, J.-R.; Kuppler, R. J.; Zhou, H.-C.: Selective gas adsorption and separation in metal–organic frameworks. *Chemical Society Reviews* **2009**, *38*, 1477-1504.
150. Ranocchiari, M.; van Bokhoven, J. A.: Catalysis by metal–organic frameworks: fundamentals and opportunities. *Physical Chemistry Chemical Physics* **2011**, *13*, 6388-6396.
151. Wang, C.; An, B.; Lin, W.: Metal–organic frameworks in solid–gas phase catalysis. *ACS Catalysis* **2018**, *9*, 130-146.
152. Banerjee, D.; Hu, Z.; Li, J.: Luminescent metal–organic frameworks as explosive sensors. *Dalton transactions* **2014**, *43*, 10668-10685.
153. Kumar, P.; Deep, A.; Kim, K.-H.: Metal organic frameworks for sensing applications. *TrAC Trends in Analytical Chemistry* **2015**, *73*, 39-53.
154. Koo, W.-T.; Jang, J.-S.; Kim, I.-D.: Metal-organic frameworks for chemiresistive sensors. *Chem* **2019**, *5*, 1938-1963.
155. Yi, F.-Y.; Chen, D.; Wu, M.-K.; Han, L.; Jiang, H.-L.: Chemical sensors based on metal-organic frameworks. *ChemPlusChem* **2016**, *81*, 675.
156. Lu, Y.; Yan, B.: Lanthanide organic–inorganic hybrids based on functionalized metal–organic frameworks (MOFs) for a near-UV white LED. *Chemical Communications* **2014**, *50*, 15443-15446.
157. Keskin, S.; Kızılel, S.: Biomedical applications of metal organic frameworks. *Industrial & Engineering Chemistry Research* **2011**, *50*, 1799-1812.
158. Horcajada, P.; Serre, C.; Vallet-Regí, M.; Sebban, M.; Taulelle, F.; Férey, G.: Metal–organic frameworks as efficient materials for drug delivery. *Angewandte chemie* **2006**, *118*, 6120-6124.
159. Della Rocca, J.; Liu, D.; Lin, W.: Nanoscale metal–organic frameworks for biomedical imaging and drug delivery. *Accounts of chemical research* **2011**, *44*, 957-968.
160. Wang, L.; Zheng, M.; Xie, Z.: Nanoscale metal–organic frameworks for drug delivery: a conventional platform with new promise. *Journal of Materials Chemistry B* **2018**, *6*, 707-717.
161. Li, X.; Yang, X.; Xue, H.; Pang, H.; Xu, Q.: Metal–organic frameworks as a platform for clean energy applications. *EnergyChem* **2020**, *2*, 100027.
162. Varsha, M.; Nageswaran, G.: Direct Electrochemical Synthesis of Metal Organic Frameworks. *Journal of the Electrochemical Society* **2020**.
163. Martinez Joaristi, A.; Juan-Alcañiz, J.; Serra-Crespo, P.; Kapteijn, F.; Gascon, J.: Electrochemical synthesis of some archetypical Zn2+, Cu2+, and Al3+ metal organic frameworks. *Crystal Growth & Design* **2012**, *12*, 3489-3498.
164. Campagnol, N.; Van Assche, T.; Boudewijns, T.; Denayer, J.; Binnemans, K.; De Vos, D.; Fransaer, J.: High pressure, high temperature electrochemical synthesis of metal–organic frameworks: films of MIL-100 (Fe) and HKUST-1 in different morphologies. *Journal of Materials Chemistry A* **2013**, *1*, 5827-5830.

165. Yuan, W.; O'Connor, J.; James, S. L.: Mechanochemical synthesis of homo-and hetero-rare-earth (III) metal–organic frameworks by ball milling. *CrystEngComm* **2010**, *12*, 3515-3517.
166. Tao, C.-A.; Wang, J.-F.: Synthesis of Metal Organic Frameworks by Ball-Milling. *Crystals* **2021**, *11*, 15.
167. Masoomi, M. Y.; Bagheri, M.; Morsali, A.: High adsorption capacity of two Zn-based metal–organic frameworks by ultrasound assisted synthesis. *Ultrasonics sonochemistry* **2016**, *33*, 54-60.
168. Masoomi, M. Y.; Morsali, A.: Sonochemical synthesis of nanoplates of two Cd (II) based metal–organic frameworks and their applications as precursors for preparation of nano-materials. *Ultrasonics sonochemistry* **2016**, *28*, 240-249.
169. Noh, S.-J.; Kim, J.: Solvothermal synthesis and gas permeation properties of nanoporous HKUST-1 membranes. *Membrane Journal* **2012**, *22*, 435-440.
170. McKinstry, C.; Cathcart, R. J.; Cussen, E. J.; Fletcher, A. J.; Patwardhan, S. V.; Sefcik, J.: Scalable continuous solvothermal synthesis of metal organic framework (MOF-5) crystals. *Chemical Engineering Journal* **2016**, *285*, 718-725.
171. Nie, M.; Lu, S.; Li, Q.; Liu, X.; Du, S.: Facile solvothermal synthesis of HKUST-1 as electrocatalyst for hydrogen evolution reaction. *Scientia Sinica Chimica* **2016**, *46*, 357-364.
172. Dhakshinamoorthy, A.; Asiri, A. M.; Garcia, H.: 2D metal–organic frameworks as multifunctional materials in heterogeneous catalysis and electro/photocatalysis. *Advanced Materials* **2019**, *31*, 1900617.
173. Zhu, H.; Liu, D.: The synthetic strategies of metal–organic framework membranes, films and 2D MOFs and their applications in devices. *Journal of Materials Chemistry A* **2019**, *7*, 21004-21035.
174. Liu, Z.; Zhu, J.; Peng, C.; Wakihara, T.; Okubo, T.: Continuous flow synthesis of ordered porous materials: from zeolites to metal–organic frameworks and mesoporous silica. *Reaction Chemistry & Engineering* **2019**, *4*, 1699-1720.
175. Rasmussen, E. G.; Kramlich, J.; Novosselov, I. V.: Scalable Continuous Flow Metal–Organic Framework (MOF) Synthesis Using Supercritical CO2. *ACS Sustainable Chemistry & Engineering* **2020**, *8*, 9680-9689.
176. Bayliss, P. A.; Ibarra, I. A.; Pérez, E.; Yang, S.; Tang, C. C.; Poliakoff, M.; Schröder, M.: Synthesis of metal–organic frameworks by continuous flow. *Green Chemistry* **2014**, *16*, 3796-3802.
177. Huo, J.; Brightwell, M.; El Hankari, S.; Garai, A.; Bradshaw, D.: A versatile, industrially relevant, aqueous room temperature synthesis of HKUST-1 with high space-time yield. *Journal of Materials Chemistry A* **2013**, *1*, 15220-15223.
178. Ameloot, R.; Vermoortele, F.; Vanhove, W.; Roeffaers, M. B.; Sels, B. F.; De Vos, D. E.: Interfacial synthesis of hollow metal–organic framework capsules demonstrating selective permeability. *Nature chemistry* **2011**, *3*, 382-387.
179. Faustini, M.; Kim, J.; Jeong, G.-Y.; Kim, J. Y.; Moon, H. R.; Ahn, W.-S.; Kim, D.-P.: Microfluidic approach toward continuous and ultrafast synthesis of metal–organic framework crystals and hetero structures in confined microdroplets. *Journal of the American Chemical Society* **2013**, *135*, 14619-14626.
180. Gimeno-Fabra, M.; Munn, A. S.; Stevens, L. A.; Drage, T. C.; Grant, D. M.; Kashtiban, R. J.; Sloan, J.; Lester, E.; Walton, R. I.: Instant MOFs: continuous synthesis of metal–organic frameworks by rapid solvent mixing. *Chemical Communications* **2012**, *48*, 10642-10644.
181. Bartneck, M.; Schulte, V. A.; Paul, N. E.; Diez, M.; Lensen, M. C.; Zwadlo-Klarwasser, G.: Induction of specific macrophage subtypes by defined micro-patterned structures. *Acta biomaterialia* **2010**, *6*, 3864-3872.

182. Zhuang, J. L.; Ceglarek, D.; Pethuraj, S.; Terfort, A.: Rapid room-temperature synthesis of metal–organic framework HKUST-1 crystals in bulk and as oriented and patterned thin films. *Advanced functional materials* **2011**, *21*, 1442-1447.
183. Wang, X.; Cheng, Q.; Yu, Y.; Zhang, X.: A general and scalable approach with controlled nucleation and controlled growth for size predicable synthesis of nanoscale MOFs. *Angew. Chem., Int. Ed* **2018**, *57*, 7836-7840.
184. Seetharaj, R.; Vandana, P.; Arya, P.; Mathew, S.: Dependence of solvents, pH, molar ratio and temperature in tuning metal organic framework architecture. *Arabian journal of chemistry* **2019**, *12*, 295-315.
185. Chu, Q.; Liu, G.-X.; Okamura, T.-a.; Huang, Y.-Q.; Sun, W.-Y.; Ueyama, N.: Structure modulation of metal–organic frameworks via reaction pH: Self-assembly of a new carboxylate containing ligand N-(3-carboxyphenyl) iminodiacetic acid with cadmium (II) and cobalt (II) salts. *Polyhedron* **2008**, *27*, 812-820.
186. Pan, L.; Frydel, T.; Sander, M. B.; Huang, X.; Li, J.: The effect of pH on the dimensionality of coordination polymers. *Inorganic chemistry* **2001**, *40*, 1271-1283.
187. Tovar, T. M.; Zhao, J.; Nunn, W. T.; Barton, H. F.; Peterson, G. W.; Parsons, G. N.; LeVan, M. D.: Diffusion of CO2 in large crystals of Cu-BTC MOF. *Journal of the American Chemical Society* **2016**, *138*, 11449-11452.
188. Majano, G.; Martin, O.; Hammes, M.; Smeets, S.; Baerlocher, C.; Pérez-Ramírez, J.: Solvent-Mediated Reconstruction of the Metal–Organic Framework HKUST-1 (Cu3 (BTC) 2). *Advanced Functional Materials* **2014**, *24*, 3855-3865.
189. Van Ngo, T.; Moussa, M.; Tung, T. T.; Coghlan, C.; Losic, D.: Hybridization of MOFs and graphene: A new strategy for the synthesis of porous 3D carbon composites for high performing supercapacitors. *Electrochimica Acta* **2020**, *329*, 135104.

VITA

EDUCATIONAL BACKGROUND

Bachelor of Engineering, Chemical Engineering GPA 16.1/20.0

Sharif University of Technology (SUT), Tehran. Iran
September 2011 - June 2016

Doctor of Philosophy, Chemical Engineering GPA 3.64/4

University of Illinois at Chicago (UIC), Chicago, IL. USA
August 2016 – present

RESEARCH EXPERIENCE

University of Illinois at Chicago August 2016 - Present

Graduate Research Assistant Advisor: Prof. Meenesh. R. Singh

Title: Towards Crystallization and Microfluidic Developments for High-throughput Screening

AbbVie Inc laboratories

Research Intern

Advisors: Dr. Manish S. Kelkar, Dr. Moussa Boukerche, Dr. Nandkishor K. Nere

- Analyzed different designs for developing a microfluidic platform for studying forms and morphology of crystals under controlled supersaturation. (Summer 2018)
- Developed a multi-well microfluidic mixer for screening morphology and form of APIs. (Summer 2019)
- Developed a computational model for wet milling with the in-line fine dissolution of APIs. (Summer 2020)

Teaching Experience

Teaching Assistant, University of Illinois at Chicago

- Chemical Engineering Senior Design (CHE 396), Fall 2016
- Transport Phenomena (CHE 312), Spring 2017

- Mathematical Methods in Chemical Engineering (CHE 445), Fall 2017
- General Chemistry II Lab (CHEM 125), Spring 2018
- General Chemistry II Lab (CHEM 124), Spring 2018
- Chemical Engineering Unit Operation Lab (CHE 381), Fall 2018
- Mathematical Methods in Chemical Engineering (CHE 445), Fall 2018
- Biology of Cells Organisms (BIOS 110), Spring 2019 - Spring 2021
- Biology of Cells Organisms (BIOS 110), Spring 2019 - Summer 2021

AWARDS

1. Chancellor's Student Service and Leadership Award (CSSLA), UIC, Spring 2018
2. Graduate Student Council Travel Award (GSC), UIC, Fall 2018
3. Provost's Graduate Internship Award (PGIA), UIC, Summer 2020
4. Provost's Graduate Research Award (PGRA), UIC, Fall 2021
5. AIChE Woman in Chemical Engineering (WIC), Fall 2021

PATENTS

Meenesh R. Singh, and Paria Coliaie," Continuous-Flow, Well Mixed, Microfluidic Crystallization Device for Screening Polymorphs, Morphologies and Crystallization Kinetics at Controlled Supersaturation" PCT/US20/36353, 2020

PUBLICATIONS

Published

1. Paria Coliaie*, Manish S. Kelkar, Nandkishor K. Nere, and Meenesh R. Singh "Continuous- flow, Well-mixed, Microfluidic Crystallization Device for Screening of Polymorphs, Morphology, and Crystallization Kinetics at Controlled Supersaturation", Lab on a Chip, June 2019

2. Paria Coliaie*, Manish S. Kelkar, Marianne Langston, Daniel Patience, Dimitri Skliar, Chengxiang Liu, Nandkishor K. Nere, and Meenesh R. Singh" Advanced Continuous-Flow Microfluidic Device for Parallel Screening of Crystal Polymorphs, Morphology and Kinetics at Controlled Supersaturation", Lab on a Chip, June 2021